

## **Copyright Warning & Restrictions**

The copyright law of the United States (Title 17, United States Code) governs the making of photocopies or other reproductions of copyrighted material.

Under certain conditions specified in the law, libraries and archives are authorized to furnish a photocopy or other reproduction. One of these specified conditions is that the photocopy or reproduction is not to be “used for any purpose other than private study, scholarship, or research.” If a user makes a request for, or later uses, a photocopy or reproduction for purposes in excess of “fair use” that user may be liable for copyright infringement,

This institution reserves the right to refuse to accept a copying order if, in its judgment, fulfillment of the order would involve violation of copyright law.

**Please Note: The author retains the copyright while the New Jersey Institute of Technology reserves the right to distribute this thesis or dissertation**

Printing note: If you do not wish to print this page, then select “Pages from: first page # to: last page #” on the print dialog screen

The Van Houten library has removed some of the personal information and all signatures from the approval page and biographical sketches of theses and dissertations in order to protect the identity of NJIT graduates and faculty.

## ABSTRACT

# COMPUTATION AND CONTROL OF FLOW-INDUCED NOISE BEHIND A CIRCULAR CYLINDER USING AN ACOUSTIC ANALOGY APPROACH

by  
**Sirivit Taechajedcadarungsri**

The computational aeroacoustics (CAA) research, which focuses on predicting acoustics by means of advanced numerical techniques, has recently gained a great deal of progress. In most applications, the prediction of both the sound source and its far-field propagation is necessary as required by regulations. Recently, powerful computers and reliable algorithms have allowed the prediction of far-field noise through the use of Computational Fluid Dynamics (CFD) data as near-field sound sources. One of the most useful analytical methods, used for the computation of noise, is Lighthill's acoustic analogy. The latter will be used in the present study.

Lighthill's acoustic analogy, combined with the two-dimensional incompressible Navier-Stokes flow computation at low Mach Number ( $M \ll 1$ ), is used to predict the noise generated by laminar vortex shedding from a circular cylinder at the Reynolds number values  $Re = 100$  and  $Re = 160$ . The computed velocity and pressure in the flow field are used as input data for noise source functions. The noise prediction is determined by using Curle's solution of Lighthill's acoustic analogy. Due to the fact that the magnitude of the quadrupole noise source ( $\mathcal{O}(M^3)$ ) for this type of flow is much smaller than that of the dipole source ( $\mathcal{O}(M^2)$ ) at low Mach Number, this study concentrates on investigating only the effect of the dipole source on the flow field.

The noise amplitude and frequency obtained by using Curle's solution agree well with published data. For both values of Reynolds numbers  $Re = 100$  and

$Re = 160$ , the "lift" dipole source function, caused by the lift force acting on a circular cylinder, is the dominant source term that affects the total acoustic density fluctuation. The objective of this research is to study the suppression of flow-induced noise behind a circular cylinder using a flow control method. The selected method is the electro-magnetic feedback control method developed by Chen and Aubry (2000). The results show that at  $Re = 100$  and  $Re = 160$  the nondimensional acoustic density fluctuation is decreased by five orders of magnitude.



**COMPUTATION AND CONTROL OF FLOW-INDUCED NOISE  
BEHIND A CIRCULAR CYLINDER USING AN ACOUSTIC  
ANALOGY APPROACH**

by  
**Sirivit Taechajedcadarungsri**

**A Dissertation  
Submitted to the Faculty of  
New Jersey Institute of Technology  
in Partial Fulfillment of the Requirements for the Degree of  
Doctor of Philosophy in Mechanical Engineering**

**Department of Mechanical Engineering**

**January 2002**

Copyright © 2002 by Sirivit Taechajedcadarungsri

ALL RIGHTS RESERVED

## APPROVAL PAGE

### COMPUTATION AND CONTROL OF FLOW-INDUCED NOISE BEHIND A CIRCULAR CYLINDER USING AN ACOUSTIC ANALOGY APPROACH

**Sirivit Taechajedcadarungsri**

Nadine Aubry, Ph.D., Dissertation Advisor Chairperson and Professor, Department of Mechanical Engineering, Professor, Department of Mathematical Sciences, New Jersey Institute of Technology, Newark NJ	Date
---	------

Ernest S. Geskin, Ph.D., Committee Member Professor, Department of Mechanical Engineering, New Jersey Institute of Technology, Newark NJ	Date
--	------

Chao Zhu, Ph.D., Committee Member Assistant Professor, Department of Mechanical Engineering, New Jersey Institute of Technology, Newark NJ	Date
--	------

Pushpendra Singh, Ph.D., Committee Member Associate Professor, Department of Mechanical Engineering, New Jersey Institute of Technology, Newark NJ	Date
--	------

Demetrios T. Papageorgiou, Ph.D., Committee Member Professor, Department of Mathematical Sciences, New Jersey Institute of Technology, Newark NJ	Date
--	------

## BIOGRAPHICAL SKETCH

**Author:** Sirivit Taechajedcadarungsri

**Degree:** Doctor of Philosophy in Mechanical Engineering

**Date:** January 2002

### Undergraduate and Graduate Education:

- Doctor of Philosophy in Mechanical Engineering, 2002  
New Jersey Institute of Technology, Newark, NJ
- Master of Science in Mechanical Engineering, 1998  
New Jersey Institute of Technology, Newark, NJ
- Bachelor of Science in Mechanical Engineering, 1989  
Khonkean University, Khonkean, Thailand

**Major:** Mechanical Engineering

To my family

## ACKNOWLEDGMENT

I would like to extend my sincerest appreciation to my advisor, Prof. Nadine Aubry for providing me with the motivation, and valuable guidance throughout my entire course of study. Her resourceful knowledge and patience were the key to the completion of my research. A special word of gratitude goes to Dr. Pushpendra Singh for his subsequent input and feedback on my dissertation. I would like to thank Prof. Demetrios T. Papageorgiou for his time and helpful advice. I would also like to thank the members of my dissertation committee, Prof. Ernest S. Geskin and Dr. Chao Zhu for their suggestions and guidance.

I give my deepest appreciation to Royal Thai Government who made coming to NJIT possible for me. Special thanks to Dr. Ronald S. Kane, Dean of Graduate Studies, and the Department of Mechanical Engineering for allocating funds necessary for me to conduct my research.

I am grateful to Miss Sharyn Serafin who organizes our group meeting every week. Thanks to my colleagues and fellow graduate students for their valuable opinions and constant support, in particular, Dr. Wiwat Kamalpornwijit and Miss Dawn J. Bennett.

Finally, my heartfelt thanks to my special friend, Miss Mingming Ho, for her moral support, encouragement and understanding that strengthen my belief in myself during the moment of despair. I am greatly indebted to my parents and sisters for nurturing and cherishing my academic endeavors and without whose help and support I would have never made it this far.

# TABLE OF CONTENTS

Chapter	Page
1 INTRODUCTION . . . . .	1
1.1 Background . . . . .	2
1.1.1 Wake Flow Behind a Circular Cylinder and Its Control . . . . .	2
1.1.2 Acoustic Background . . . . .	5
1.2 Motivation . . . . .	8
1.3 Objectives . . . . .	10
1.4 Dissertation Organization . . . . .	12
2 REVIEW OF FLOW FIELD COMPUTATIONAL METHODS . . . . .	14
2.1 Governing Equations . . . . .	14
2.2 Initial and Boundary Conditions . . . . .	16
2.3 Applied Electro-Magnetic Forces . . . . .	17
2.4 Pressure and Force Coefficients . . . . .	19
2.5 An Adaptive Scheme for the Vorticity . . . . .	20
2.5.1 Numerical Methods . . . . .	20
2.6 Feedback Control of Cylinder Wake . . . . .	22
3 Lighthill's ACOUSTIC THEORY . . . . .	23
3.1 Analysis of Lighthill Equation . . . . .	23
3.2 The Solution of Lighthill's Equation for Stationary Solid Boundaries and Uniform Moving Medium . . . . .	30

# TABLE OF CONTENTS (Continued)

Chapter		Page
3.2.1	Three-Dimensional Fields . . . . .	30
3.2.2	2-D Dimensionless Fields . . . . .	35
4	COMPUTATIONAL RESULTS . . . . .	38
4.1	Flow Field . . . . .	38
4.1.1	Without Control . . . . .	38
4.1.2	With Control . . . . .	45
4.2	Acoustic Field . . . . .	54
4.2.1	Without Control . . . . .	54
4.2.2	With Control . . . . .	78
4.3	Sound Pressure Level . . . . .	85
4.3.1	Sound Pressure Level (SPL) at $Re = 100$ . . . . .	94
4.3.2	Sound Pressure Level (SPL) at $Re = 160$ . . . . .	94
5	CONCLUSIONS . . . . .	102
APPENDIX A SOME INTEGRAL FORMULAE FROM VECTOR ANALYSIS		105
APPENDIX B DERIVATION OF THE INHOMOGENEOUS WAVE EQUATION FOR A UNIFORMLY MOVING MEDIUM . . . . .		107
APPENDIX C THE NUMERICAL RESULTS IN DIMENSIONAL FORM FOR SOUND PRESSURE LEVEL CALCULATIONS . . . . .		109
REFERENCES . . . . .		136



## LIST OF TABLES

Table	Page
4.1 Sound Pressure Level . . . . .	93
4.2 Change in Sound Level . . . . .	93

## LIST OF FIGURES

Figure	Page
1.1 Generation of æolian tones.[Howe, 1998] . . . . .	9
1.2 Flow configuration and coordinate system in physical space . . . . .	10
2.1 Flow configuration and system of coordinates . . . . .	15
2.2 Sketch of the cylinder consisting of electrodes and magnets . . . . .	18
4.1 The grid used around the cylinder with $400 \times 256$ grid points . . . . .	39
4.2 Streamlines of the flow at the Reynolds number value $Re = 100$ for the time interval $760 \leq t \leq 800$ . . . . .	41
4.3 Time history of the drag and lift coefficients at the Reynolds number value $Re = 100$ . . . . .	42
4.4 Variation of the drag and lift coefficients on the surface of the cylinder at the Reynolds number value $Re = 100$ . . . . .	43
4.5 Pressure coefficient of the flow on the surface of the cylinder at the Reynolds number value $Re = 100$ at times $t = 400, 500, 600, 700, 800 \dots$	44
4.6 Streamlines of the flow at the Reynolds number value $Re = 160$ for the time interval $760 \leq t \leq 800$ . . . . .	46
4.7 Time history of the drag and lift coefficients at the Reynolds number value $Re = 160$ . . . . .	47
4.8 Variation of the drag and lift coefficients on the surface of the cylinder at the Reynolds number value $Re = 160$ . . . . .	48
4.9 Pressure coefficient of the flow on the surface of the cylinder at the Reynolds number value $Re = 160$ at times $t = 400, 500, 600, 700, 800 \dots$	49
4.10 Streamlines of the flow with control at the Reynolds number value $Re =$ $100$ for the time interval $620 \leq t \leq 638$ . The control is inserted at time $t = 620$ . . . . .	50

Figure	Page
4.11 Time history of the drag and lift coefficients at the Reynolds number value $Re = 100$ . The control is inserted at time $t = 620$ . . . . .	51
4.12 Variation of the drag and lift coefficients on the surface of the cylinder at the Reynolds number value $Re = 100$ with and without control for the time interval $760 \leq t \leq 800$ . The control is inserted at time $t = 620$	52
4.13 Pressure coefficient of the flow on the surface of the cylinder at the Reynolds number value $Re = 100$ at times $t = 620, 630, 650, 750, 780$ . The control is inserted at time $t = 620$ . . . . .	53
4.14 Streamlines of the flow with control at the Reynolds number value $Re = 160$ for the time interval $620 \leq t \leq 638$ . The control is inserted at time $t = 620$ . . . . .	55
4.15 Time history of the drag and lift coefficients at the Reynolds number value $Re = 160$ . The control is inserted at time $t = 620$ . . . . .	56
4.16 Variation of the drag and lift coefficients on the surface of the cylinder at the Reynolds number value $Re = 160$ with and without control for the time interval $760 \leq t \leq 800$ . The control is inserted at time $t = 620$	57
4.17 Pressure coefficient of the flow on the surface of the cylinder at the Reynolds number value $Re = 160$ at times $t = 620, 630, 650, 750, 780$ . The control is inserted at time $t = 620$ . . . . .	58
4.18 Drag and lift dipoles at the Reynolds number value $Re = 100$ using various numbers of subintervals in the integral of Equation (3.50), that is $Mterms = 500, 1000, 5000, 8000, 10000$ . . . . .	60
4.19 Drag and lift dipoles at the Reynolds number value $Re = 100$ using various numbers of subintervals in the integral of Equation (3.50), that is $Mterms = 5000$ , and $8000$ and various time derivative increments $dt_{ret} = 5 \times 10^{-5}, 5 \times 10^{-8}$ , and $5 \times 10^{-12}$ . . . . .	62
4.20 Drag and lift dipoles at the Reynolds number value $Re = 100$ using the number of subintervals in the integral of Equation (3.50), that is $Mterms = 5000$ . The results are compared with those of You <i>et al.</i> , 1998 . . . . .	63

Figure	Page
4.21 Acoustic density at the Reynolds number value $Re = 160$ using the number of subintervals in the integral of Equation (3.50), that is $Mterms = 5000$ . The results are compared with those of You <i>et al.</i> , 1998 . . . . .	64
4.22 Drag dipole at the Reynolds number value $Re = 100$ using the number of subintervals $Mterms = 5000$ in the integral of Equation (3.50) for various observer positions . . . . .	65
4.23 Lift dipole at the Reynolds number value $Re = 100$ using the number of subintervals $Mterms = 5000$ in the integral of Equation (3.50) for various observer positions . . . . .	66
4.24 Acoustic density at the Reynolds number value $Re = 100$ using the number of subintervals $Mterms = 5000$ in the integral of Equation (3.50) for various observer positions . . . . .	67
4.25 Contour of the acoustic density at the Reynolds number value $Re = 100$ using the number of subintervals $Mterms = 5000$ in the integral of Equation (3.50) and the far-field domain $(-2000 \leq x_1, x_2 \leq 2000)$ . . .	69
4.26 Drag and lift dipoles at the Reynolds number value $Re = 160$ using various numbers of subintervals in the integral of Equation (3.50), that is $Mterms = 500, 1000, 5000, 8000, 10000$ . . . . .	70
4.27 Drag and lift dipoles at the Reynolds number value $Re = 160$ using various numbers of subintervals in the integral of Equation (3.50), that is $Mterms = 5000$ and $8000$ for various time derivative increments $dt_{ret} = 5 \times 10^{-5}, 5 \times 10^{-8}$ , and $5 \times 10^{-12}$ . . . . .	71
4.28 Drag and lift Dipoles at the Reynolds number value $Re = 160$ using the number of subintervals in the integral of Equation (3.50), that is $Mterms = 5000$ . The results are compared with those of You <i>et al.</i> , 1998 . . . . .	72
4.29 Acoustic density at the Reynolds number value $Re = 160$ using the number of subintervals in the integral of Equation (3.50), that is $Mterms = 5000$ . The results are compared with those of You <i>et al.</i> , 1998 . . . . .	73
4.30 Drag dipoles at the Reynolds number value $Re = 160$ using the number of subintervals $Mterms = 5000$ in the integral of Equation (3.50) for various observer positions . . . . .	74

Figure	Page
4.31 Lift dipole at the Reynolds number value $Re = 160$ using the number of subintervals $Mterms = 5000$ in the integral of Equation (3.50) for various observer positions . . . . .	75
4.32 Acoustic density at the Reynolds number value $Re = 160$ using the number of subintervals $Mterms = 5000$ in the integral of Equation (3.50) for various observer positions. . . . .	76
4.33 Contour of the acoustic density at the Reynolds number value $Re = 160$ using the number of subintervals $Mterms = 5000$ in the integral of Equation (3.50) in the far-field domain $(-2000 \leq x_1, x_2 \leq 2000)$ . . . .	77
4.34 Drag and lift dipoles at the Reynolds number value $Re = 100$ with and without control . . . . .	79
4.35 Acoustic density at the Reynolds number value $Re = 100$ with and without control . . . . .	80
4.36 Drag dipoles with and without control at the Reynolds number value $Re = 100$ using the number of subintervals $Mterms = 5000$ in the integral of Equation (3.50) for various observer positions . . . . .	81
4.37 Lift dipole with and without control at the Reynolds number value $Re = 100$ using the number of subintervals $Mterms = 5000$ in the integral of Equation (3.50) for various observer positions . . . . .	82
4.38 Acoustic density with and without control at the Reynolds number value $Re = 100$ using the number of subintervals $Mterms = 5000$ in the integral of Equation (3.50) for various observer positions. . . . .	83
4.39 Contour of the acoustic density at the Reynolds number value $Re = 160$ using the number of subintervals $Mterms = 5000$ in the integral of Equation (3.50) in the far-field domain $(-2000 \leq x_1, x_2 \leq 2000)$ . . . .	84
4.40 Drag and lift dipoles at the Reynolds number value $Re = 160$ with and without control . . . . .	86
4.41 Acoustic density at the Reynolds number value $Re = 160$ with and without control . . . . .	87

Figure	Page
4.42 Drag dipoles with and without control at the Reynolds number value $Re = 160$ using the number of subintervals $Mterms = 5000$ in the integral of Equation (3.50) for various observer positions . . . . .	88
4.43 Lift dipole with and without control at the Reynolds number value $Re = 160$ using the number of subintervals $Mterms = 5000$ in the integral of Equation (3.50) for various observer positions . . . . .	89
4.44 Acoustic density with and without control at the Reynolds number value $Re = 160$ using the number of subintervals $Mterms = 5000$ in the integral of Equation (3.50) for various observer positions. . . . .	90
4.45 Contour of the acoustic density at the Reynolds number value $Re = 160$ using the number of subintervals $Mterms = 5000$ in the integral of Equation (3.50) in the far-field domain $(-2000 \leq x_1, x_2 \leq 2000)$ . . . .	91
4.46 Directivity patterns for overall sound pressure level with and without control generated by the drag dipole ( $SPL_{D1}$ ) at the Reynolds number $Re = 100$ , Mach number $M = 0.000215$ , and cylinder diameter $D = 0.02$ m. The observers locations are at 128D away from the cylinder. Axes units are decibels (dB, re: $20 \times 10^{-15}$ ) . . . . .	96
4.47 Directivity patterns for overall sound pressure level with and without control generated by the lift dipole ( $SPL_{D2}$ ) at the Reynolds number $Re = 100$ , Mach number $M = 0.000215$ , and cylinder diameter $D = 0.02$ m. The observers locations are at 128D away from the cylinder. Axes units are decibels (dB, re: $20 \times 10^{-15}$ ) . . . . .	97
4.48 Directivity patterns for overall sound pressure level with and without control generated by the total dipole ( $SPL_{D12}$ ) at the Reynolds number $Re = 100$ , Mach number $M = 0.000215$ , and cylinder diameter $D = 0.02$ m. The observers locations are at 128D away from the cylinder. Axes units are decibels (dB, re: $20 \times 10^{-15}$ ) . . . . .	98
4.49 Directivity patterns for overall sound pressure level with and without control generated by the drag dipole ( $SPL_{D1}$ ) at the Reynolds number $Re = 160$ , Mach number $M = 0.000342$ , and cylinder diameter $D = 0.02$ m. The observers locations are at 128D away from the cylinder. Axes units are decibels (dB, re: $20 \times 10^{-15}$ ) . . . . .	99

Figure	Page
4.50 Directivity patterns for overall sound pressure level with and without control generated by the lift dipole ( $SPL_{D2}$ ) at the Reynolds number $Re = 160$ , Mach number $M = 0.000342$ , and cylinder diameter $D = 0.02$ m. The observers locations are at 128D away from the cylinder. Axes units are decibels (dB, re: $20 \times 10^{-15}$ ) . . . . .	100
4.51 Directivity patterns for overall sound pressure level with and without control generated by the total dipole ( $SPL_{D12}$ ) at the Reynolds number $Re = 160$ , Mach number $M = 0.000342$ , and cylinder diameter $D = 0.02$ m. The observers locations are at 128D away from the cylinder. Axes units are decibels (dB, re: $20 \times 10^{-15}$ .) . . . . .	101
C.1 Acoustic Pressures generated by the drag dipole sources with and without control at the Reynolds number value $Re = 100$ , Mach number $M = 0.000215$ , and cylinder diameter $D = 0.02$ m using the number of subintervals $Mterms = 5000$ in the integral of Equation (3.50) for observer positions at 128D away from the cylinder. Acoustic Pressure calculated from degree $\theta = 0^\circ$ to $\theta = 120^\circ$ with a degree step $\delta\theta = 30^\circ$ where angle direction shown in Figure 2.1 . . . . .	110
C.2 Acoustic Pressures generated by the drag dipole sources with and without control at the Reynolds number value $Re = 100$ , Mach number $M = 0.000215$ , and cylinder diameter $D = 0.02$ m using the number of subintervals $Mterms = 5000$ in the integral of Equation (3.50) for observer positions at 128D away from the cylinder. Acoustic Pressure calculated from degree $\theta = 150^\circ$ to $\theta = 240^\circ$ with a degree step $\delta\theta = 30^\circ$ where angle direction shown in Figure 2.1 . . . . .	111
C.3 Acoustic Pressures generated by the drag dipole sources with and without control at the Reynolds number value $Re = 100$ , Mach number $M = 0.000215$ , and cylinder diameter $D = 0.02$ m using the number of subintervals $Mterms = 5000$ in the integral of Equation (3.50) for observer positions at 128D away from the cylinder. Acoustic Pressure calculated from degree $\theta = 270^\circ$ to $\theta = 360^\circ$ with a degree step $\delta\theta = 30^\circ$ where angle direction shown in Figure 2.1 . . . . .	112
C.4 Acoustic Pressures generated by the lift dipole sources with and without control at the Reynolds number value $Re = 100$ , Mach number $M = 0.000215$ , and cylinder diameter $D = 0.02$ m using the number of subintervals $Mterms = 5000$ in the integral of Equation (3.50) for observer positions at 128D away from the cylinder. Acoustic Pressure calculated from degree $\theta = 0^\circ$ to $\theta = 120^\circ$ with a degree step $\delta\theta = 30^\circ$ where angle direction shown in Figure 2.1 . . . . .	113

C.5	Acoustic Pressures generated by the lift dipole sources with and without control at the Reynolds number value $Re = 100$ , Mach number $M = 0.000215$ , and cylinder diameter $D = 0.02$ m using the number of subintervals $Mterms = 5000$ in the integral of Equation (3.50) for observer positions at $128D$ away from the cylinder. Acoustic Pressure calculated from degree $\theta = 150^\circ$ to $\theta = 240^\circ$ with a degree step $\delta\theta = 30^\circ$ where angle direction shown in Figure 2.1 . . . . .	114
C.6	Acoustic Pressures generated by the lift dipole sources with and without control at the Reynolds number value $Re = 100$ , Mach number $M = 0.000215$ , and cylinder diameter $D = 0.02$ m using the number of subintervals $Mterms = 5000$ in the integral of Equation (3.50) for observer positions at $128D$ away from the cylinder. Acoustic Pressure calculated from degree $\theta = 270^\circ$ to $\theta = 360^\circ$ with a degree step $\delta\theta = 30^\circ$ where angle direction shown in Figure 2.1 . . . . .	115
C.7	Acoustic Pressures generated by the total dipole sources with and without control at the Reynolds number value $Re = 100$ , Mach number $M = 0.000215$ , and cylinder diameter $D = 0.02$ m using the number of subintervals $Mterms = 5000$ in the integral of Equation (3.50) for observer positions at $128D$ away from the cylinder. Acoustic Pressure calculated from degree $\theta = 0^\circ$ to $\theta = 120^\circ$ with a degree step $\delta\theta = 30^\circ$ where angle direction shown in Figure 2.1 . . . . .	116
C.8	Acoustic Pressures generated by the total dipole sources with and without control at the Reynolds number value $Re = 100$ , Mach number $M = 0.000215$ , and cylinder diameter $D = 0.02$ m using the number of subintervals $Mterms = 5000$ in the integral of Equation (3.50) for observer positions at $128D$ away from the cylinder. Acoustic Pressure calculated from degree $\theta = 150^\circ$ to $\theta = 240^\circ$ with a degree step $\delta\theta = 30^\circ$ where angle direction shown in Figure 2.1 . . . . .	117
C.9	Acoustic Pressures generated by the total dipole sources with and without control at the Reynolds number value $Re = 100$ , Mach number $M = 0.000215$ , and cylinder diameter $D = 0.02$ m using the number of subintervals $Mterms = 5000$ in the integral of Equation (3.50) for observer positions at $128D$ away from the cylinder. Acoustic Pressure calculated from degree $\theta = 270^\circ$ to $\theta = 360^\circ$ with a degree step $\delta\theta = 30^\circ$ where angle direction shown in Figure 2.1 . . . . .	118



C.10	Acoustic Pressures generated by the drag dipole sources with and without control at the Reynolds number value $Re = 160$ , Mach number $M = 0.000342$ , and cylinder diameter $D = 0.02$ m using the number of subintervals $Mterms = 5000$ in the integral of Equation (3.50) for observer positions at $128D$ away from the cylinder. Acoustic Pressure calculated from degree $\theta = 0^\circ$ to $\theta = 120^\circ$ with a degree step $\delta\theta = 30^\circ$ where angle direction shown in Figure 2.1 . . . . .	119
C.11	Acoustic Pressures generated by the drag dipole sources with and without control at the Reynolds number value $Re = 160$ , Mach number $M = 0.000342$ , and cylinder diameter $D = 0.02$ m using the number of subintervals $Mterms = 5000$ in the integral of Equation (3.50) for observer positions at $128D$ away from the cylinder. Acoustic Pressure calculated from degree $\theta = 150^\circ$ to $\theta = 240^\circ$ with a degree step $\delta\theta = 30^\circ$ where angle direction shown in Figure 2.1 . . . . .	120
C.12	Acoustic Pressures generated by the drag dipole sources with and without control at the Reynolds number value $Re = 160$ , Mach number $M = 0.000342$ , and cylinder diameter $D = 0.02$ m using the number of subintervals $Mterms = 5000$ in the integral of Equation (3.50) for observer positions at $128D$ away from the cylinder. Acoustic Pressure calculated from degree $\theta = 270^\circ$ to $\theta = 360^\circ$ with a degree step $\delta\theta = 30^\circ$ where angle direction shown in Figure 2.1 . . . . .	121
C.13	Acoustic Pressures generated by the lift dipole sources with and without control at the Reynolds number value $Re = 160$ , Mach number $M = 0.000342$ , and cylinder diameter $D = 0.02$ m using the number of subintervals $Mterms = 5000$ in the integral of Equation (3.50) for observer positions at $128D$ away from the cylinder. Acoustic Pressure calculated from degree $\theta = 0^\circ$ to $\theta = 120^\circ$ with a degree step $\delta\theta = 30^\circ$ where angle direction shown in Figure 2.1 . . . . .	122
C.14	Acoustic Pressures generated by the lift dipole sources with and without control at the Reynolds number value $Re = 160$ , Mach number $M = 0.000342$ , and cylinder diameter $D = 0.02$ m using the number of subintervals $Mterms = 5000$ in the integral of Equation (3.50) for observer positions at $128D$ away from the cylinder. Acoustic Pressure calculated from degree $\theta = 150^\circ$ to $\theta = 240^\circ$ with a degree step $\delta\theta = 30^\circ$ where angle direction shown in Figure 2.1 . . . . .	123

- C.15 Acoustic Pressures generated by the lift dipole sources with and without control at the Reynolds number value  $Re = 160$ , Mach number  $M = 0.000342$ , and cylinder diameter  $D = 0.02$  m using the number of subintervals  $Mterms = 5000$  in the integral of Equation (3.50) for observer positions at  $128D$  away from the cylinder. Acoustic Pressure calculated from degree  $\theta = 270^\circ$  to  $\theta = 360^\circ$  with a degree step  $\delta\theta = 30^\circ$  where angle direction shown in Figure 2.1 . . . . . 124
- C.16 Acoustic Pressures generated by the total dipole sources with and without control at the Reynolds number value  $Re = 160$ , Mach number  $M = 0.000342$ , and cylinder diameter  $D = 0.02$  m using the number of subintervals  $Mterms = 5000$  in the integral of Equation (3.50) for observer positions at  $128D$  away from the cylinder. Acoustic Pressure calculated from degree  $\theta = 0^\circ$  to  $\theta = 120^\circ$  with a degree step  $\delta\theta = 30^\circ$  where angle direction shown in Figure 2.1 . . . . . 125
- C.17 Acoustic Pressures generated by the total dipole sources with and without control at the Reynolds number value  $Re = 160$ , Mach number  $M = 0.000342$ , and cylinder diameter  $D = 0.02$  m using the number of subintervals  $Mterms = 5000$  in the integral of Equation (3.50) for observer positions at  $128D$  away from the cylinder. Acoustic Pressure calculated from degree  $\theta = 150^\circ$  to  $\theta = 240^\circ$  with a degree step  $\delta\theta = 30^\circ$  where angle direction shown in Figure 2.1 . . . . . 126
- C.18 Acoustic Pressures generated by the total dipole sources with and without control at the Reynolds number value  $Re = 160$ , Mach number  $M = 0.000342$ , and cylinder diameter  $D = 0.02$  m using the number of subintervals  $Mterms = 5000$  in the integral of Equation (3.50) for observer positions at  $128D$  away from the cylinder. Acoustic Pressure calculated from degree  $\theta = 270^\circ$  to  $\theta = 360^\circ$  with a degree step  $\delta\theta = 30^\circ$  where angle direction shown in Figure 2.1 . . . . . 127
- C.19 Directivity patterns for overall sound pressure level without control generated by the drag dipole ( $SPL_{D1}$ ) and lift dipole ( $SPL_{D2}$ ) at the Reynolds number  $Re = 100$ , Mach number  $M = 0.000215$ , and cylinder diameter  $D = 0.02$  m. The observers locations are at  $128D$  away from the cylinder. Axes units are decibels (dB, re: $20 \times 10^{-15}$ ) . 128
- C.20 Directivity patterns for overall sound pressure level without control generated by the total dipole ( $SPL_{D12}$ ) at the Reynolds number  $Re = 100$ , Mach number  $M = 0.000215$ , and cylinder diameter  $D = 0.02$  m. The observers locations are at  $128D$  away from the cylinder. Axes units are decibels (dB, re: $20 \times 10^{-15}$ ) . . . . . 129

C.21	Directivity patterns for overall sound pressure level with control generated by the drag dipole ( $SPL_{D1}$ ) and lift dipole ( $SPL_{D2}$ ) at the Reynolds number $Re = 100$ , Mach number $M = 0.000215$ , and cylinder diameter $D = 0.02$ m. The observers locations are at $128D$ away from the cylinder. Axes units are decibels (dB, re: $20 \times 10^{-15}$ ) . . . . .	130
C.22	Directivity patterns for overall sound pressure level with control generated by the total dipole ( $SPL_{D12}$ ) at the Reynolds number $Re = 100$ , Mach number $M = 0.000215$ , and cylinder diameter $D = 0.02$ m. The observers locations are at $128D$ away from the cylinder. Axes units are decibels (dB, re: $20 \times 10^{-15}$ ) . . . . .	131
C.23	Directivity patterns for overall sound pressure level without control generated by the drag dipole ( $SPL_{D1}$ ) and lift dipole ( $SPL_{D2}$ ) at the Reynolds number $Re = 160$ , Mach number $M = 0.000342$ , and cylinder diameter $D = 0.02$ m. The observers locations are at $128D$ away from the cylinder. Axes units are decibels (dB, re: $20 \times 10^{-15}$ ) . .	132
C.24	Directivity patterns for overall sound pressure level without control generated by the total dipole ( $SPL_{D12}$ ) at the Reynolds number $Re = 160$ , Mach number $M = 0.000342$ , and cylinder diameter $D = 0.02$ m. The observers locations are at $128D$ away from the cylinder. Axes units are decibels (dB, re: $20 \times 10^{-15}$ ) . . . . .	133
C.25	Directivity patterns for overall sound pressure level with control generated by the drag dipole ( $SPL_{D1}$ ) and lift dipole ( $SPL_{D2}$ ) at the Reynolds number $Re = 160$ , Mach number $M = 0.000342$ , and cylinder diameter $D = 0.02$ m. The observers locations are at $128D$ away from the cylinder. Axes units are decibels (dB, re: $20 \times 10^{-15}$ ) . . . . .	134
C.26	Directivity patterns for overall sound pressure level with control generated by the total dipole ( $SPL_{D12}$ ) at the Reynolds number $Re = 160$ , Mach number $M = 0.000342$ , and cylinder diameter $D = 0.02$ m. The observers locations are at $128D$ away from the cylinder. Axes units are decibels (dB, re: $20 \times 10^{-15}$ ) . . . . .	135

# CHAPTER 1

## INTRODUCTION

The fundamental problem in aeroacoustics is to accurately predict the far-field sound radiated in the flow field (e.g. Howe (1998), Zorumski (1993)). Recent developments in computer technology and numerical techniques have allowed the prediction of the sound from the flow field. Nonetheless, computing the far-field sound by direct numerical simulation on a very large computational domain is very expensive and extremely difficult, even for simple flows (Crighton (1993) and Lighthill (1992)). Fortunately, with advanced computer technology and reliable numerical methods, Computational Fluid Dynamics (CFD) is now capable of providing a reliable approximation to all flow variables at any point in the flow field. Therefore, rather than using direct numerical simulation for predicting the far-field noise, researchers have developed the acoustic analogy, which utilizes the information from CFD results as the near-field noise sources to compute the far-field noise. In this case, all flow variables are determined using CFD methods such as Direct Numerical Simulation (DNS) or Large Eddy Simulation (LES). The far-field noise can then be computed using CFD results as the near-field noise source. Currently, many acoustic researchers are using an acoustic analogy approach for noise prediction in many types of flow. The objective of this study is to investigate the possibility of suppressing flow-induced noise behind a circular cylinder at low Mach number numerically by using Lighthill's acoustic analogy approach.

This chapter reviews both the control of the flow past a circular cylinder and the sound prediction using the acoustic analogy approach. In other words, both the development of the theory of aeroacoustics, initiated by the work of Lighthill in the

mid-1950's, and the recent advances made in computing the sound radiated by a wake flow will be discussed.

## 1.1 Background

### 1.1.1 Wake Flow Behind a Circular Cylinder and Its Control

While literature has long addressed the fundamental understanding of the flow around a circular cylinder, it is only recently that the focus has shifted towards the issue of flow control. It is well accepted that at very low Reynolds number values ( $Re \ll 1$ , where  $Re = 2u_\infty a/\nu$ ,  $u_\infty$  being the free stream velocity,  $a$  the cylinder radius and  $\nu$  the kinematic viscosity), the flow is stable and symmetric both upstream and downstream. As the Reynolds number increases over the critical value ( $Re \geq 46$ ), the flow becomes unsteady and a train of vortices, known as the Von Karman vortex street, periodically sheds from the upper and lower surface of the cylinder. Vortex shedding increases the drag force and produces a strong unsteady force, or lift force, acting on the cylinder in the direction normal to the mainstream. According to studies conducted by Williamson (1996) and Henderson *et al.* (1996)), the flow becomes three-dimensional (3D) and 3D calculation is required at high Reynolds number values ( $Re \geq 200$ ).

The increased drag and lift forces caused by vortex shedding may lead to some engineering issues, such as the vibration of structures and frames, and acoustic problems. Therefore, controlling the wake behind a bluff body is an important issue from a practical engineering point of view. Many researchers have recently focused on controlling vortex shedding with either passive or active control methods.

Passive control techniques have been well accepted for many years as they do not require any external energy input into the flow. Examples include the works of Apelt and West (1975), Apelt, West, and Szewczyk (1973), Unal and

Rockwell (1988), Cimbala and Grag (1991). Recently Kwon and Choi (1996) have studied the use of a splitter plate to control vortex shedding behind a circular cylinder. The effect of base bleed to control the wake was also investigated by Wood (1946), Bearman (1967), Schumn, Berger and Monkewitz (1994). There are other passive control methods used to control vortex shedding, such as the use of a small secondary cylinder placed in the flow field (Strykowski and Hannemann (1991)). Besides passive control techniques, active control methods, applying some sorts of energy into the flow, have also been well developed in order to solve vortex shedding problems. Some of these active control techniques include the use of a rotary oscillation of a circular cylinder (Kang and Choi 1999), the insertion of two small vortices (Tang and Aubry 1998), the forced vibration of the cylinder (Wehrmann 1965), the effect of sound (Blevins 1985), etc.

With the development of advanced control theory, feedback control methods have been applied to control fluid flows. For example, Park, Ladd and Hendricks (1993, 1994) have presented a computational study of the feedback control of vortex shedding behind a circular cylinder at low Reynolds number, using a single sensor and a pair of blowing/suction actuators. They reported a complete suppression of vortex shedding at the Reynolds number value  $Re = 60$ . Gunzburger and Lee (1996) have developed computationally an active feedback control of the lift. By means of injection and suction of fluid through orifices on the cylinder, they could indeed reduce the magnitude of the lift. Their results suggested that the application of their feedback system caused an efficient reduction in the size of the oscillations. Min and Choi (1999) developed a method of controlling vortex shedding behind a bluff body using suboptimal feedback control theory. For this purpose, they defined three different cost functionals, all related to the pressure distribution on the cylinder surface. They reported that the minimization of the second cost functional which consisted of the square of the difference between the target pressure and the real

flow pressure on the cylinder surface provided the largest drag reduction for a given magnitude of the blowing/suction system.

Among these control approaches, the use of electromagnetic forces to control vortex shedding has been widely investigated over the past few years. Electromagnetic laws state that the cross product of magnetic and electric fields produces an electromagnetic force known as Lorentz force, ( $\vec{F}_l$ ). The production of the Lorentz force offers an alternative possibility for the control fluid flows. The influence of the Lorentz force, however, greatly depends on the conductivity of the fluid. Highly conductive fluids require only an external magnetic field for the generation of a strong Lorentz force while weak electrolyte fluids require an additional electric field in order to produce a Lorentz force that is sufficiently large enough to be effective in flow control. Therefore, flow control by electromagnetic force generated by the application of electric and magnetic field can be applied to both strongly and weakly conducting fluid flows.

Henoch and Stace (1995) have experimentally investigated the influence of an applied streamwise electromagnetic force on a salt water turbulent boundary layer over a flat plate. In their experiment, the Lorentz force was created by the interaction of a permanent magnetic field and an applied electric field from a magnet and electrode array integral to the surface of the plate. Their results showed that the applied Lorentz force can decrease the boundary layer thickness and suppress the intensity of the turbulent fluctuation across the boundary. Crawford and Karniadakis (1997) presented the numerical simulation of a channel flow subjected to an electromagnetic force whose results agree with Henoch and Stace (1995)'s experimental results.

Studying the cylinder wake in a magnetic field, Lahjomri *et al.* (1993) investigated experimentally the cylinder wake in a conducting fluid. They presented that

the electromagnetic forces resulting from the action of a longitudinal magnetic field were able to stabilize the flow and delay the appearance of the Von Karman vortex street. Mutschke *et al.* (1997) studied two- and three- dimensional instabilities in the wake of a circular cylinder subjected to an aligned magnetic field. By increasing the magnitude of the magnetic field, they were able to suppress vortex shedding behind the cylinder. Weier *et al.* (1998, 2000) applied an active open loop control of wake flow around a cylinder using electromagnetic forces. Both experimental and computational results were presented. Recently, feedback control of vortex shedding behind a circular cylinder using Lorentz force was achieved by Chen and Aubry (2000).

### 1.1.2 Acoustic Background

Acoustic theory has been methodically developed since the pioneering works of Rayleigh (1896) and Stokes (1868). Earlier theories were developed with an attempt to provide basic understanding to the sound source and intensity in terms of the details of the flow. However, flow generated noise was not well understood before the work of Lighthill. In 1952, Lighthill introduced a theory of Aerodynamic Sound, that is the sound generated by vorticity in an unbound fluid. His theory led to significant developments in understanding noise generated by a flow field. Much of Lighthill's work (1952, 1954, 1962, 1963) concentrated on developing a theory for predicting jet noise, initially motivated by the need to reduce the noise generated by jet engines in order to satisfy the commercial aircraft certification.

Lighthill's theory (1952) is based on the sound generated by a region of the unsteady flow in a finite fluid domain. In his theory, Lighthill considers the sound generated by a fluid flow in an infinite domain at low Mach number. Sound, once generated, is expected to be a very small component of the whole fluid motion so that its feedback on the fluid flow is assumed to be negligible. This assumption



would not be valid if compressibility effects were important when the same fluid was coupled to a resonator or when bubbles were present in the case of liquids. Lighthill reformulated the Navies-Stokes equations into an exact, inhomogeneous, linear wave equation for the far-field acoustic density fluctuation and developed what is now known as Lighthill's Acoustic Analogy. In this analogy, the governing equations of fluid motion are rearranged in such a way that the left-hand side consists of a wave function in an undisturbed medium, and the right-hand side consists of an acoustic source term or, the externally applied stress,  $T_{ij}$  exerted onto the fluid (also referred to as Lighthill's stress tensor). This external stress field is acoustically equivalent to a distribution of quadrupole sources acting on the acoustic medium. After obtaining the strengths of source terms in the flow regions where the latter are significant, Lighthill's acoustic analogy allows the prediction of acoustic fluctuations radiated in the flow. The derivation of Lighthill's acoustic analogy is discussed in detail in Chapter 3.

Further developments in the acoustic analogy were done by Curle (1955) who extended Lighthill's theory to include the effects of solid boundaries in the flow. Curle showed that sound generated by the influence of solid boundaries upon the flow field was equivalent to a distribution of dipole sources and derived the equation for predicting sound in the presence of solid boundaries at low Mach number. Curle presented the solution of Lighthill's acoustic equation included both dipole and quadrupole sound sources.

Acoustic analogies have been developed for different applications by many researchers (Howe (1975), Phillips (1960), Lilley (1974), Powell (1964), Ffowcs Williams and Hawkings (1969)). Powell derived the equations relating vorticity to sound generation in terms of the vorticity field. Once the vorticity field is computed, using Powell's theory allows one to obtain the far-field sound generated

in the flow field. Phillips, Lilley, and Howe derived the equations in the case where the homogeneous part is a nonlinear wave equation. These acoustic analogies are applicable to certain problems, but remain analytically and computationally complicated. However, these pioneering works have driven the recent advances in computational aeroacoustics.

In recent years, due to the advances in computer technology and mature developments in computational fluid dynamics techniques, many researchers have been applying the concept of the acoustic analogy approach to solve acoustic problems in turbulent flows. Since the radiated sound is often several orders of magnitude smaller than the source fluctuations in the flow field, small errors in the source terms may lead to large (relative) errors in computing acoustic fluctuations. Hence, the accuracy of the unsteady source flow results from computational techniques or directly from experimental data is crucial in this problem.

The following works have used the acoustic analogy approach to compute the sound from turbulence and compare the acoustic analogy results with theoretical or experimental solutions. Lilley (1993, 1994, 1996) applied the acoustic analogy approach to calculate sound radiated by a turbulent flow; the sources were computed using Direct Numerical Simulation (DNS)/ Large Eddy Simulation (LES). Lilley derived an analytical equation for the numerical constant used to calculate the acoustic power output, known as Proudman's constant  $\alpha$  (1952), in terms of fourth-order, space-retard time covariances. Sarkar and Hussaini (1993) computed sound radiation using an hybrid method, which coupled the DNS results of the compressible Navies-Stokes equations with the acoustic analogy. Their results agreed well with the analytical solution.

Wang, Lele, and Moin (1996) studied sound generated during local laminar breakdown in a low Mach number boundary layer using an acoustic analogy approach

and obtained results that were comparable with available experimental results. Mankbadi *et al.* (1994) used LES and Lighthill’s acoustic analogy approach to determine the sound radiated by a supersonic jet. Mankbadi presented that using this method, the result agreed with experimental results. Bechara *et al.* (1995) computed the sound from simple and coaxial free jets using the  $\kappa - \epsilon$  turbulent model to compute the sound source in the flow and predict the radiated sound by using the acoustic analogies developed by Ribner (1969) and Goldstein and Rosenbaum (1973). The result was similar to the experimental data presented by Lush (1971).

Recently, Mitchell, Lele, and Moin (1992) investigated the far-field sound radiated from a compressible co-rotating vortex pair, which was computed by direct computation of the unsteady compressible Navier-Stokes equations. After validating their results with the noise prediction made by Möhring (1978), a modified form of Lighthill’s acoustic analogy (1952), and an acoustic analogy derived by Powell (1964), they concluded that all three predictions agreed with the simulation. Mitchell, Lele, and Moin (1995) also verified Lighthill’s acoustic analogy by comparing it with DNS results for subsonic and supersonic axisymmetric jets. Colonius, Lele, and Moin (1994) studied the scattering of sound waves from a vortex and validated their results. Whitmire (1995) validated Lighthill’s acoustic analogy by comparing it with the direct computation of the far-field sound for a three-dimensional broadband turbulent flow. Lighthill’s acoustic analogy, therefore, is now well accepted and widely applied.

## 1.2 Motivation

The tremendous success of computer technology and computational fluid dynamics techniques in the past decade has renewed and powered the concept of acoustic analogy for a better understanding of flow-induced noise phenomena. Using CFD

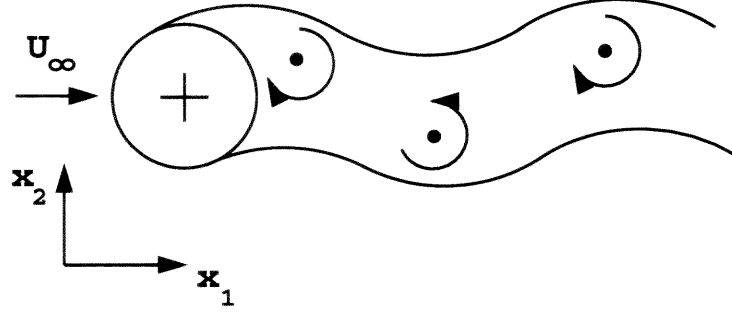


**Figure 1.1** Generation of æolian tones.[Howe, 1998]

results as input to a computational acoustic theory is currently a useful and practical technology. This leads to significant progress towards the understanding of noise generation and the reduction of noise in the flow field. Noise pollution is a major drawback of many hi-tech equipment and machinery. The advanced high speed fan may cause a high noise level, which violates environmental regulations; the airport curfews prohibit the night landing of large commercial aircrafts due to a serious noise problem impacting residential and commercial localities. Many research studies have been focusing on developing technologies for advanced, low-noise, and high performance systems for some engineering applications. An increasing need for noise reduction has generated many advanced noise-controlling techniques. The study on controlling of noise generated by the flow past a circular cylinder may lead to solutions to some engineering challenges such as *aeolian tones* (Howe, 1998; Phillips, 1956) which are the characteristic of sound production by flow across telegraph wires or power lines (Figure 1.1), noise generation on aircraft landing gear, (composed of some hydraulic circular cylinders or circular frame), structure noise, automobile antenna noise, etc.

In general, there are three types of noise sources in fluid flow: monopole, dipole, and quadrupole. The monopole source is caused by the movement and geometry of the solid object in the flow field. The dipole source is important when mean

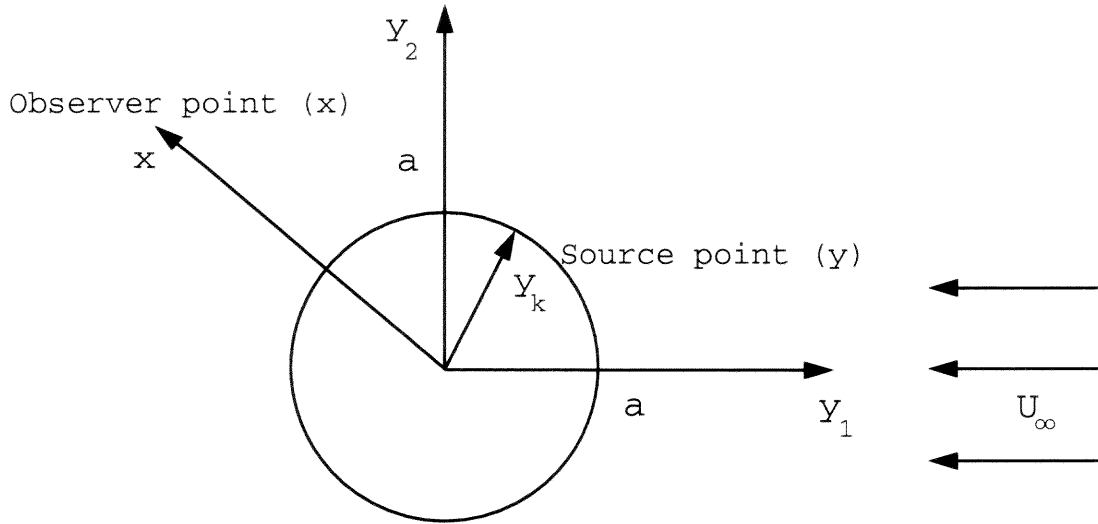


**Figure 1.2** Flow configuration and coordinate system in physical space

mass density variations occur within the source region, while the strength of the quadrupole source is determined by the unsteady Reynolds stress. In this study, the dipole noise source is generated by the drag and lift fluctuations; the quadrupole noise source is generated by the disturbed unsteady flow behind a bluff body. Thus, in order to control the noise induced by a wake flow, reducing dipole and quadrupole noise sources by using one of the CFD control technique is feasible.

### 1.3 Objectives

A primary objective of this research is to compute the aeroacoustic sound generated by the flow past a circular cylinder at low Mach number ( $M$ ) using Lighthill's acoustic analogy. (see Figure (1.2)) The computation and control techniques for the wake flow behind a circular cylinder have been developed by our research team over the past few years. The simulation results, created by Tang and Aubry (1997) and Chen and Aubry (2000), will be used in this study as the input noise source in order to generate the far-field noise of the same flow.

Results of noise sources were obtained from the two-dimensional numerical simulation of the Navier-Stokes (NS) equations in an exponential coordinate system by Tang and Aubry (1997). In their work, the non-dimensional *vorticity/stream function* formulation of the NS equations is solved by computational fluid dynamics techniques. In addition, an exponential mapping is used to deal with a very large physical domain, while the computational domain remains relatively small in order to avoid the well-known blockage effect. The computation starts with the potential flow as the initial condition and assumes the non-slip boundary conditions on the surface of the body. An adaptive scheme is developed in order to increase the efficiency of the numerical results. This scheme increases the size of the computational domain as the vorticity moves away from the body. Two important numerical methods are used: an alternating-direction-implicit (ADI) algorithm for solving the vorticity transport equation and Fast Fourier Transform (FFT) for solving the Poisson equation with second-order accuracy as in Hockney 1970. (See Tang and Aubry (1997) for more details)

An approximate description of the acoustic source functions was obtained after solving the incompressible NS equations numerically. The radiated far-field sounds can then be computed based on Curle's theory, an extension of Lighthill's acoustic analogy. This study emphasizes the evaluation of noise generated by dipole source functions. The effect of the quadrupole source  $\mathcal{O}(M^4)$  on the radiated far-field noise is negligible compared to that of the dipole source  $\mathcal{O}(M^3)$  at a low Mach number  $M \ll 1$  (Curle (1955), Wang, Lele and Moin (1996), You *et al.*, (1998)). To our knowledge, the investigation of the far-field noise behind a circular cylinder using Curle's solution of the Lighthill's acoustic analogy has been performed only by You *et al.*, (1998). The results will be compared to You *et al.* work.

The secondary objective is to apply the control technique developed by Chen and Aubry (2000) to control the radiated noise behind a circular cylinder and explore its efficiency in controlling far-field noise. In order to meet the objectives, the following tasks were performed:

- Computation of vortex shedding behind a circular cylinder at Reynolds numbers of 100 and 160 by solving the unsteady two-dimensional incompressible NS equations.
- Development of a numerical code based on a finite difference method to solve Lighthill's wave equation in the time domain.
- Comparison of the noise prediction results with previous numerical results.
- Computation of flow behind a circular cylinder at Reynolds numbers of 100 and 160 with control.
- Investigation of noise radiation by using flow control.

The current work is unique in using active flow control to reduce the radiated far-field noise in the flow behind a cylinder at Reynolds number values for which the uncontrolled flow consists of vortex shedding.

## **1.4 Dissertation Organization**

The dissertation is organized into five chapters. Chapter 2 provides reviews of the governing equations and numerical methods used in the flow simulation. The review of active, feedback control used in this study is discussed in this chapter. The derivation of Lighthill's acoustic analogy is summarized in Chapter 3. In chapter 4, the numerical results for the flow field and the noise prediction are presented. The investigation is performed in order to establish a better understanding of the noise

generation before and after applying the control technique at Reynolds numbers of 100 and 160. A discussion of the results and conclusions are then given in Chapter 5. Some integral formulae from vector analysis and the derivation of the inhomogeneous wave equation for a uniformly moving medium are summarized in appendix A and B. Finally, in appendix C, the numerical results in dimensional forms for sound pressure level calculations are provided.



## CHAPTER 2

### REVIEW OF FLOW FIELD COMPUTATIONAL METHODS

#### 2.1 Governing Equations

Following previous work, the two-dimensional Navier-Stokes (2D-NS) equations with an additional term representing the applied Lorentz force, have been used to simulate the flow field and near field acoustic source functions. The two-dimensional Navier-Stokes (2D-NS) equations become as follows:

$$\frac{\partial u}{\partial x} + \frac{\partial v}{\partial y} = 0 \quad (2.1)$$

$$\frac{\partial u}{\partial t} + u \frac{\partial u}{\partial x} + v \frac{\partial u}{\partial y} = -\frac{1}{\rho} \frac{\partial P}{\partial x} + \nu \left( \frac{\partial^2 u}{\partial x^2} + \frac{\partial^2 u}{\partial y^2} \right) + \frac{F_{lx}}{\rho} \quad (2.2)$$

$$\frac{\partial v}{\partial t} + u \frac{\partial v}{\partial x} + v \frac{\partial v}{\partial y} = -\frac{1}{\rho} \frac{\partial P}{\partial y} + \nu \left( \frac{\partial^2 v}{\partial x^2} + \frac{\partial^2 v}{\partial y^2} \right) + \frac{F_{ly}}{\rho} \quad (2.3)$$

where  $\vec{F}_l$  is the Lorentz force which results from the vector product of the current density  $\vec{j}$  (*Amps/m<sup>2</sup>*) and the magnetic induction  $\vec{B}$  (*Tesla*)

$$\vec{F}_l = \vec{j} \times \vec{B} \quad (2.4)$$

The current density  $\vec{j}$  is given by Ohm's law as the sum of the current due to the presence of an electric field  $\vec{E}$  and the current induced by the motion of the electro-conducting medium at speed  $\vec{U}$  in the magnetic field. That is:

$$\vec{j} = \sigma(\vec{E} + \vec{U} \times \vec{B})$$

where  $\sigma(S/m)$  denotes the electrical conductivity.

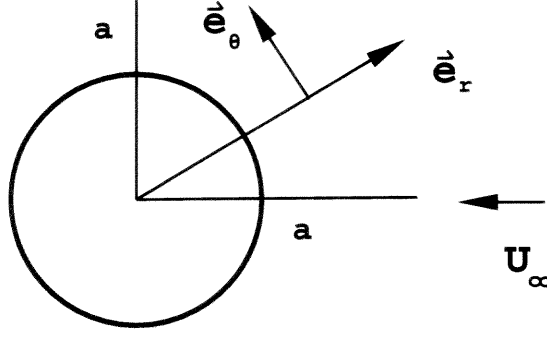


**Figure 2.1** Flow configuration and system of coordinates

In weakly conducting fluids like seawater, the induced electrical current ( $\vec{j} = \sigma \vec{U} \times \vec{B}$ ) is not noticeable compared to the current associated with the applied electric field, and is thus neglected. The Lorentz force then becomes:

$$\vec{F}_l = \sigma \vec{E} \times \vec{B}$$

The two-dimensional Navier-Stokes (2D-NS) equations in terms of vorticity and streamfunction, with an additional term representing the applied Lorentz force, have been used to simulate the flow field. The modified *vorticity/streamfunction* formulations are derived in an exponential-polar coordinate system  $(\xi, \eta)$  defined by

$$r = e^{2\pi\xi} \tag{2.5}$$

$$\theta = 2\pi\eta \tag{2.6}$$

where  $(r, \theta)$  are the polar coordinates (see figure 2.1).

After using non-dimensional variables,

$$\begin{aligned} \omega^* &= \omega a / u_\infty, & \Psi^* &= \Psi / a u_\infty, & u_r^* &= u_r / u_\infty, \\ u_\theta^* &= u_\theta / u_\infty, & t^* &= t u_\infty / a, & \theta^* &= \theta, \\ r^* &= r / a, & B^* &= B / B_0, & j^* &= j / \sigma u_\infty B_0, \end{aligned}$$

where  $a$  is cylinder radius,  $u_\infty$  is free stream velocity,  $B_0$  refers to the magnetic field and  $\sigma$  is the electrical conductivity, the dimensionless modified *vorticity/streamfunction* formulations become

$$E \frac{\partial \omega}{\partial t} + \frac{\partial(U_\xi \omega)}{\partial \xi} + \frac{\partial(U_\eta \omega)}{\partial \eta} = \frac{2}{Re} \left( \frac{\partial^2 \omega}{\partial \xi^2} + \frac{\partial^2 \omega}{\partial \eta^2} \right) + NE^{\frac{1}{2}} \left( \frac{\partial F_{l\theta}}{\partial \xi} + 2\pi F_{l\theta} - \frac{\partial F_{lr}}{\partial \eta} \right) \quad (2.7)$$

$$\frac{\partial^2 \Psi}{\partial \xi^2} + \frac{\partial^2 \Psi}{\partial \eta^2} = -E\omega \quad (2.8)$$

where the new dependent variables,  $U_\xi, U_\eta$ , and  $E$ , the *interaction parameter*  $N$  and the Reynolds number  $Re$  are defined as:

$$\begin{aligned} U_\xi &= E^{\frac{1}{2}} u_r = \frac{\partial \Psi}{\partial \eta} \\ U_\eta &= E^{\frac{1}{2}} u_\theta = -\frac{\partial \Psi}{\partial \xi} \\ E &= 4\pi^2 e^{4\pi\xi} \\ N &= \frac{\sigma B_0^2 a}{\rho u_\infty} = \frac{j_0 B_0 a}{\rho u_\infty^2} \\ Re &= \frac{2u_\infty a}{\nu}. \end{aligned}$$

## 2.2 Initial and Boundary Conditions

The simulation starts initially with the potential flow for the whole domain, except on the surface of the cylinder where the non-slip condition is imposed. Therefore, at  $t = 0$ ,

$$\omega = 0, \quad \Psi = -2sh(2\pi\xi)sin(2\pi\eta) \quad for \quad \xi > 0,$$

and on the cylinder surface at  $t = 0$

$$\omega = -\frac{1}{E} \frac{\partial^2 \Psi}{\partial \xi^2} \quad for \quad \xi = 0$$

Assumed that the flow satisfies no-slip boundary conditions on the surface of the body and consists of potential flow at infinity, the boundary conditions can be obtained as follows:

Outside the cylinder surface,  $\xi = \xi_\infty$

$$\omega = 0, \quad \Psi = -2sh(2\pi\xi)\sin(2\pi\eta) \quad for \quad \xi = \infty,$$

and on the cylinder surface, where  $\xi = 0$ ,

$$\Psi = 0, \quad \omega = -\frac{1}{E} \frac{\partial^2 \Psi}{\partial \xi^2}.$$

### 2.3 Applied Electro-Magnetic Forces

Exploring further the works of Weier *et al.*, (1998), Chen and Aubry (200) apply the same configurations into the simulation code in order to numerically control vortex shedding behind a circular cylinder by means of electro-magnetic forces localized on the cylinder surface. As shown on Figure (2.2), the cylinder consists of two half cylinders mounted together, each half of cylinder consisting of a special array of electrodes and permanent magnets. The electro-magnetic forces, known as Lorentz forces, are defined as follows:

$$\vec{F} = e^{-\alpha(r-1)}g(\theta)\vec{e}_\theta \quad with \quad g(\theta) = \begin{cases} 1 & 5^\circ \leq \theta \leq 175^\circ \\ -1 & 185^\circ \leq \theta \leq 355^\circ \\ 0 & elsewhere \end{cases} \quad (2.9)$$

where  $\alpha$  represents the electro-magnetic penetration parameter. Experimental investigations have indicated that a reasonable value of  $\alpha$  is  $\alpha = 5\pi/4$ . For further details, see Weier *et al.*, (1998) and Chen and Aubry (2000).

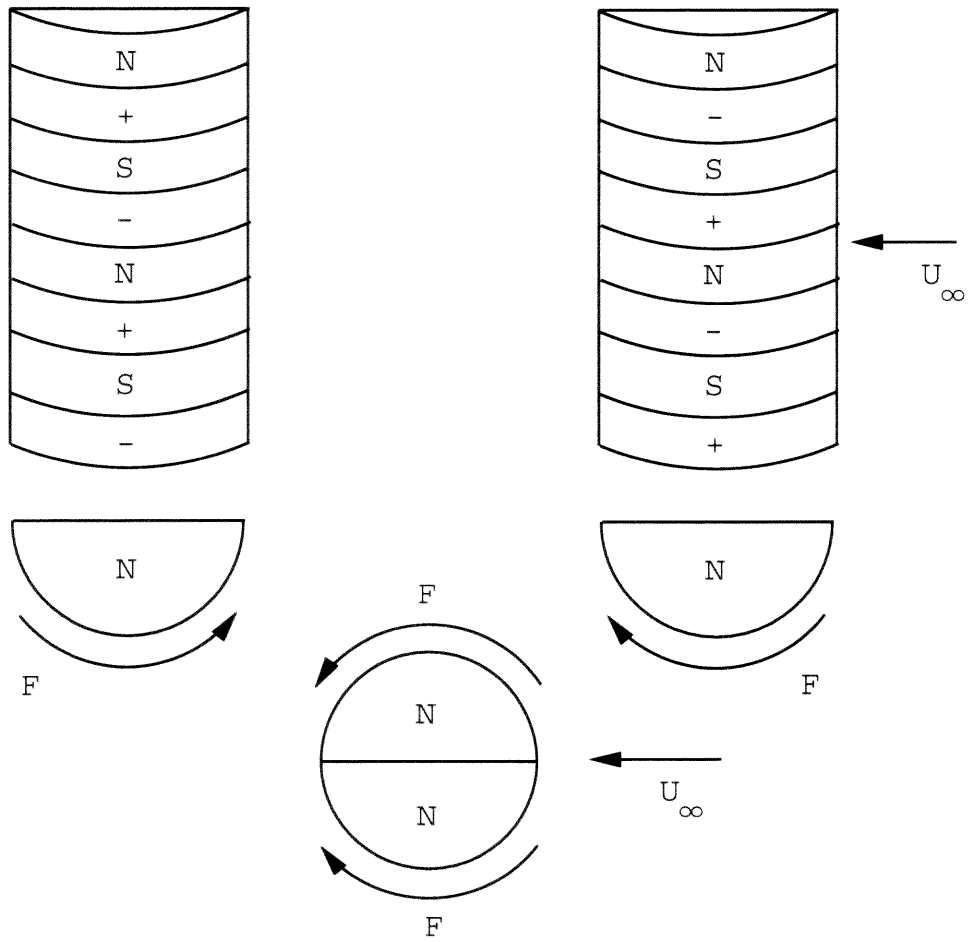


**Figure 2.2** Sketch of the cylinder consisting of electrodes and magnets

## 2.4 Pressure and Force Coefficients

### *Pressure Coefficients*

The pressure coefficient at any angle  $\theta$  is defined as:

$$C_p^\theta = \frac{P_\theta - P_\infty}{\frac{1}{2}\rho u_\infty^2},$$

that is

$$\begin{aligned} C_p^\theta = 1 + \frac{4}{Re} \int_0^\eta \frac{\partial \omega}{\partial \xi} d\eta + 4\pi N \int_0^\eta F_{l\theta} d\eta + 4\pi \int_0^\infty \frac{\partial u_r}{\partial t} e^{2\pi\xi} d\xi \\ + 2 \int_0^\infty u_\theta \frac{\partial u_r}{\partial \eta} d\xi - 4\pi \int_0^\infty u_\theta^2 d\xi + \frac{4}{Re} \int_0^\infty \frac{\partial \omega}{\partial \eta} d\xi. \end{aligned} \quad (2.10)$$

### *Force Coefficient*

The nondimensional total drag and lift, or total drag and lift coefficients, are defined as

$$\begin{aligned} C_d &= \frac{F_{tx}}{\frac{1}{2}\rho u_\infty^2 d} \\ C_l &= \frac{F_{ty}}{\frac{1}{2}\rho u_\infty^2 d} \end{aligned}$$

where  $d$  is the cylinder diameter. Then, the drag coefficient is defined as:

$$\begin{aligned} C_d &= \frac{F_{px} + F_{\tau x}}{\frac{1}{2}\rho u_\infty^2 d} \\ &= C_{pd} + C_{\tau d} \\ &= -\frac{\mu}{\frac{1}{2}\rho u_\infty^2 d} \int_0^{2\pi} \frac{\partial \omega}{\partial r} \sin\theta d\theta - \frac{\sigma B_0^2}{\frac{1}{2}\rho u_\infty^2 d} \int_0^{2\pi} F_\theta \sin\theta d\theta + \frac{\mu}{\frac{1}{2}\rho u_\infty^2 d} \int_0^{2\pi} \omega \sin\theta d\theta \\ &= \frac{2}{Re} \int_0^1 (2\pi\omega - \frac{\partial \omega}{\partial \xi}) \sin(2\pi\eta) d\eta - 2\pi N \int_0^1 F_\theta \sin(2\pi\eta) d\eta \end{aligned} \quad (2.11)$$

where  $C_{pd}$  and  $C_{\tau d}$  are the pressure drag and friction drag coefficients respectively.

Using the same approach, the lift coefficient is defined as:

$$\begin{aligned}
 C_l &= \frac{F_{py} + F_{\tau y}}{\frac{1}{2}\rho u_\infty^2 d} \\
 &= C_{pl} + C_{\tau l} \\
 &= \frac{2}{Re} \int_0^1 (2\pi\omega - \frac{\partial\omega}{\partial\xi}) \cos(2\pi\eta) d\eta - 2\pi N \int_0^1 F_\theta \cos(2\pi\eta) d\eta. \quad (2.12)
 \end{aligned}$$

## 2.5 An Adaptive Scheme for the Vorticity

In order to increase the efficiency of this numerical program, an adaptive scheme was developed by Tang and Aubry (1997). This scheme provides a moving boundary for the vorticity transport equation, (Eq. (2.7)), which moves further and further away from the body as the vorticity is transported outward. From this adaptive scheme, the amount of computational time is reduced and the evolution of the vorticity is followed closely in such a way that it could not move away to the external boundary during the computational time. See Tang and Aubry(1997) for more details about these numerical techniques.

### 2.5.1 Numerical Methods

The numerical method, used to solve the vorticity transport equation, Eq. (2.7), consists of the Alternative-Direction Implicit (ADI) algorithm. The streamfunction equation, Eq. (2.8), is integrated by means of a Fast Fourier Transform (FFT) algorithm. Overall the accuracy of the numerical scheme is second order in space and first order in time.

An ADI algorithm is implemented to solve the vorticity transport equation, Eq. (2.7), leading to the discretized formulae:

$$\begin{aligned}
E_i \frac{\omega_{(i,j)}^{n+\frac{1}{2}} - \omega_{(i,j)}^n}{\frac{1}{2}\Delta t} + \frac{(U_\eta \omega^{n+\frac{1}{2}})_{(i,j+1)} - (U_\eta \omega^{n+\frac{1}{2}})_{(i,j-1)}}{2\Delta\eta} - \frac{2}{Re} \frac{\omega_{(i,j+1)}^{n+\frac{1}{2}} - 2\omega_{(i,j)}^{n+\frac{1}{2}} + \omega_{(i,j-1)}^{n+\frac{1}{2}}}{\Delta\eta^2} = \\
- \frac{(U_\xi \omega^n)_{(i+1,j)} - (U_\xi \omega^n)_{(i-1,j)}}{2\Delta\xi} + \frac{2}{Re} \frac{\omega_{(i+1,j)}^n - 2\omega_{(i,j)}^n + \omega_{(i-1,j)}^n}{\Delta\xi^2} \\
+ NE_i^{\frac{1}{2}} \left[ \frac{F_{l\theta(i+1,j)} - F_{l\theta(i-1,j)}}{2\Delta\xi} + 2\pi F_{l\theta(i,j)} \right] \\
\\
E_i \frac{\omega_{(i,j)}^{n+1} - \omega_{(i,j)}^{n+\frac{1}{2}}}{\frac{1}{2}\Delta t} + \frac{(U_\xi \omega^{n+1})_{(i+1,j)} - (U_\xi \omega^{n+1})_{(i-1,j)}}{2\Delta\xi} - \frac{2}{Re} \frac{\omega_{(i+1,j)}^{n+1} - 2\omega_{(i,j)}^{n+1} + \omega_{(i-1,j)}^{n+1}}{\Delta\xi^2} = \\
- \frac{(U_\eta \omega^{n+\frac{1}{2}})_{(i,j+1)} - (U_\eta \omega^{n+\frac{1}{2}})_{(i,j-1)}}{2\Delta\eta} + \frac{2}{Re} \frac{\omega_{(i,j+1)}^{n+\frac{1}{2}} - 2\omega_{(i,j)}^{n+\frac{1}{2}} + \omega_{(i,j-1)}^{n+\frac{1}{2}}}{\Delta\eta^2} \\
+ NE_i^{\frac{1}{2}} \left[ \frac{F_{l\theta(i+1,j)} - F_{l\theta(i-1,j)}}{2\Delta\xi} + 2\pi F_{l\theta(i,j)} \right]
\end{aligned}$$

where  $i, j$  refer to the  $\xi, \eta$  direction respectively and  $U_\xi, U_\eta$  are  $\xi, \eta$  velocity components which are calculated at the  $n^{th}$  time step.

The streamfunction was solved by adopting an efficient algorithm using Fast Fourier Transforms (FFT) with second-order accuracy, as in Hockney (1970):

$$\frac{\Psi_{(i+1,j)}^n - 2\Psi_{(i,j)}^n + \Psi_{(i-1,j)}^n}{\Delta\xi^2} + \frac{\Psi_{(i,j+1)}^n - 2\Psi_{(i,j)}^n + \Psi_{(i,j-1)}^n}{\Delta\eta^2} = -E_i \Psi_{(i,j)}^n$$

In this numerical scheme, the second-order accuracy to calculate the vorticity flux in Eq. (2.7) can be obtained as follow:

$$\frac{\partial \omega_{(0,j)}^n}{\partial \xi} = \frac{-3\omega_{(0,j)}^n + 4\omega_{(1,j)}^n - \omega_{(2,j)}^n}{2\Delta\xi}$$



## 2.6 Feedback Control of Cylinder Wake

In this study, the feedback control technique developed by Chen and Aubry (2000) for manipulating wake flows is used. Due to the fact that vortex shedding is accompanied by flow separation from the solid body and by the asymmetry of the pressure on the surface of the cylinder. Their technique is based on closed loop control using flow information consisting of the detection of the separation point. Once sensors on the surface of the body detect the occurrence of the separation point, the actuators (arrays of electrodes and magnets generating a Lorentz force) will be activated. The activated actuators are used to suppress the total drag coefficient in order to control the flow and suppress vortex shedding. Using the suppression of the pressure drag coefficient as a constraint, they derived the interaction parameter equation as

$$N = -\frac{1}{\pi Re} \frac{\int_0^1 \frac{\partial \omega}{\partial \xi} \sin(2\pi\eta) d\eta}{\int_0^1 F_\theta \sin(2\pi\eta) d\eta} \quad (2.13)$$

They selected the location of actuators to be  $10^\circ$  degrees upstream of the separation point. The expression of the Lorentz force  $\vec{F}$  then becomes

$$\vec{F} = e^{-\alpha(r-1)} g(\theta) \vec{e}_\theta \quad \text{with} \quad g(\theta) = \begin{cases} 1 & \theta' - 10^\circ \leq \theta \leq 175^\circ \\ -1 & 185^\circ \leq \theta \leq 370^\circ - \theta' \\ 0 & \text{elsewhere} \end{cases} \quad (2.14)$$

where  $\theta'$  is the location of separation point detected at any time on the upper surface of cylinder.

## CHAPTER 3

### LIGHTHILL'S ACOUSTIC THEORY

#### 3.1 Analysis of Lighthill Equation

The analysis of the aerodynamic sound of fluid-structure interactions is embraced in the consideration of the governing equation of fluid motion. First the governing equations of fluid motion that is the conservation of mass and momentum are represented, and then Lighthill's equation is reviewed.

##### *Equation of Continuity*

Conservation of mass states that the time rate of change of fluid mass within a fixed space  $V$  is equal to the net flux due to convection across the boundaries of  $V$ . This is expressed in terms of the velocity  $\mathbf{v}$  and the fluid density  $\rho$  by the equation of continuity

$$\frac{\partial \rho}{\partial t} + \nabla \cdot (\rho \mathbf{v}) = 0, \quad (3.1)$$

or

$$\frac{1}{\rho} \frac{D\rho}{Dt} + \nabla \cdot (\mathbf{v}) = 0, \quad (3.2)$$

where  $D/Dt = \partial/\partial t + \mathbf{v} \cdot \nabla$ .

When the flow is incompressible, the continuity equation becomes

$$\nabla \cdot \mathbf{v} = 0. \quad (3.3)$$

### ***Equation of Momentum***

The momentum equation expresses the time rate of change of momentum of a fluid particle in terms of the *viscous stress tensor*  $e_{ij}$ , the pressure  $p$ , and body forces  $F$  per unit volume.

$$\begin{aligned}\frac{\rho Du_i}{Dt} &= \frac{\partial e_{ij}}{\partial y_j} - \frac{\partial p}{\partial y_i} + F_i \\ &\equiv -\frac{\partial p_{ij}}{\partial y_j} + F_i ,\end{aligned}\tag{3.4}$$

where

$$p_{ij} = p\delta_{ij} - e_{ij} ,\tag{3.5}$$

$$e_{ij} = \mu \left( \frac{\partial u_i}{\partial y_j} + \frac{\partial u_j}{\partial y_i} \right) - \frac{2}{3}\mu\delta_{ij}\frac{\partial u_k}{\partial y_k} .\tag{3.6}$$

Here  $\rho$  is the density;  $u_i$  is the unsteady source velocity;  $\mu$  is the kinematic viscosity;  $p_{ij}$  is the *compressive stress tensor*; and  $e_{ij}$  is the *viscous stress tensor* expressions.

### ***Equation of State***

In general, an energy equation and conservation equation should be considered along with a thermodynamic equation of the state. However, in this study, the assumption is made such that the energy is conserved and, therefore, a separate equation for energy is not needed.

The equation of state, needed in acoustic studies, relates the thermodynamic properties of the fluid considered. In particular, pressure can be related to density and entropy,

$$p = p(\rho, s), \quad (3.7)$$

where  $s$  is the entropy per unit mass. When energy loss can be neglected, as it is often the case of acoustics, the entropy remains constant. This is known as isentropic process. The pressure is then a function of density alone, such that

$$p = p(\rho). \quad (3.8)$$

For any fluid( liquid or gas), the general isentropic equation of state may be expressed as, a Taylor series in terms of the condensation  $(\rho - \rho_o)/\rho_o$ , (Blackstock; 2000):

$$p = p_o + A \frac{\rho - \rho_o}{\rho_o} + \frac{B}{2!} \left( \frac{\rho - \rho_o}{\rho_o} \right)^2 + \frac{C}{3!} \left( \frac{\rho - \rho_o}{\rho_o} \right)^3 + \dots \quad (3.9)$$

The coefficients  $A, B, C, \dots$  are obtained from further analysis or from experiments. In acoustics, the condensation is usually very small, and the first order term becomes the dominant term. In order to determine the term  $A$ , the new thermodynamic variable, sound speed  $c$ , is defined as follows:

$$\begin{aligned} c^2 &\equiv 1 / \left( \frac{\partial \rho}{\partial P} \right)_{s=\text{constant}} \\ &= \left( \frac{dP}{d\rho} \right)_{s=\text{constant}}. \end{aligned} \quad (3.10)$$

The differentiation of Eq. (3.9) then leads to

$$c^2 = \frac{A}{\rho_o} + \frac{B}{\rho_o} \frac{\rho - \rho_o}{\rho_o} + \frac{C}{2!\rho_o} \left( \frac{\rho - \rho_o}{\rho_o} \right)^2 + \dots \quad (3.11)$$

Rewriting Eq. (3.11) in terms of the acoustic pressure ( $p - p_o$ ) and the acoustic density ( $\rho - \rho_o$ ), it becomes

$$(p - p_o) = c^2(\rho - \rho_o) \left\{ 1 + \frac{B}{2!A} \frac{\rho - \rho_o}{\rho_o} + \frac{C}{3!A} \left( \frac{\rho - \rho_o}{\rho_o} \right)^2 + \dots \right\}. \quad (3.12)$$

Using the linearized isentropic equation of state in order to simplify Eq. (3.12), the acoustic pressure equation then becomes:

$$(p - p_o) = c^2(\rho - \rho_o). \quad (3.13)$$

Lighthill (1952) considered the radiation of sound in a far-field/subsonic flow without any solid boundaries. The back-reaction of the sound on the source flow field was assumed to be negligible. Lighthill's equation was derived by rearranging the governing equation of fluid motion.

By multiplying the continuity equation, Eq. (3.1), by  $\mathbf{v}$  and adding to the momentum equation, Eq. (3.4), the equation for the rate of change of the momentum density  $\rho\mathbf{v}$  is formulated as

$$\frac{\partial \rho u_i}{\partial t} + \frac{\partial \rho u_i u_j}{\partial y_j} = - \frac{\partial (p \delta_{ij} - e_{ij})}{\partial y_j} + F_i. \quad (3.14)$$

The  $\rho u_i u_j$  term, or *Reynolds stress*, appears in this equation. At any point in the flow, the order of magnitude of the *Reynolds stress* relative to the *viscous stress*  $e_{ij}$  (3.6) is determined by the value of the *Reynolds number*  $\text{Re}$ . In the flow region where  $\text{Re} \gg 1$ , the viscous transport of momentum is negligible compared with the momentum transport due to turbulence convection.

Now consider the sound generated by a finite region of rotational flow in an unbounded fluid flow. When body forces are neglected, the momentum equation, Eq. (3.14), can be rewritten as

$$\frac{\partial \rho u_i}{\partial t} = -\frac{\partial \tau_{ij}}{\partial y_j}, \quad (3.15)$$

where  $\tau_{ij}$  is the *momentum flux* tensor (Howe(1998)),

$$\tau_{ij} = \rho u_i u_j + (p - p_o)\delta_{ij} - e_{ij}, \quad (3.16)$$

and  $p_o$  is the uniform pressure at infinity.

In an ideal, linear acoustic medium and isentropic flow, it can be shown that  $\tau_{ij}^o = (p - p_o)\delta_{ij} \equiv c_o^2(\rho - \rho_o)\delta_{ij}$ , where  $\rho_o$  and  $c_o$  are the mean density and sound speed. By eliminating  $\rho u_i$  between Eq. (3.15) (where  $\tau_{ij} \rightarrow \tau_{ij}^o$ ) and the continuity equation, the equations of linear acoustics for the perturbation density  $\rho - \rho_o$  and the perturbation pressure  $p - p_o$  can be rewritten as

$$\left(\frac{\partial^2}{\partial t^2} - c_o^2 \nabla^2\right)(\rho - \rho_o) = 0, \quad (3.17)$$

and

$$(\frac{1}{c_o^2} \frac{\partial^2}{\partial t^2} - \nabla^2)(p - p_o) = 0. \quad (3.18)$$

In the real fluid, the sound generation is equivalent to that produced in an ideal acoustic medium that is forced by the stress distribution  $T_{ij} = \tau_{ij} - \tau_{ij}^o$ , that is

$$T_{ij} = \rho u_i u_j + [(p - p_o) - c_o^2(\rho - \rho_o)]\delta_{ij} - e_{ij}, \quad (3.19)$$

where  $T_{ij}$  is called the *Lighthill stress tensor*. The Reynolds stress  $\rho u_i u_j$  is nonlinear and is significant only within the rotational source field. The second term, caused by the nonlinearity of the wave amplitude and by the variation of the mean density in the source flow, is the excess of momentum transfer by the pressure compared with the momentum transfer in an ideal fluid density  $\rho_o$  and sound speed  $c_o$ . The last term represents the *viscous stress tensor*  $e_{ij}$  that weakens the sound. Linear in the perturbation quantities, it can be neglected for an approximation of the sound in the radiation zone and when the Reynolds number in the source region is sufficiently large.

From the assumption that the flow emanates from a region of uniform temperature, the effect of heat conduction should be small and negligible. Therefore, compared with the Equation of State, Eq. (3.12), the second term in the right hand side of Eq. (3.19) is sufficiently small and negligible within the flow. Hence, the Lighthill stress tensor,  $T_{ij}$ , is approximately equal to  $\rho u_i u_j$  inside the flow, and it becomes

$$T_{ij} \approx \rho u_i u_j . \quad (3.20)$$

Lighthill's acoustic analogy equation for the aerodynamic sound generation is obtained by adding and subtracting  $c_o^2 \partial(\rho - \rho_o)/\partial y_i$  to Eq. (3.15), and then rewriting the equation as the momentum equation for the mean fluid density  $\rho$  and sound speed  $c_o$  under the externally applied stress  $T_{ij}$

$$\frac{\partial \rho u_i}{\partial t} + \frac{\partial(c_o^2(\rho - \rho_o))}{\partial y_i} = -\frac{\partial T_{ij}}{\partial y_j} . \quad (3.21)$$

By differentiating the continuity equation, Eq. (3.1) with respect to  $t$ , taking the divergence of equation Eq. (3.21), and subtracting the results, *Lighthill's equation*, which is the exact, nonhomogenous counterpart of Eq. (3.17) is obtained:

$$(\frac{\partial^2}{\partial t^2} - c_o^2 \nabla^2)(\rho - \rho_o) = \frac{\partial^2 T_{ij}}{\partial y_i \partial y_j} , \quad (3.22)$$

Since Lighthill's equation is an exact consequence of the laws of conservation of mass and momentum, no approximation is made in this equation. The study of the aerodynamic sound, in many applications, consists in solving the Lighthill equation for the radiation into an ideal, stationary fluid produced by a distribution of sound sources whose strength per unit volume is the Lighthill stress tensor  $T_{ij}$ . The source term  $\partial^2 T_{ij}/\partial y_i \partial y_j$  represents not only the sound emission but also the convection by the mean flow and refraction due to the sound speed, the scattering of the sound by turbulence, and the viscous and thermal dissipation of the sound by the flow. Nonlinear effects on propagation and dissipation are usually very small, and will be neglected within the source region. From Lighthill's acoustic analogy (1952,



1954), the unsteady flow region is the aeroacoustic sound source, the *compressibility* of which can be neglected. The predictions of aerodynamic sound are therefore obtained by estimating  $T_{ij}$  based on the equation of motion of an incompressible fluid. This incompressible flow approach is acceptable for low Mach number values ( $M^2 \ll 1$ ) and when the wavelength of the sound is much larger than the dimension of the source region.

### 3.2 The Solution of Lighthill's Equation for Stationary Solid Boundaries and Uniform Moving Medium

In this section, the derivation of Lighthill's equation (3.22) for stationary solid boundaries is represented. This was first derived by Curle (1955). First the solution of Lighthill's equation in three-dimensional (3D) fields is presented. This formulation will then be reduced to the two-dimensional (2D) case.

#### 3.2.1 Three-Dimensional Fields

In this dissertation, the acoustic problem involving sound propagation in a uniform flow past a circular cylinder is considered. Therefore, Lighthill's equation, Eq. (3.22), must be transformed into the equation that represents an acoustic wave in a moving medium. In order to utilize the same procedure that is used to solve the inhomogeneous, uniformly moving medium wave equation (see appendix B), a coordinate system  $\vec{y}'$  which moves with the mean flow of uniform velocity  $U_\infty$  in the  $y_1$ – direction is introduced:

$$y'_i = y_i - \delta_{1i} U_\infty \tau \quad (3.23)$$

Using this new coordinate system, the acoustic equation in a uniformly moving medium can be changed to an equivalent stationary-medium acoustic equation.

Recalling that Lighthill's equation is obtained directly from the continuity and momentum equations, and that these governing equations are invariant under the coordinating transformation of Eq (3.23), Lighthill's equation in the new coordinate system reads:

$$\left( \frac{\partial^2}{\partial \tau^2} - c_o^2 \frac{\partial^2}{\partial y'_i \partial y'_i} \right) (\rho - \rho_o) = \frac{\partial^2 T'_{ij}}{\partial y'_i \partial y'_j}, \quad (3.24)$$

where

$$T'_{ij} = \rho u'_i u'_j + [(p - p_o) - c_o^2(\rho - \rho_o)] \delta_{ij} - e_{ij} \quad (3.25)$$

is Lighthill's stress tensor in terms of the velocity,

$$u'_i = u_i - \delta_{1i} U_\infty \quad (3.26)$$

determined in the moving frame of reference.

Now introducing the fixed-frame coordinates  $y_i$  into Eq. (3.24), and keeping the moving-frame velocities, Eq. (3.24) in the stationary- coordinate system is rewritten as

$$\left( \frac{D^2}{D\tau^2} - c_o^2 \frac{\partial^2}{\partial y_i \partial y_i} \right) (\rho - \rho_o) = \frac{\partial^2 T'_{ij}}{\partial y_i \partial y_j}, \quad (3.27)$$

where

$$\frac{D(\cdot)}{D\tau} = \frac{\partial(\cdot)}{\partial \tau} + U_\infty \frac{\partial(\cdot)}{\partial y_1}. \quad (3.28)$$

Using the same procedure, Eq. (3.21) can be written as follows:

$$\frac{D\rho u_i}{D\tau} + \frac{\partial(c_o^2(\rho - \rho_o))}{\partial y_i} = -\frac{\partial T'_{ij}}{\partial y_j}. \quad (3.29)$$

Since Eq. (3.27) has the same form as Eq. (B.1) in Appendix B, it is also expected to have the same solution. By applying the solution of the inhomogeneous, uniformly moving medium, wave equation to the modified Lighthill's equation (3.27) in the case of the flow past a stationary circular cylinder and a uniformly moving medium, Eq. (B.8) is reduced to:

$$\begin{aligned}
\rho'(\vec{x}, t) &= \frac{1}{c_o^2} \int_{-\infty}^{\infty} \int_V G(\vec{y}, \tau | \vec{x}, t) \frac{\partial^2 T'_{ij}}{\partial y_i \partial y_j} d\vec{y} d\tau \\
&+ \int_{-\infty}^{\infty} \int_S G(\vec{y}, \tau | \vec{x}, t) \left( \frac{\partial}{\partial n} \rho'(\vec{y}, \tau) \right) d\mathcal{S}(\vec{y}) d\tau \\
&- \int_{-\infty}^{\infty} \int_S \rho'(\vec{y}, \tau) \left( \frac{\partial}{\partial n} G(\vec{y}, \tau | \vec{x}, t) \right) d\mathcal{S}(\vec{y}) d\tau. \tag{3.30}
\end{aligned}$$

where  $\rho' = (\rho - \rho_o)$  and  $G(\vec{y}, \tau | \vec{x}, t)$  is any solution of the inhomogeneous wave equation (B.2).

Expanding the first term of Eq.(3.30) and applying the divergence theorem, Eq.(A.1), to change the volume integrals into surface integrals, it becomes:

$$\begin{aligned}
\rho'(\vec{x}, t) &= \frac{1}{c_o^2} \int_{-\infty}^{\infty} \int_V T'_{ij} \frac{\partial^2 G}{\partial y_i \partial y_j} d\vec{y} d\tau \\
&+ \frac{1}{c_o^2} \int_{-\infty}^{\infty} \int_S G(\vec{y}, \tau | \vec{x}, t) n_i \frac{\partial}{\partial y_i} \left( T'_{ij} + c_o^2 \delta_{ij} \rho'(\vec{y}, \tau) \right) d\mathcal{S}(\vec{y}) d\tau \\
&- \frac{1}{c_o^2} \int_{-\infty}^{\infty} \int_S n_j \left( T'_{ij} + c_o^2 \delta_{ij} \rho'(\vec{y}, \tau) \right) \frac{\partial G}{\partial y_i} d\mathcal{S}(\vec{y}) d\tau. \tag{3.31}
\end{aligned}$$

where  $G \equiv G(\vec{y}, \tau | \vec{x}, t)$ .

By using Eqs. (3.29), (3.25), Eq. (3.31) becomes:

$$\begin{aligned}
\rho'(\vec{x}, t) &= \frac{1}{c_o^2} \int_{-\infty}^{\infty} \int_V T'_{ij} \frac{\partial^2 G}{\partial y_i \partial y_j} d\vec{y} d\tau \\
&+ \frac{1}{c_o^2} \int_{-\infty}^{\infty} \int_S \frac{\partial G}{\partial y_i} \mathcal{F}_i d\mathcal{S}(\vec{y}) d\tau \tag{3.32}
\end{aligned}$$

where

$$\mathcal{F}_i \equiv -(p - p_o)n_i + e_{ij}n_j \quad (3.33)$$

is the  $i$ -th component of the force per unit area exerted by the boundaries on the fluid.

Eq. (3.32) is the fundamental equation for the sound generation in the case of fixed solid boundaries (e.g. a circular cylinder) and uniform flow. Provided the source distribution  $T_{ij}$  and  $\mathcal{F}_i$ , the generation of sound from this fundamental equation can then be determined.

The first term of Eq. (3.32) represents the generation of sound by quadrupole sources. In other words, it corresponds to the solution of Lighthill's equation when there is no solid boundaries in the flow. The second term represents the sound generated by unsteady forces exerted on the fluid by the solid boundaries.

In any given problem, there are many possible choices for choosing the fundamental solution  $G$  in Eq. (3.32). However, it should be an optimal approximation to the sound field from the known source terms,  $T_{ij}$  and  $\mathcal{F}_i$ . As discussed in the literature ( Goldstein, (1974); Howe, (1998); etc. ), the fundamental solution  $G$ , or the free-space Green's function, is chosen to be:

$$G(\vec{y}, \tau \mid \vec{x}, t) = \frac{1}{4\pi r} \delta(t - \tau - \frac{r}{c_o}) . \quad (3.34)$$

Note that the Green's function was chosen to have vanishing normal derivative on the surface and was then obtained by using the expansion of Eq.(1.11.1) (Howe, 1998). See Howe (1998) for more details.

Since  $G$  depends on  $\vec{y}$  and  $\vec{x}$  through  $r = |\vec{x} - \vec{y}|$ , it follows that

$$\frac{\partial G}{\partial y_i} = -\frac{\partial G}{\partial x_i}. \quad (3.35)$$

The substitution Eq. (3.34) into Eq. (3.32) gives

$$\begin{aligned} \rho'(\vec{x}, t) &= \frac{1}{c_o^2} \frac{\partial^2}{\partial x_i \partial x_j} \int_{-\infty}^{\infty} \int_V \frac{1}{4\pi r} \delta(t - \tau - \frac{r}{c_o}) T_{ij} d\vec{y} d\tau \\ &- \frac{1}{c_o^2} \frac{\partial}{\partial x_i} \int_{-\infty}^{\infty} \int_S \frac{1}{4\pi r} \delta(t - \tau - \frac{r}{c_o}) \mathcal{F}_i \mathcal{S}(\vec{y}) d\tau. \end{aligned} \quad (3.36)$$

Since the integration of the volume and surface integrals are independent of  $\tau$  when the solid surface is fixed, the order of integration can be interchanged. it thus becomes:

$$\begin{aligned} \rho'(\vec{x}, t) &= \frac{1}{c_o^2} \frac{\partial^2}{\partial x_i \partial x_j} \int_V \left( \int_{-\infty}^{\infty} \frac{1}{4\pi r} \delta(t - \tau - \frac{r}{c_o}) T_{ij} d\tau \right) d\vec{y} \\ &- \frac{1}{c_o^2} \frac{\partial}{\partial x_i} \int_S \left( \int_{-\infty}^{\infty} \frac{1}{4\pi r} \delta(t - \tau - \frac{r}{c_o}) \mathcal{F}_i d\tau \right) \mathcal{S}(\vec{y}). \end{aligned} \quad (3.37)$$

Carrying out the integrations over  $\tau$ , it becomes

$$\begin{aligned} \rho'(\vec{x}, t) &= \frac{1}{4\pi c_o^2} \frac{\partial^2}{\partial x_i \partial x_j} \int_V \left[ \frac{T_{ij}}{r} \right]_{ret} d\vec{y} \\ &- \frac{1}{4\pi c_o^2} \frac{\partial}{\partial x_i} \int_S \left[ \frac{\mathcal{F}_i}{r} \right]_{ret} \mathcal{S}(\vec{y}), \end{aligned} \quad (3.38)$$

where the variables in the brackets is to be evaluated at the retard time:

$$\tau_{ret} = t - \frac{|\vec{x} - \vec{y}|}{c_o}. \quad (3.39)$$

In the case when  $\vec{x} \gg \vec{y}$  which is the case of the far-field sound, Eq. (3.38) can be simplified further as follows:

$$\begin{aligned} \rho'(\vec{x}, t) &= \frac{x_i x_j}{4\pi c_o^4 x^3} \int_V \frac{\partial^2}{\partial \tau_{ret}^2} T'_{ij}(\vec{y}, t - \frac{r}{c_o}) d\vec{y} \\ &- \frac{x_i}{4\pi c_o^3 x^2} \int_S \frac{\partial}{\partial \tau_{ret}} \mathcal{F}_i(\vec{y}, t - \frac{r}{c_o}) d\mathcal{S}(\vec{y}). \end{aligned} \quad (3.40)$$

### 3.2.2 2-D Dimensionless Fields

To be able to compute the far-field acoustic density fluctuation at low mach numbers, using the dimensionless-numerical information from the unsteady incompressible near-flowfield, dimensionless form of Eq. (3.40) is considered. By keeping all dimensionless parameters in the flow-field presented in Chapter 2, and non-dimensionalizing the sound speed  $c_0$  by the free stream velocity  $U_\infty$  which is known as Mach number  $M$  where  $M = U_\infty/c_0$ , Lighthill's equation, Eq. (3.27) in its dimensionless form reads:

$$\left( \frac{D^2}{D\tau^2} - \frac{1}{M^2} \frac{\partial^2}{\partial y_i \partial y_i} \right) (\rho - \rho_o) = \frac{\partial^2 T'_{ij}}{\partial y_i \partial y_j}, \quad (3.41)$$

where

$$T'_{ij} = \rho u'_i u'_j + [(p - p_o) - \frac{1}{M^2}(\rho - \rho_o)] \delta_{ij} - e_{ij}, \quad (3.42)$$

$$e_{ij} = \frac{1}{Re} \left( \frac{\partial u'_i}{\partial y_j} + \frac{\partial u'_j}{\partial y_i} \right) - \frac{2}{3} \mu \delta_{ij} \frac{\partial u'_k}{\partial y_k}, \quad (3.43)$$

$$\frac{D(\cdot)}{D\tau} = \frac{\partial(\cdot)}{\partial \tau} + U_\infty \frac{\partial(\cdot)}{\partial y_1}, \quad (3.44)$$

$$u'_i = u_i - \delta_{1i} U_\infty. \quad (3.45)$$

By using the same procedure as in the previous section and following the work of Wang *et al.* (1996) which presented the simplified form suitable for numerical

evaluation, the dimensionless form of Eq. (3.40) becomes:

$$\begin{aligned} \rho(x, t) - 1 &\approx \frac{M^4}{2\pi} \frac{x_i x_j}{|\vec{x}|^2} \int_0^\infty \frac{\partial^2}{\partial \tau_{ret}^2} \int_\Gamma T_{ij}(\vec{y}, \tau_{ret}) d^2 \vec{y} d\xi \\ &- \frac{M^3}{2\pi} \frac{x_i}{|\vec{x}|} \int_0^\infty \frac{\partial}{\partial \tau_{ret}} \int_{\partial\Gamma} \mathcal{F}_i(\vec{y}, \tau_{ret}) d\vec{y} d\xi \end{aligned} \quad (3.46)$$

where

$$\mathcal{F}_i = -(p - p_o)n_i + e_{ij}n_j \quad (3.47)$$

$$\tau_{ret} = t - M|x|\cosh\xi \quad (3.48)$$

and  $\Gamma$  and  $\partial\Gamma$  are computational domain and cylinder surface respectively.

Equation (3.46) expresses the fact that there are two types of non-dimensional noise source functions: a volume quadrupole, generated in the entire flow domain and a surface dipole, generated on the surface of the cylinder. Hereafter, those two terms are referred as "quadrupole source" and "dipole source", respectively. From Eq. (3.46), it can be observed that the magnitude of the volume quadrupole is  $\mathcal{O}(M)$  times larger than the surface dipole. Therefore, at low Mach number ( $M \ll 1$ ), the dominant term for the density fluctuation is the surface dipole.

Using the notations, used by Wang *et al.* (1996) and You *et al.* (1998), the dipole and quadrupole source functions,  $\dot{D}_i$  and  $\ddot{Q}_{ij}$ , are defined as follows:

$$\ddot{Q}_{ij} = \int_0^\infty \frac{\partial^2}{\partial \tau_{ret}^2} \int_\Gamma T_{ij}(\vec{y}, \tau_{ret}) d^2 \vec{y} d\xi \quad (3.49)$$

$$\dot{D}_i = - \int_0^\infty \frac{\partial}{\partial \tau_{ret}} \int_{\partial\Gamma} \mathcal{F}_i(\vec{y}, \tau_{ret}) d\vec{y} d\xi. \quad (3.50)$$

For numerical simulations purposes, the interval of the outer integration of Equation (3.50) is partitioned into a number,  $Mterms$ , of subintervals. Eq. (3.49)

and Eq (3.50) can be rewritten, as follows:

$$\ddot{Q}_{ij} = \int_{\xi_0}^{\xi_{max}} \frac{\partial^2}{\partial \tau_{ret}^2} \int_{\Gamma} T_{ij}(\vec{y}, \tau_{ret}) d^2 \vec{y} d\xi \quad (3.51)$$

$$\dot{D}_i = - \int_{\xi_0}^{\xi_{max}} \frac{\partial}{\partial \tau_{ret}} \int_{\partial \Gamma} \mathcal{F}_i(\vec{y}, \tau_{ret}) d\vec{y} d\xi \quad (3.52)$$

with

$$Mterms = \frac{\xi_{max} - \xi_0}{\Delta \xi} . \quad (3.53)$$

Because the influence of the quadrupole noise source ( $\mathcal{O}(M^3)$ ) for the flow past a circular cylinder is much less than that of dipole source ( $\mathcal{O}(M^2)$ ) at low Mach Number, only the calculation of the dipole source term on the flow field will be performed. By using Lighthill's acoustic analogy approach at low Mach number, the source terms are obtained from the unsteady, incompressible, flow simulation. In this case, Eq. (3.47) is obtained by providing the pressure along the cylinder surface as the results of the flow field computation (neglecting  $e_{ij}$  terms). Finally, with the known source functions, the acoustic density or acoustic pressure can be determined.



## CHAPTER 4

### COMPUTATIONAL RESULTS

#### 4.1 Flow Field

Near-field flow simulations were computed at the Reynolds number values  $Re = 100$  and  $160$ , respectively, with and without applying flow control. The numerical results from the computational fluid dynamics (CFD) code had been validated by comparison with previous works. Without any further validation, the flow numerical results are used as input for the acoustic calculations. The obtained acoustic calculations will be validated against others' results.

The convergence of the CFD flow results (e.g. vorticity distribution, drag and lift coefficients, pressure coefficient) with spatial and time resolution were achieved with reasonable accuracy. It had been reported that the refinement of both the numerical mesh and the time step by a factor of 2 changed the vorticity distribution on the body by less than 2.5%. A good agreement was found between the flow field results obtained by using a  $400 \times 256$  grid and a finer grid. The  $400 \times 256$  grid is then used for flow field computations in order to minimize data storage and computational time for calculating the sound field results. Figure (4.1) shows the  $400 \times 256$  grid used in the dissertation.

##### 4.1.1 Without Control

###### 4.1.1.1 Computations at $Re = 100$ .

The simulation of the flow at  $Re = 100$  shows that the flow becomes asymmetric after a certain time, which then develops into a Karman vortex street. Figure (4.2) presents the visualization of the flow by mean of the streamlines for the interval  $760 \leq t \leq 800$ , with a time step  $\delta t = 10$ . Early in the computation, the streamlines are symmetric, the bubble

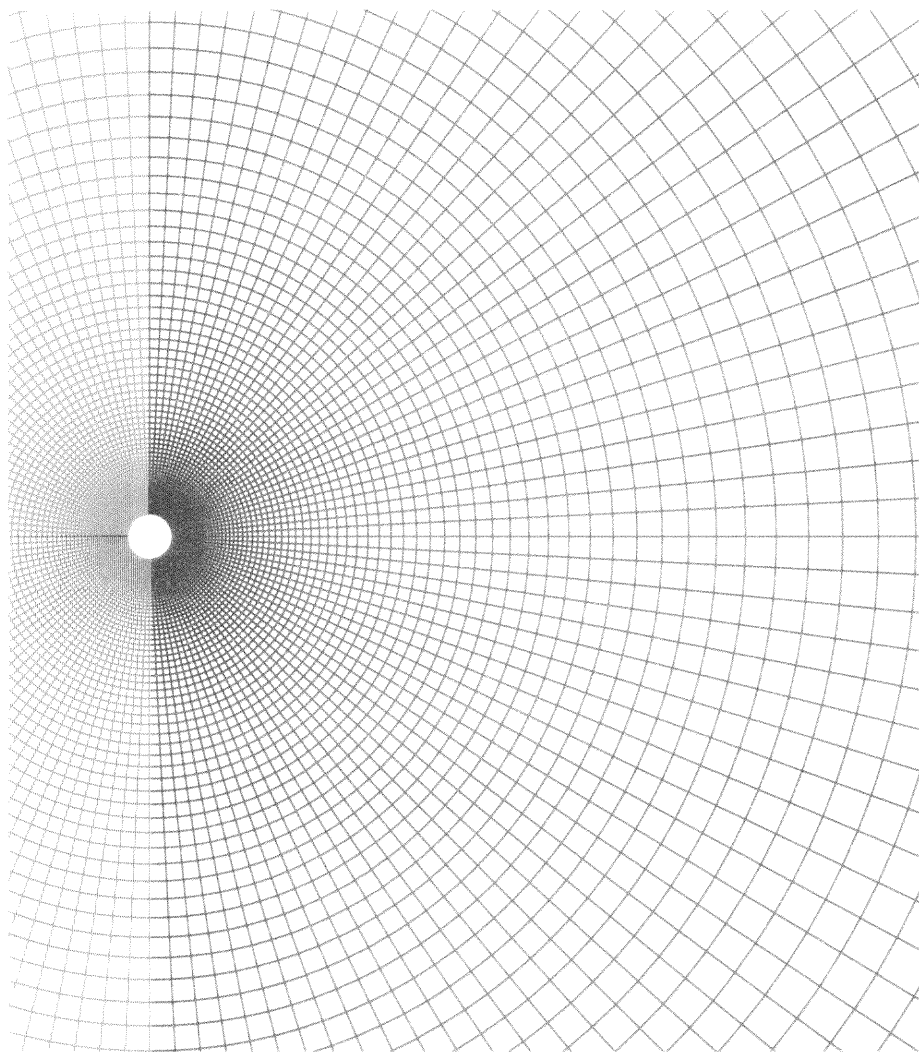
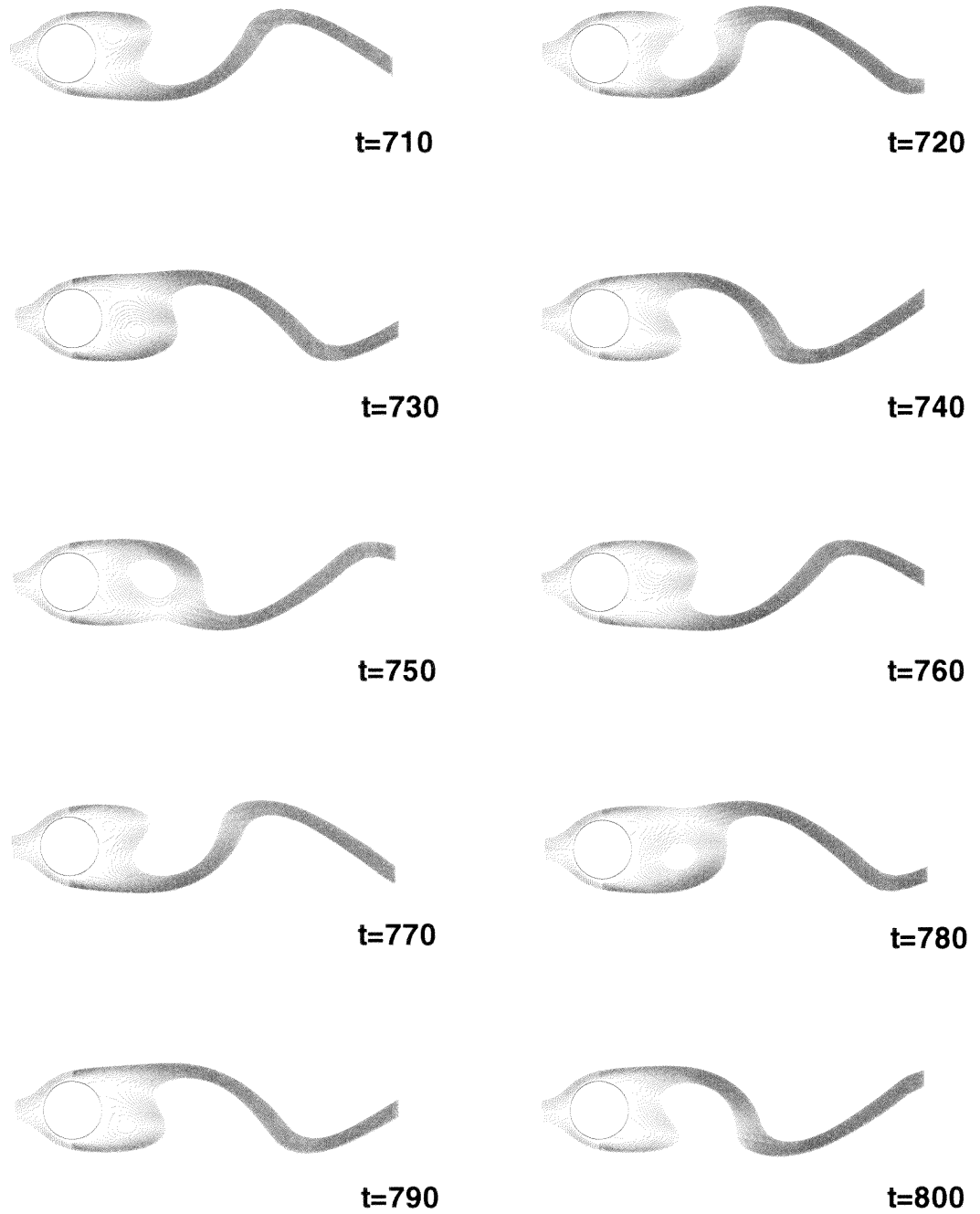


**Figure 4.1** The grid used around the cylinder with  $400 \times 256$  grid points

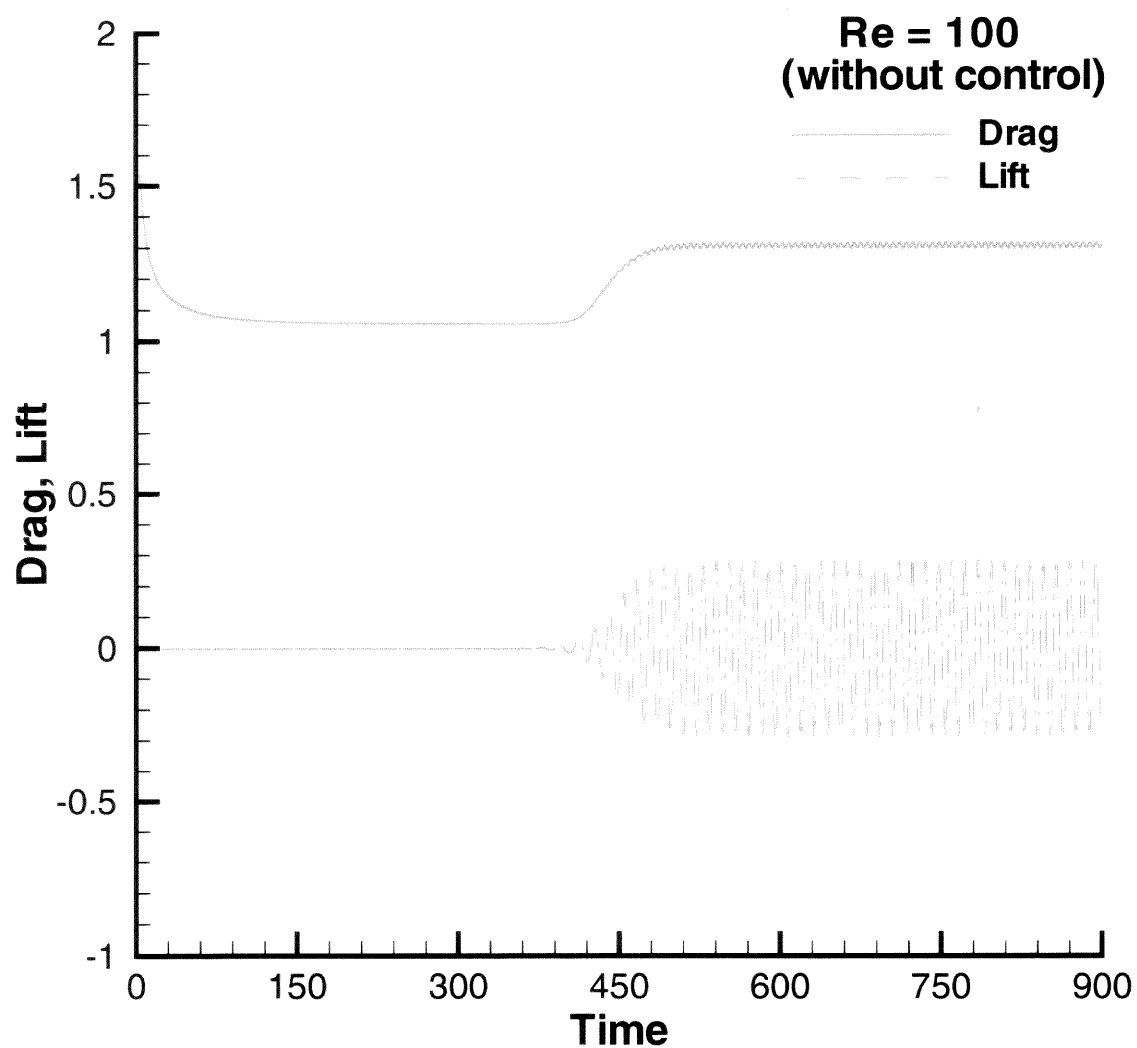
grows becoming more and more elongated. After a certain time, the growing bubble becomes unstable and undergoes an oscillatory motion in which one of the vortices becomes larger than the other one. As shown in Figure (4.2), at  $t = 750$ , the upper vortex sheds away from the body while the lower vortex is still attached to the cylinder. Later, the lower vortex becomes larger than the upper one, and then sheds away downstream. The phenomenon of vortex shedding occurs in a cycle as upper and lower vortices periodically shed away from the cylinder.

Figure (4.3) shows the drag and lift coefficients at  $Re = 100$ . In between the symmetric bubble and the vortex shedding regime, the drag increases significantly from  $c_d^{min} = 1.06$  at time  $t = 380$  to the mean drag  $c_d^{mean} = 1.31$  after  $t = 490$  in the oscillatory regime. The relative jump is thus about 23.6%. Choosing the period of time, Figure (4.4) displays the variations of drag and lift coefficient from  $t = 760$  to  $t = 800$ . Drag and lift oscillations play the major rule here as it will be shown later that they are the major causes of sound generation.

As it is well-known, drag and lift oscillation are due to the pressure fluctuation in the separated zone of the flow. During the symmetry breaking events, the increase of drag and lift coefficients corresponds to the increase of pressure on the cylinder surface. Figure (4.5) shows that the variations of the pressure coefficient at various time ( $t = 400, 500, 600, 700, 800$ ) are consistent with temporal changes in the streamline patterns (Figure (4.2)). For example, at  $t = 800$ , one observes that the upper vortex has shed downstream and that a new vortex is generated on the lower half-plane, thus causing a higher pressure on the lower part of the body.



**Figure 4.2** Streamlines of the flow at the Reynolds number value  $Re = 100$  for the time interval  $760 \leq t \leq 800$



**Figure 4.3** Time history of the drag and lift coefficients at the Reynolds number value  $Re = 100$

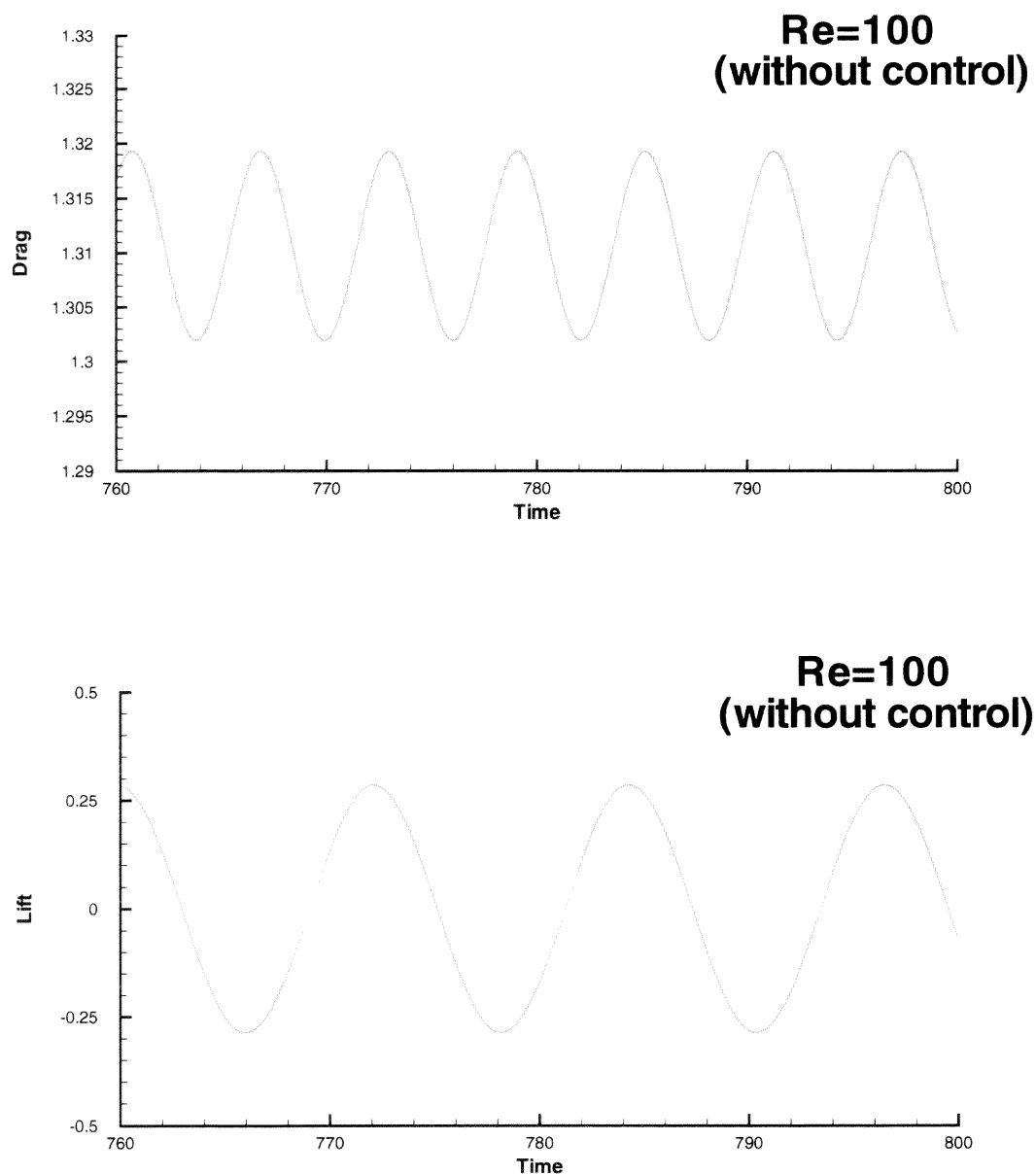


**Figure 4.4** Variation of the drag and lift coefficients on the surface of the cylinder at the Reynolds number value  $Re = 100$

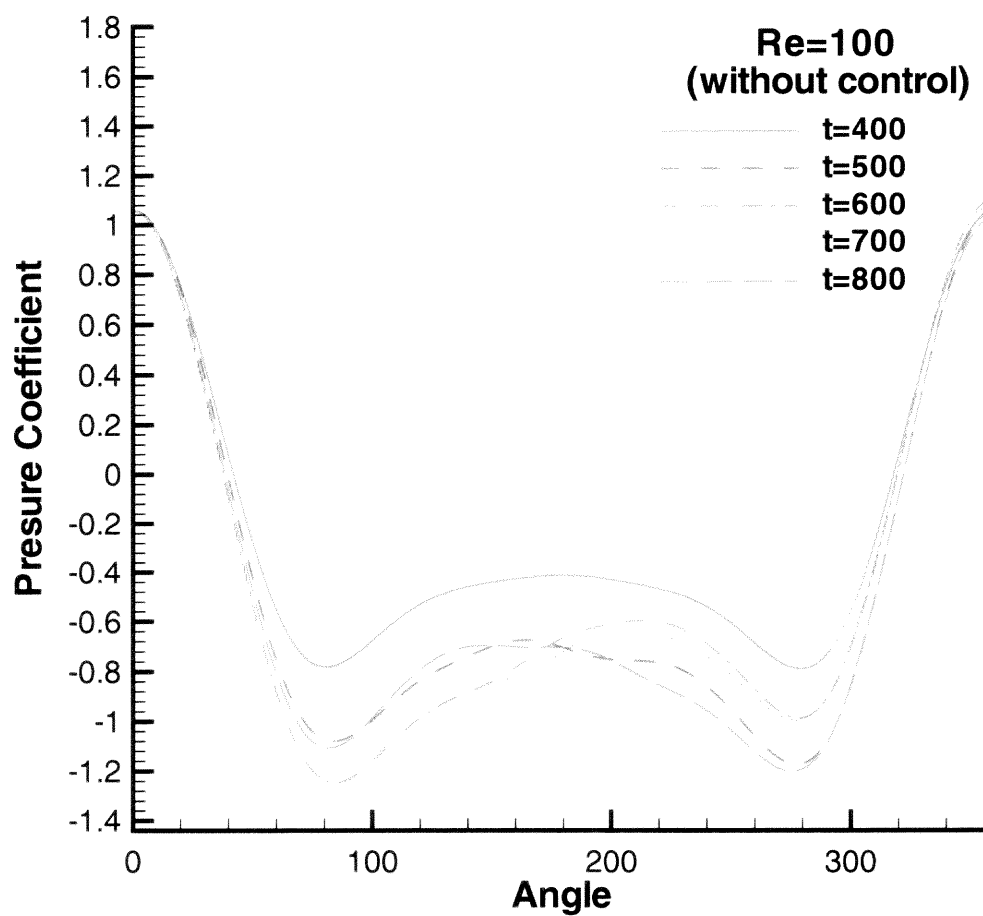


**Figure 4.5** Pressure coefficient of the flow on the surface of the cylinder at the Reynolds number value  $Re = 100$  at times  $t = 400, 500, 600, 700, 800$

#### 4.1.1.2 Computations at $Re = 160$ .

Figure (4.7) shows the drag and lift coefficients at  $Re = 160$  obtained in this study. During the symmetry breaking period, the sudden change in drag, known as the symmetry breaking instability, increases by 47.2% from  $c_d^{min} = 0.89$  to the mean drag  $c_d^{mean} = 1.31$  after  $t = 380$ . The time duration over which this increase takes place is about  $T = 100$ . Comparing the results between Figure (4.3) and Figure (4.7) shows that the intensity of the jump increases at  $Re = 160$  is higher than at  $Re = 100$ . In other words, the Reynolds number increases, the intensity of the jump also increases. The results for time average drag and lift coefficient in the asymptotic regime, shown in Figure (4.3) and Figure (4.7), are in good agreement with those presented in previous works.

### 4.1.2 With Control

#### 4.1.2.1 Computation at $Re = 100$ .

The feedback control is started at time  $t = 620$  when the Karman vortex street has settled. Figure (4.10) presents the visualization of the flow by means of the streamlines for the interval  $620 \leq t \leq 638$ , with a time step  $\delta t = 2$ . It's clearly shown that the vortex shedding is suppressed after control. Figure (4.11) shows the drag and lift coefficients at  $Re = 100$  obtained after control. Figure (4.12) shows the drag and lift coefficients for the time interval  $760 \leq t \leq 800$ . The drag coefficient undergoes a significant decrease while the lift coefficient decays to zero in the presence of the control. Figure (4.13) shows the pressure coefficient of the flow on the surface of the cylinder at times  $t = 620, 630, 650, 750$ , and  $t = 780$ , respectively.



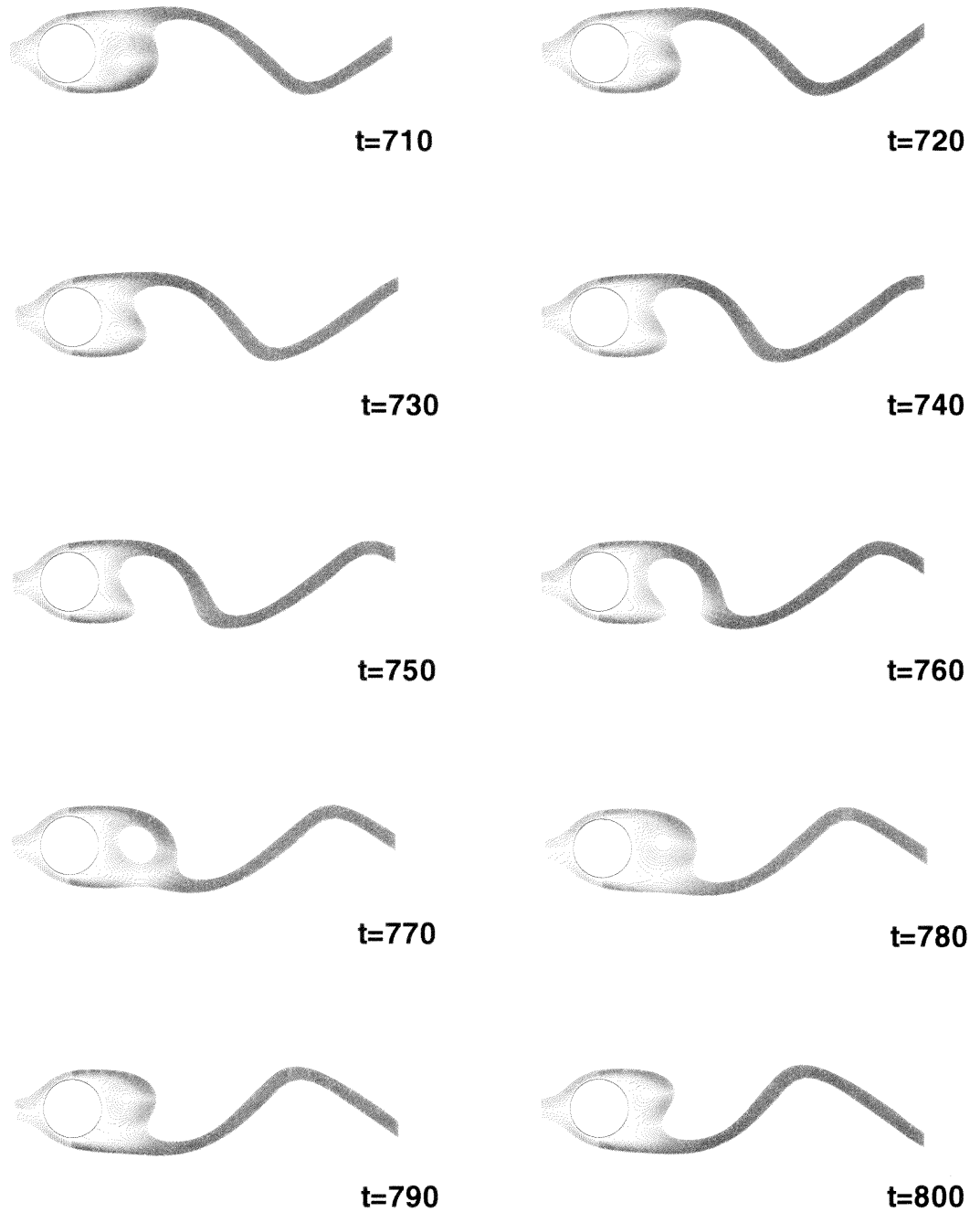


**Figure 4.6** Streamlines of the flow at the Reynolds number value  $Re = 160$  for the time interval  $760 \leq t \leq 800$

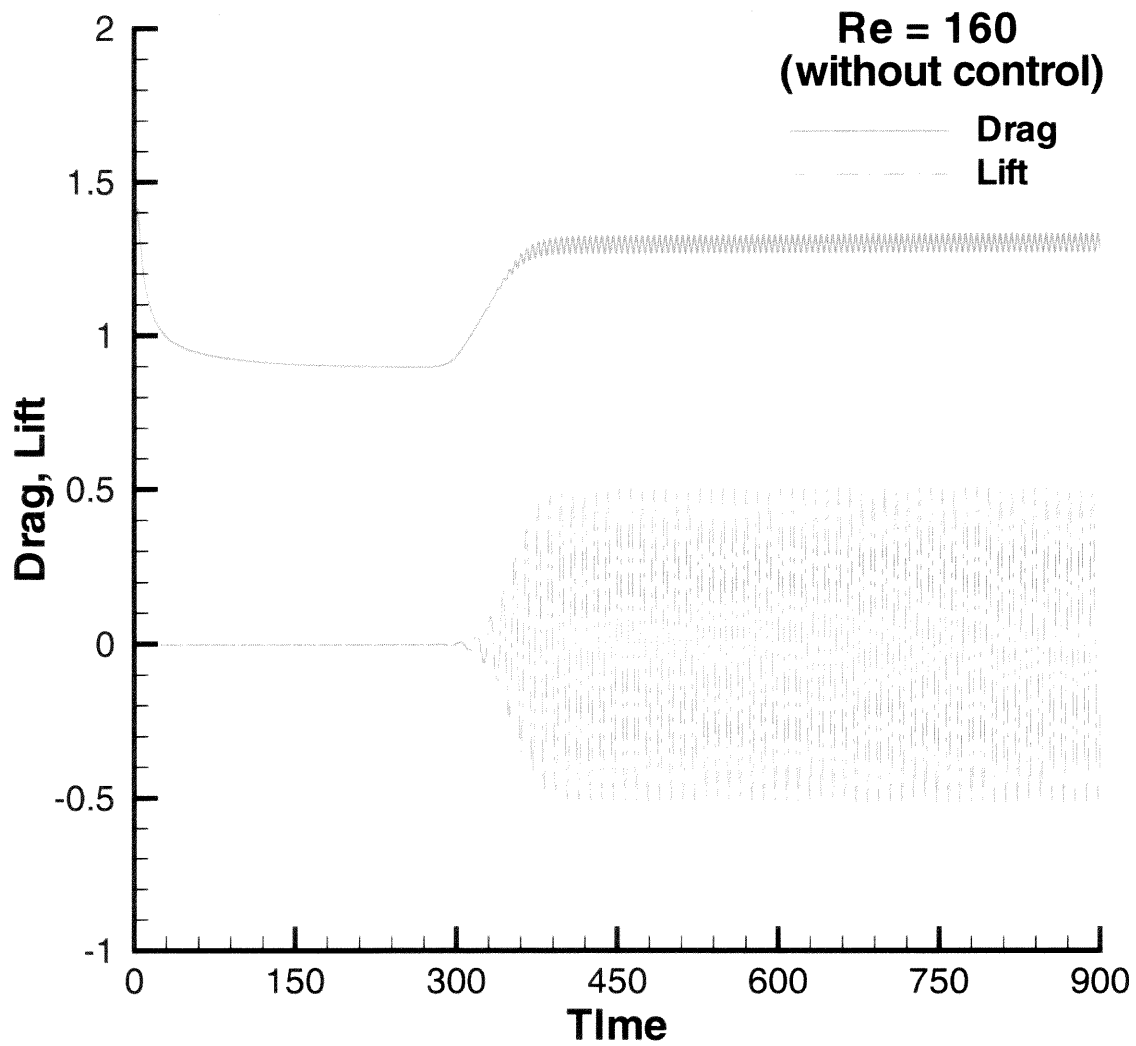


**Figure 4.7** Time history of the drag and lift coefficients at the Reynolds number value  $Re = 160$

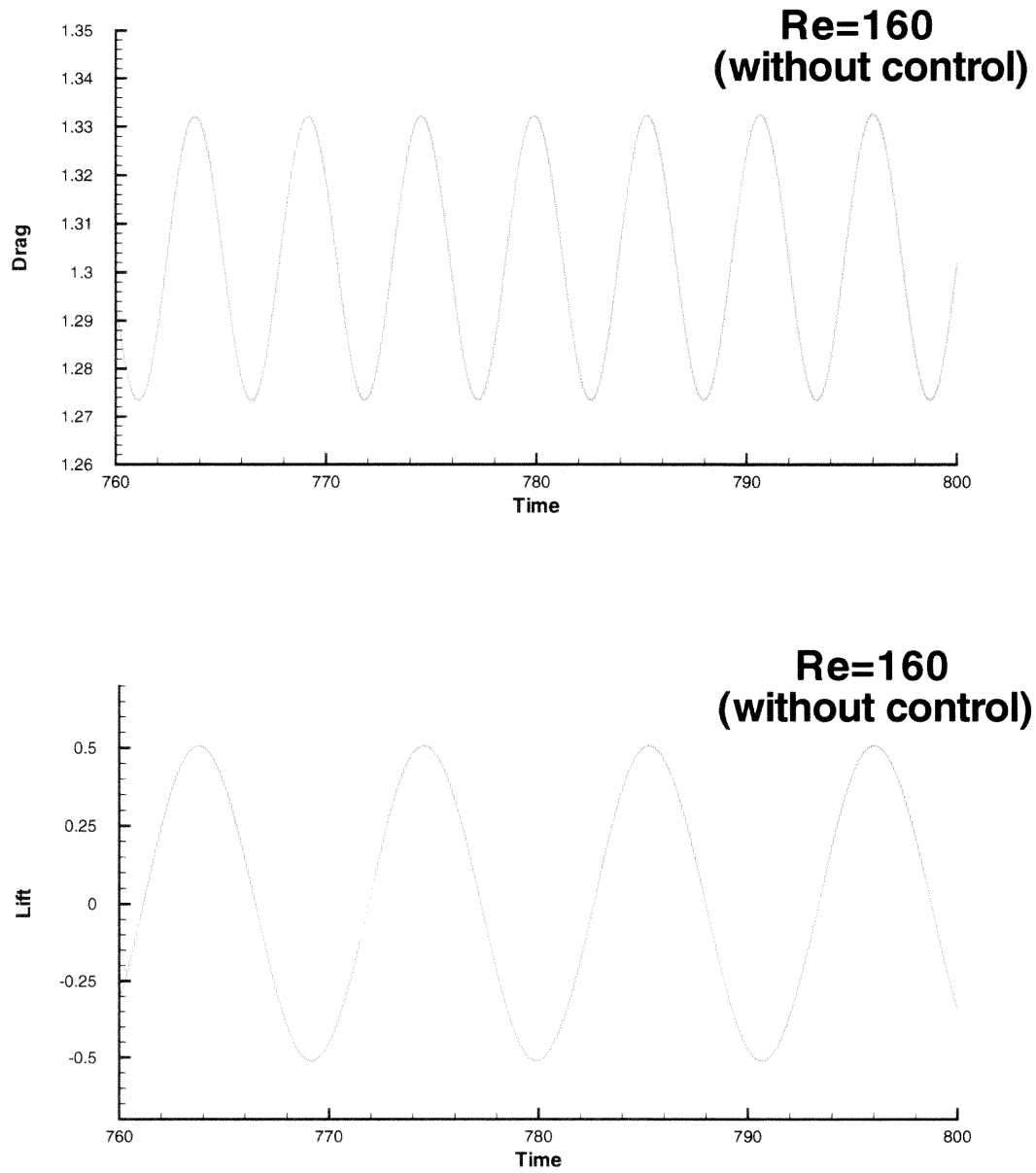


**Figure 4.8** Variation of the drag and lift coefficients on the surface of the cylinder at the Reynolds number value  $Re = 160$

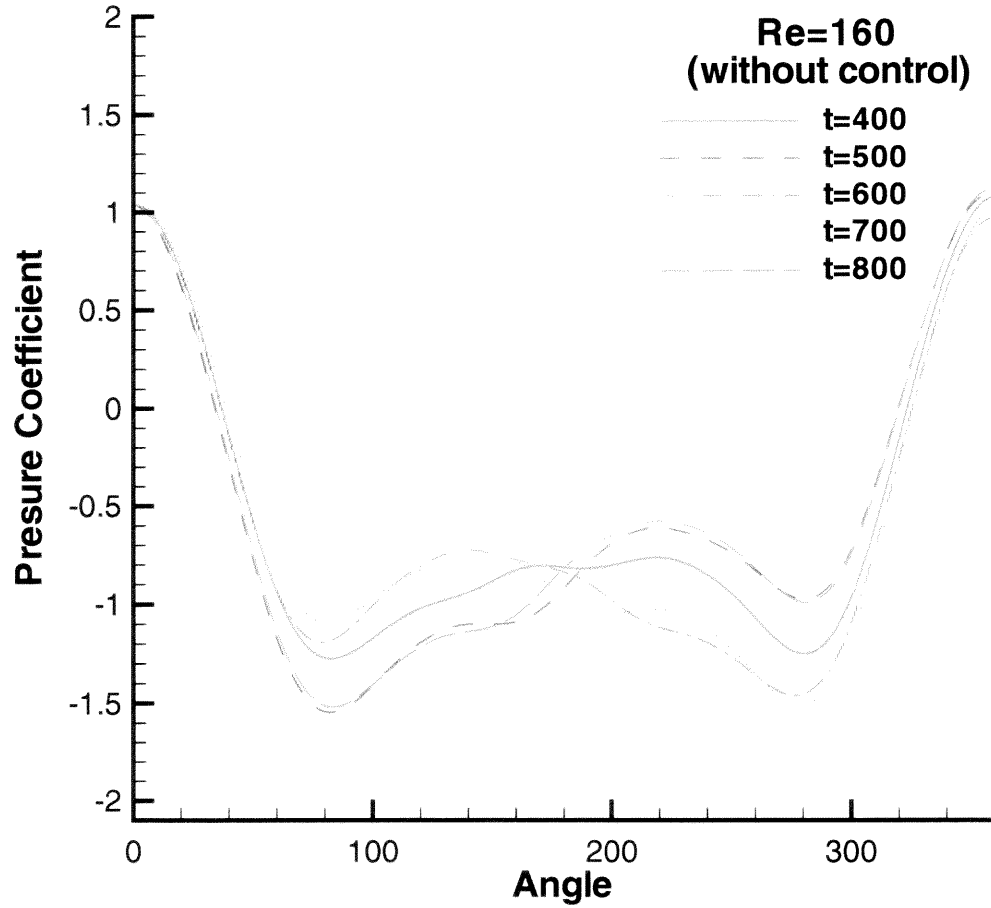


**Figure 4.9** Pressure coefficient of the flow on the surface of the cylinder at the Reynolds number value  $Re = 160$  at times  $t = 400, 500, 600, 700, 800$

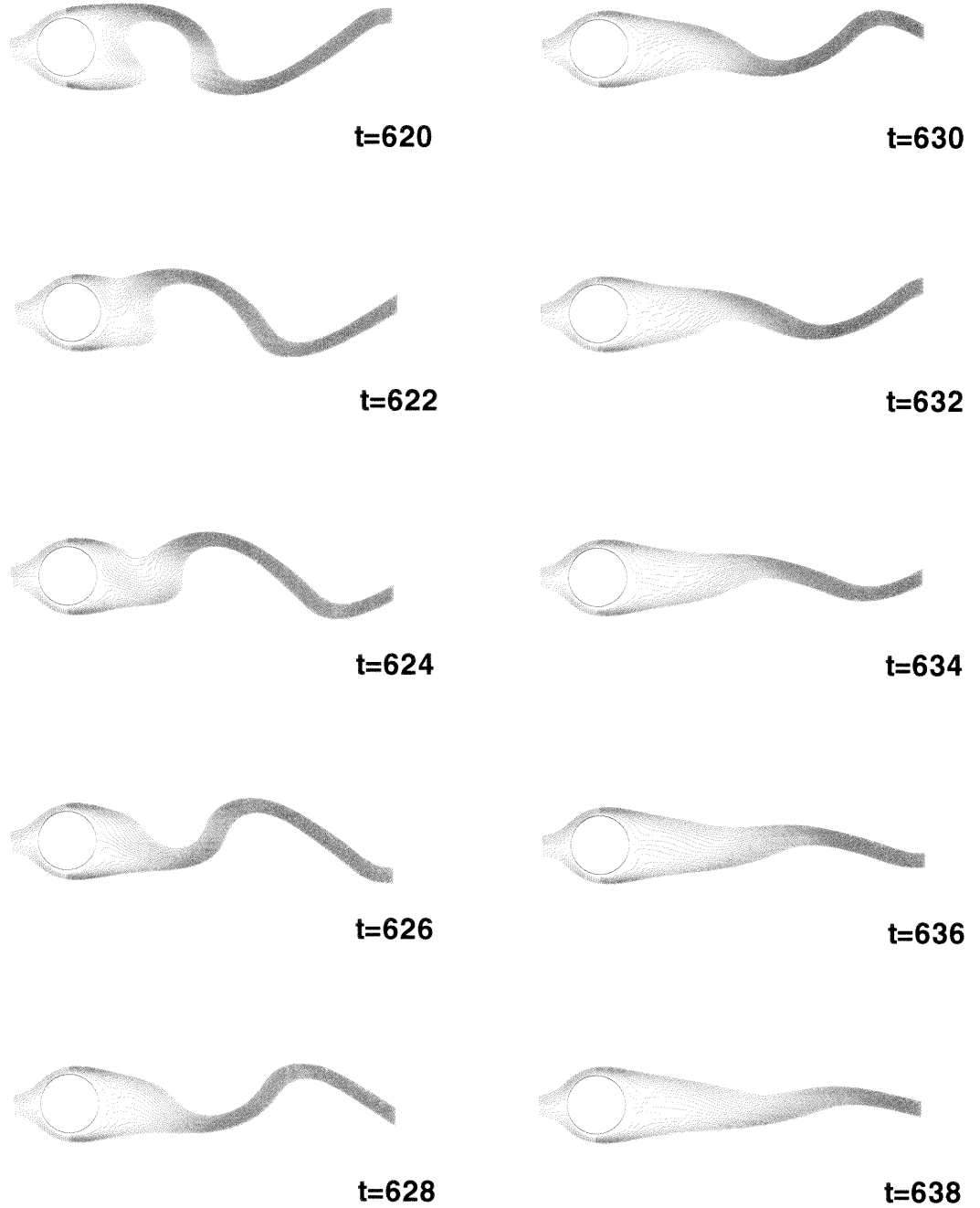


**Figure 4.10** Streamlines of the flow with control at the Reynolds number value  $Re = 100$  for the time interval  $620 \leq t \leq 638$ . The control is inserted at time  $t = 620$

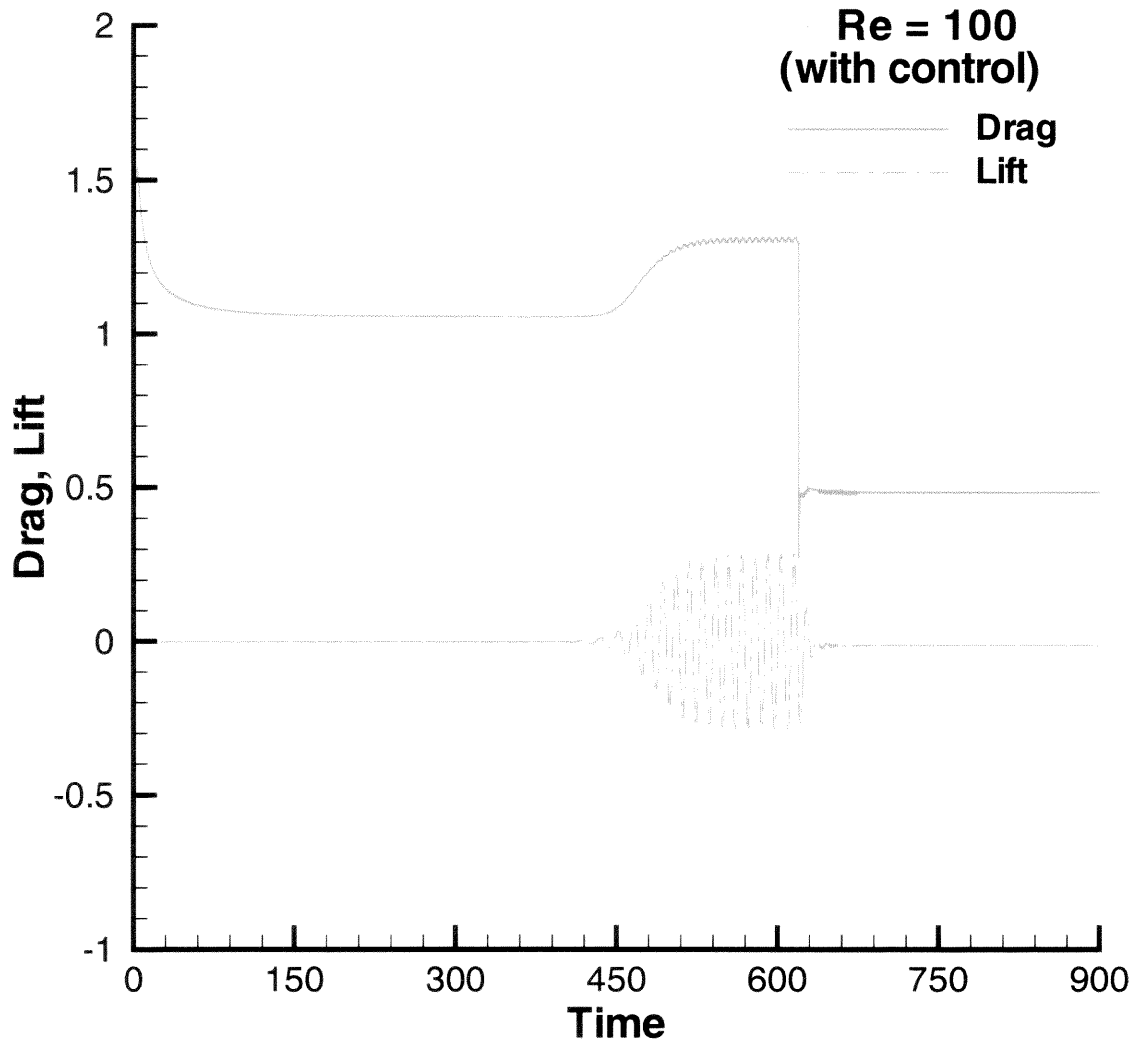


**Figure 4.11** Time history of the drag and lift coefficients at the Reynolds number value  $Re = 100$ . The control is inserted at time  $t = 620$

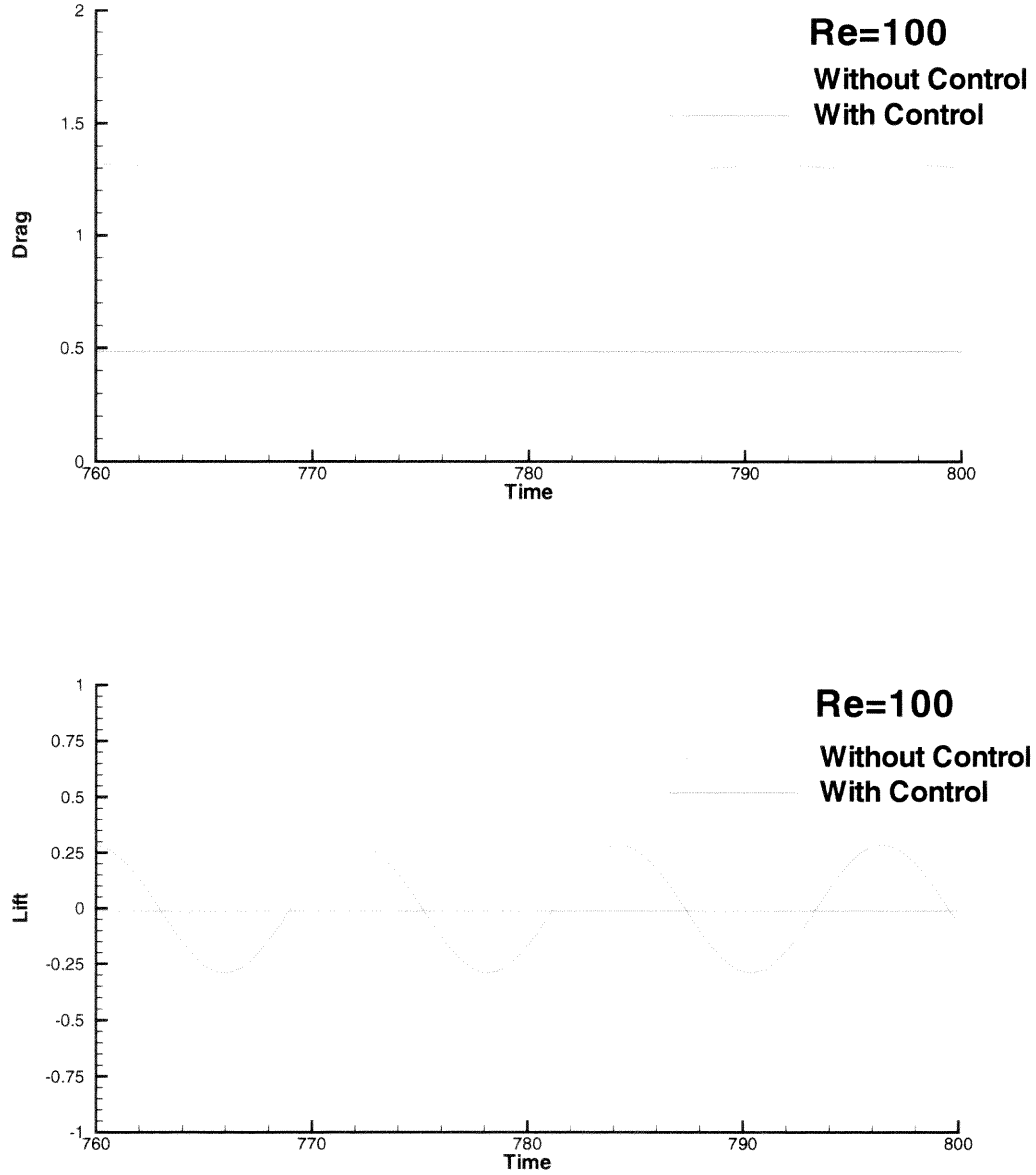


**Figure 4.12** Variation of the drag and lift coefficients on the surface of the cylinder at the Reynolds number value  $Re = 100$  with and without control for the time interval  $760 \leq t \leq 800$ . The control is inserted at time  $t = 620$

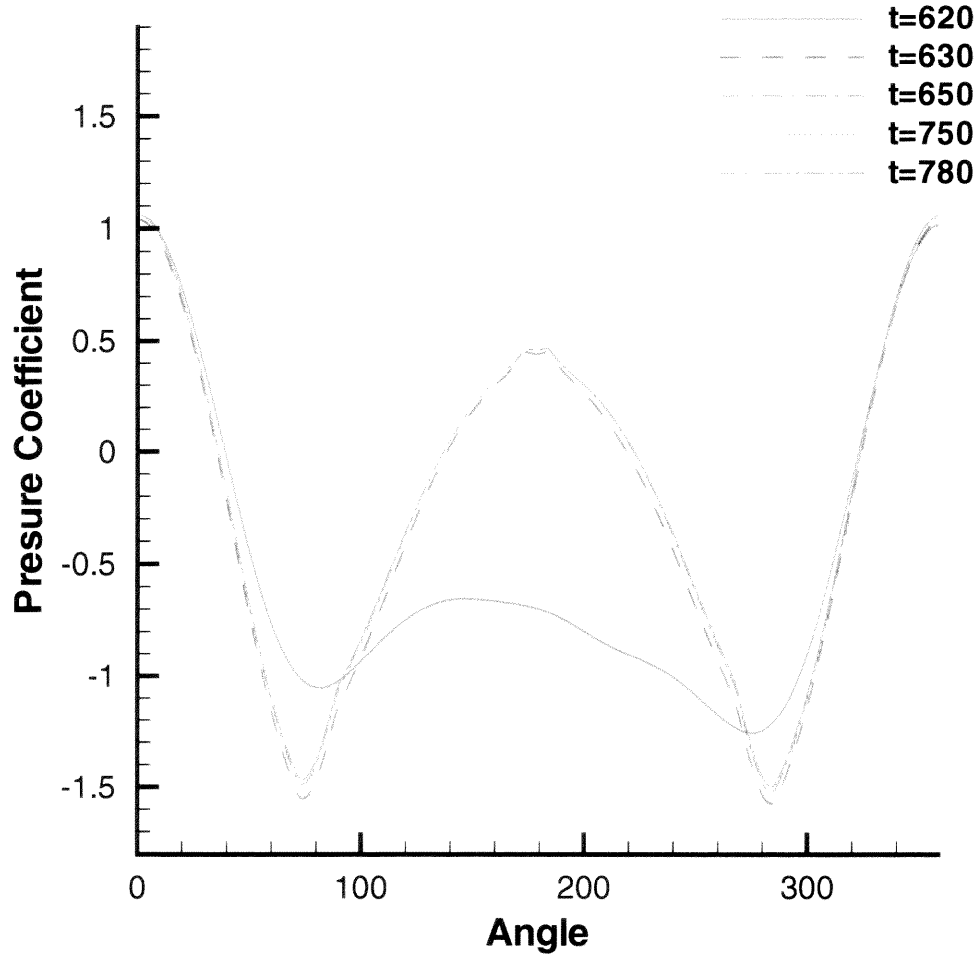


**Figure 4.13** Pressure coefficient of the flow on the surface of the cylinder at the Reynolds number value  $Re = 100$  at times  $t = 620, 630, 650, 750, 780$ . The control is inserted at time  $t = 620$



#### 4.1.2.2 Computation at $Re = 160$ .

The feedback control starts at the same as setting for the Reynolds number value  $Re = 100$ . The Karman vortex street has already settled. Figure (4.14) presents the visualization of the flow by means of the streamlines for the interval  $620 \leq t \leq 638$ , with a time step  $\delta t = 2$ . The vortex shedding is suppressed after control. Figure (4.15) shows the drag and lift coefficients at  $Re = 160$  obtained after control. Figure (4.16) shows the drag and lift coefficients for the time interval  $760 \leq t \leq 800$ . The drag coefficient undergoes a significant decrease while the lift coefficient decays to zero in the presence of the control. Figure (4.17) shows the pressure coefficient of the flow on the surface of the cylinder at times  $t = 620, 630, 650, 750$ , and  $t = 780$ , respectively.

## 4.2 Acoustic Field

### 4.2.1 Without Control

As discussed in the previous chapter, at low Mach number, the acoustic dipole, as the noise source, is the most dominant term that increases the sound level in presence of the solid boundaries. For the sound generated by the flow past a circular cylinder, the temporal variations of the drag and lift acting on the surface of the cylinder are the major noise sources due to the presence of solid boundaries. The volume quadrupole noise, corresponding to turbulent stress distributions has a negligible effect to the total acoustic density propagation.

Neglecting the volume quadrupole sources, the total acoustic density fluctuation can be determined from Eq. (3.46) by using the results of the surface dipole source function Eq. (3.50). In the 2D-Cartesian coordinate system, the results from Eq. (3.50) can be separated into two terms for the dipole source function on each axis,  $\dot{D}_1$  and  $\dot{D}_2$ . Because the surface dipole sources of the flow-generated noise behind a bluff body are from the drag and lift fluctuations in the direction of parallel

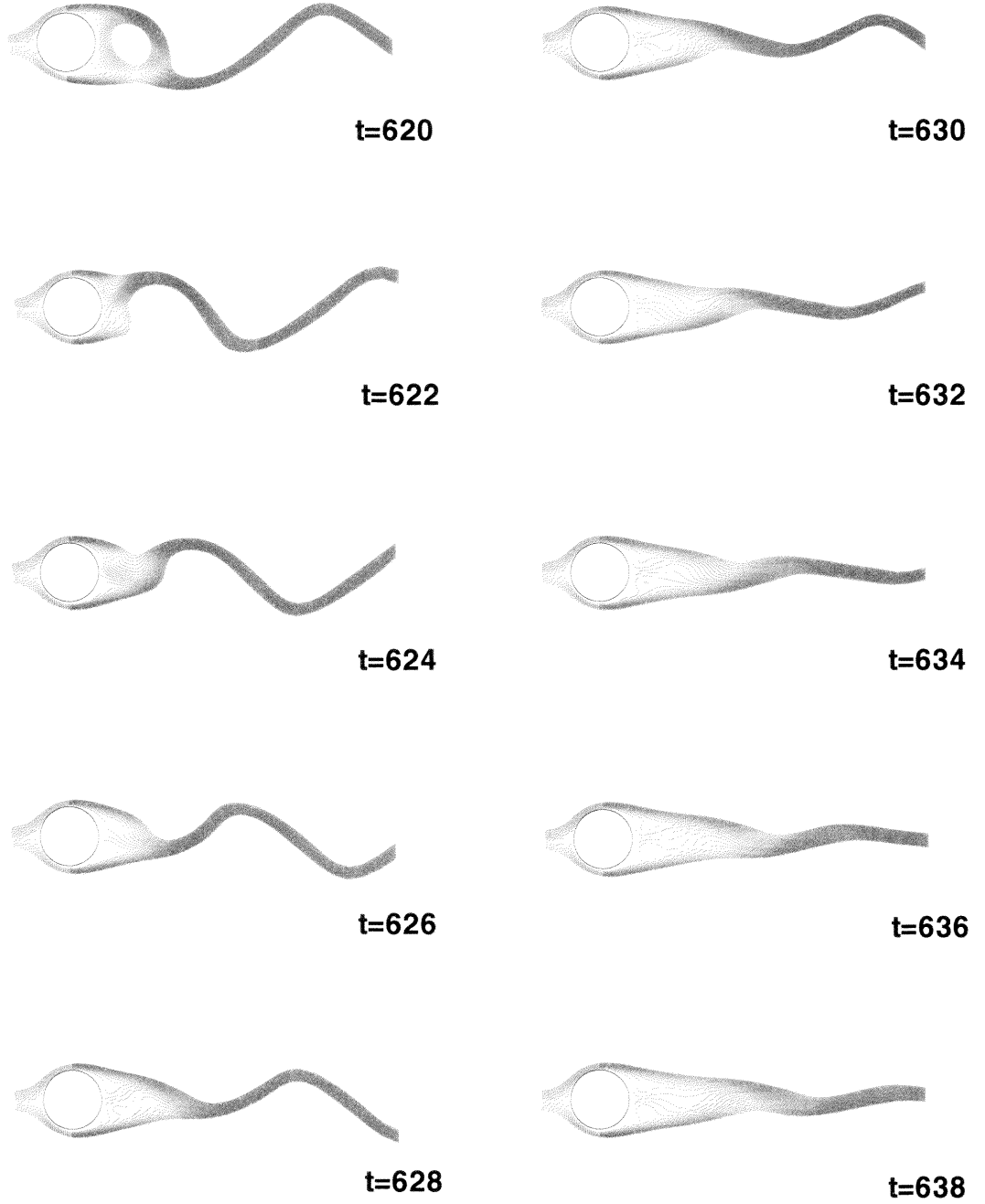


**Figure 4.14** Streamlines of the flow with control at the Reynolds number value  $Re = 160$  for the time interval  $620 \leq t \leq 638$ . The control is inserted at time  $t = 620$

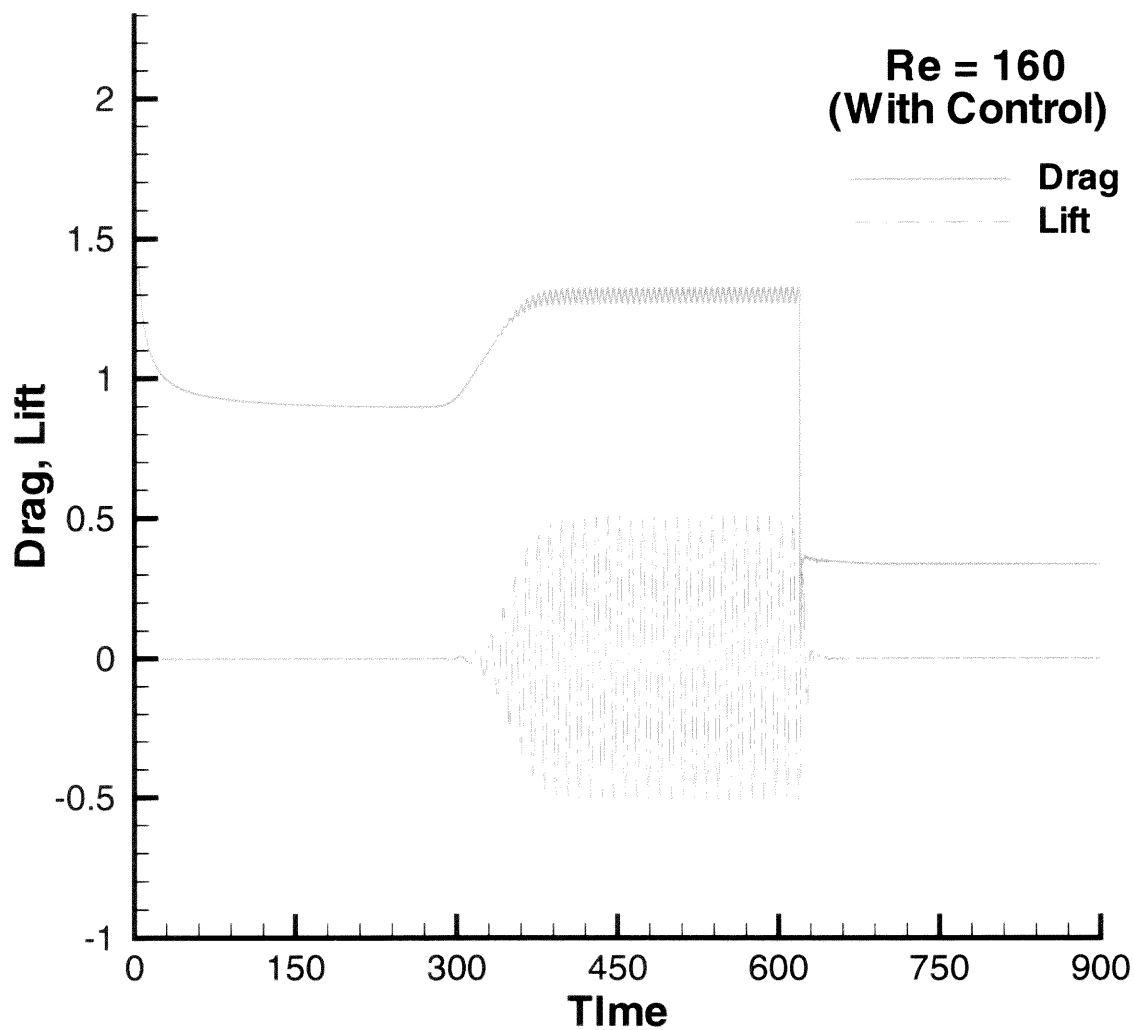


**Figure 4.15** Time history of the drag and lift coefficients at the Reynolds number value  $Re = 160$ . The control is inserted at time  $t = 620$

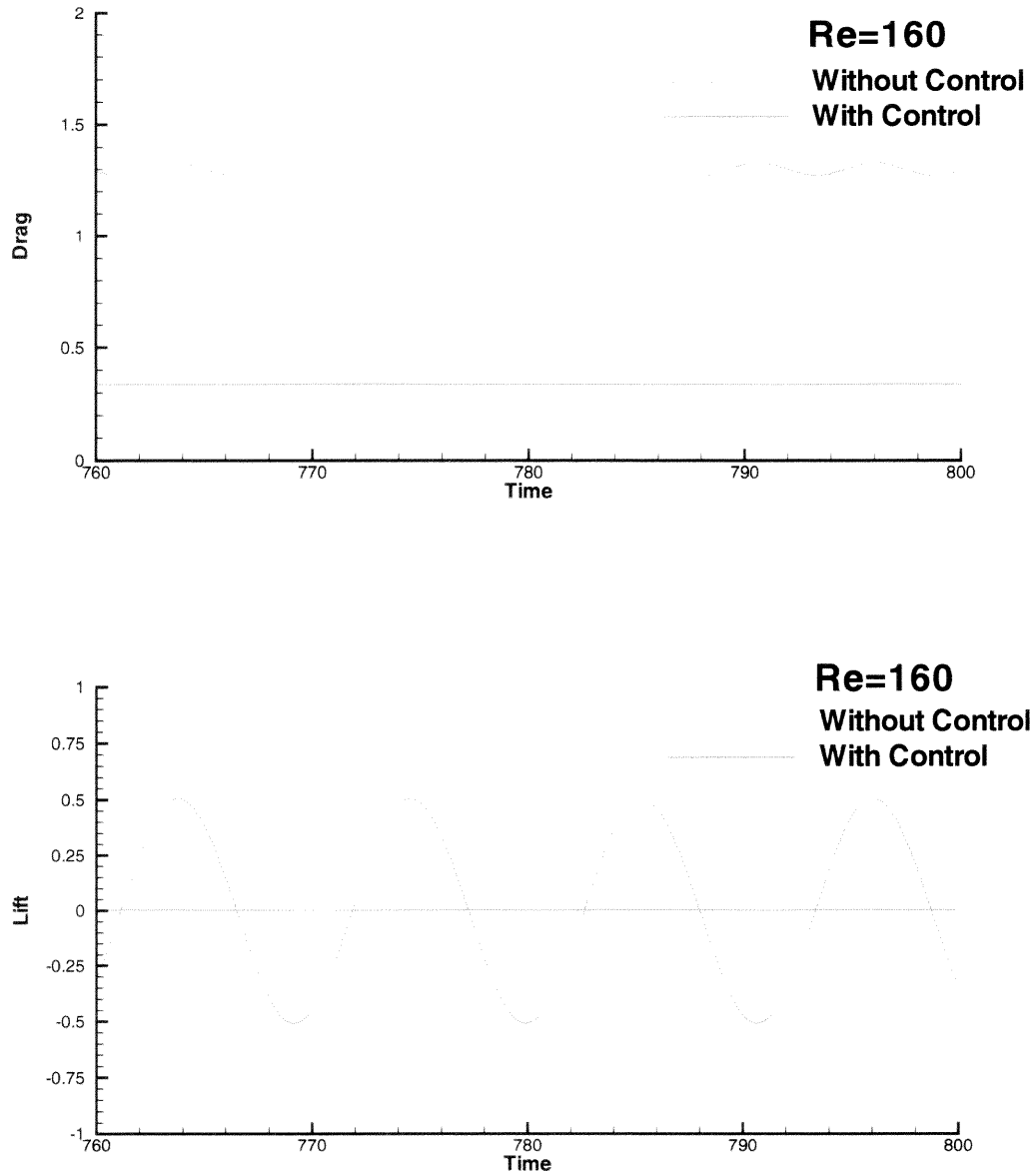


**Figure 4.16** Variation of the drag and lift coefficients on the surface of the cylinder at the Reynolds number value  $Re = 160$  with and without control for the time interval  $760 \leq t \leq 800$ . The control is inserted at time  $t = 620$

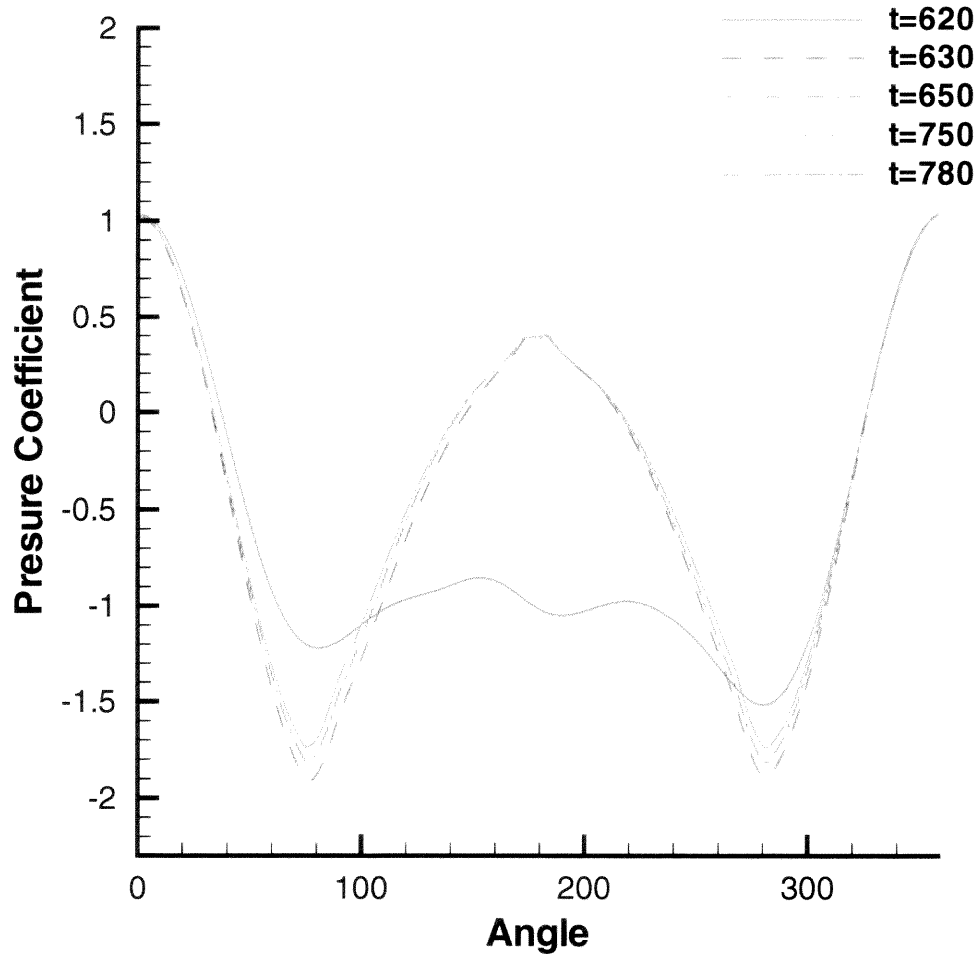


**Figure 4.17** Pressure coefficient of the flow on the surface of the cylinder at the Reynolds number value  $Re = 160$  at times  $t = 620, 630, 650, 750, 780$ . The control is inserted at time  $t = 620$

and normal to the mainstream,  $\dot{D}_1$  and  $\dot{D}_2$  are also known as the drag and lift dipole, respectively.

To compute drag and lift dipole source functions from Eq. (3.50), the surface integral, as a function of retarded time and surface source position is carried out

- by using the pressure fluctuations, obtained from solving the unsteady, incompressible Navier-Stokes equations, as an input to the function
- by numerically taking the retarded time derivation from the surface integral results
- by carry out the outer integral in order to obtain the dipole source results

The Reynolds number used in the study are  $Re = 100$  and  $160$  at Mach number  $M = 0.01$ . The results will be presented next.

#### 4.2.1.1 Computation at $Re = 100$ .

For numerical simulations purposes, the interval of the outer integration of Equation (3.50) is partitioned into subintervals, called *Mterms*. Figure (4.18) shows the convergence of the drag and lift dipole results at the Reynolds number value  $Re = 100$  as the number of subintervals of integral term increases. The numbers of subintervals (*Mterms*) that are considered here are 500, 1000, 5000, 8000, and 10000, respectively. As shown in Figure (4.18), the solution converges as the number of subintervals (*Mterms*) becomes 1000 or higher. For example; the difference between the values of drag and lift dipoles for  $Mterms = 1000$  and  $Mterms = 5000$  at each observer time is slightly less than 0.003 in both the drag dipole and the lift dipole. The difference between the drag and lift dipole values for  $Mterms = 5000$  and  $Mterms = 10000$  at each observer time is slightly less than 0.0003 in drag dipole and 0.0001 in lift dipole. Hereafter,  $Mterms = 5000$  is used to compute the acoustic density fluctuation ( $\rho'$ ).

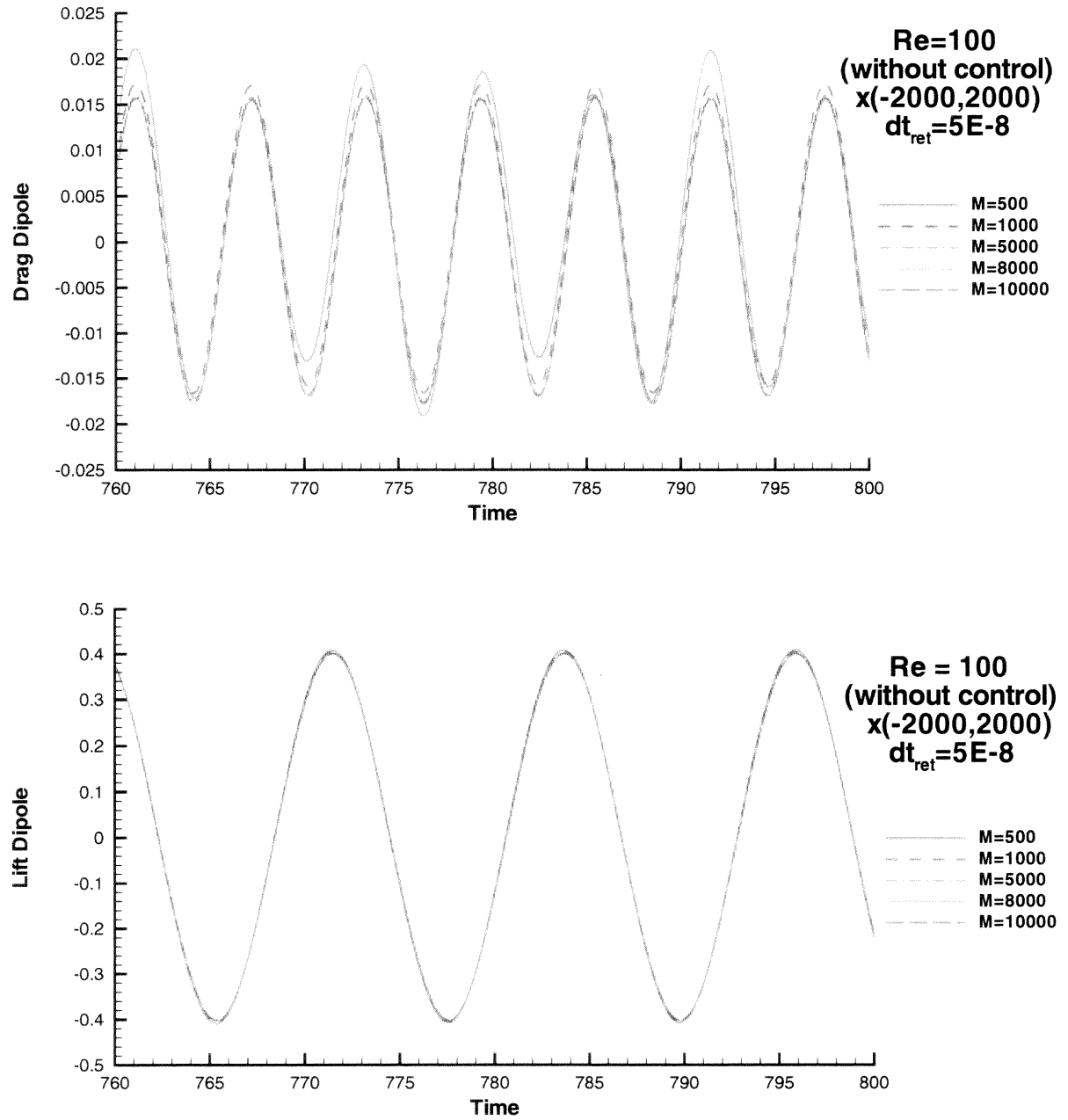


**Figure 4.18** Drag and lift dipoles at the Reynolds number value  $Re = 100$  using various numbers of subintervals in the integral of Equation (3.50), that is  $Mterms = 500, 1000, 5000, 8000, 10000$

The convergence of the drag and lift dipole values at  $Re = 100$  when choosing the time interval  $dt_{ret}$  for calculating the retard time derivative in Equation (3.50) has also been investigated. Figure (4.19) shows the convergence of the drag and lift dipole results with  $dt_{ret} = 5 \times 10^{-5}$ ,  $5 \times 10^{-8}$ , and  $5 \times 10^{-12}$ , respectively, by using  $Mterms = 5000$  and  $8000$ . In addition, some of the results from Figure (4.18) is presented in these plots for comparison. The difference between the results using  $dt_{ret} = 5 \times 10^{-5}$ ,  $5 \times 10^{-8}$ , and  $5 \times 10^{-12}$ , is slightly less than  $2 \times 10^{-4}$ .

The values of the drag and lift dipole source functions at a far field location  $x_1 = -2000$  and  $x_2 = 2000$ , at the Mach number value  $M = 0.01$ , and at the Reynolds number value  $Re = 100$  are shown in Figure (4.20). The results show that the amplitude of the lift dipole is much larger than the amplitude of the drag dipole. Therefore, the lift dipole is the major of the total dipole and causes most of the acoustic density fluctuation whose results are shown in Figure (4.21).

Figure (4.21) shows the results of the acoustic density fluctuations at the Reynolds number  $Re = 100$ . Comparing the results of the dipole source function with the acoustic density fluctuations clearly shows that the lift dipole source function is the major contributor to the variation of the acoustic density. The same frequency is obtained for both the lift dipole source function and the acoustic density fluctuation. The results obtained for the drag and lift dipole source functions, and acoustic density fluctuation are in good agreement with the results presented by the work of You, *et al.* (1998), as also shown in Figures (4.20), (4.21).

The investigation has been carried out further by changing the observer positions as shown in Figures (4.22), (4.23) and (4.24). When the observer position is closer to the cylinder, the lift dipole source function at each location is still the main contributor to the total dipole, and the amplitude of both drag and lift dipole source functions become larger. Notice that both drag and lift dipoles have the



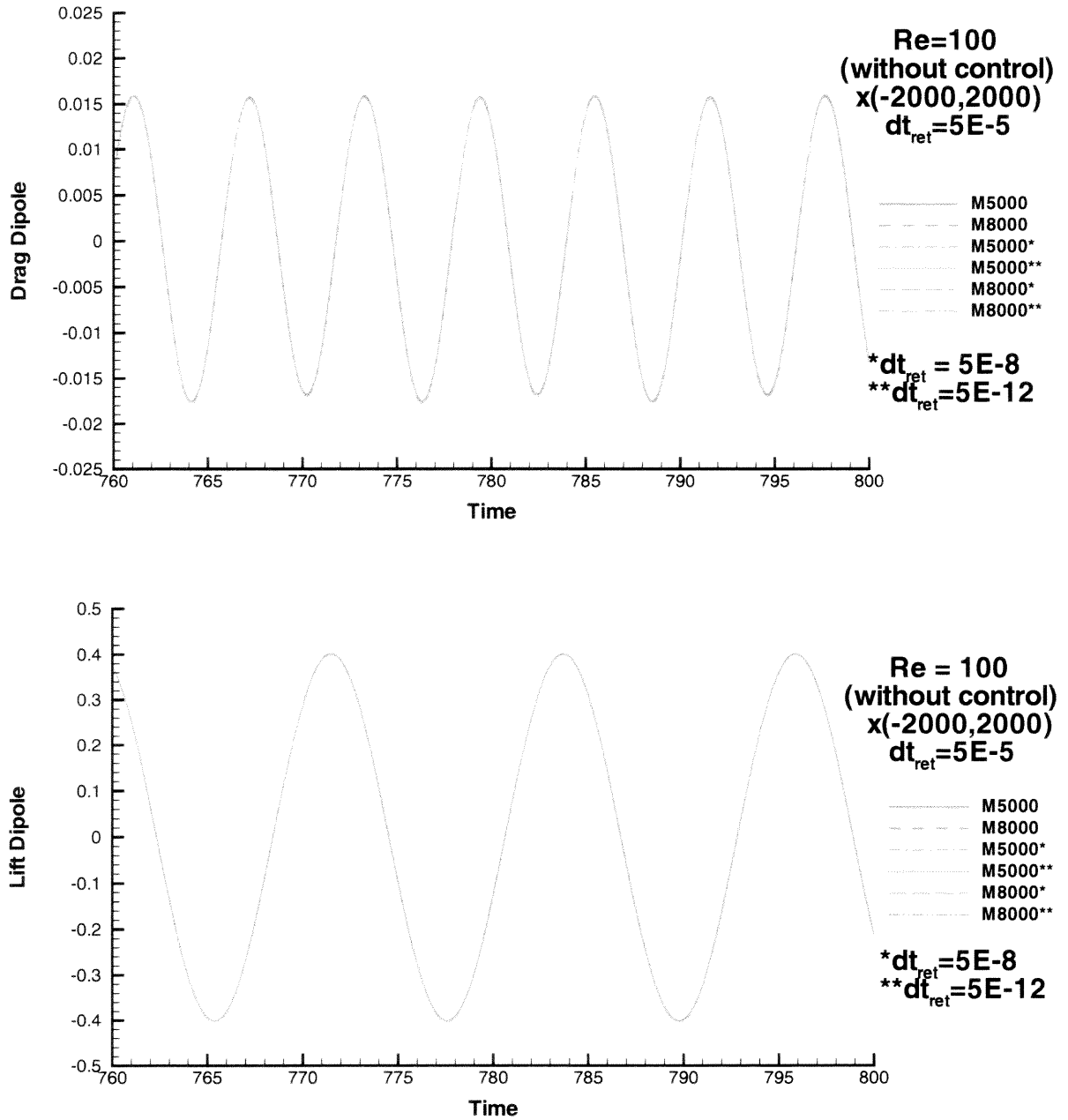


**Figure 4.19** Drag and lift dipoles at the Reynolds number value  $Re = 100$  using various numbers of subintervals in the integral of Equation (3.50), that is  $M_{terms} = 5000$ , and  $8000$  and various time derivative increments  $dt_{ret} = 5 \times 10^{-5}$ ,  $5 \times 10^{-8}$ , and  $5 \times 10^{-12}$

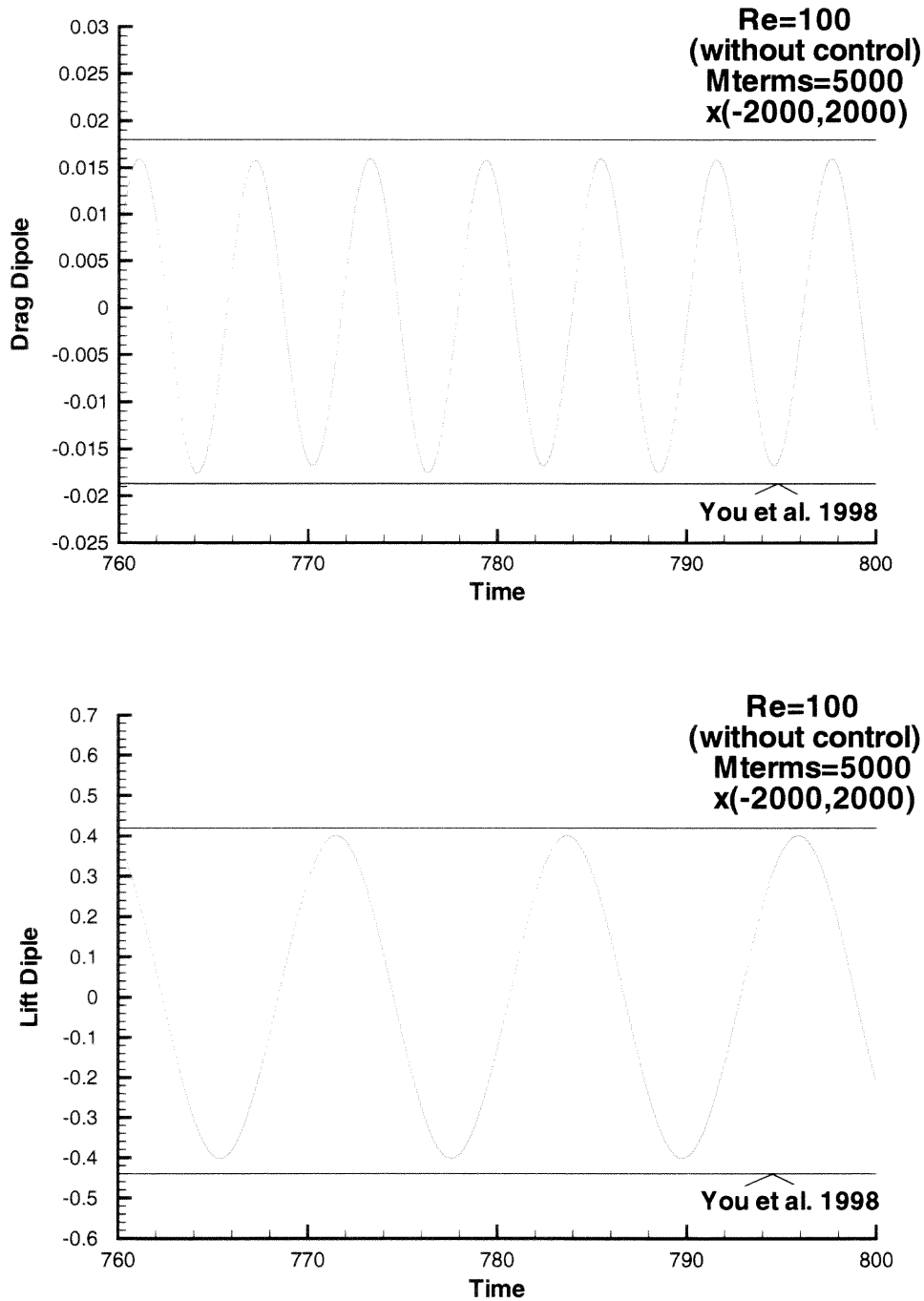


**Figure 4.20** Drag and lift dipoles at the Reynolds number value  $Re = 100$  using the number of subintervals in the integral of Equation (3.50), that is  $Mterms = 5000$ . The results are compared with those of You *et al.*, 1998

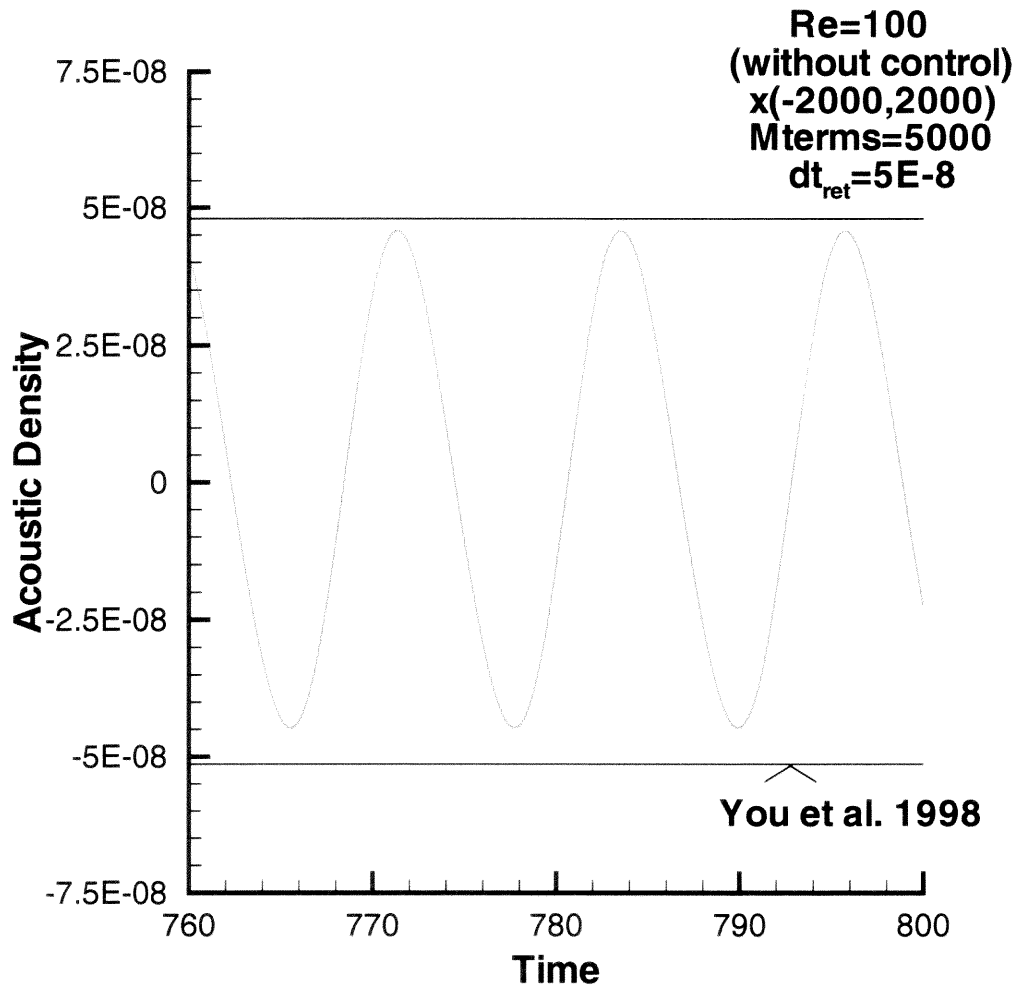


**Figure 4.21** Acoustic density at the Reynolds number value  $Re = 160$  using the number of subintervals in the integral of Equation (3.50), that is  $Mterms = 5000$ . The results are compared with those of You *et al.*, 1998

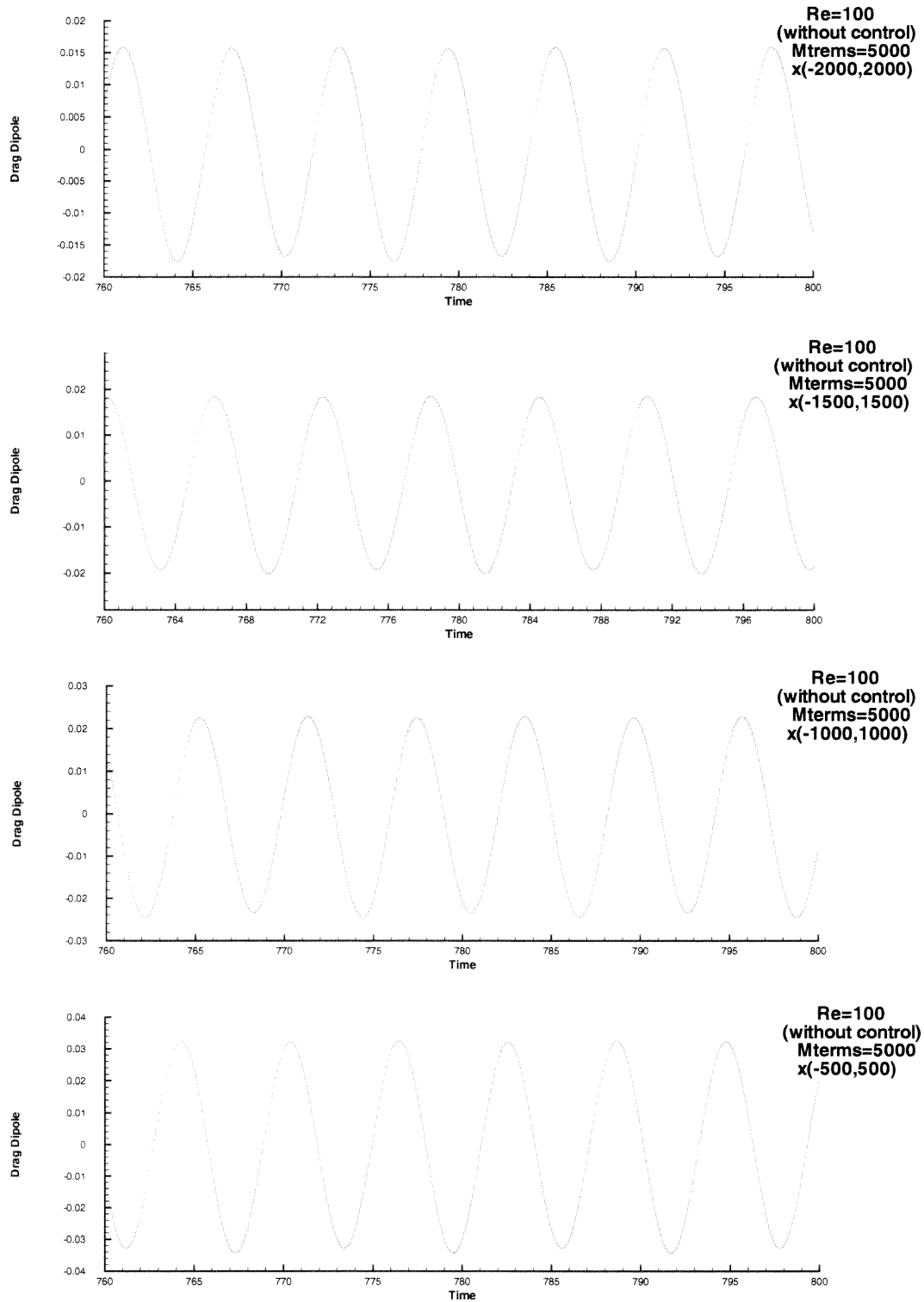


**Figure 4.22** Drag dipole at the Reynolds number value  $Re = 100$  using the number of subintervals  $Mterms = 5000$  in the integral of Equation (3.50) for various observer positions

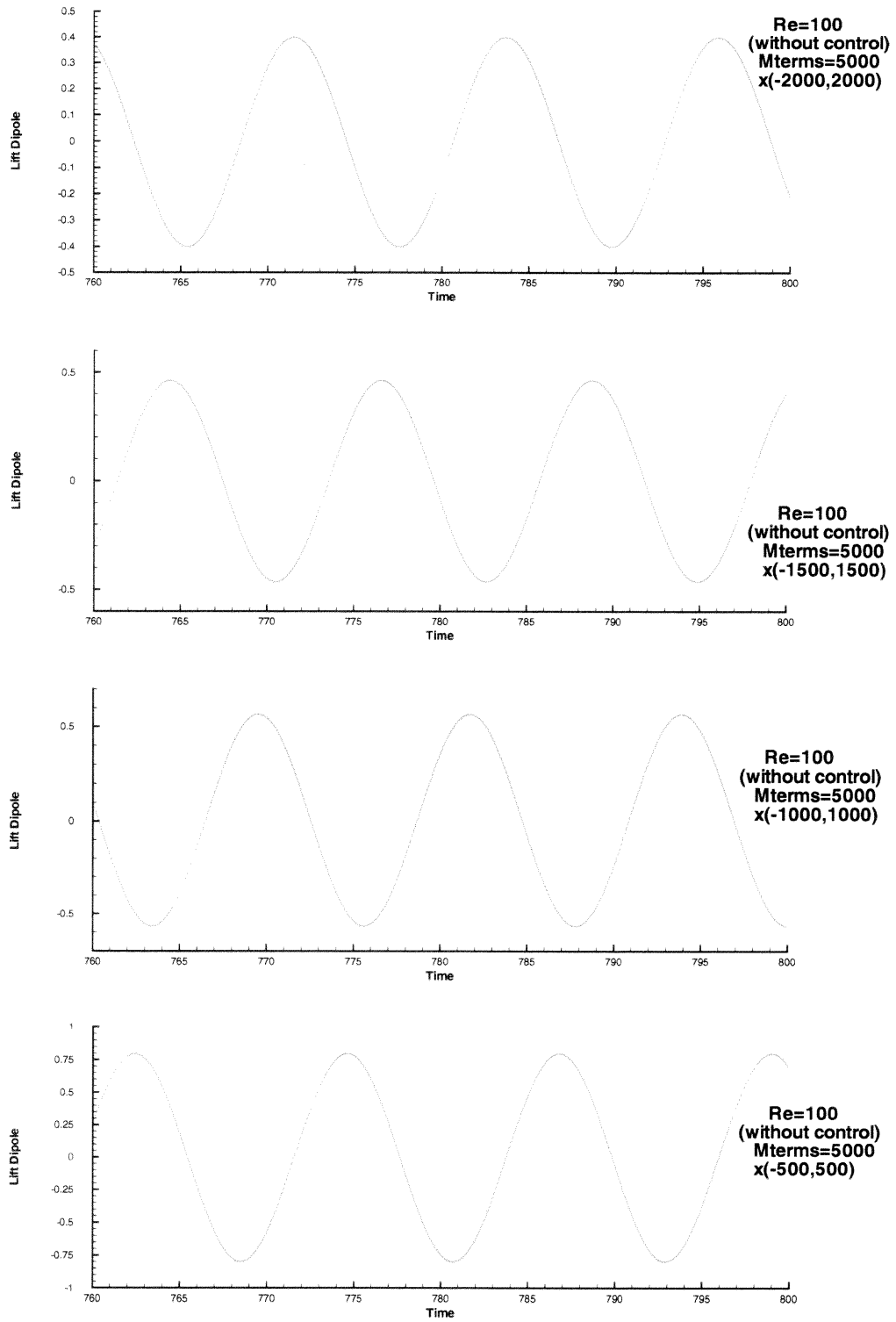


**Figure 4.23** Lift dipole at the Reynolds number value  $Re = 100$  using the number of subintervals  $Mterms = 5000$  in the integral of Equation (3.50) for various observer positions

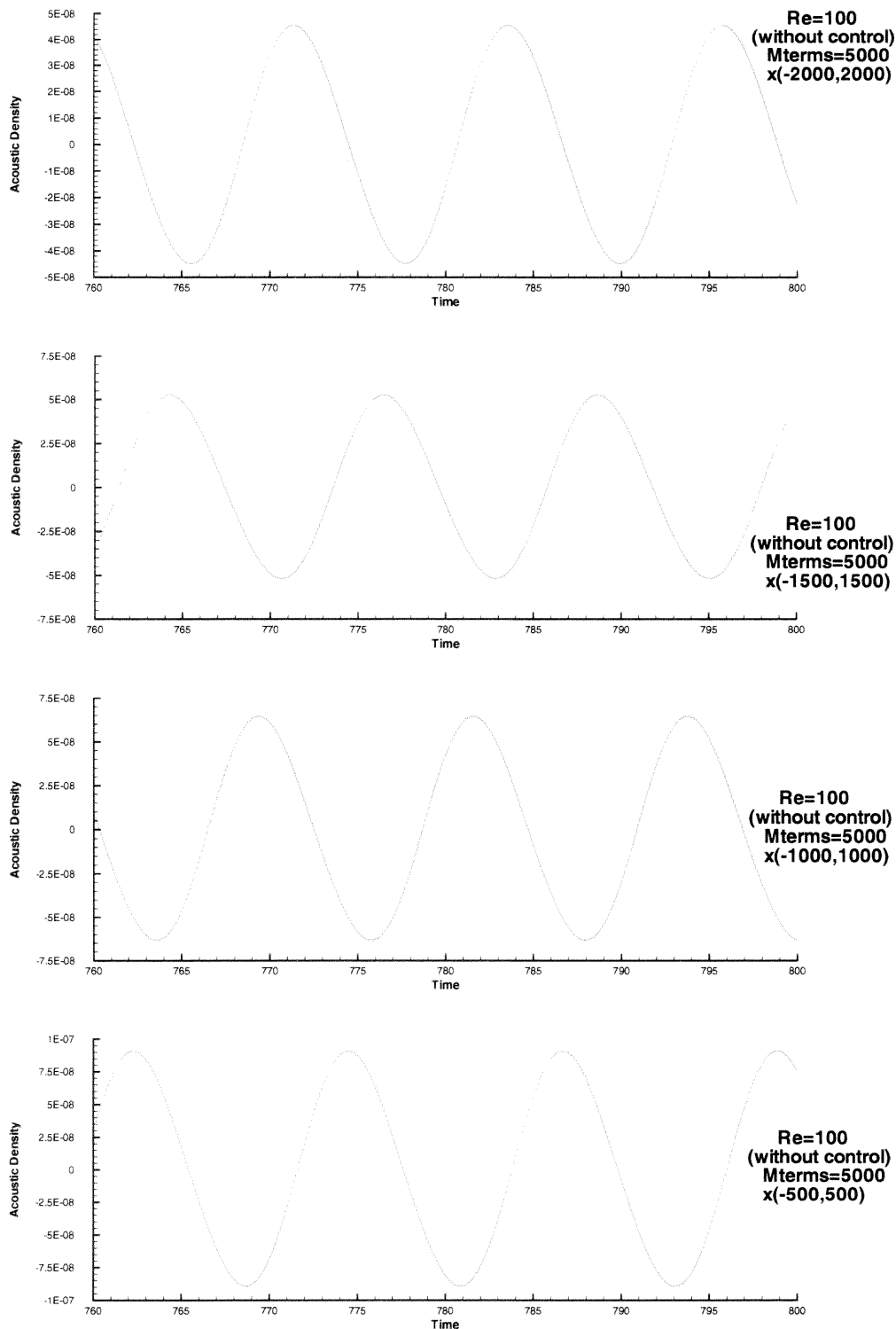


**Figure 4.24** Acoustic density at the Reynolds number value  $Re = 100$  using the number of subintervals  $Mterms = 5000$  in the integral of Equation (3.50) for various observer positions

same frequency as the drag and lift in the near-field flow. The same frequency are obtained for both the lift dipole source function and the acoustic density fluctuation as moving the observer positions.

Figure (4.25) shows the contour of the far-field acoustic density at the Reynolds number  $Re = 100$  and the Mach number  $M = 0.01$ . The contour results agree well with those of You *et al.*

#### 4.2.1.2 Computations at $Re = 160$ .

The same procedure is used for investigating the results at the Reynolds number  $Re = 160$ . Figure (4.26) shows the convergence of the drag and lift dipole values using the same set of the numbers of the subinterval ( $Mterms$ ) as chosen for  $Re = 100$ . The difference between the drag and lift dipole values for  $Mterms = 1000$  and  $Mterms = 5000$  at each observer time is slightly less than 0.014 for the former and less than 0.007 for the latter. The difference between the drag and lift dipole values for  $Mterms = 5000$  and  $Mterms = 10000$  at each observer time is slightly less than 0.002 in drag dipole and 0.007 in lift dipole. Figure (4.27) shows the convergence of the drag and lift dipole values for  $dt_{ret} = 5 \times 10^{-5}$ ,  $5 \times 10^{-8}$ , and  $5 \times 10^{-12}$ , at  $Re = 160$  by using  $Mterms = 1000$  and 8000. The difference between these results is slightly less than  $5 \times 10^{-5}$ . A good agreement with the work of You *et al.* is obtained for the drag and lift dipole, as well as for the acoustic density fluctuation, as shown in Figures (4.28), (4.29). Notice that the acoustic results presented at the Reynolds number  $Re = 160$  have higher amplitude and frequency than those at the Reynolds number  $Re = 100$ . Figure (4.33) shows the contour of far-field acoustic density at the Reynolds number  $Re = 160$  for the far-field domain ( $-2000 \leq x_1, x_2 \leq 2000$ ).

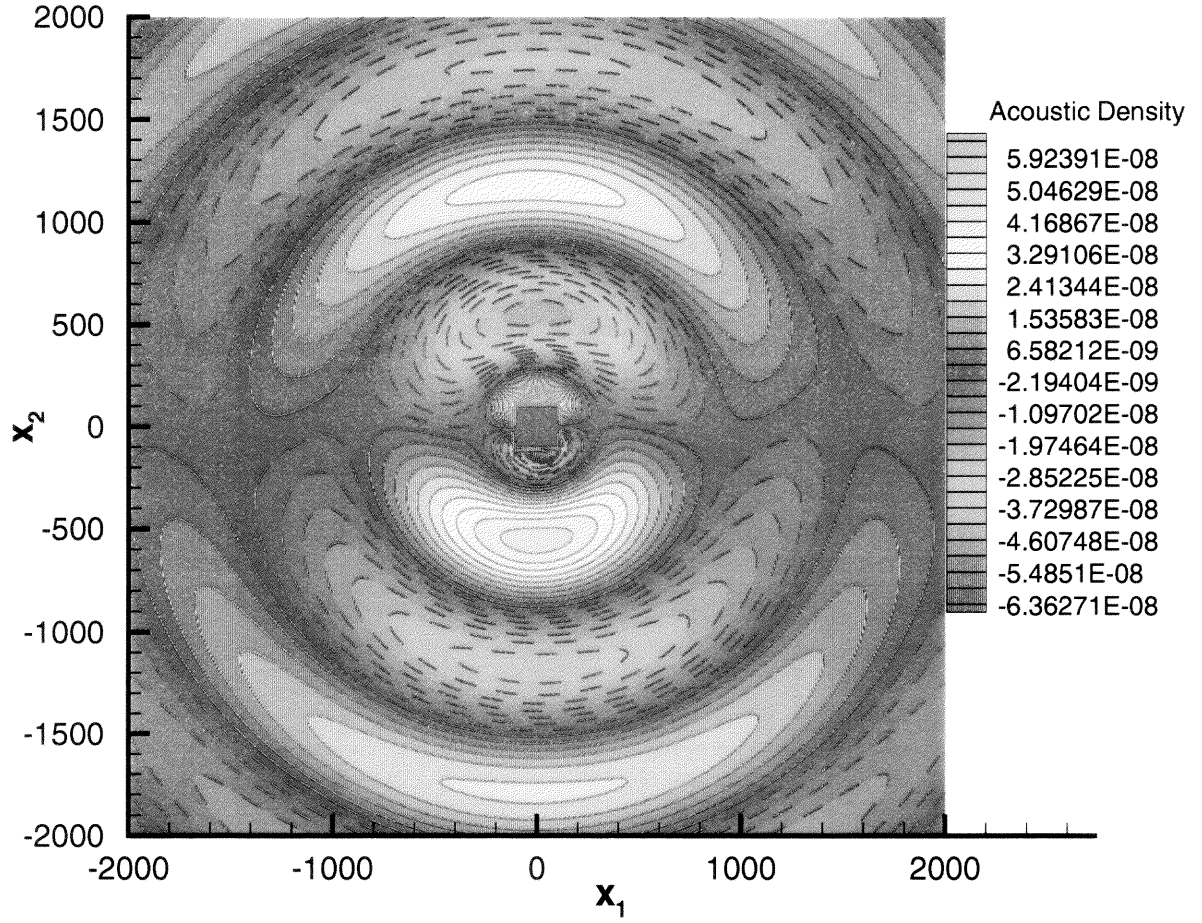


**Figure 4.25** Contour of the acoustic density at the Reynolds number value  $Re = 100$  using the number of subintervals  $Mterms = 5000$  in the integral of Equation (3.50) and the far-field domain ( $-2000 \leq x_1, x_2 \leq 2000$ )



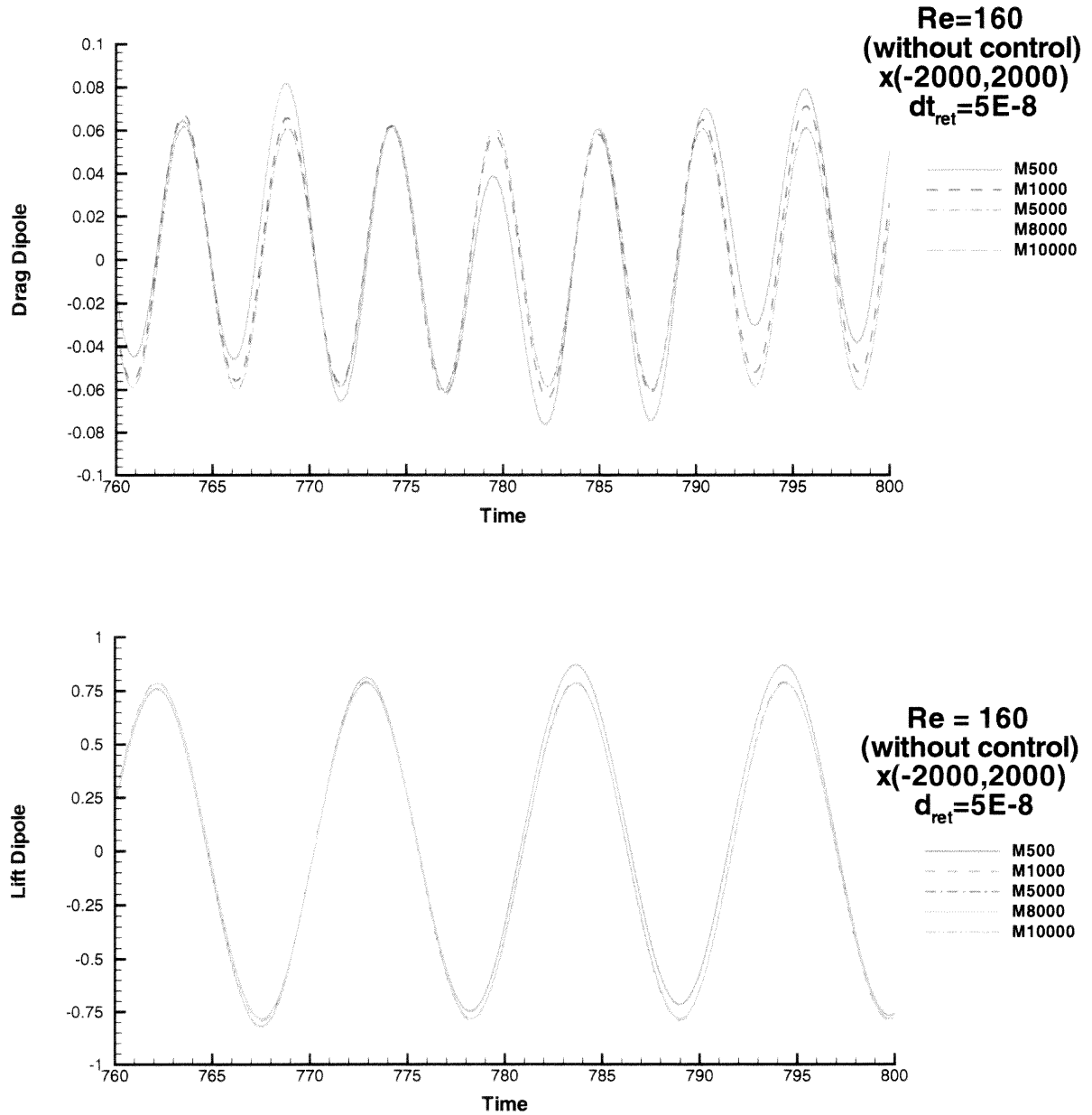


**Figure 4.26** Drag and lift dipoles at the Reynolds number value  $Re = 160$  using various numbers of subintervals in the integral of Equation (3.50), that is  $Mterms = 500, 1000, 5000, 8000, 10000$

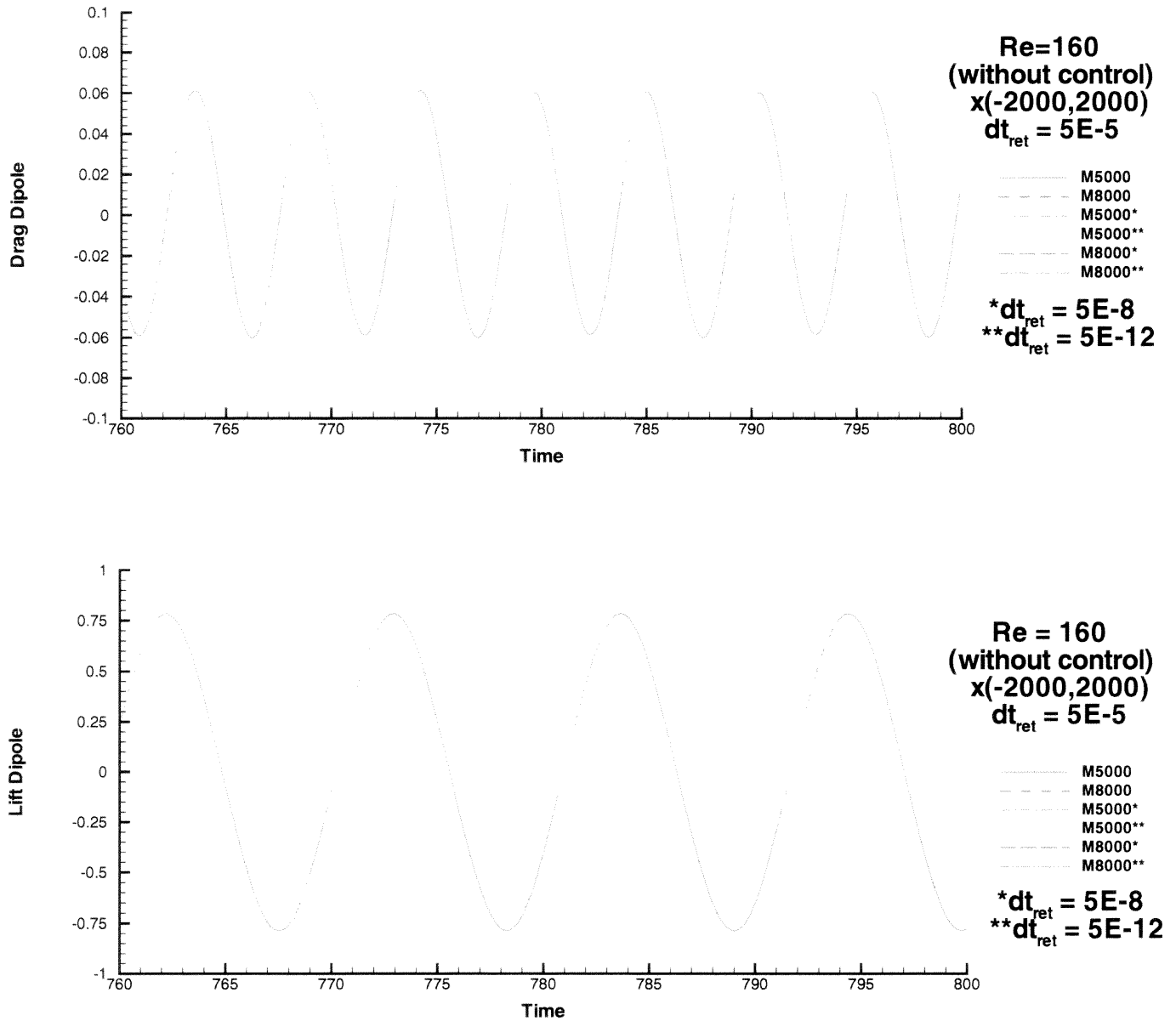


**Figure 4.27** Drag and lift dipoles at the Reynolds number value  $Re = 160$  using various numbers of subintervals in the integral of Equation (3.50), that is  $Mterms = 5000$  and  $8000$  for various time derivative increments  $dt_{ret} = 5 \times 10^{-5}$ ,  $5 \times 10^{-8}$ , and  $5 \times 10^{-12}$

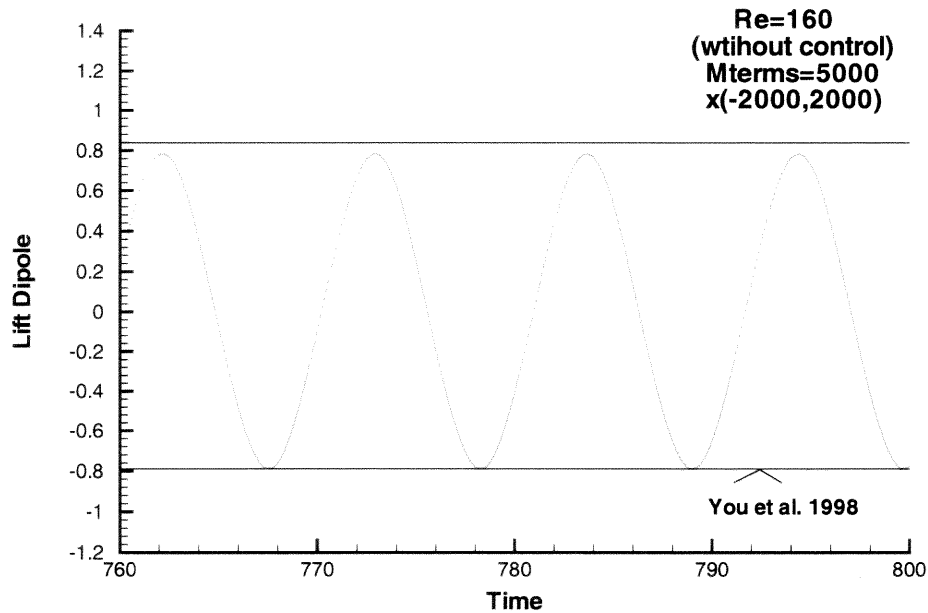
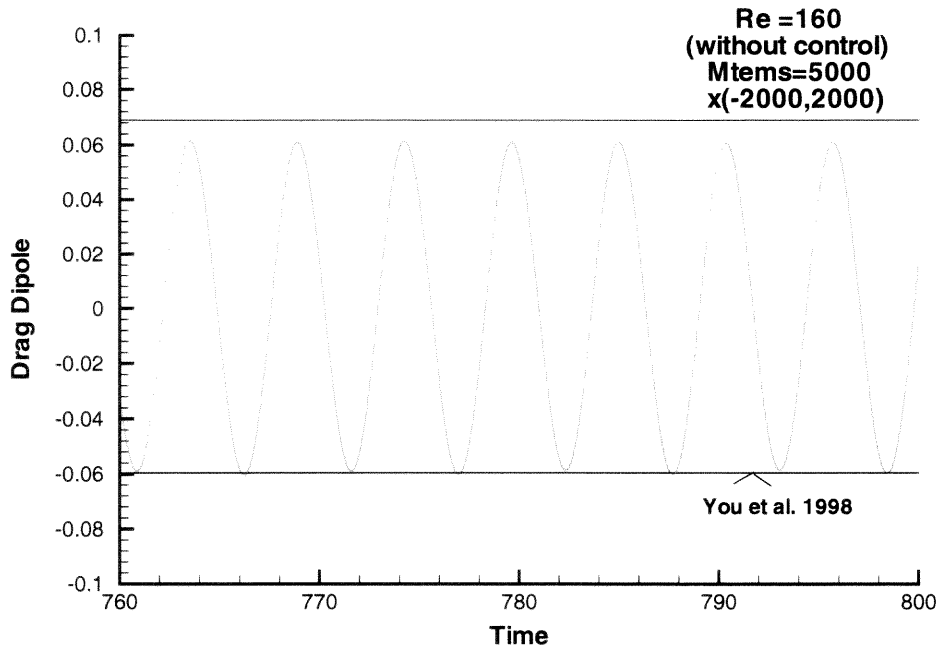


**Figure 4.28** Drag and lift Dipoles at the Reynolds number value  $Re = 160$  using the number of subintervals in the integral of Equation (3.50), that is  $M_{terms} = 5000$ . The results are compared with those of You *et al.*, 1998

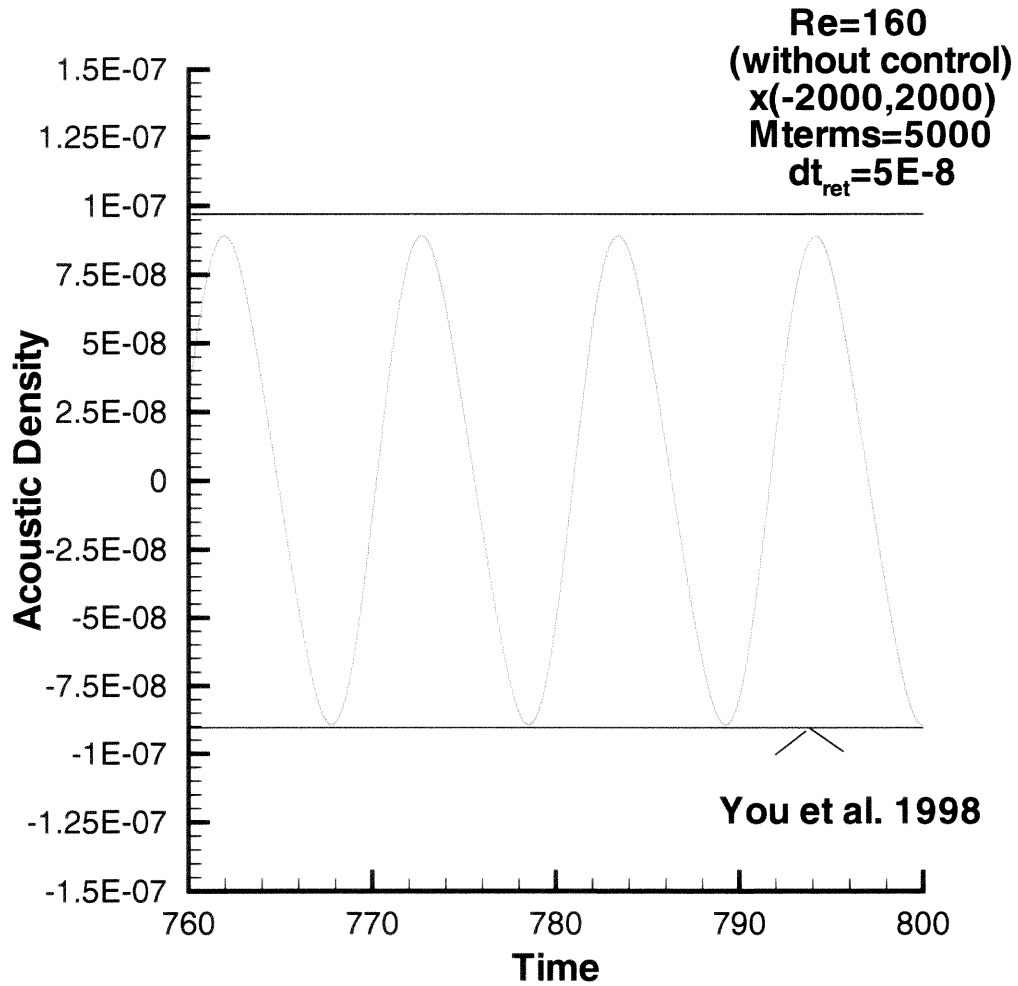


**Figure 4.29** Acoustic density at the Reynolds number value  $Re = 160$  using the number of subintervals in the integral of Equation (3.50), that is  $Mterms = 5000$ . The results are compared with those of You *et al.*, 1998

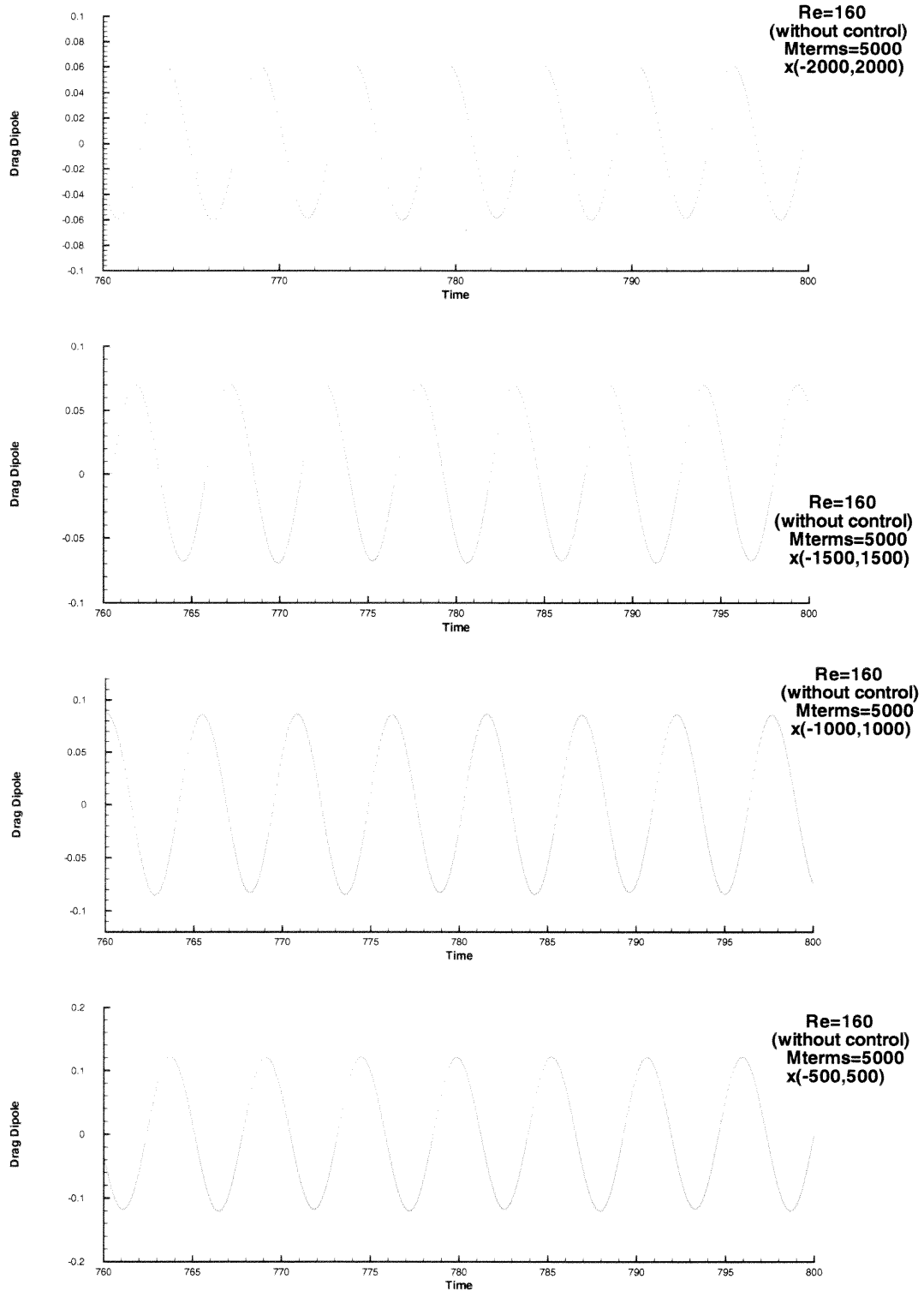


**Figure 4.30** Drag dipoles at the Reynolds number value  $Re = 160$  using the number of subintervals  $Mterms = 5000$  in the integral of Equation (3.50) for various observer positions

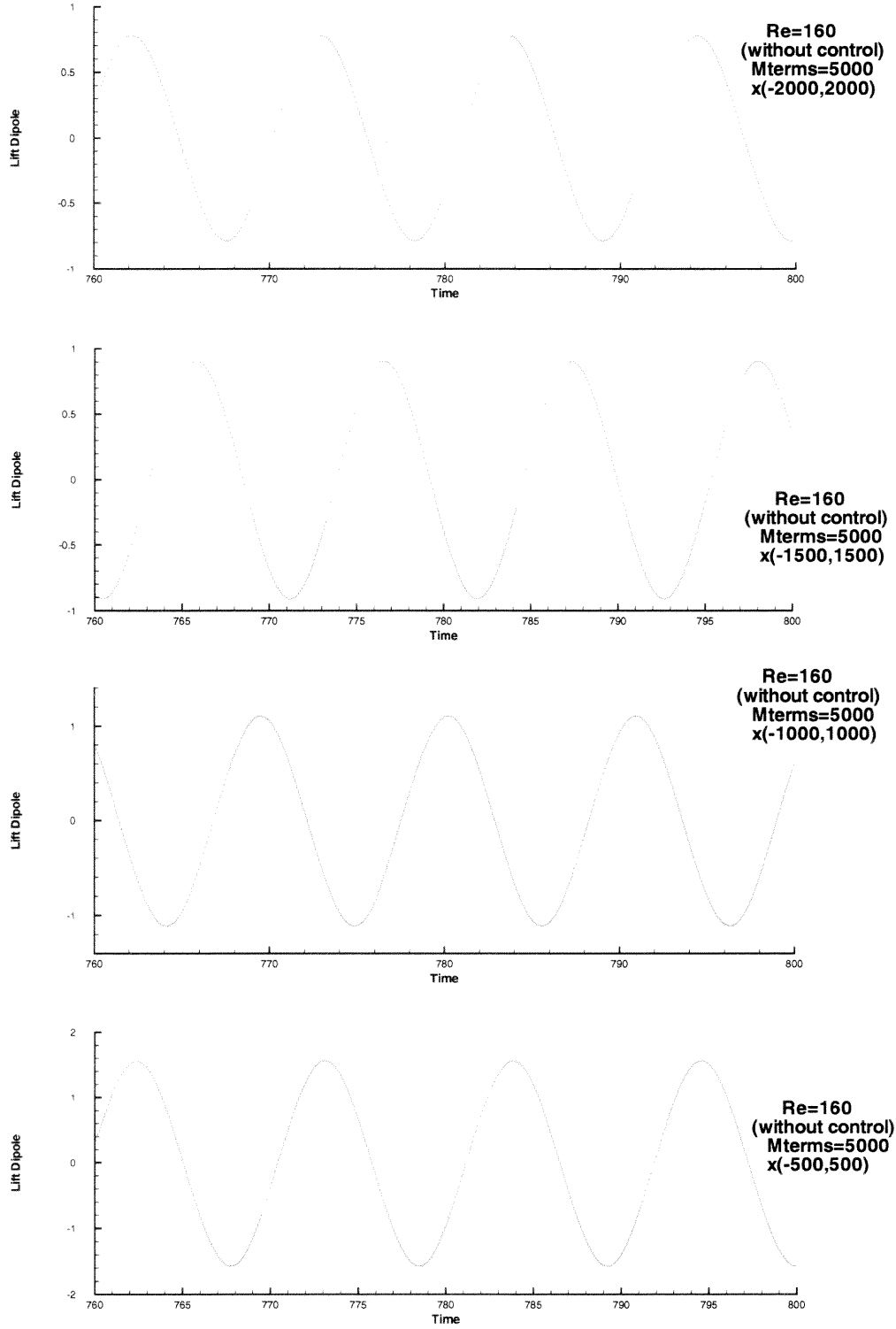


**Figure 4.31** Lift dipole at the Reynolds number value  $Re = 160$  using the number of subintervals  $Mterms = 5000$  in the integral of Equation (3.50) for various observer positions

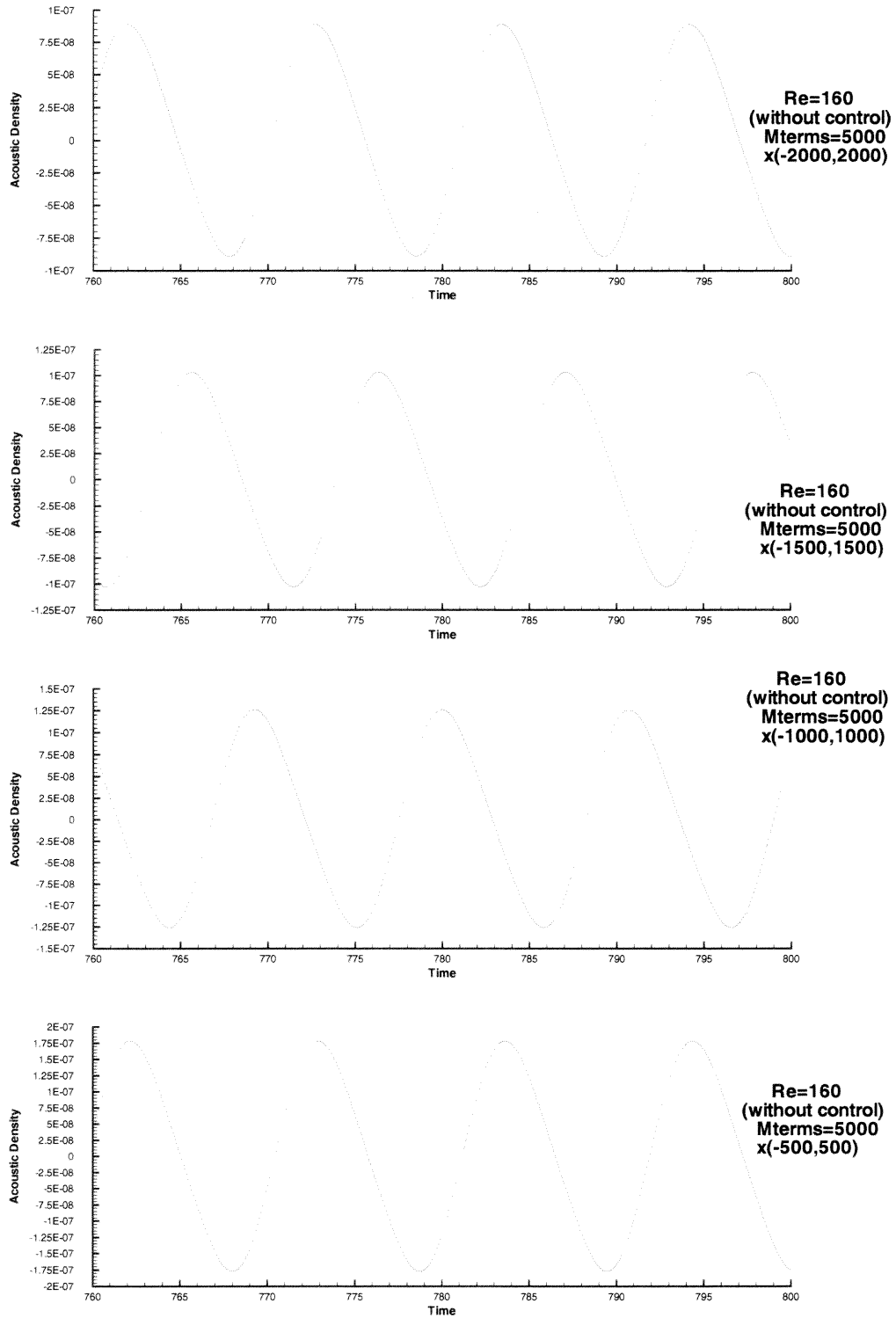


**Figure 4.32** Acoustic density at the Reynolds number value  $Re = 160$  using the number of subintervals  $Mterms = 5000$  in the integral of Equation (3.50) for various observer positions.

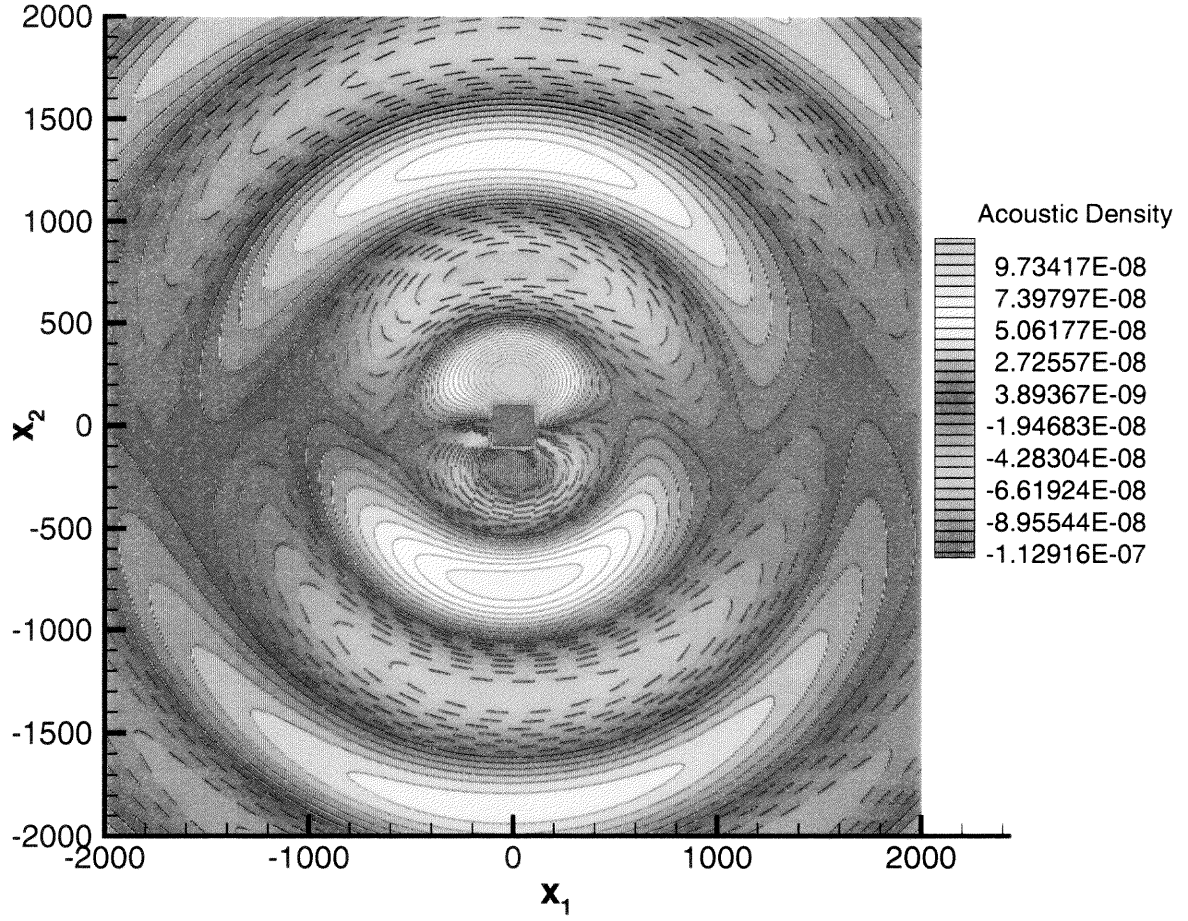


**Figure 4.33** Contour of the acoustic density at the Reynolds number value  $Re = 160$  using the number of subintervals  $Mterms = 5000$  in the integral of Equation (3.50) in the far-field domain ( $-2000 \leq x_1, x_2 \leq 2000$ )



### 4.2.2 With Control

#### 4.2.2.1 Computations at $Re = 100$ .

The investigation is performed to show whether it is possible to suppress the generation of sound in the same flow. Figures (4.34), (4.35) show the drag dipole, lift dipole, and acoustic density fluctuation at the Reynolds number  $Re = 100$  with and without applying flow control. After control, the drag and lift dipole are decreased significantly and so is the acoustic density fluctuation. The results show that the non-dimensional acoustic density fluctuation is decreased by five orders of magnitude after control.

Figure (4.36), (4.37) and (4.38) show the control results as the observer moves toward the cylinder. The suppression of the acoustic density fluctuation is obtained at every location. Figure (4.39) shows the contour of the far-field acoustic density at the Reynolds number  $Re = 100$  and the Mach number  $M = 0.01$ . After applying feedback control, the drag and lift forces are significantly decreased and no longer vibrated vertically along the horizontal axis. This phenomenon creates the difficulties for the interpretation of the directivity patterns of sound generated by this control technique. Figure (4.39) shows the instantaneous acoustic density contour. The consideration of the acoustic density variation over a period of time will provide more meaningful results. Later in this chapter, the sound pressure level (SPL), i.e. the mean value of acoustic pressure over a period of time, will be calculated and will give the overall directivity of sound after control. The instantaneous directivity that occurred in Figure (4.39) with a certain angle was generated by the balance between the drag and lift dipoles. This is due to the fact that the drag force in the flow field increased by means of the Lorentz force causes the drag dipole to increase. The drag dipole becomes noticeable after the control.

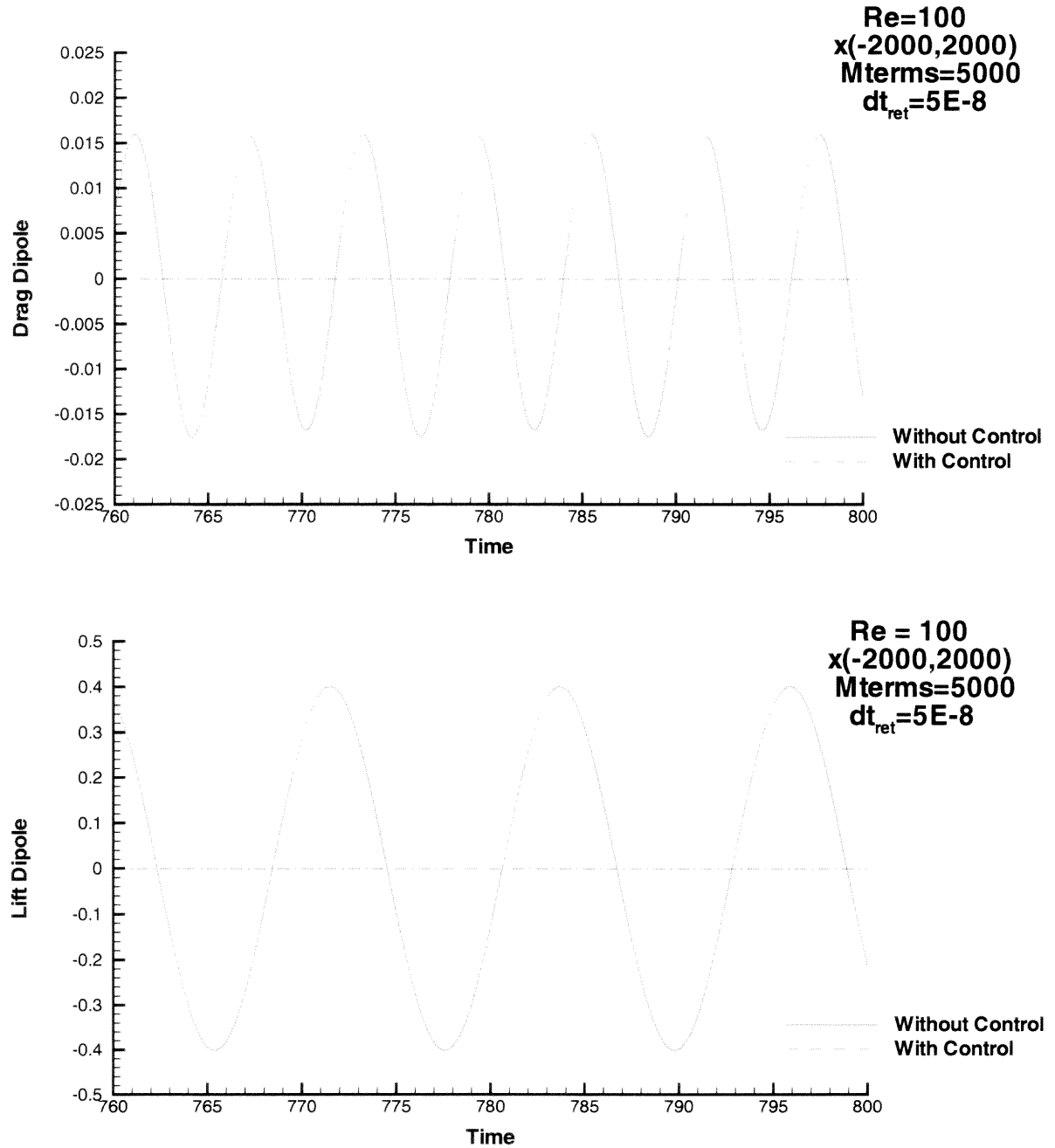


**Figure 4.34** Drag and lift dipoles at the Reynolds number value  $Re = 100$  with and without control

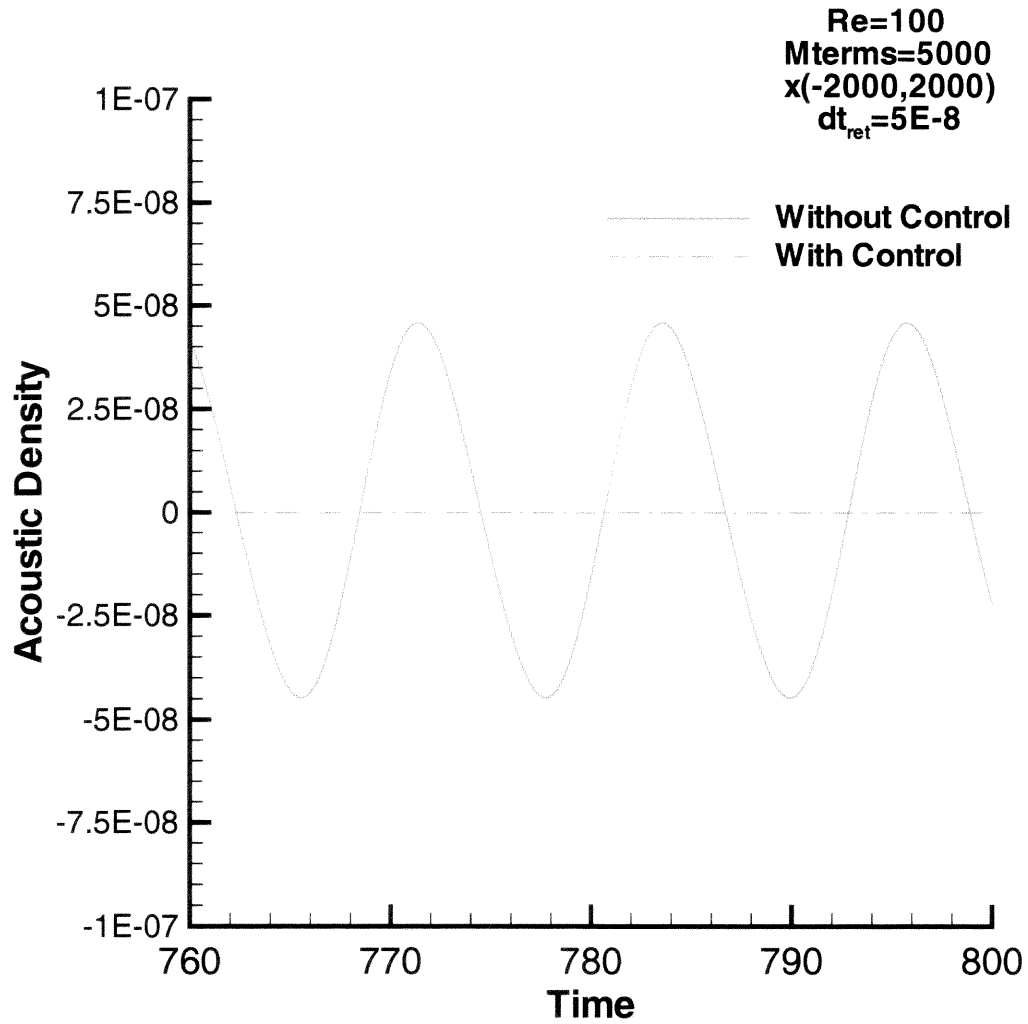


**Figure 4.35** Acoustic density at the Reynolds number value  $Re = 100$  with and without control

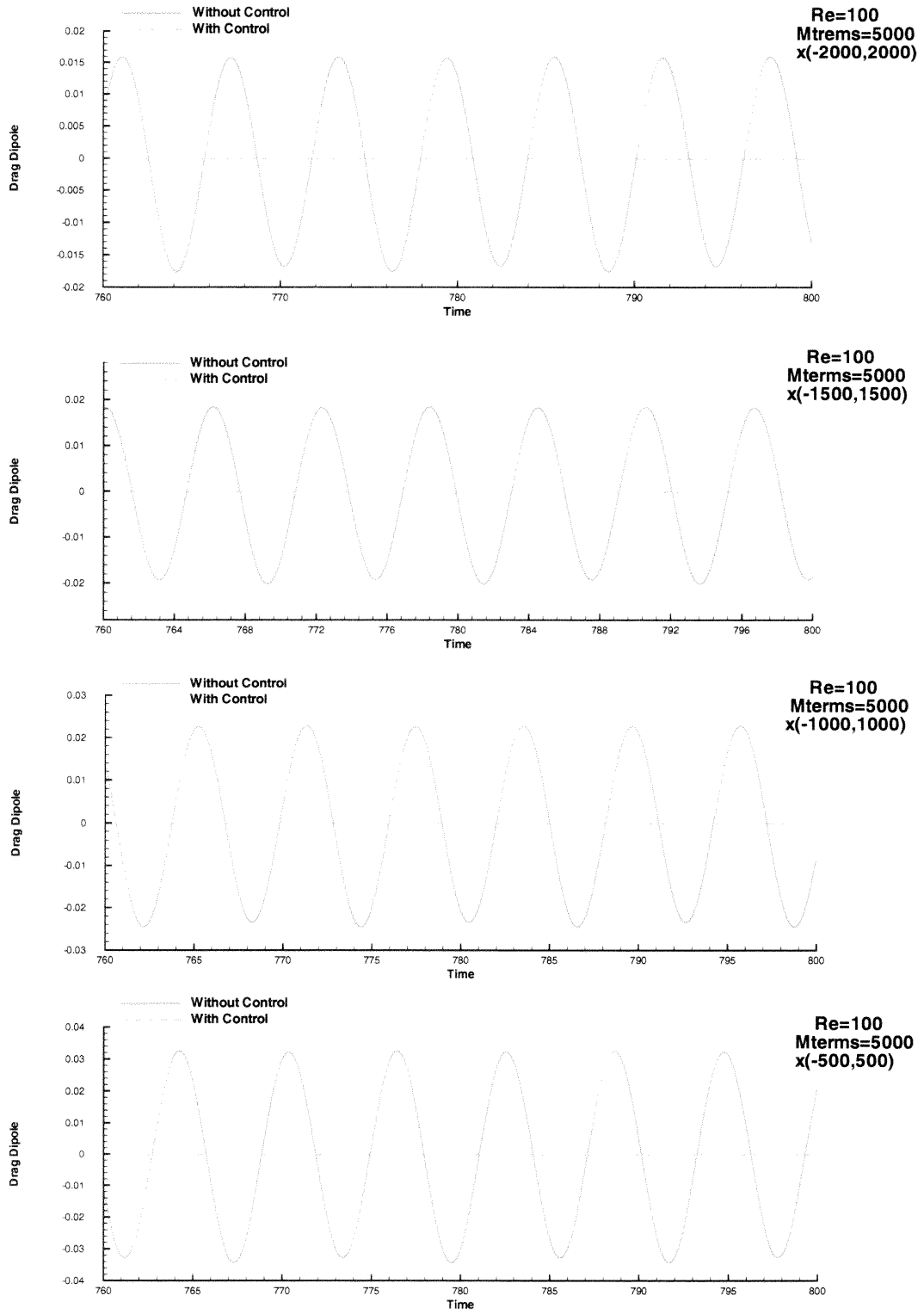


**Figure 4.36** Drag dipoles with and without control at the Reynolds number value  $Re = 100$  using the number of subintervals  $Mterms = 5000$  in the integral of Equation (3.50) for various observer positions

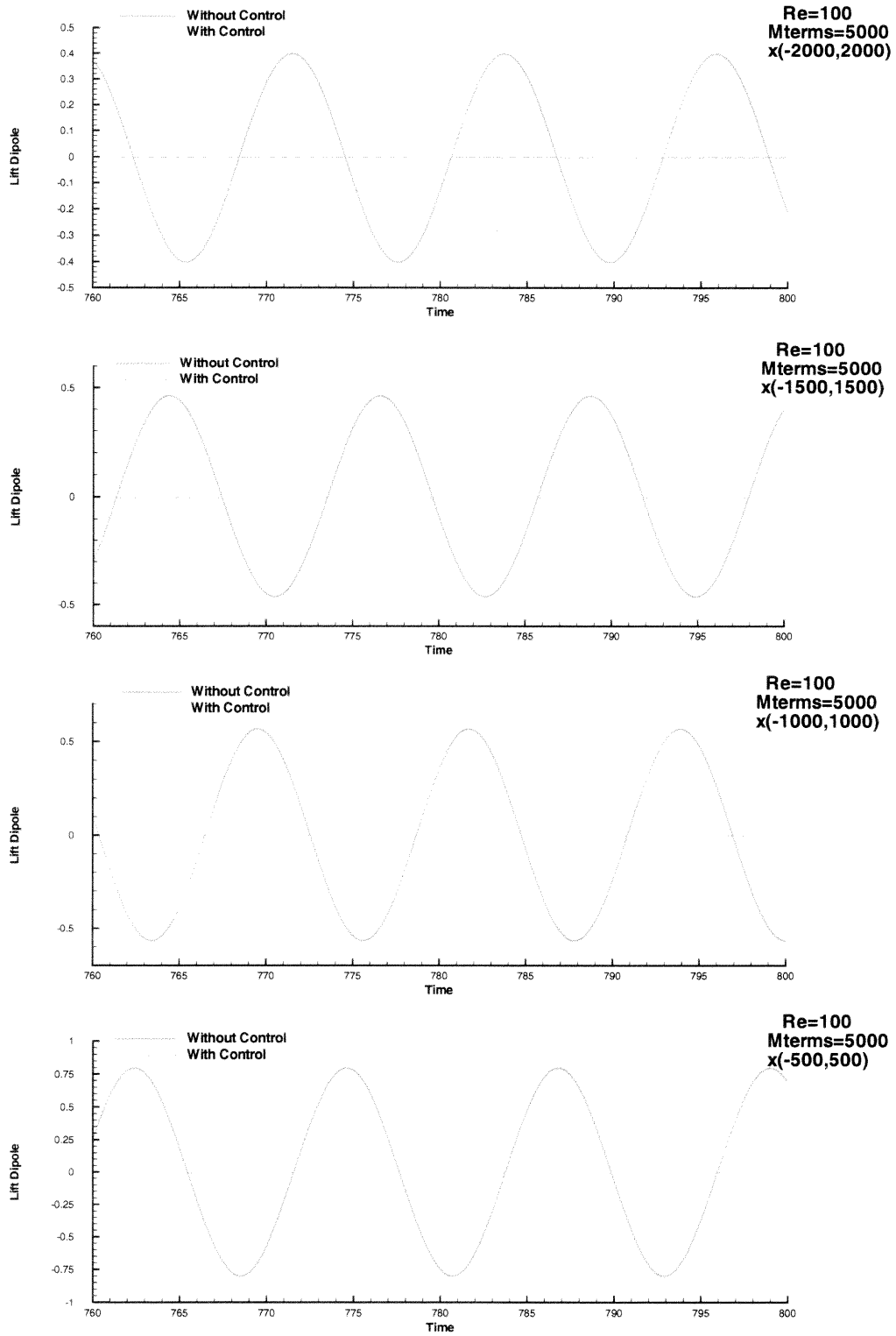


**Figure 4.37** Lift dipole with and without control at the Reynolds number value  $Re = 100$  using the number of subintervals  $Mterms = 5000$  in the integral of Equation (3.50) for various observer positions

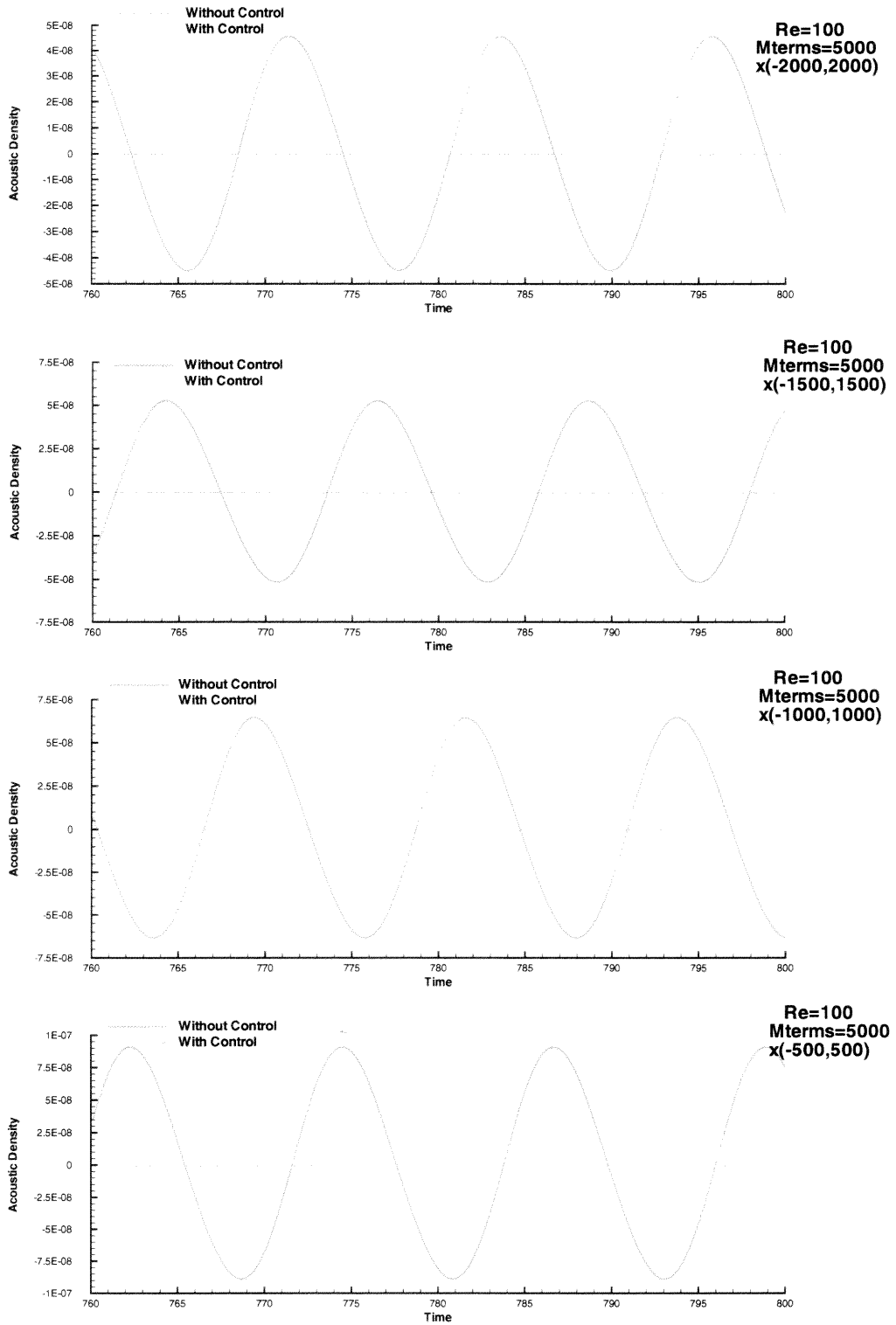


**Figure 4.38** Acoustic density with and without control at the Reynolds number value  $Re = 100$  using the number of subintervals  $Mterms = 5000$  in the integral of Equation (3.50) for various observer positions.

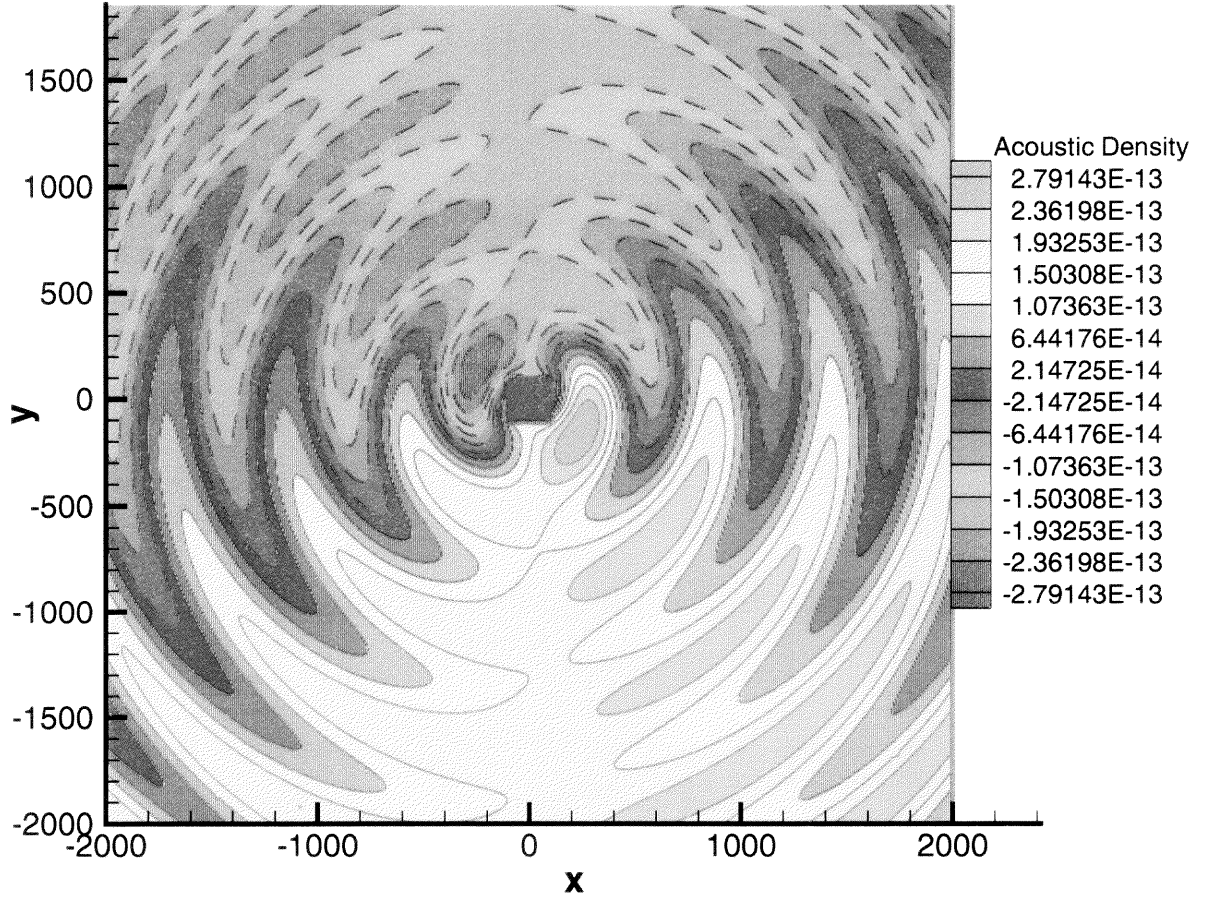


**Figure 4.39** Contour of the acoustic density at the Reynolds number value  $Re = 160$  using the number of subintervals  $Mterms = 5000$  in the integral of Equation (3.50) in the far-field domain ( $-2000 \leq x_1, x_2 \leq 2000$ )

#### 4.2.2.2 Computations at $Re = 160$ .

The investigation is performed to show whether it is possible to suppress the generation of sound at the Reynolds number  $Re = 160$ . Figures (4.40), (4.41) show the drag dipole, lift dipole, and acoustic density fluctuation with and without flow control. After control, the drag and lift dipole are decreased significantly and so is the acoustic density fluctuation. The results shows that the non-dimensional acoustic density fluctuation is decreased approximately by five orders of magnitude after applying control.

Figures (4.42), (4.43) and (4.44) show the control results as the observer moves toward the cylinder. The suppression of the acoustic density fluctuation is obtained at every location. Figure (4.45) shows the contour of the far-field acoustic density at the Reynolds number  $Re = 160$  and the Mach number  $M = 0.01$ . The instantaneous directivity in Figure (4.39) shows that sound wave propagates with a small angle from the horizontal axis ( $x_1$ ). As the Reynolds number increases, the drag dipole relatively increases and the lift dipole is no longer the dominant term.

### 4.3 Sound Pressure Level

In order to investigate the noise suppression by this control technique, sound pressure level (SPL) was used to compare the results of noise generation before and after control. In order to compare with the experimental results of Revell *et al.* (1977) and Weier *et al.* (1998), the dimensional parameters were calculated based on the Reynolds number values  $Re = 100$  and  $Re = 160$  with the cylinder diameter  $D = 0.02\text{ m}$ , the flow Mach numbers  $M = 0.000215$  and  $M = 0.000342$ , freestream speed of sound  $340\text{ m/s}$ . The air density ( $\rho_o$ ) and the air dynamic viscosity ( $\mu$ ) used in this study are  $1120\text{ kg/m}^3$  and  $1.78 \times 10^{-5}\text{ kg/m} \cdot \text{sec}$  respectively. The acoustic pressures were obtained by using the equation of state (3.13).



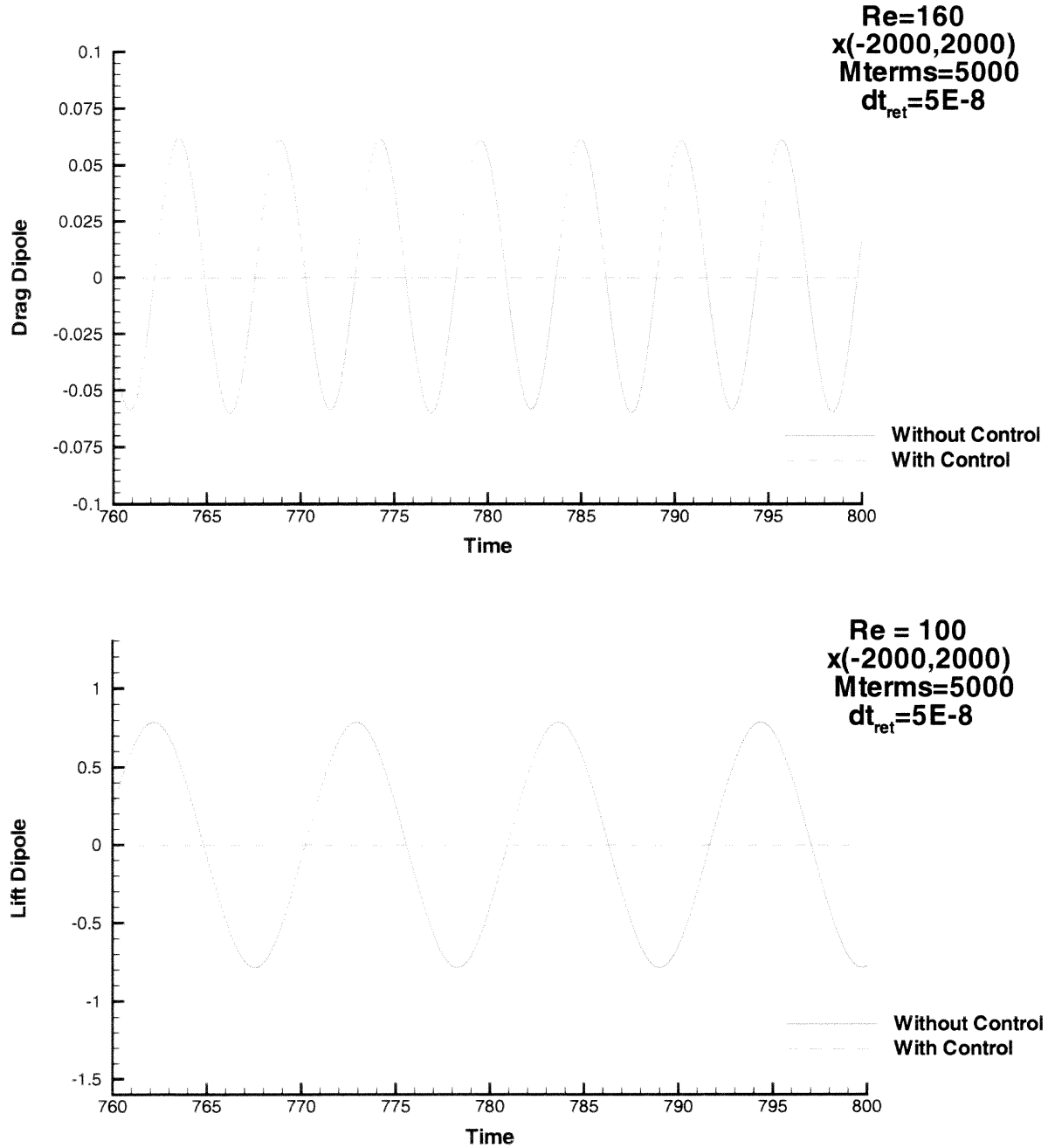


**Figure 4.40** Drag and lift dipoles at the Reynolds number value  $Re = 160$  with and without control

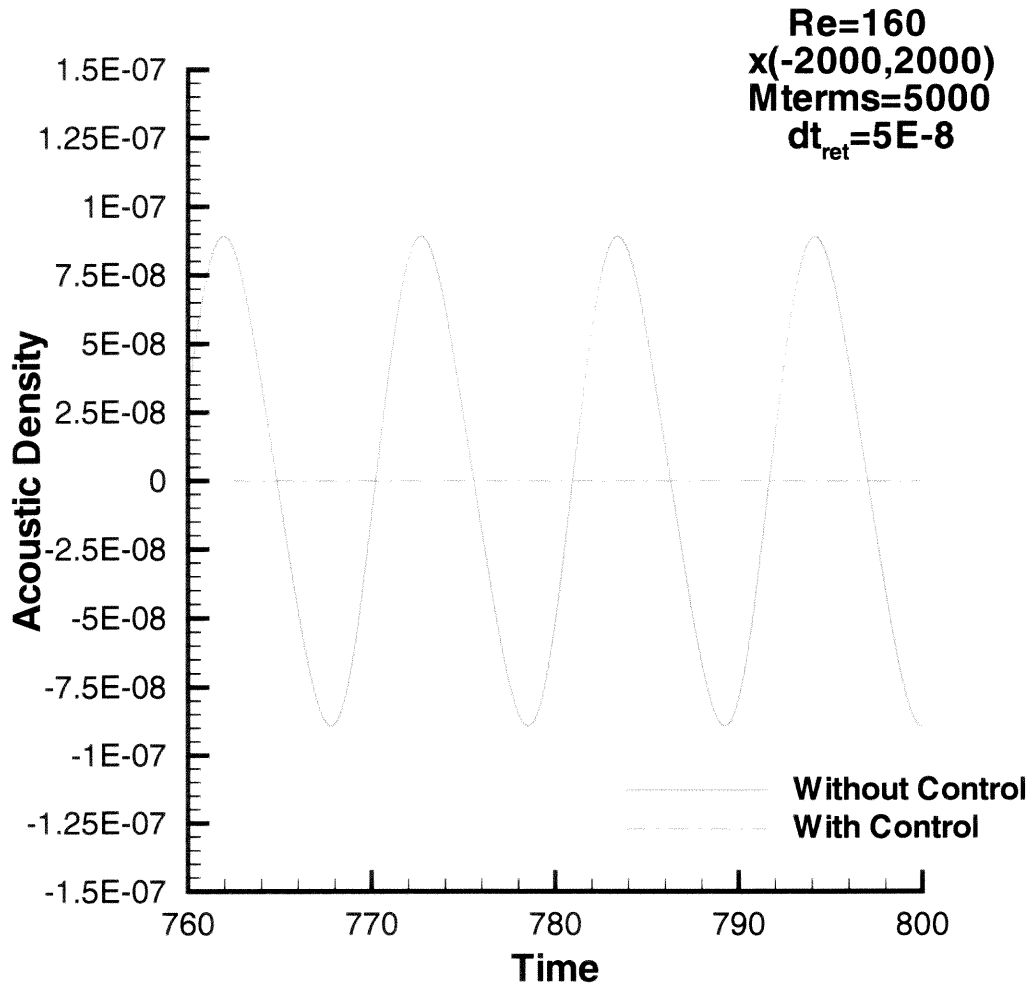


**Figure 4.41** Acoustic density at the Reynolds number value  $Re = 160$  with and without control

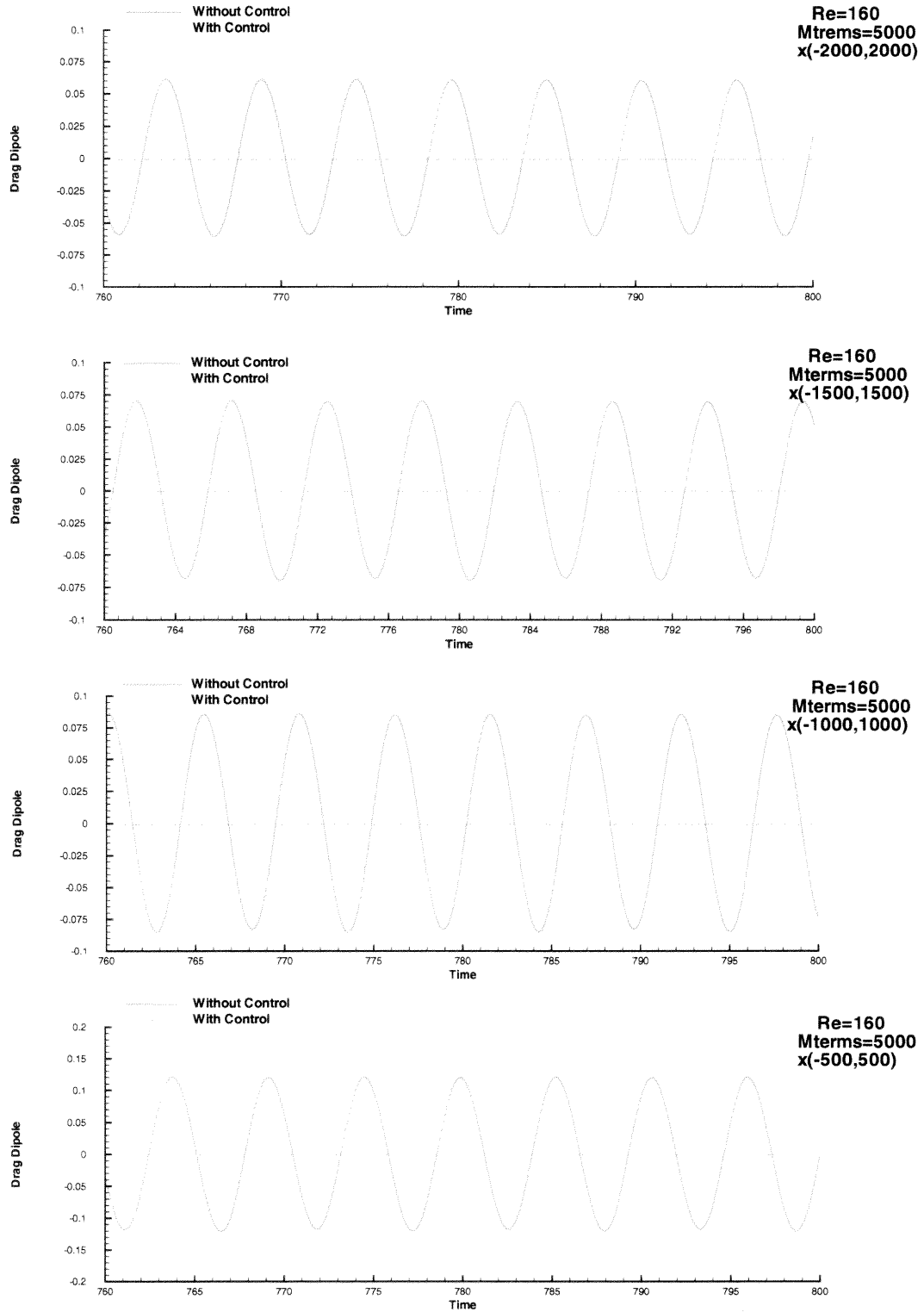


**Figure 4.42** Drag dipoles with and without control at the Reynolds number value  $Re = 160$  using the number of subintervals  $Mterms = 5000$  in the integral of Equation (3.50) for various observer positions

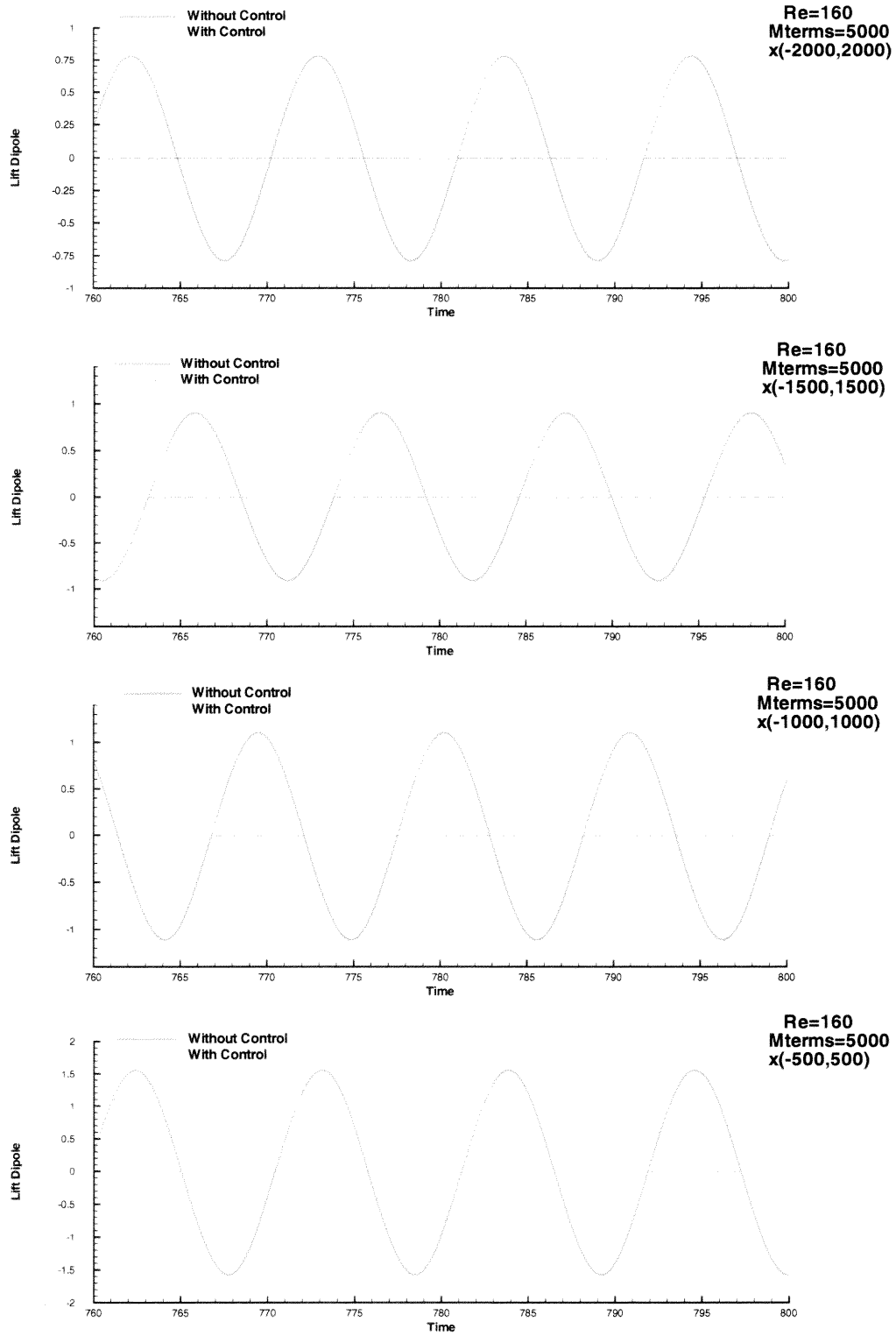


**Figure 4.43** Lift dipole with and without control at the Reynolds number value  $Re = 160$  using the number of subintervals  $Mterms = 5000$  in the integral of Equation (3.50) for various observer positions

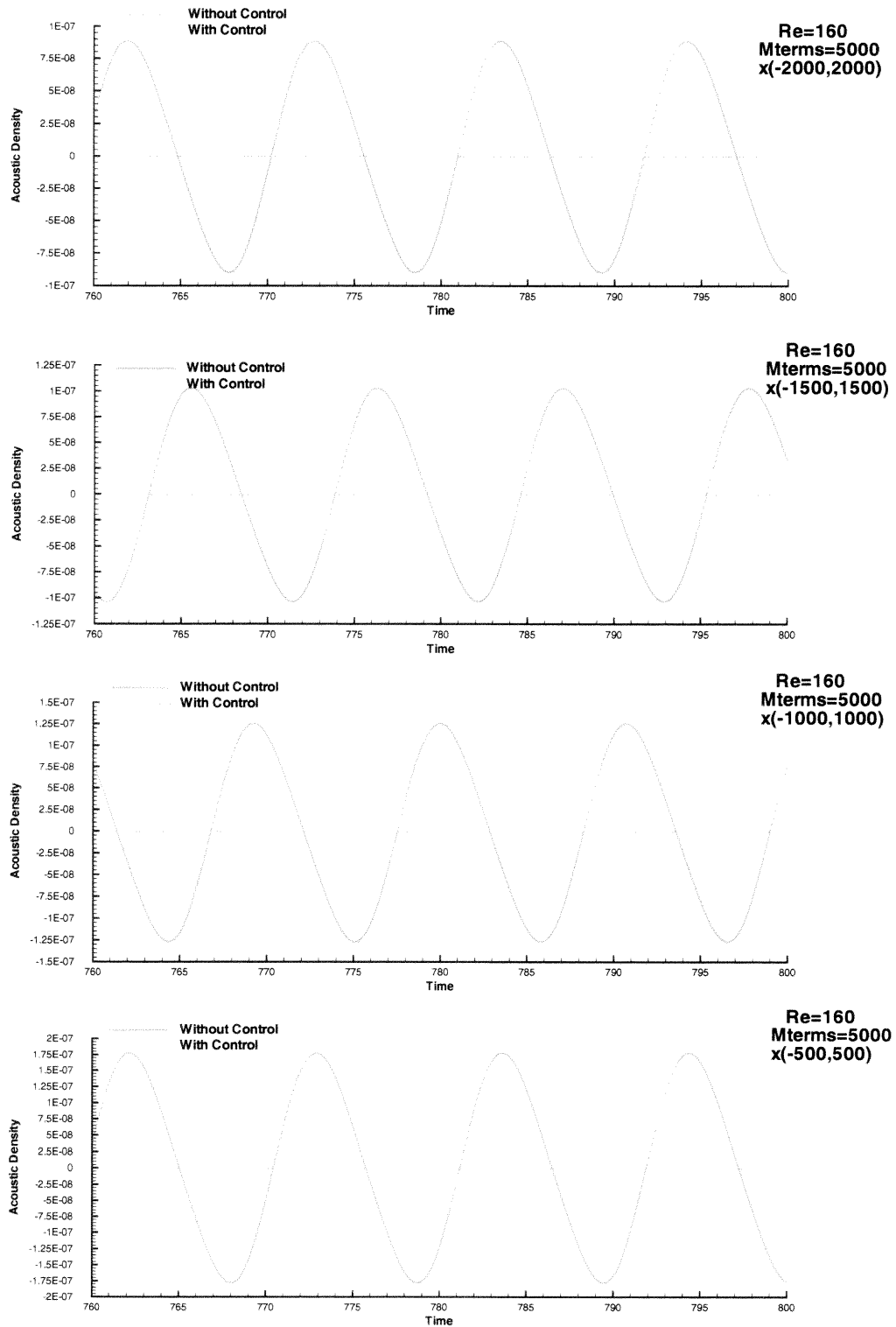


**Figure 4.44** Acoustic density with and without control at the Reynolds number value  $Re = 160$  using the number of subintervals  $Mterms = 5000$  in the integral of Equation (3.50) for various observer positions.

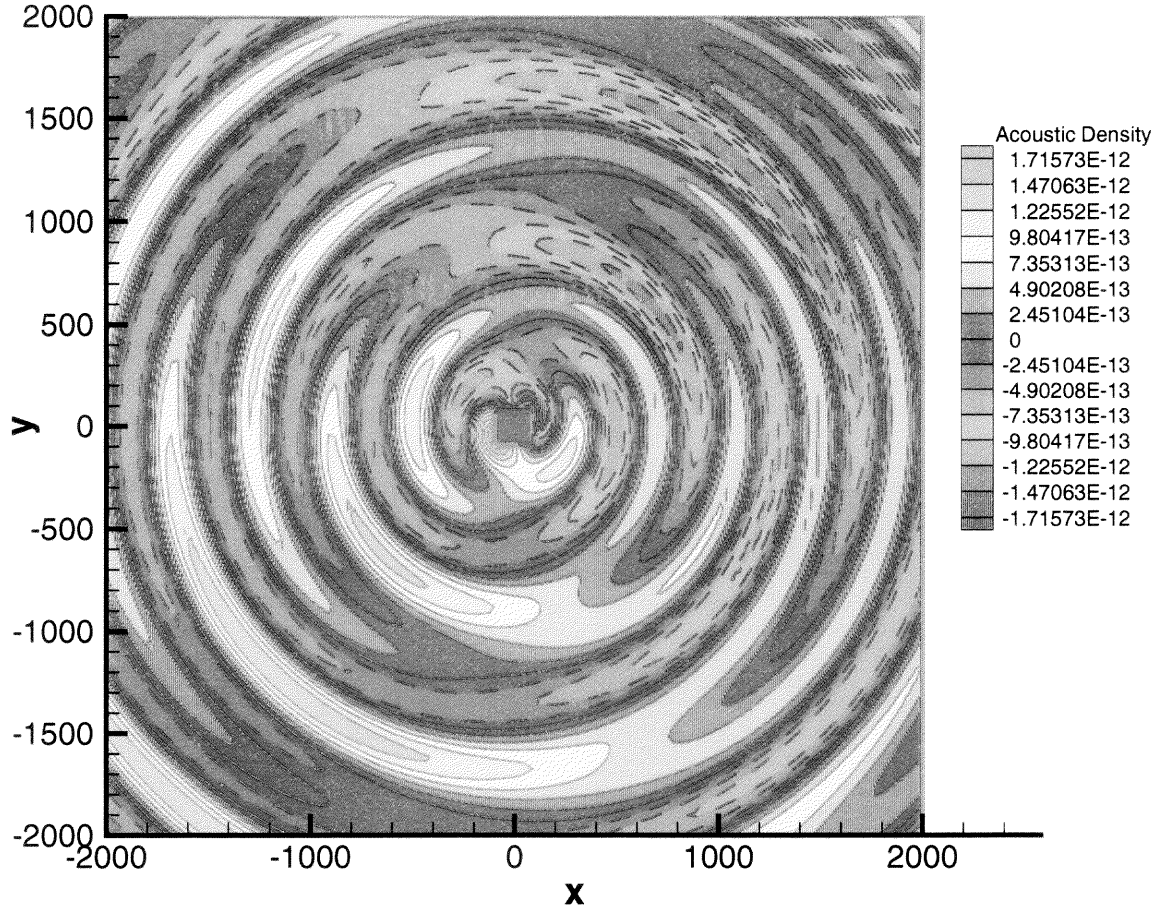


**Figure 4.45** Contour of the acoustic density at the Reynolds number value  $Re = 160$  using the number of subintervals  $M_{terms} = 5000$  in the integral of Equation (3.50) in the far-field domain ( $-2000 \leq x_1, x_2 \leq 2000$ )

Because sound travels as a wave of compression and rarefaction (positive and negative pressures) with respect to the steady state, the mean value of the sound pressure fluctuation, in most practical situations, fluctuates evenly about zero. An attempt at using a simple mean value conveys no useful information. Therefore, the average of the acoustic pressure is obtained by using the *root mean square (rms)* value. The *rms* pressure will then be used to calculate the sound pressure level in the decibel scale. The sound pressure level (SPL) is defined as

$$SPL = 20 \log_{10} \left( \frac{P_{rms}}{P_{ref}} \right) \quad (4.1)$$

where  $P_{ref}$  is the reference pressure.

The common reference pressure for airborne acoustic measurements is  $20 \times 10^{-6} \text{Newton/meter}^2$  ( $20\mu\text{N/m}^2$ ). This reference pressure is the pressure that approximates the threshold of human hearing and provides a positive set of decibel (dB) values, started from 0 when the *rms* pressure is the same as the reference pressure. However, the numerical *rms* pressures obtained in this study were below the threshold of human hearing which resulted in negative decibel (dB). Therefore, in order to obtain positive decibel (dB) values and be able to compare quantitatively the level of sound with and without control, the reference pressure used in this study is  $20 \times 10^{-15} \text{N/m}^2$ .

A list of pressures and the corresponding sound pressure level (SPL) in decibel (dB), using  $20 \times 10^{-6} \text{N/m}^2$  and  $20 \times 10^{-15} \text{N/m}^2$  as the reference pressures, is presented in Table 4.1 (White, 1918). Table 4.2 (White, 1918) indicates approximate decibel (dB) values corresponding to perceived changes in loudness, as well as the comparison of sound pressure levels (SPL). Later in this study,  $dB^*$  refers to the decibel scale at the reference pressure  $P_{ref} = 20 \times 10^{-15} \text{N/m}^2$ .

Sound Pressure ( $N/m^2$ )	Sound Pressure Level (dB, re: $20 \times 10^{-6}$ )	Sound Pressure Level (dB, re: $20 \times 10^{-15}$ )	Environmental condition
$20 \times 10^{-15}$		0	
$20 \times 10^{-13}$		20	
$20 \times 10^{-12}$		60	
$20 \times 10^{-10}$		100	
$20 \times 10^{-8}$		140	
$20 \times 10^{-6}$	0	180	Threshold of hearing
0.0002	20	200	Broadcasting studio
0.002	40	220	Library
0.02	60	240	Conversational Speech
0.2	80	260	Typical factory
2	100	280	Symphony orchestra
20	120	300	Aircraft takeoff
200	140	320	Threshold of pain

**Table 4.1** Sound Pressure Level

Change in Sound Level		Change in Perceived "Loudness"
(dB, re: $20 \times 10^{-6}$ )	(dB, re: $20 \times 10^{-15}$ )	
3 dB	183	Just perceptible
5 dB	185	Noticeable difference
10 dB	190	Twice (or $\frac{1}{2}$ ) as loud
15 dB	195	Large change
20 dB	200	Four times (or $\frac{1}{4}$ ) as loud

**Table 4.2** Change in Sound Level



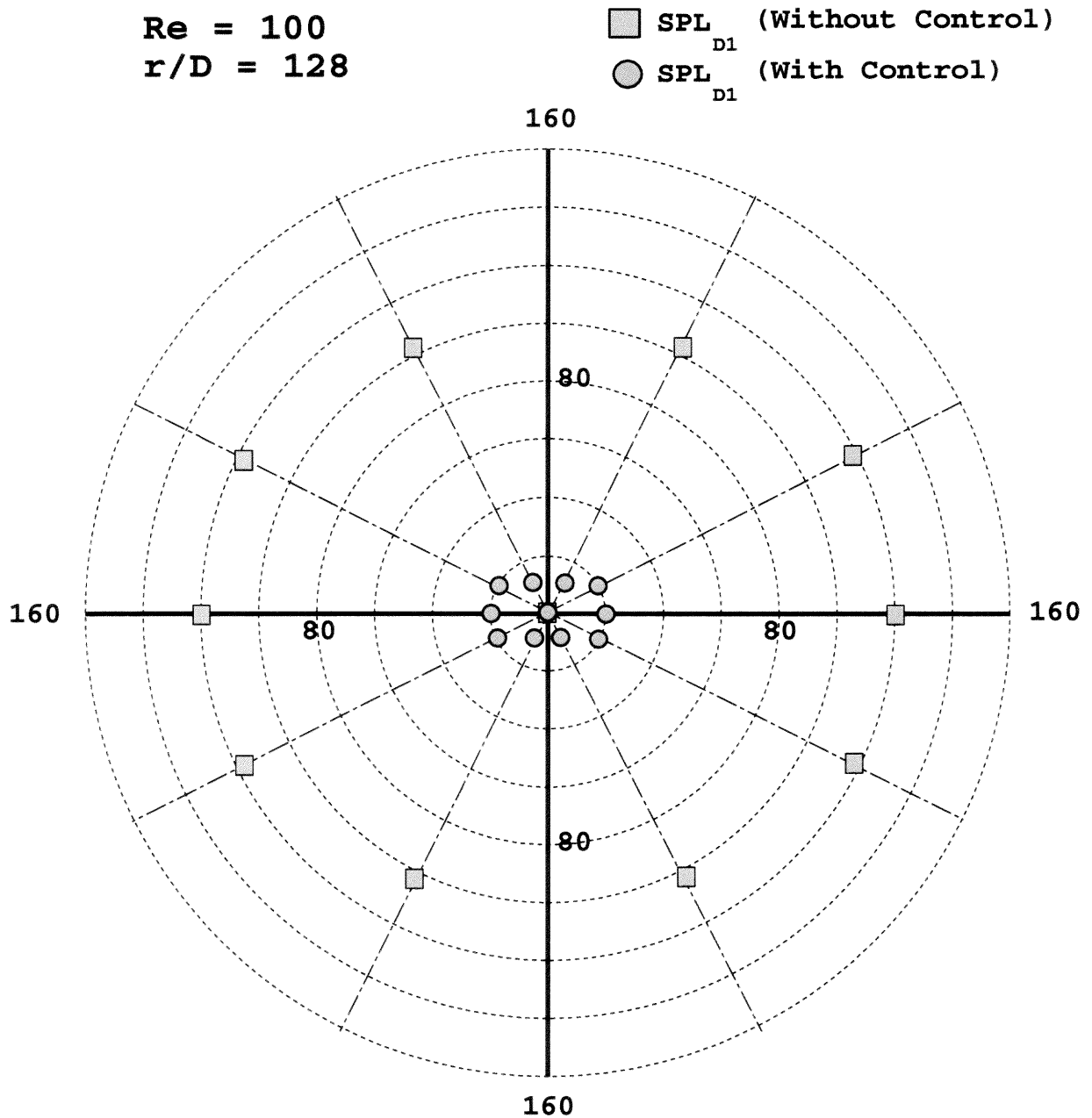
#### 4.3.1 Sound Pressure Level (SPL) at $Re = 100$

Figure (4.46) shows the directivity patterns for the overall sound pressure level with and without control generated by the drag dipole ( $SPL_{D1}$ ) at Reynolds number values  $Re = 100$ , Mach number  $M = 0.000215$ , and cylinder diameter  $D = 0.02$  m. The observer is located at  $128D$  from the cylinder. From the results, SPL was suppressed by  $98.97 \text{ dB}^*$  after control. From Table 4.2, it is about 27 times less noise than in the flow without control. Figure (4.47) shows the directivity patterns for the overall sound pressure level with and without control generated by the lift dipole ( $SPL_{D2}$ ). From the results, one can observe that SPL is suppressed by  $137.64 \text{ dB}^*$  after control. From Table 4.2, it corresponds to about 37 times less noise than in the flow without control. Figure (4.48) shows the comparison between the sound pressure level generated by the flow with and without control. From the results, SPL is suppressed by  $125.22 \text{ dB}^*$  after control. This corresponds to about 33 times less noise than in the flow without control. Notice that the directivity patterns for the sound field without control tend to propagate in vertical direction due to the lift in the flow field. However, after a period of time the directivity patterns for the sound field with control tend to propagate in the horizontal direction due to the action of the Lorentz force.

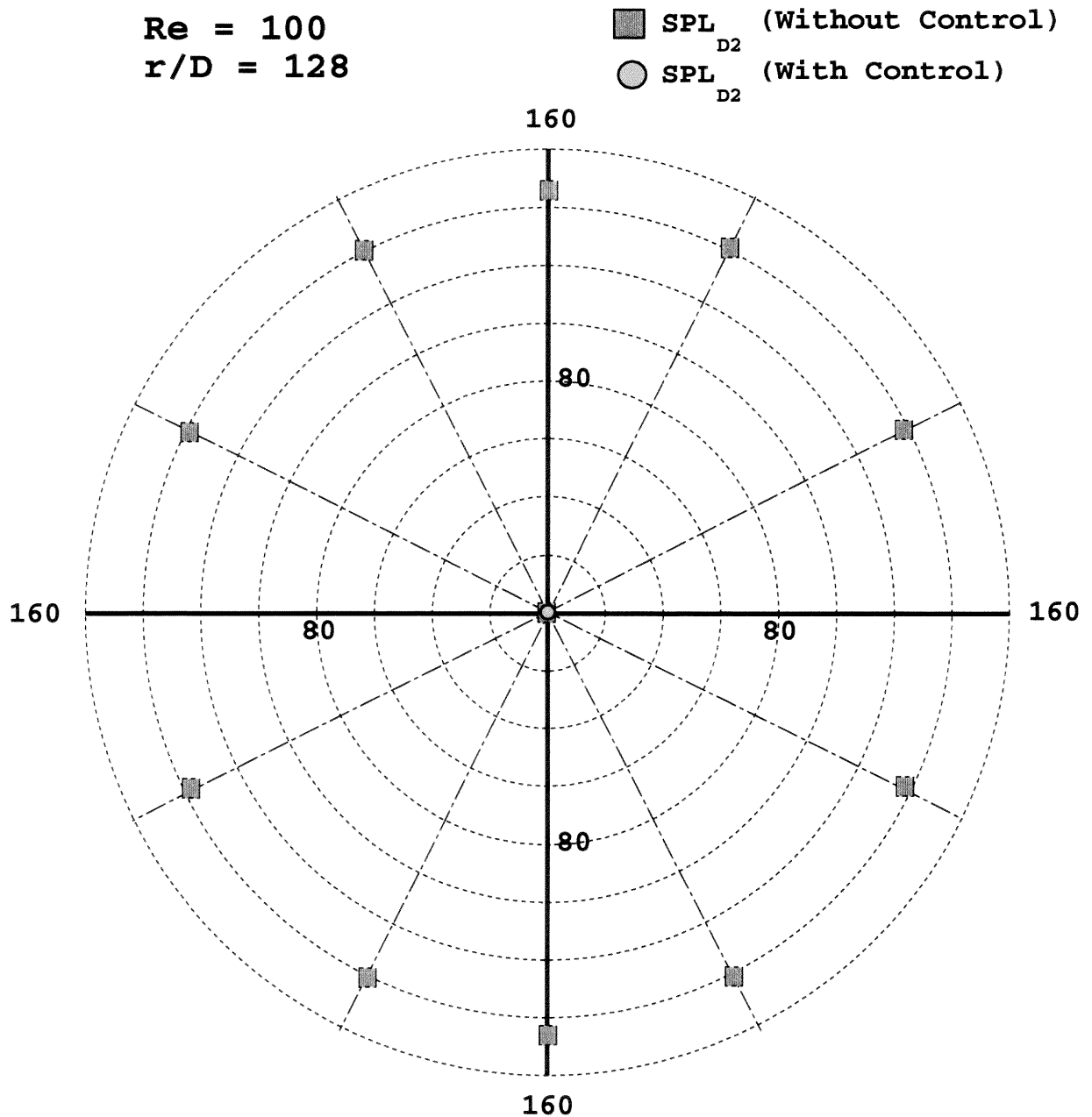
#### 4.3.2 Sound Pressure Level (SPL) at $Re = 160$

Figure (4.49) shows the directivity patterns for overall sound pressure level with and without control generated by the drag dipole ( $SPL_{D1}$ ) at the Reynolds number  $Re = 160$ , Mach number  $M = 0.000342$ , and cylinder diameter  $D = 0.02$  m. The observer is located at  $128D$  from the cylinder. From the results, one observes that SPL is suppressed by  $95.56 \text{ dB}^*$  after control. From table 4.2, this corresponds to about 26 times less noise than in the flow without control. Figure (4.50) shows

the directivity patterns for overall sound pressure level with and without control generated by the lift dipole ( $SPL_{D2}$ ). From the results, one can observe that SPL is suppressed by  $120.91\text{ dB}^*$  after control. From table 4.2, this corresponds to about 32 times less noise than in the flow without control. Figure (4.51) shows the comparison between the sound pressure level generated by the flow with and without control. From the results, SPL is suppressed by  $116.65\text{ dB}^*$  after control. This corresponds to about 31 times less noise than in the flow without control. The directivity patterns for the sound field without control tend to propagate in the vertical direction due to the lift in the flow field. However, after a period of time, the directivity patterns for the sound field with control tend to propagate in the horizontal direction due to the action of the Lorentz force acting.



**Figure 4.46** Directivity patterns for overall sound pressure level with and without control generated by the drag dipole ( $SPL_{D1}$ ) at the Reynolds number  $Re = 100$ , Mach number  $M = 0.000215$ , and cylinder diameter  $D = 0.02$  m. The observers locations are at  $128D$  away from the cylinder. Axes units are decibels (dB, re:  $20 \times 10^{-15}$  )



**Figure 4.47** Directivity patterns for overall sound pressure level with and without control generated by the lift dipole ( $SPL_{D2}$ ) at the Reynolds number  $Re = 100$ , Mach number  $M = 0.000215$ , and cylinder diameter  $D = 0.02$  m. The observers locations are at  $128D$  away from the cylinder. Axes units are decibels (dB, re:  $20 \times 10^{-15}$  )

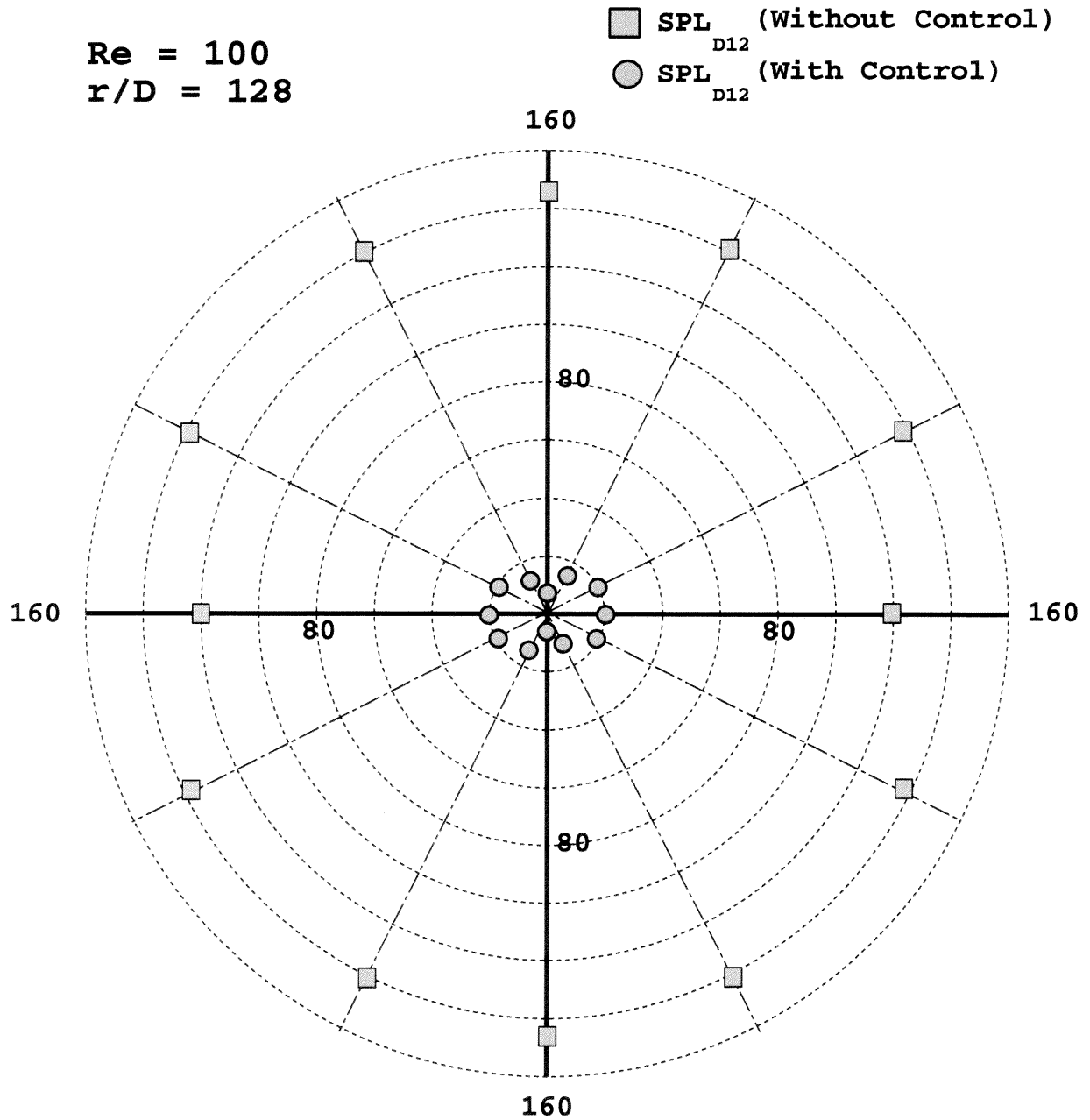


**Figure 4.48** Directivity patterns for overall sound pressure level with and without control generated by the total dipole ( $SPL_{D12}$ ) at the Reynolds number  $Re = 100$ , Mach number  $M = 0.000215$ , and cylinder diameter  $D = 0.02$  m. The observers locations are at  $128D$  away from the cylinder. Axes units are decibels (dB, re:  $20 \times 10^{-15}$  )

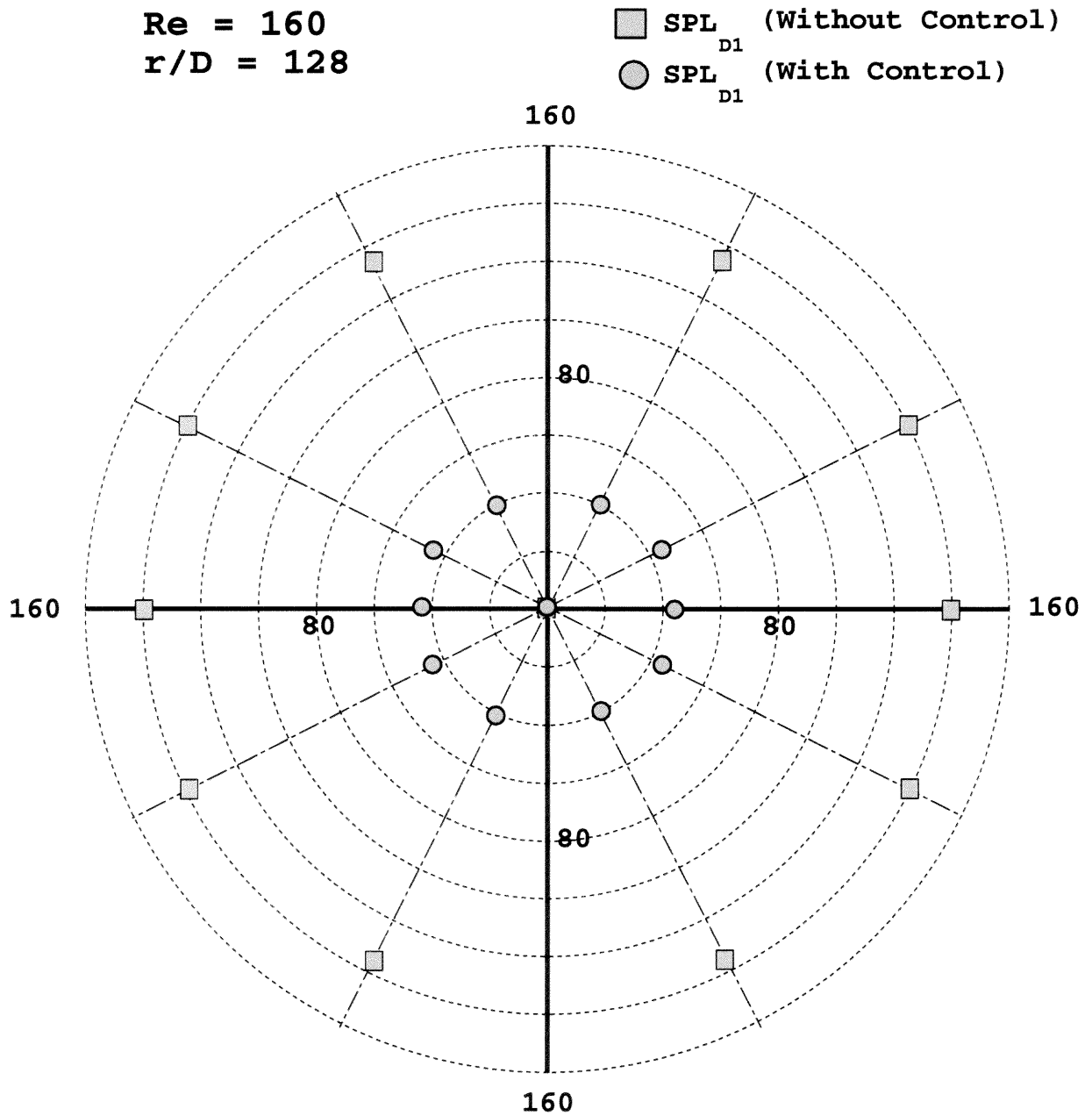


**Figure 4.49** Directivity patterns for overall sound pressure level with and without control generated by the drag dipole ( $SPL_{D1}$ ) at the Reynolds number  $Re = 160$ , Mach number  $M = 0.000342$ , and cylinder diameter  $D = 0.02$  m. The observers locations are at  $128D$  away from the cylinder. Axes units are decibels (dB, re:  $20 \times 10^{-15}$ )

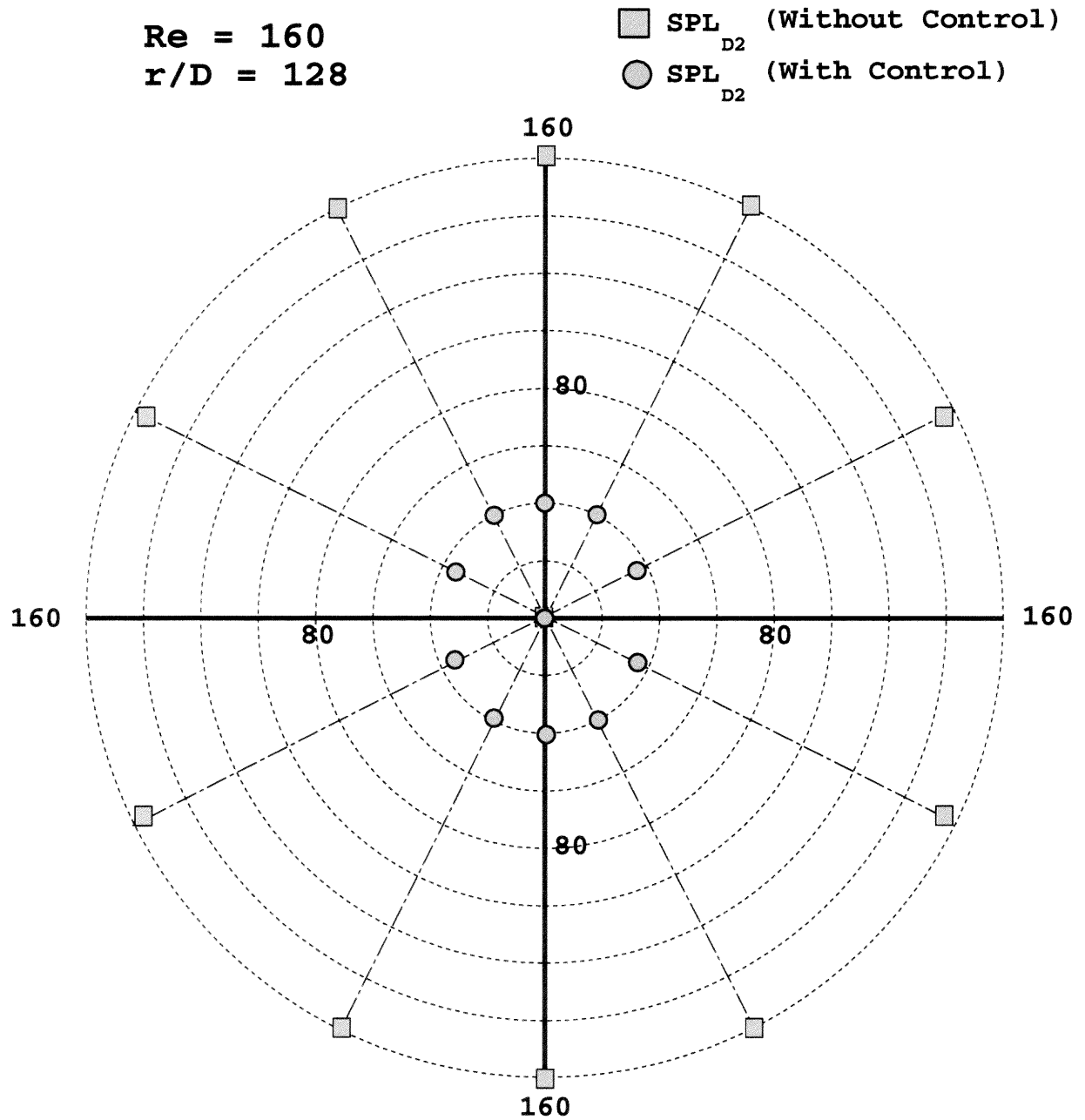


**Figure 4.50** Directivity patterns for overall sound pressure level with and without control generated by the lift dipole ( $SPL_{D2}$ ) at the Reynolds number  $Re = 160$ , Mach number  $M = 0.000342$ , and cylinder diameter  $D = 0.02$  m. The observers locations are at  $128D$  away from the cylinder. Axes units are decibels (dB, re:  $20 \times 10^{-15}$  )

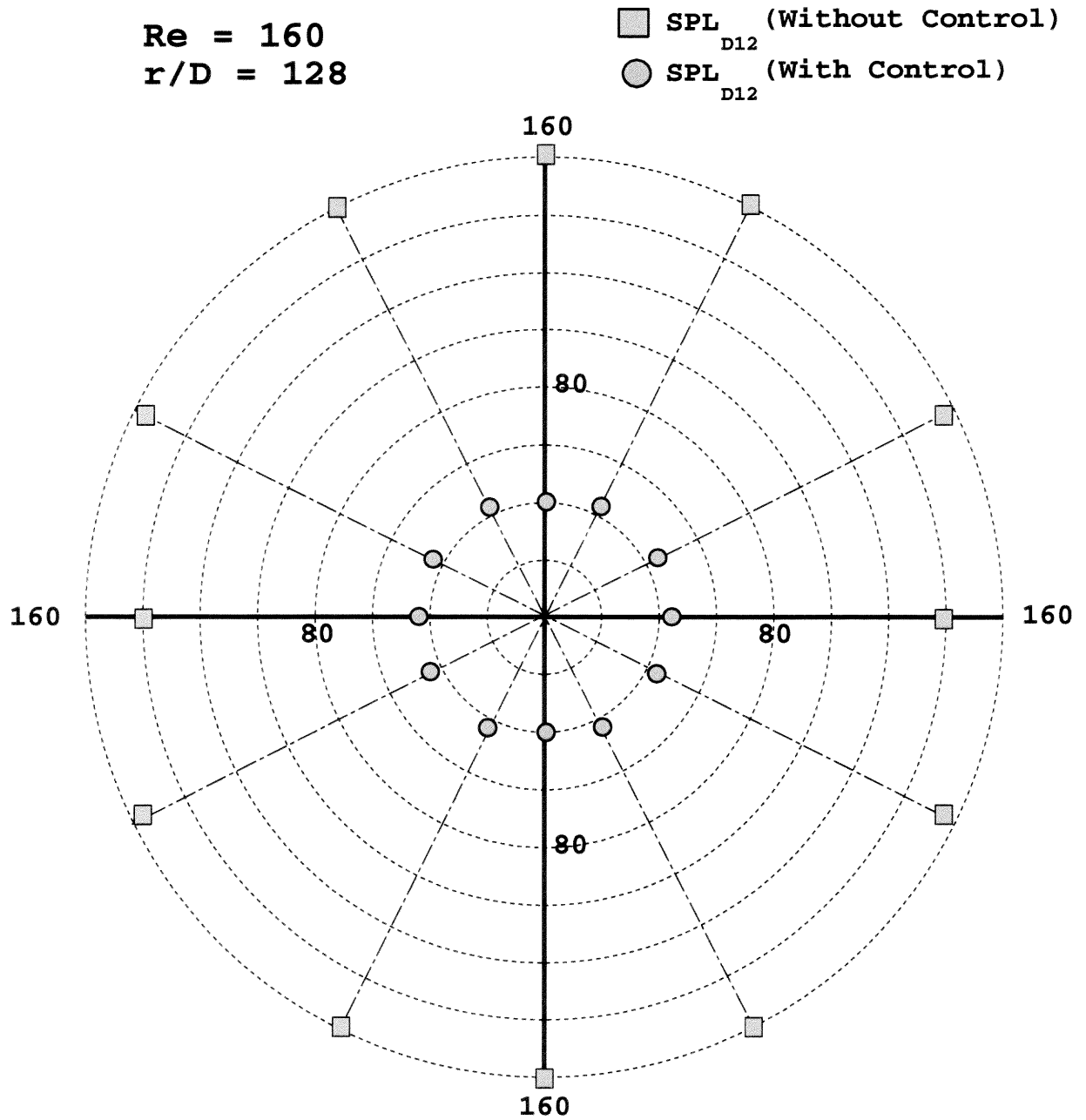


**Figure 4.51** Directivity patterns for overall sound pressure level with and without control generated by the total dipole ( $SPL_{D12}$ ) at the Reynolds number  $Re = 160$ , Mach number  $M = 0.000342$ , and cylinder diameter  $D = 0.02$  m. The observers locations are at  $128D$  away from the cylinder. Axes units are decibels (dB, re:  $20 \times 10^{-15}$  )



## CHAPTER 5

### CONCLUSIONS

In this study, Lighthill's acoustic analogy approach has been applied to compute the noise source functions and acoustic density fluctuation. Laminar vortex shedding of the flow past a circular cylinder at the Reynolds number values of 100 and 160 has been simulated by solving the unsteady two-dimensional incompressible Navier-Stokes equations. Neglecting the volume quadrupole source functions, the acoustic source functions have been obtained from the surface dipole source functions. Using Curle's solution of Lighthill's acoustic analogy, the surface dipole source functions have been determined from the computed near-field flow.

The drag and lift dipole source functions are the product of drag and lift forces acting on the surface of the cylinder. At low Mach number, the lift dipole source function is the main contributor to the total dipole source function, and causes the majority of the acoustic density fluctuation. The results obtained in this study agree well with those of previous work (You *et al.* (1998)).

The noise generated by the flow past a circular cylinder mainly occurs due to the variations of drag and lift in the near-field flow. Because variations of drag and lift are caused by the pressure fluctuation generated by periodic vortex shedding, This flow control technique that suppresses vortex shedding can also significantly decrease noise generation in the flow field. In this particular study, electro-magnetic forces have been used for both flow and acoustics control. For the numerical results at the Reynolds number values of 100 and 160 and Mach number values  $M = 0.01$ , the non-dimensional acoustic density fluctuation is decreased by five orders of magnitude.

In order to obtain quantitative values of sound generation, all parameters were converted to the dimensional forms. Based on the experimental works of Revell *et*

*al.* (1977) and Weier *et al.* (1998), the cylinder diameter was chosen to be 0.02 m. The calculation was then performed at the Reynolds number values  $Re = 100$  and  $Re = 160$ , and the flow Mach number values  $M = 0.000215$  and  $M = 0.000342$ . The results showed that the sound pressure level for the flow with control were 30-35 times lower than that without control. One of the control effects was to make the directivity patterns of the sound field move outward along the horizontal axis. The changes in directivity patterns are caused by the applied Lorentz forces along the cylinder surface. To our knowledge, this is the first time that one was able to demonstrate the suppression of flow induced noise in the flow past a circular cylinder using active, feedback control.

The present work of applying electro-magnetic body forces for flow control has been focused by many researchers in recent years. This control technique has been practically used in some applications. Some examples of the application of the Lorentz force to control fluid flows are the recent research and development (R&D) on magnetohydrodynamic (MHD) ship propulsion and drag reduction of marine vehicles which will result in increased speed, lower fuel assumption, reduced signatures, etc. The experiment work of Weier *et al.* (1998) has shown that the application of a Lorentz force to wake flows can successfully result in the suppression of Von Karman vortex street. Most applications, so far, have used "sea water" as the fluid medium. The present control technique is efficient when the electrical conductivity of the surrounding fluid is about 3-10 S/m, a level indeed reached by sea water. In other words, this control technique can be applied to any weakly conducting fluid.

The present study has concentrated on air as the fluid medium. There is, so far, no application or experimental work performed using air as the fluid medium. However, it has been possible to raise up the electrical conductivity of air to be at least as high as the conductivity of sea water (Lu *et al.*, (1999,2001)). This was

achieved by adding alkali salt in air, using an organic carrier instead of alkali salt, or spraying an ionized aerosol in the air. It may thus be feasible to apply the Lorentz force as a way to control aerodynamics, as well as the sound it generates. Note that not only electro-magnetic body forces, i.e. Lorentz forces, but also any form of body force applied tangentially to the solid surface can be used to modify the boundary layer around the surface in order to prevent the boundary layer from separating.

## APPENDIX A

### SOME INTEGRAL FORMULAE FROM VECTOR ANALYSIS

In this section, some useful integral formulae frequently used to derive acoustic equations are presented. To this purpose let  $\mathcal{V}$  be a closed region of space bounded by a regular surface  $\mathcal{S}$ , and  $\varphi_1$  and  $\varphi_2$  be any two functions defined on  $\mathcal{V}$ . Then, the divergence theorem applied to the vector  $\varphi_1 \nabla \varphi_2$  gives

$$\int_{\mathcal{V}} \nabla \cdot (\varphi_1 \nabla \varphi_2) d\vec{y} = \int_{\mathcal{S}} (\varphi_1 \nabla \varphi_2) \cdot \hat{n} d\mathcal{S}(\vec{y}). \quad (\text{A.1})$$

After expanding the divergence in Eq. (A.1), and rewriting  $\nabla \varphi_2 \cdot \hat{n}$  to  $\partial \varphi_2 / \partial n$  where  $\partial \varphi_2 / \partial n$  is the derivative in the direction of the positive normal, the well-known *Green's first identity* is obtained:

$$\int_{\mathcal{V}} \nabla \varphi_1 \cdot \nabla \varphi_2 d\vec{y} + \int_{\mathcal{V}} \varphi_1 \nabla^2 \varphi_2 d\vec{y} = \int_{\mathcal{S}} \varphi_1 \frac{\partial \varphi_2}{\partial n} d\mathcal{S}(\vec{y}). \quad (\text{A.2})$$

Let  $\varphi_1 = \varphi_2$  and  $\varphi_2$  be a solution of Laplace's equation. Eq. (A.2) becomes

$$\int_{\mathcal{V}} (\nabla \varphi_2)^2 d\vec{y} = \int_{\mathcal{S}} \varphi_2 \frac{\partial \varphi_2}{\partial n} d\mathcal{S}(\vec{y}). \quad (\text{A.3})$$

By interchanging the roles of the functions  $\varphi_1$  and  $\varphi_2$  in Eq. (A.2), it can be obtained:

$$\int_{\mathcal{V}} \nabla \varphi_2 \cdot \nabla \varphi_1 d\vec{y} + \int_{\mathcal{V}} \varphi_2 \nabla^2 \varphi_1 d\vec{y} = \int_{\mathcal{S}} \varphi_2 \frac{\partial \varphi_1}{\partial n} d\mathcal{S}(\vec{y}). \quad (\text{A.4})$$

Subtracting Eq. (A.4) from Eq. (A.2), the well-known relation between a volume integral and a surface integral is obtained:

$$\int_{\mathcal{V}} (\varphi_1 \nabla^2 \varphi_2 - \varphi_2 \nabla^2 \varphi_1) d\vec{y} = \int_{\mathcal{S}} (\varphi_1 \frac{\partial \varphi_2}{\partial n} - \varphi_2 \frac{\partial \varphi_1}{\partial n}) d\mathcal{S}(\vec{y}), \quad (A.5)$$

known as *Green's second identity* or, frequently, as *Green's theorem*.

If  $\vec{V}_{\mathcal{S}}(\vec{y}, t)$  denotes the velocity at any point  $\vec{y}$  of the surface  $\mathcal{S}$ , Leibniz's rule shows that

$$\frac{d}{dt} \int_{\mathcal{V}} \varphi d\vec{y} = \int_{\mathcal{V}} \frac{\partial \varphi}{\partial t} d\vec{y} + \int_{\mathcal{S}} \vec{V}_{\mathcal{S}} \cdot \hat{n} \varphi d\mathcal{S}(\vec{y}), \quad (A.6)$$

where the function  $\varphi(\vec{y}, t)$  is defined on  $\mathcal{V}$ .

## APPENDIX B

### DERIVATION OF THE INHOMOGENEOUS WAVE EQUATION FOR A UNIFORMLY MOVING MEDIUM

In this section, the derivation of the inhomogeneous, uniformly moving medium, wave equation is presented.

Considering the inhomogeneous, uniformly moving medium, wave equation

$$\left(\frac{1}{c_o^2} \frac{D^2}{D\tau^2} - \nabla^2\right)\rho' = \frac{1}{c_o^2}\chi(\vec{y}, \tau) , \quad (B.1)$$

in terms of a fundamental solution  $G(\vec{y}, \tau \mid \vec{x}, t)$  of the wave equation:

$$\left(\frac{1}{c_o^2} \frac{D^2}{D\tau^2} - \nabla^2\right)G = \delta(\vec{x} - \vec{y})\delta(\vec{t} - \vec{\tau}) \quad (B.2)$$

for a point source  $\chi(\vec{y}, \tau)$  where

$$\frac{D(\cdot)}{D\tau} = \frac{\partial(\cdot)}{\partial\tau} + U_\infty \frac{\partial(\cdot)}{\partial y^1} \quad (B.3)$$

and

$$G = \frac{DG}{D\tau} = 0 \quad (B.4)$$

for  $t < \tau$  .

Then applying *Green's theorem* to  $\rho'$  and  $G$  and integrating both sides with respect to  $\tau$  from  $-\infty$  to  $+\infty$ , it becomes:

$$\int_{-\infty}^{\infty} \int_S \left( G \frac{\partial \rho'}{\partial n} - \rho' \frac{\partial G}{\partial n} \right) dS d\tau = \int_{-\infty}^{\infty} \int_V (G \nabla^2 \rho' - \rho' \nabla^2 G) d\vec{y} d\tau$$

$$\begin{aligned}
&= \frac{1}{c_o^2} \int_{-\infty}^{\infty} \int_{\mathcal{V}} \left( G \frac{D^2 \rho'}{D\tau^2} - \rho' \frac{D^2 G}{D\tau^2} \right) d\vec{y} d\tau \\
&+ \int_{-\infty}^{\infty} \int_{\mathcal{V}} \left( -G \frac{\chi(\vec{y}, \tau)}{c_o^2} \right) d\vec{y} d\tau \\
&+ \int_{-\infty}^{\infty} \int_{\mathcal{V}} \left( \delta(\vec{x} - \vec{y}) \delta(\vec{t} - \vec{\tau}) \rho' \right) d\vec{y} d\tau. \quad (\text{B.5})
\end{aligned}$$

Expanding the integrand of the left hand side;

$$\left( G \frac{D^2 \rho'}{D\tau^2} - \rho' \frac{D^2 G}{D\tau^2} \right) = \frac{\partial}{\partial \tau} \left( G \frac{D\rho'}{D\tau} - \rho' \frac{D G}{D\tau} \right) + U_{\infty} \frac{\partial}{\partial y_1} \left( G \frac{D\rho'}{D\tau} - \rho' \frac{D G}{D\tau} \right), \quad (\text{B.6})$$

and applying Leibniz's rule to the first term and the divergence theorem to the second, it becomes:

$$\int_{-\infty}^{\infty} \int_{\mathcal{V}} \left( G \frac{D^2 \rho'}{D\tau^2} - \rho' \frac{D^2 G}{D\tau^2} \right) d\vec{y} d\tau = - \int_{-\infty}^{\infty} \int_{\mathcal{S}} V_{sn} \left( G \frac{D\rho'}{D\tau} - \rho' \frac{D G}{D\tau} \right) d\mathcal{S} d\tau \quad (\text{B.7})$$

where  $V_{sn} = \vec{V}_s \cdot \vec{n}$ .

Substituting Eq. (B.7) into Eq. (B.5), and integrating over the delta functions term, it can be obtained as:

$$\begin{aligned}
\rho'(\vec{x}, t) &= \frac{1}{c_o^2} \int_{-\infty}^{\infty} \int_{\mathcal{V}} \chi(\vec{y}, \tau) G(\vec{y}, \tau | \vec{x}, t) d\vec{y} d\tau \\
&+ \int_{-\infty}^{\infty} \int_{\mathcal{S}} G(\vec{y}, \tau | \vec{x}, t) \left( \frac{\partial}{\partial n} + \frac{V_{sn}}{c_o^2} \frac{D}{D\tau} \right) \rho'(\vec{y}, \tau) d\mathcal{S}(\vec{y}) d\tau \\
&- \int_{-\infty}^{\infty} \int_{\mathcal{S}} \rho'(\vec{y}, \tau) \left( \frac{\partial}{\partial n} + \frac{V_{sn}}{c_o^2} \frac{D}{D\tau} \right) G(\vec{y}, \tau | \vec{x}, t) d\mathcal{S}(\vec{y}) d\tau. \quad (\text{B.8})
\end{aligned}$$

## APPENDIX C

### THE NUMERICAL RESULTS IN DIMENSIONAL FORM FOR SOUND PRESSURE LEVEL CALCULATIONS

The following sets of results were computed for sound pressure level (SPL) predictions at different angles around the cylinder. The physical parameters were chosen to match the parameters used in the experimental works of Revell *et al.* (1977) and Weier *et al.* (1998). Revell *et al.* (1977) measured the SPL at several angles around the cylinder for the Reynolds number value  $Re = 90,000$  where the microphone location was 128 cylinder diameters ( $128D$ ) away from the center of the cylinder. Weier *et al.* (1998) experimentally applied electromagnetic forces on the cylinder surface at the Reynolds number value  $Re = 760$ . Both experiments used the same size of cylinder diameter ( $D = 0.02$  m). Finally, the plots of the directivity patterns for overall sound pressure level with and without control are included in this appendix.



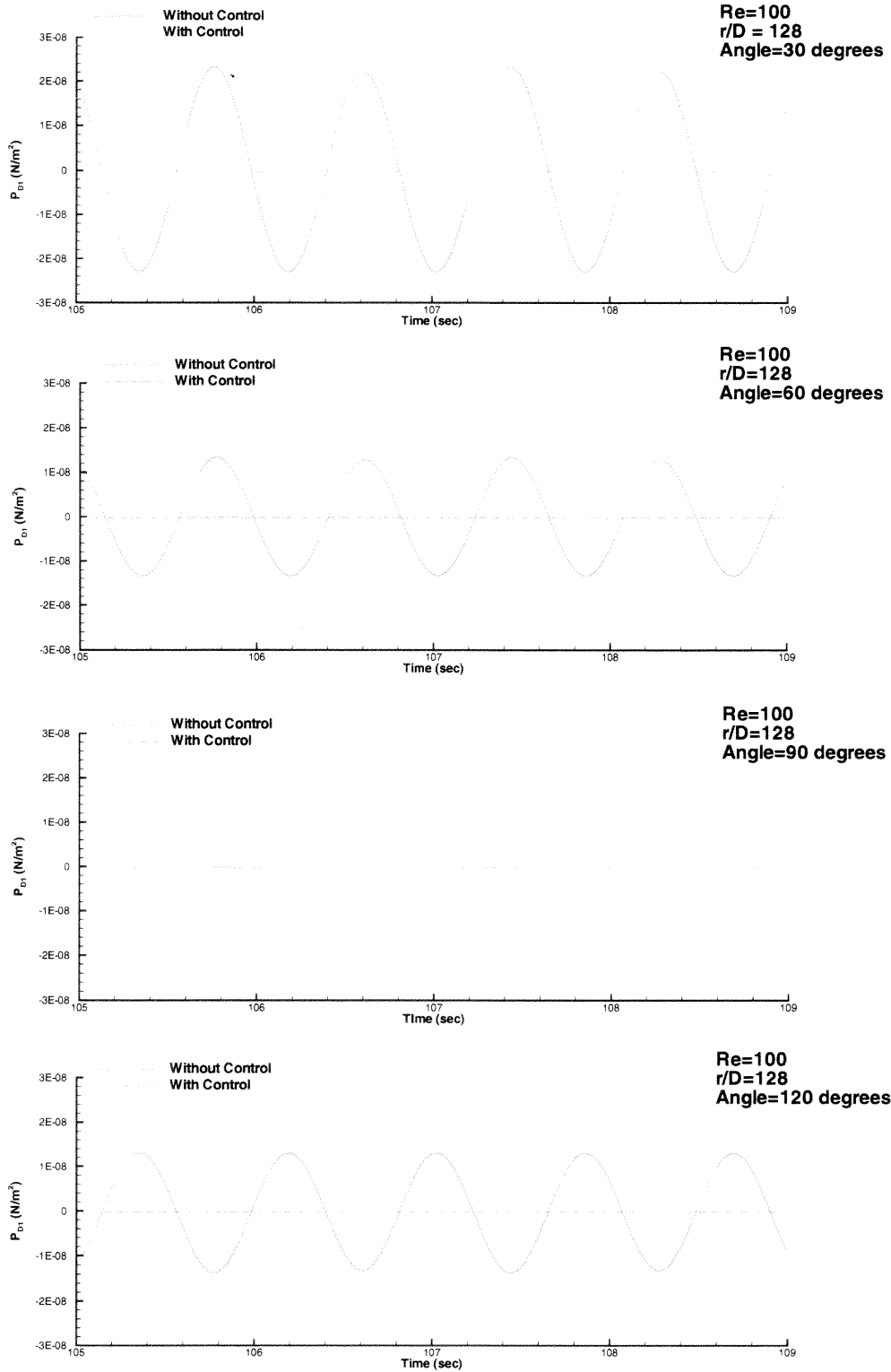


**Figure C.1** Acoustic Pressures generated by the drag dipole sources with and without control at the Reynolds number value  $Re = 100$ , Mach number  $M = 0.000215$ , and cylinder diameter  $D = 0.02$  m using the number of subintervals  $Mterms = 5000$  in the integral of Equation (3.50) for observer positions at  $128D$  away from the cylinder. Acoustic Pressure calculated from degree  $\theta = 0^\circ$  to  $\theta = 120^\circ$  with a degree step  $\delta\theta = 30^\circ$  where angle direction shown in Figure 2.1

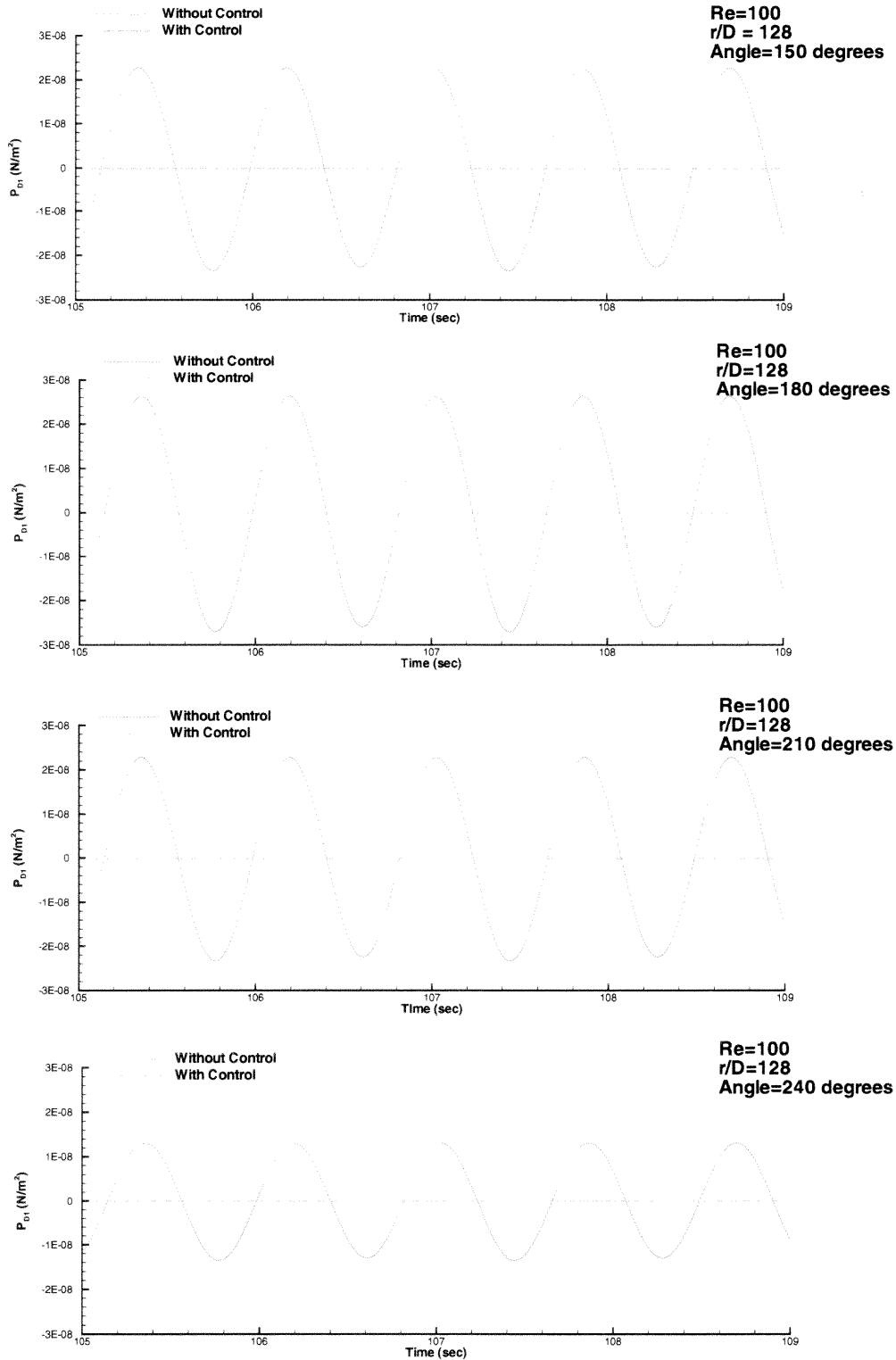


**Figure C.2** Acoustic Pressures generated by the drag dipole sources with and without control at the Reynolds number value  $Re = 100$ , Mach number  $M = 0.000215$ , and cylinder diameter  $D = 0.02$  m using the number of subintervals  $Mterms = 5000$  in the integral of Equation (3.50) for observer positions at  $128D$  away from the cylinder. Acoustic Pressure calculated from degree  $\theta = 150^\circ$  to  $\theta = 240^\circ$  with a degree step  $\delta\theta = 30^\circ$  where angle direction shown in Figure 2.1

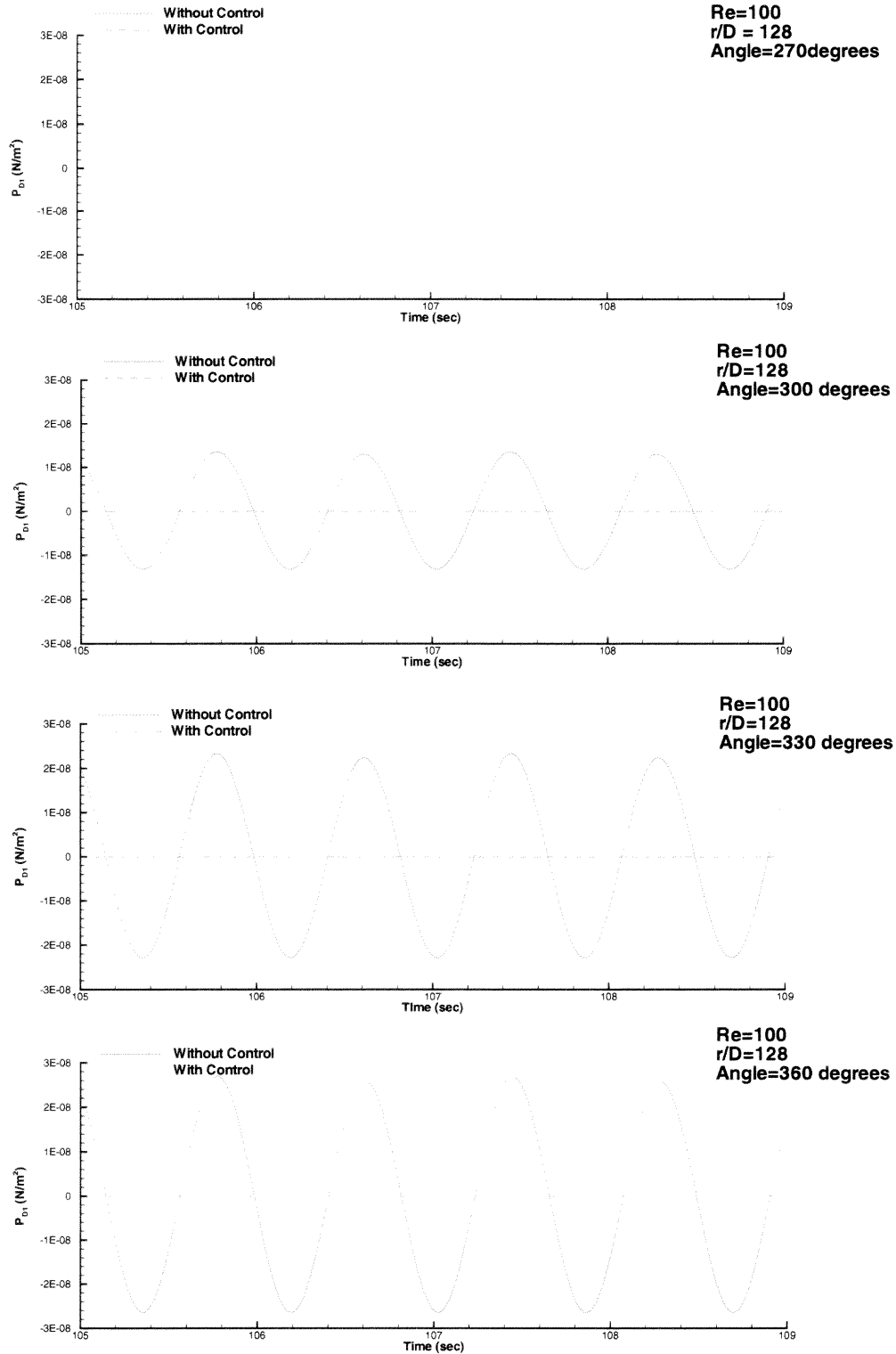


**Figure C.3** Acoustic Pressures generated by the drag dipole sources with and without control at the Reynolds number value  $Re = 100$ , Mach number  $M = 0.000215$ , and cylinder diameter  $D = 0.02$  m using the number of subintervals  $Mterms = 5000$  in the integral of Equation (3.50) for observer positions at  $128D$  away from the cylinder. Acoustic Pressure calculated from degree  $\theta = 270^\circ$  to  $\theta = 360^\circ$  with a degree step  $\delta\theta = 30^\circ$  where angle direction shown in Figure 2.1

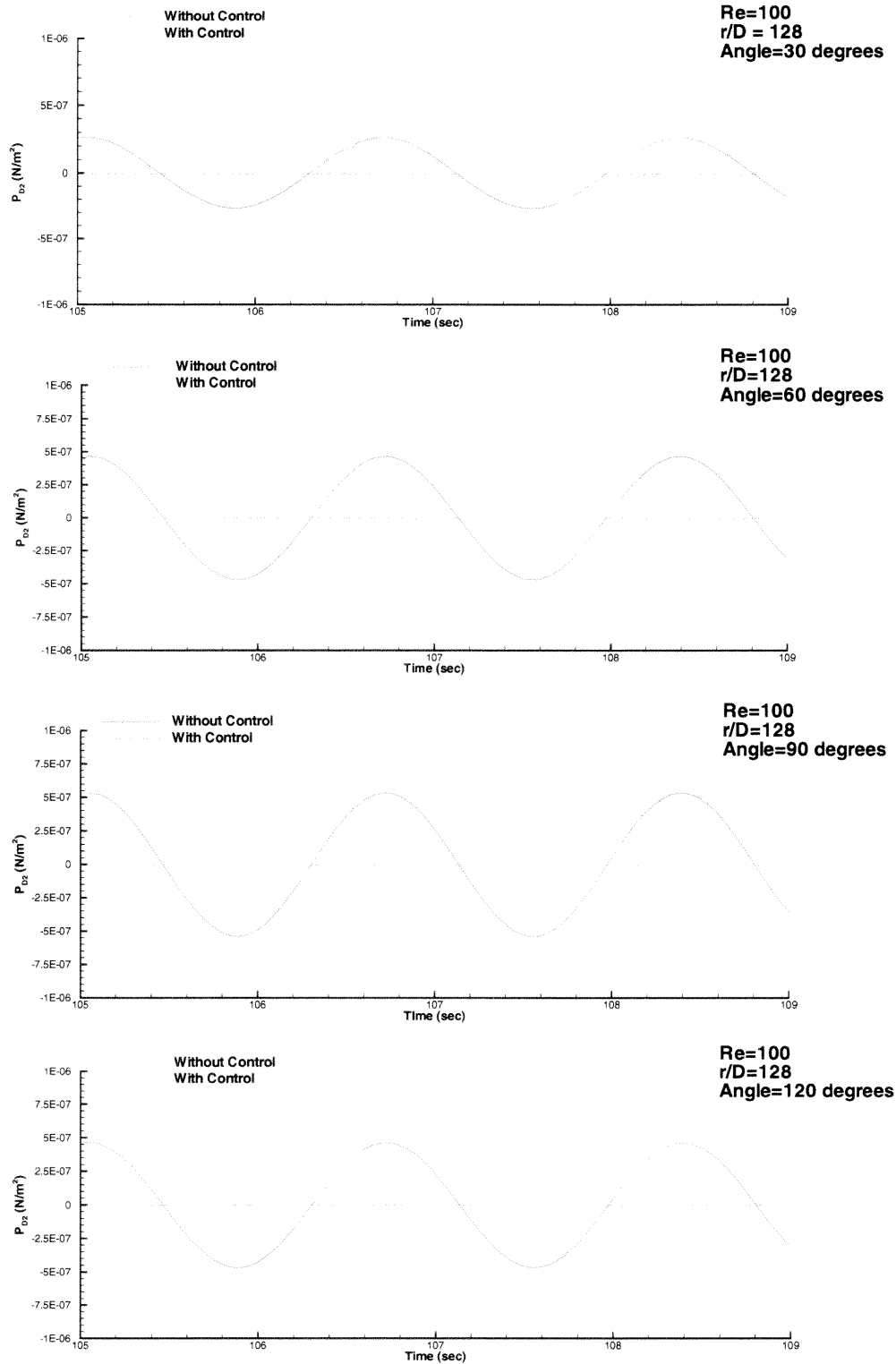


**Figure C.4** Acoustic Pressures generated by the lift dipole sources with and without control at the Reynolds number value  $Re = 100$ , Mach number  $M = 0.000215$ , and cylinder diameter  $D = 0.02$  m using the number of subintervals  $Mterms = 5000$  in the integral of Equation (3.50) for observer positions at  $128D$  away from the cylinder. Acoustic Pressure calculated from degree  $\theta = 0^\circ$  to  $\theta = 120^\circ$  with a degree step  $\delta\theta = 30^\circ$  where angle direction shown in Figure 2.1

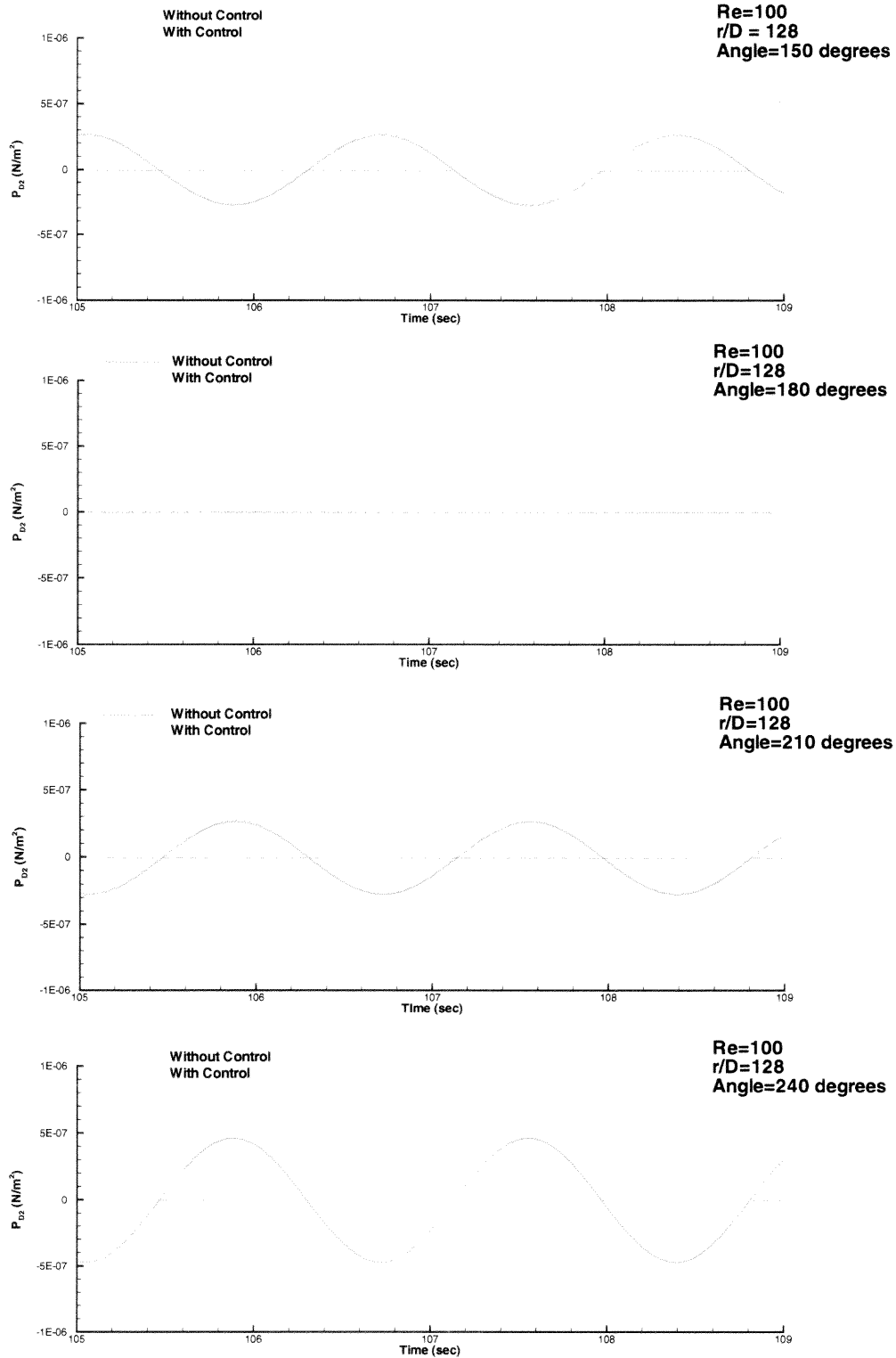


**Figure C.5** Acoustic Pressures generated by the lift dipole sources with and without control at the Reynolds number value  $Re = 100$ , Mach number  $M = 0.000215$ , and cylinder diameter  $D = 0.02$  m using the number of subintervals  $Mterms = 5000$  in the integral of Equation (3.50) for observer positions at  $128D$  away from the cylinder. Acoustic Pressure calculated from degree  $\theta = 150^\circ$  to  $\theta = 240^\circ$  with a degree step  $\delta\theta = 30^\circ$  where angle direction shown in Figure 2.1

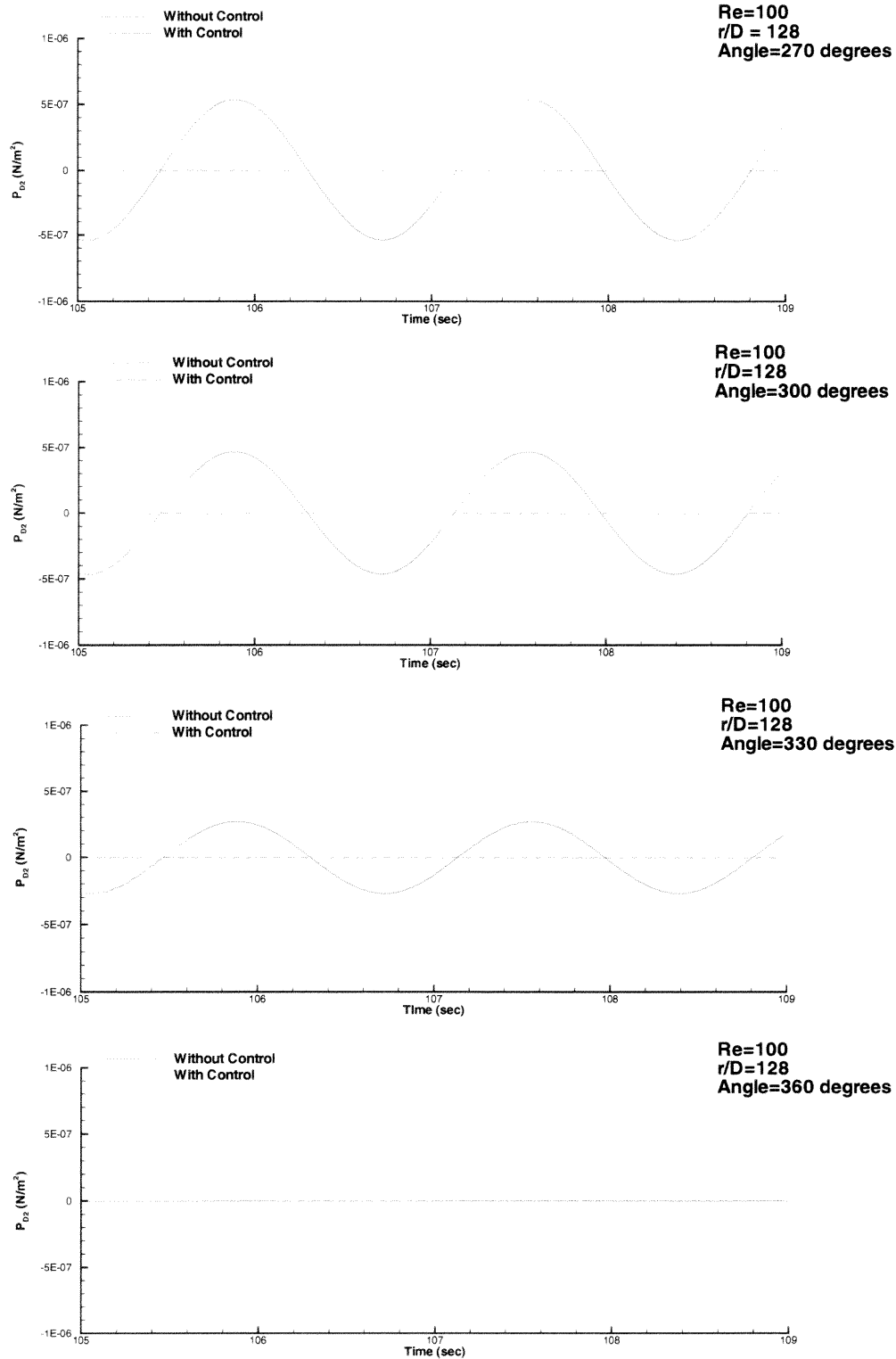


**Figure C.6** Acoustic Pressures generated by the lift dipole sources with and without control at the Reynolds number value  $Re = 100$ , Mach number  $M = 0.000215$ , and cylinder diameter  $D = 0.02$  m using the number of subintervals  $Mterms = 5000$  in the integral of Equation (3.50) for observer positions at  $128D$  away from the cylinder. Acoustic Pressure calculated from degree  $\theta = 270^\circ$  to  $\theta = 360^\circ$  with a degree step  $\delta\theta = 30^\circ$  where angle direction shown in Figure 2.1

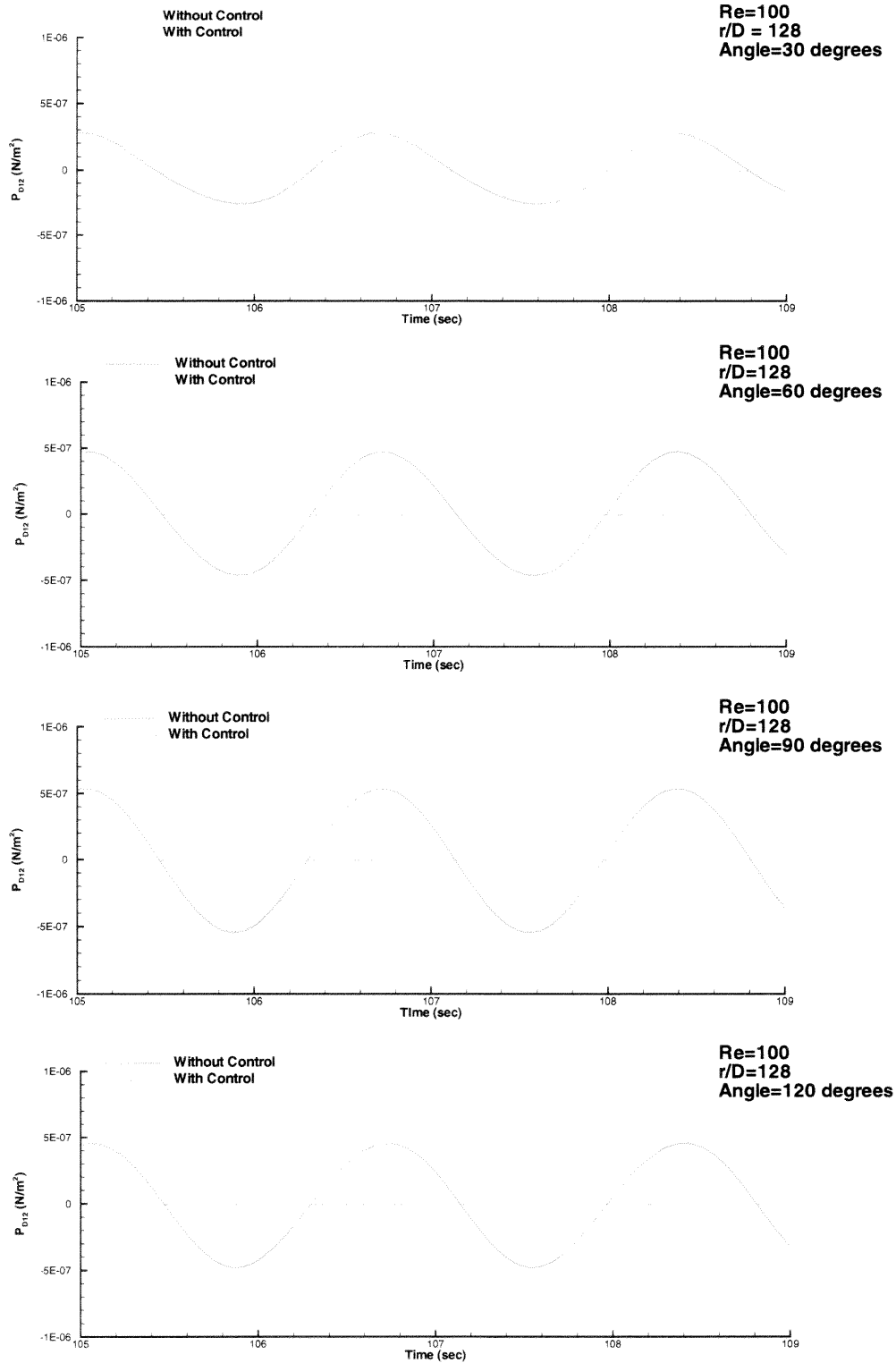


**Figure C.7** Acoustic Pressures generated by the total dipole sources with and without control at the Reynolds number value  $Re = 100$ , Mach number  $M = 0.000215$ , and cylinder diameter  $D = 0.02$  m using the number of subintervals  $Mterms = 5000$  in the integral of Equation (3.50) for observer positions at  $128D$  away from the cylinder. Acoustic Pressure calculated from degree  $\theta = 0^\circ$  to  $\theta = 120^\circ$  with a degree step  $\delta\theta = 30^\circ$  where angle direction shown in Figure 2.1

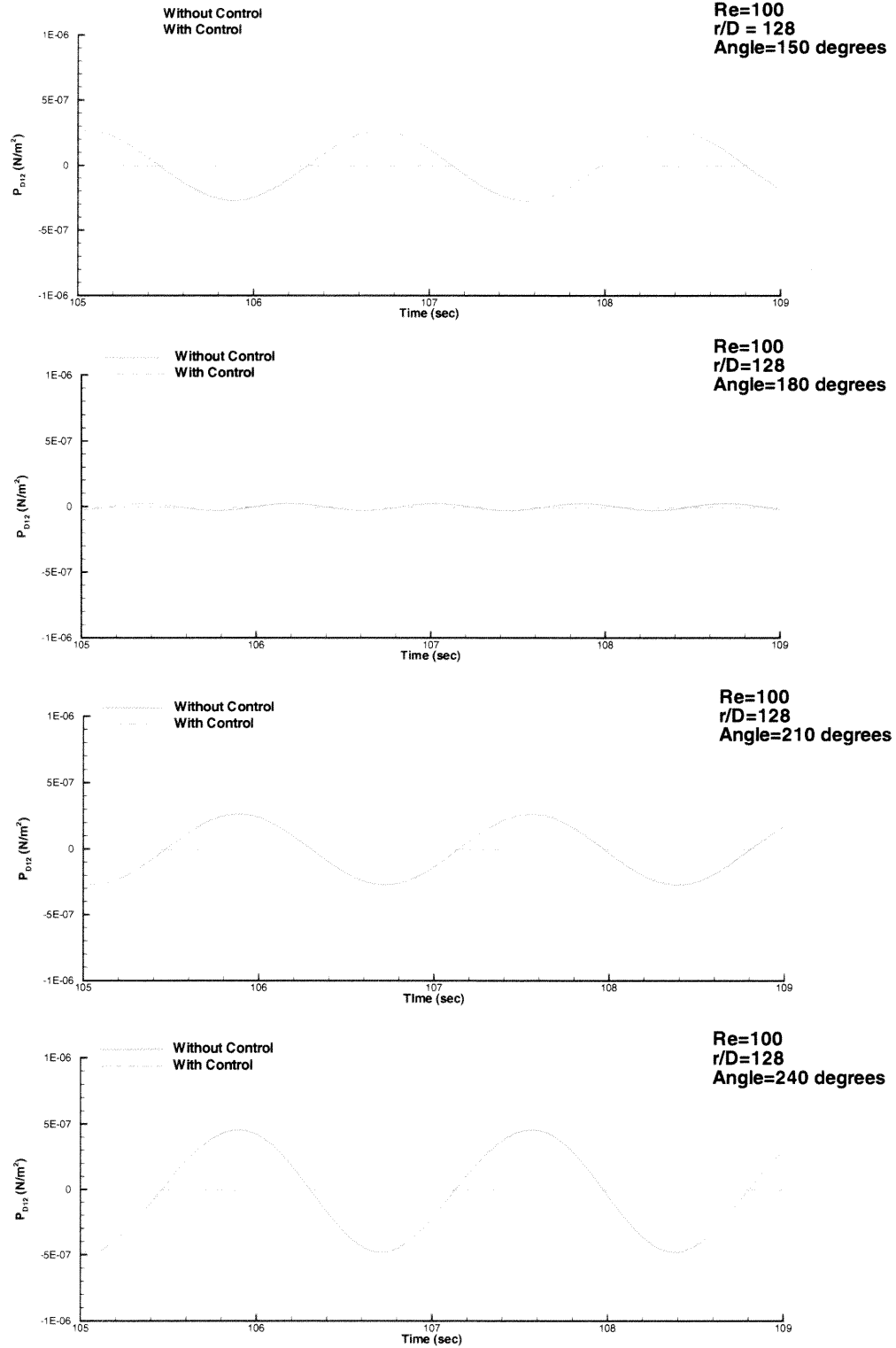


**Figure C.8** Acoustic Pressures generated by the total dipole sources with and without control at the Reynolds number value  $Re = 100$ , Mach number  $M = 0.000215$ , and cylinder diameter  $D = 0.02$  m using the number of subintervals  $Mterms = 5000$  in the integral of Equation (3.50) for observer positions at  $128D$  away from the cylinder. Acoustic Pressure calculated from degree  $\theta = 150^\circ$  to  $\theta = 240^\circ$  with a degree step  $\delta\theta = 30^\circ$  where angle direction shown in Figure 2.1



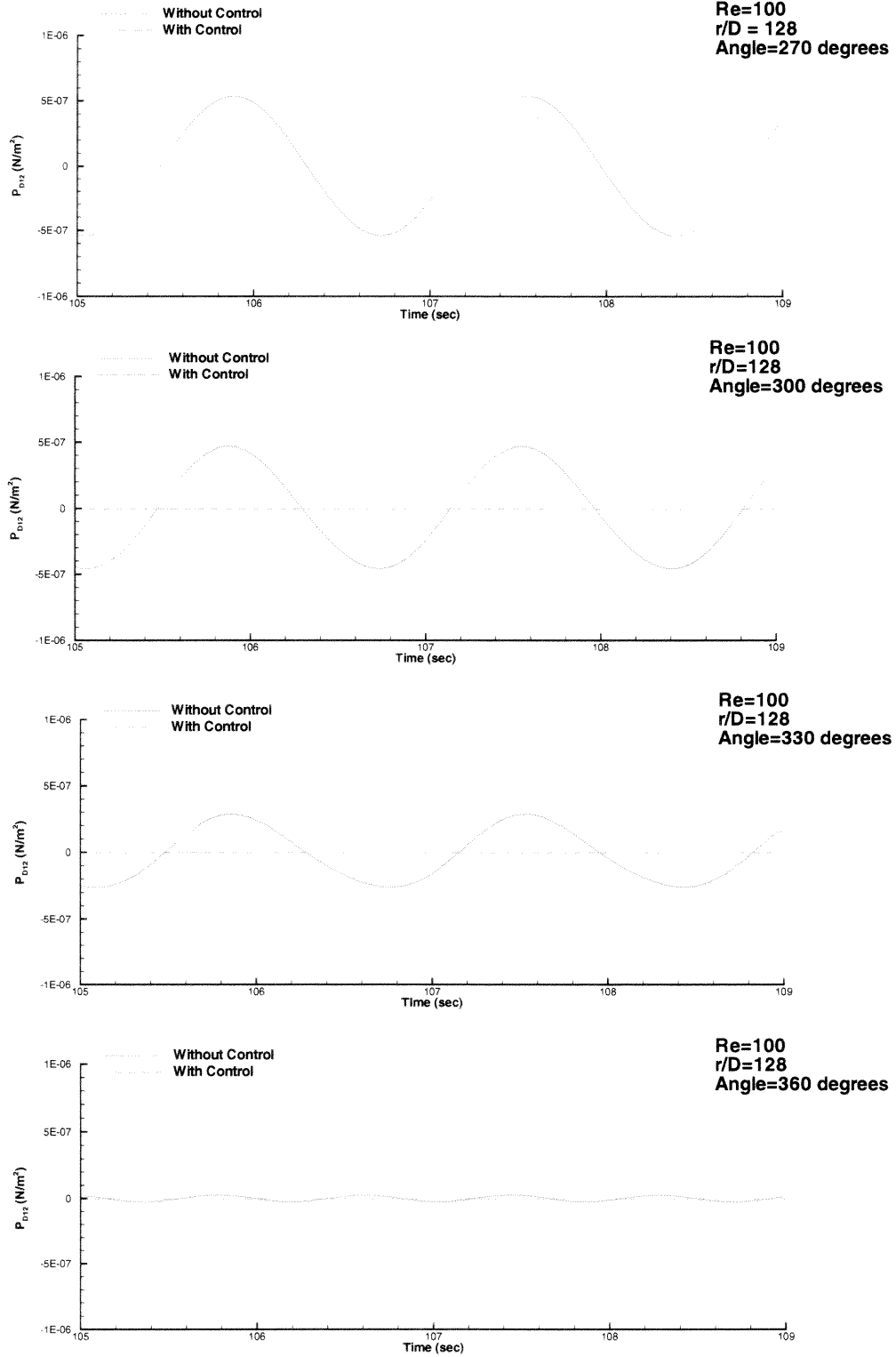


**Figure C.9** Acoustic Pressures generated by the total dipole sources with and without control at the Reynolds number value  $Re = 100$ , Mach number  $M = 0.000215$ , and cylinder diameter  $D = 0.02$  m using the number of subintervals  $Mterms = 5000$  in the integral of Equation (3.50) for observer positions at  $128D$  away from the cylinder. Acoustic Pressure calculated from degree  $\theta = 270^\circ$  to  $\theta = 360^\circ$  with a degree step  $\delta\theta = 30^\circ$  where angle direction shown in Figure 2.1

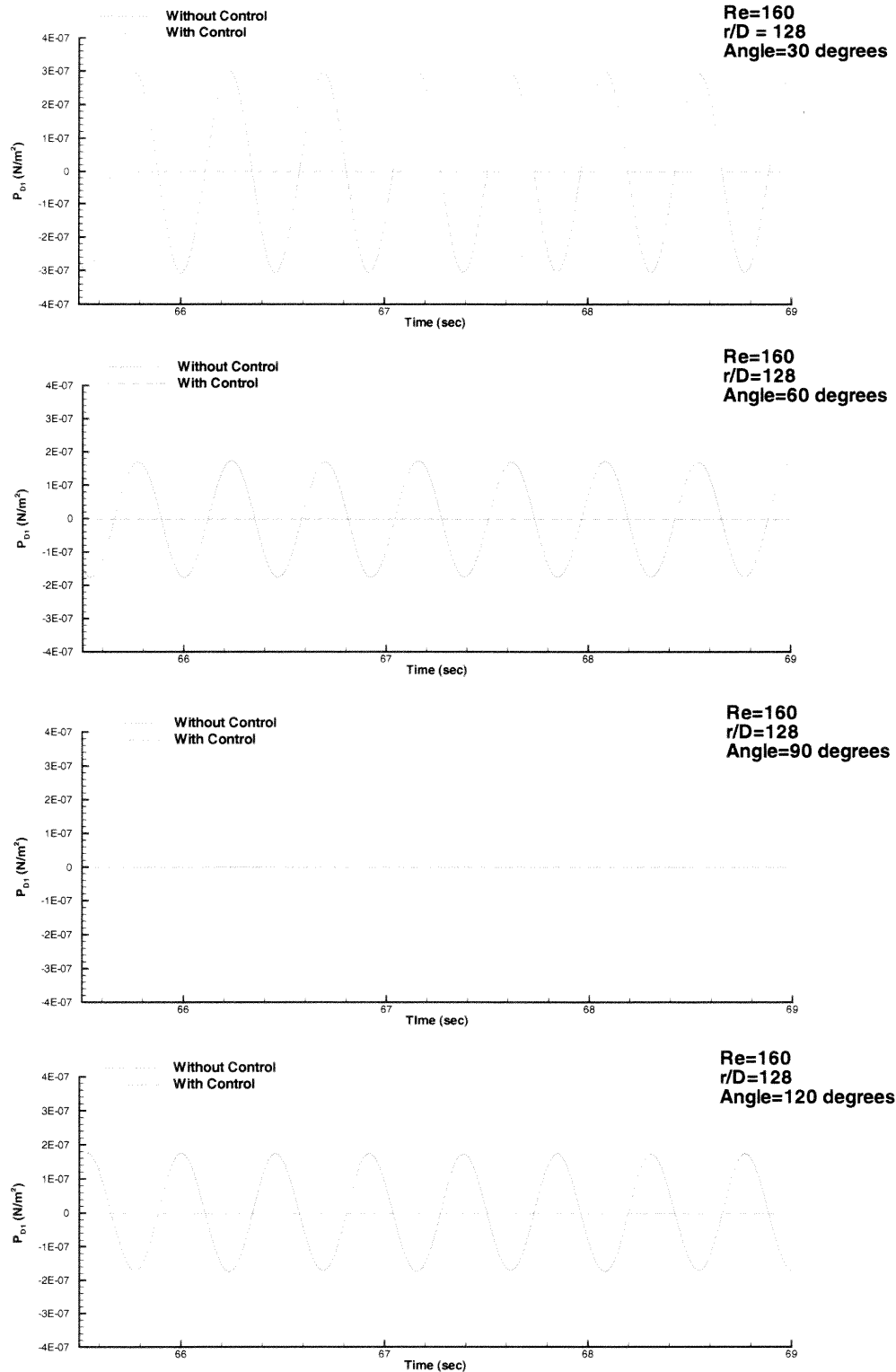


**Figure C.10** Acoustic Pressures generated by the drag dipole sources with and without control at the Reynolds number value  $Re = 160$ , Mach number  $M = 0.000342$ , and cylinder diameter  $D = 0.02$  m using the number of subintervals  $Mterms = 5000$  in the integral of Equation (3.50) for observer positions at  $128D$  away from the cylinder. Acoustic Pressure calculated from degree  $\theta = 0^\circ$  to  $\theta = 120^\circ$  with a degree step  $\delta\theta = 30^\circ$  where angle direction shown in Figure 2.1

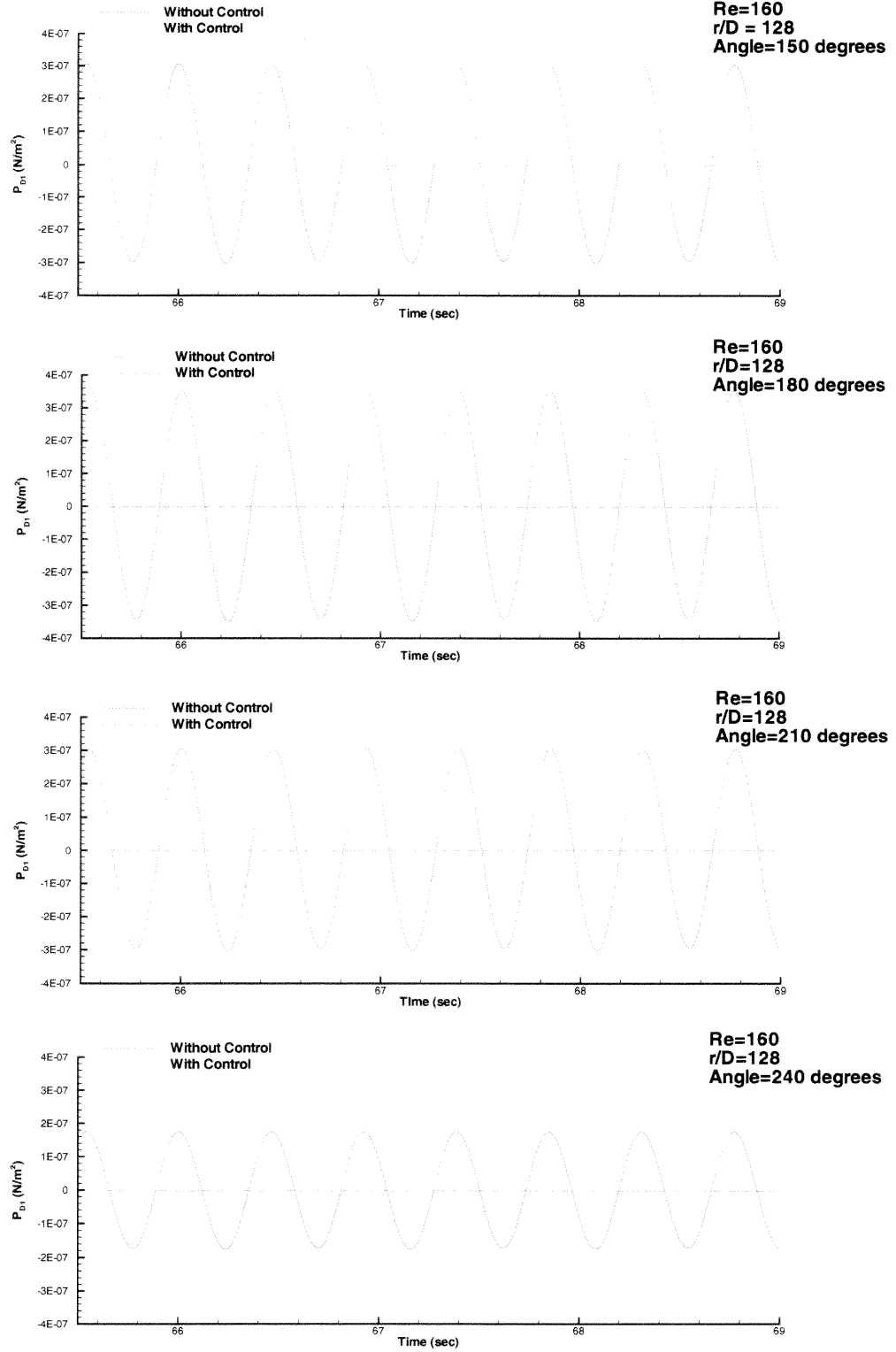


**Figure C.11** Acoustic Pressures generated by the drag dipole sources with and without control at the Reynolds number value  $Re = 160$ , Mach number  $M = 0.000342$ , and cylinder diameter  $D = 0.02$  m using the number of subintervals  $Mterms = 5000$  in the integral of Equation (3.50) for observer positions at  $128D$  away from the cylinder. Acoustic Pressure calculated from degree  $\theta = 150^\circ$  to  $\theta = 240^\circ$  with a degree step  $\delta\theta = 30^\circ$  where angle direction shown in Figure 2.1

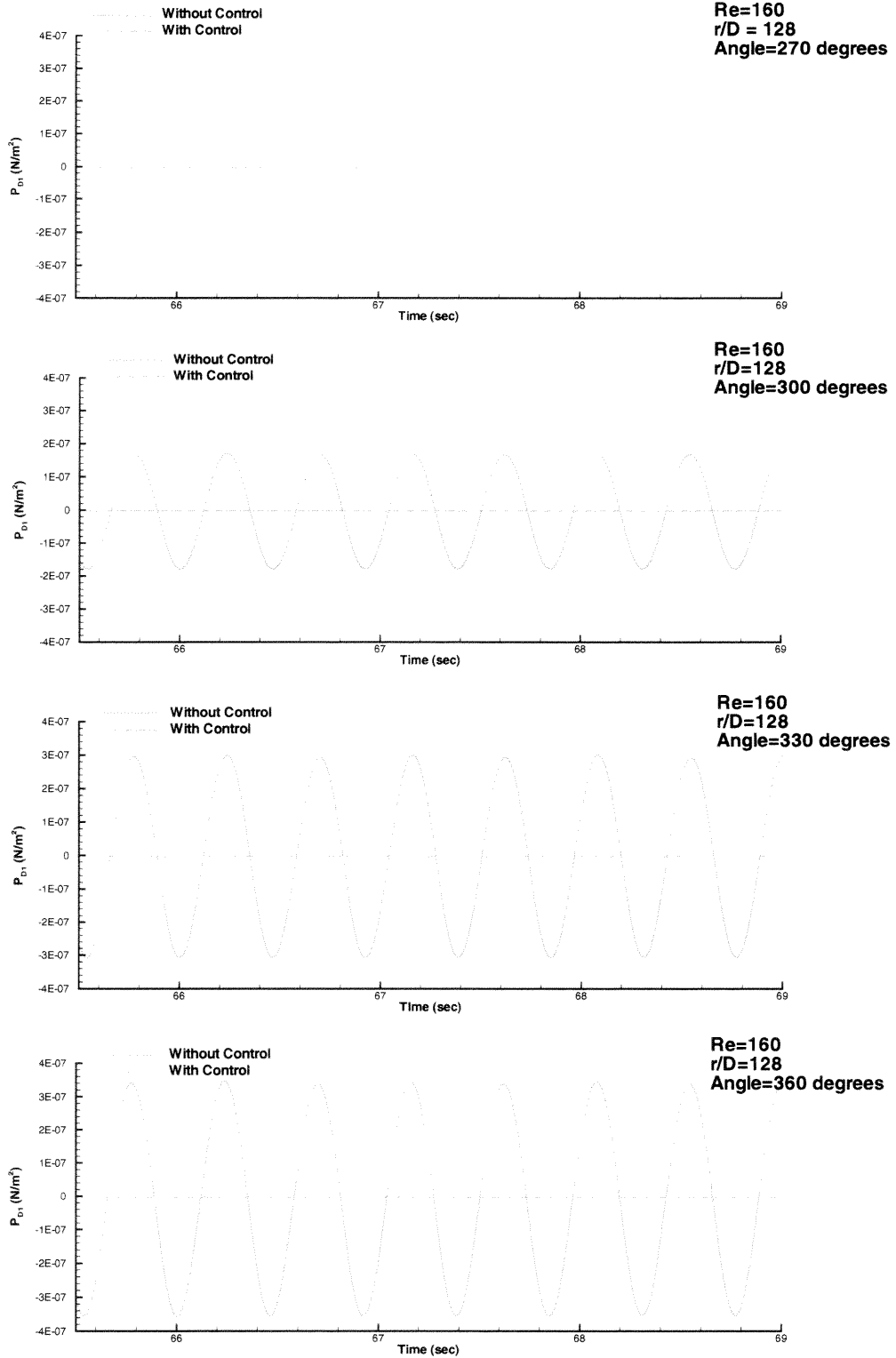


**Figure C.12** Acoustic Pressures generated by the drag dipole sources with and without control at the Reynolds number value  $Re = 160$ , Mach number  $M = 0.000342$ , and cylinder diameter  $D = 0.02$  m using the number of subintervals  $Mterms = 5000$  in the integral of Equation (3.50) for observer positions at 128D away from the cylinder. Acoustic Pressure calculated from degree  $\theta = 270^\circ$  to  $\theta = 360^\circ$  with a degree step  $\delta\theta = 30^\circ$  where angle direction shown in Figure 2.1

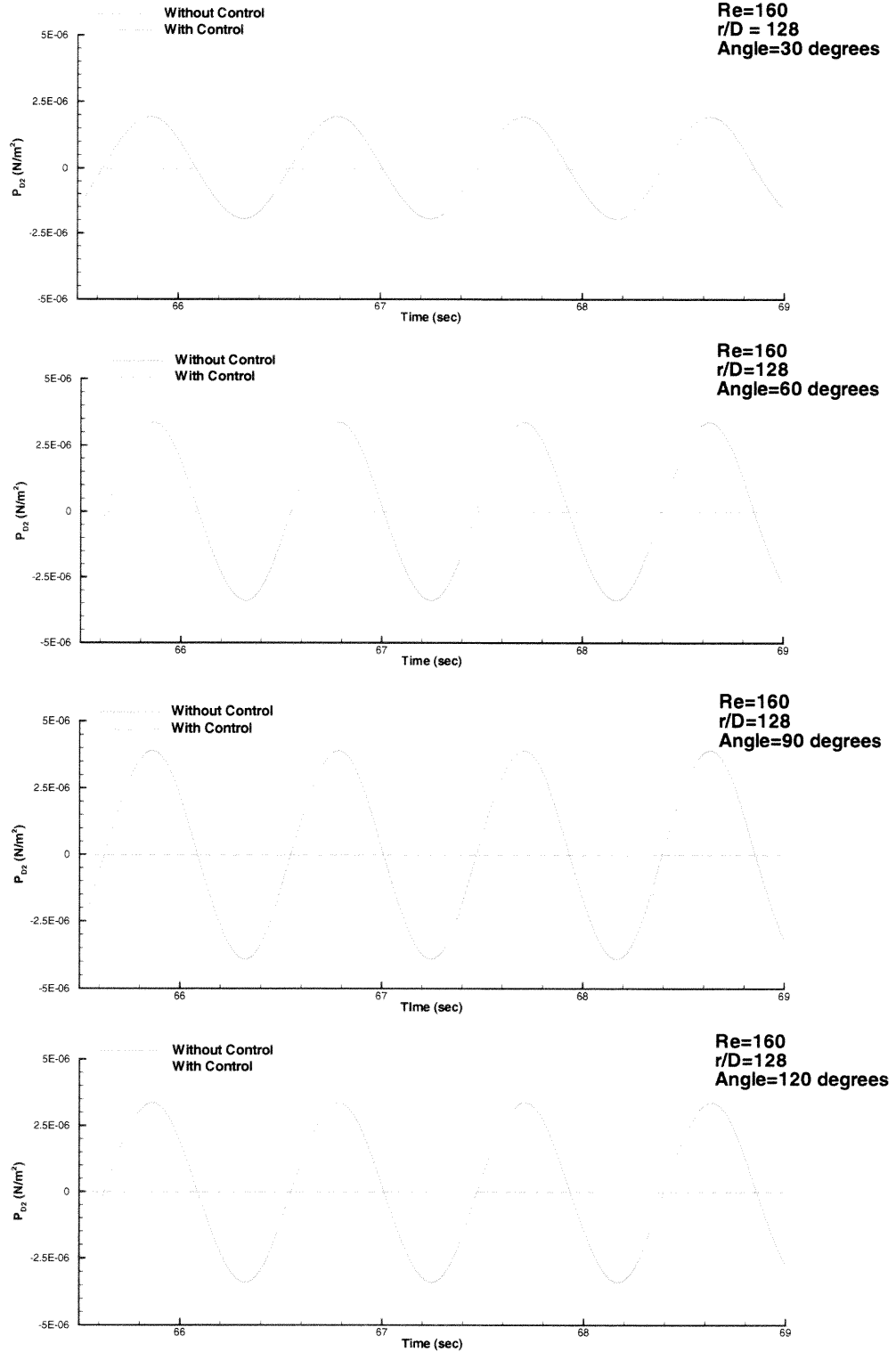


**Figure C.13** Acoustic Pressures generated by the lift dipole sources with and without control at the Reynolds number value  $Re = 160$ , Mach number  $M = 0.000342$ , and cylinder diameter  $D = 0.02$  m using the number of subintervals  $Mterms = 5000$  in the integral of Equation (3.50) for observer positions at  $128D$  away from the cylinder. Acoustic Pressure calculated from degree  $\theta = 0^\circ$  to  $\theta = 120^\circ$  with a degree step  $\delta\theta = 30^\circ$  where angle direction shown in Figure 2.1

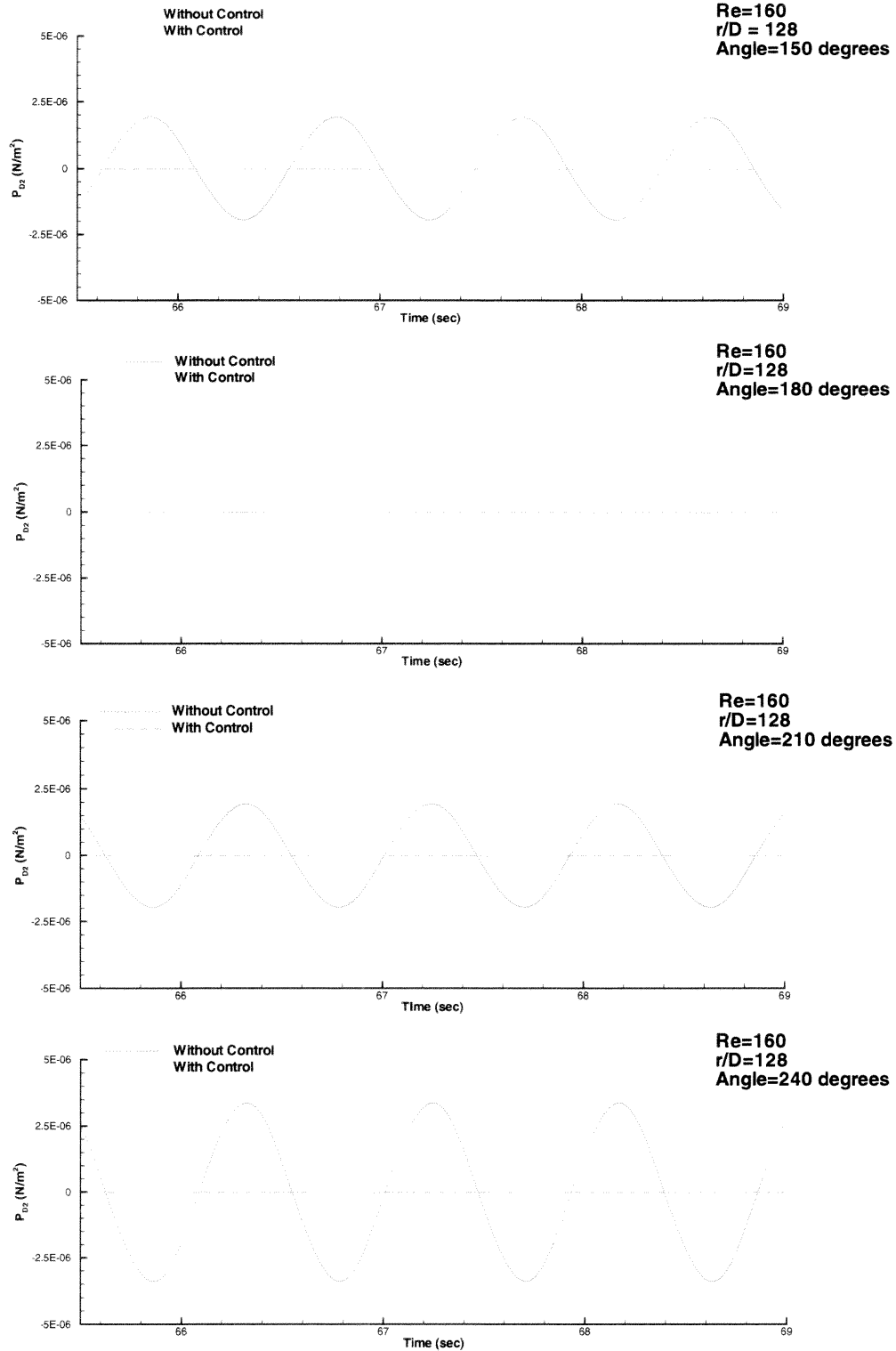


**Figure C.14** Acoustic Pressures generated by the lift dipole sources with and without control at the Reynolds number value  $Re = 160$ , Mach number  $M = 0.000342$ , and cylinder diameter  $D = 0.02$  m using the number of subintervals  $Mterms = 5000$  in the integral of Equation (3.50) for observer positions at  $128D$  away from the cylinder. Acoustic Pressure calculated from degree  $\theta = 150^\circ$  to  $\theta = 240^\circ$  with a degree step  $\delta\theta = 30^\circ$  where angle direction shown in Figure 2.1

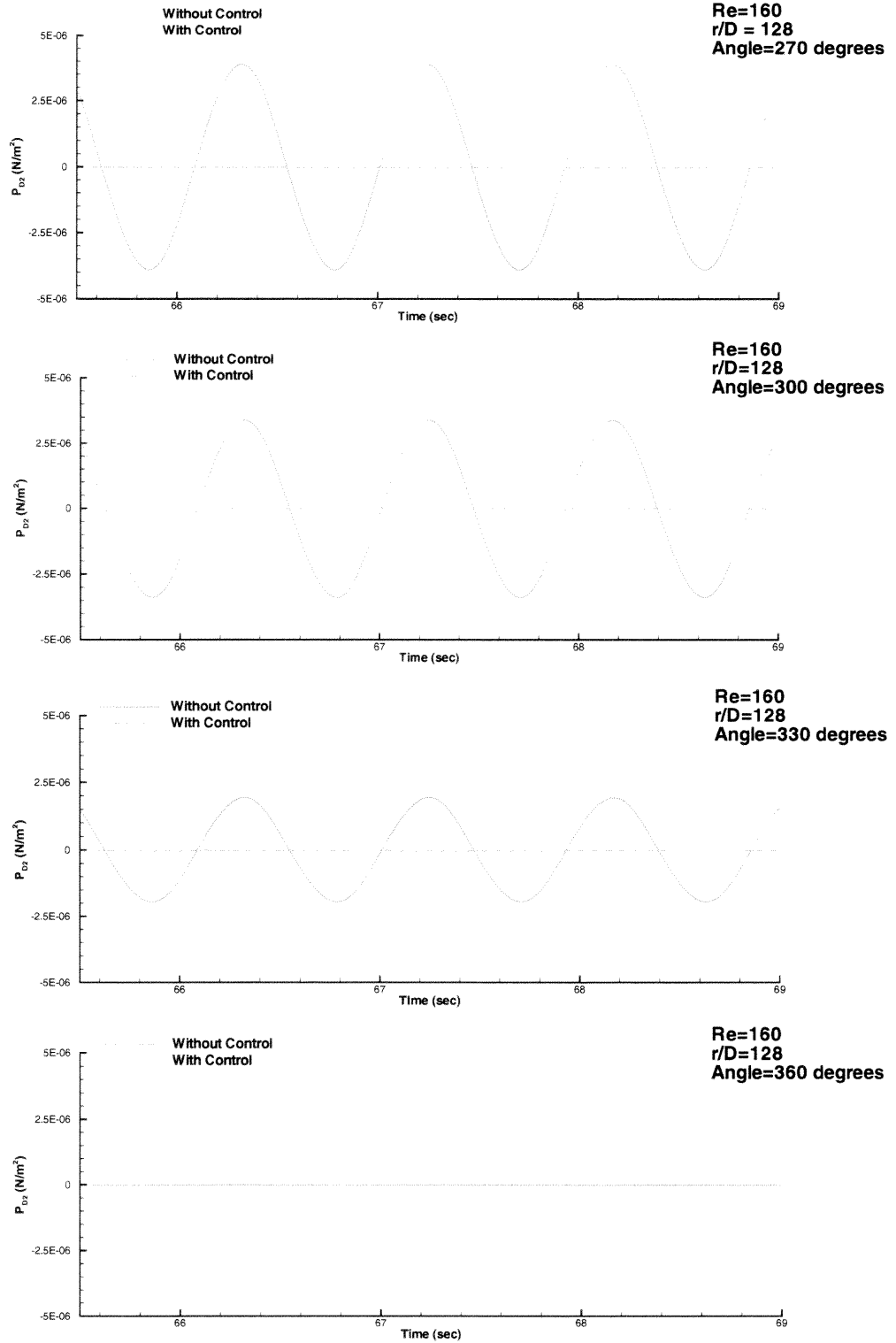


**Figure C.15** Acoustic Pressures generated by the lift dipole sources with and without control at the Reynolds number value  $Re = 160$ , Mach number  $M = 0.000342$ , and cylinder diameter  $D = 0.02$  m using the number of subintervals  $Mterms = 5000$  in the integral of Equation (3.50) for observer positions at  $128D$  away from the cylinder. Acoustic Pressure calculated from degree  $\theta = 270^\circ$  to  $\theta = 360^\circ$  with a degree step  $\delta\theta = 30^\circ$  where angle direction shown in Figure 2.1

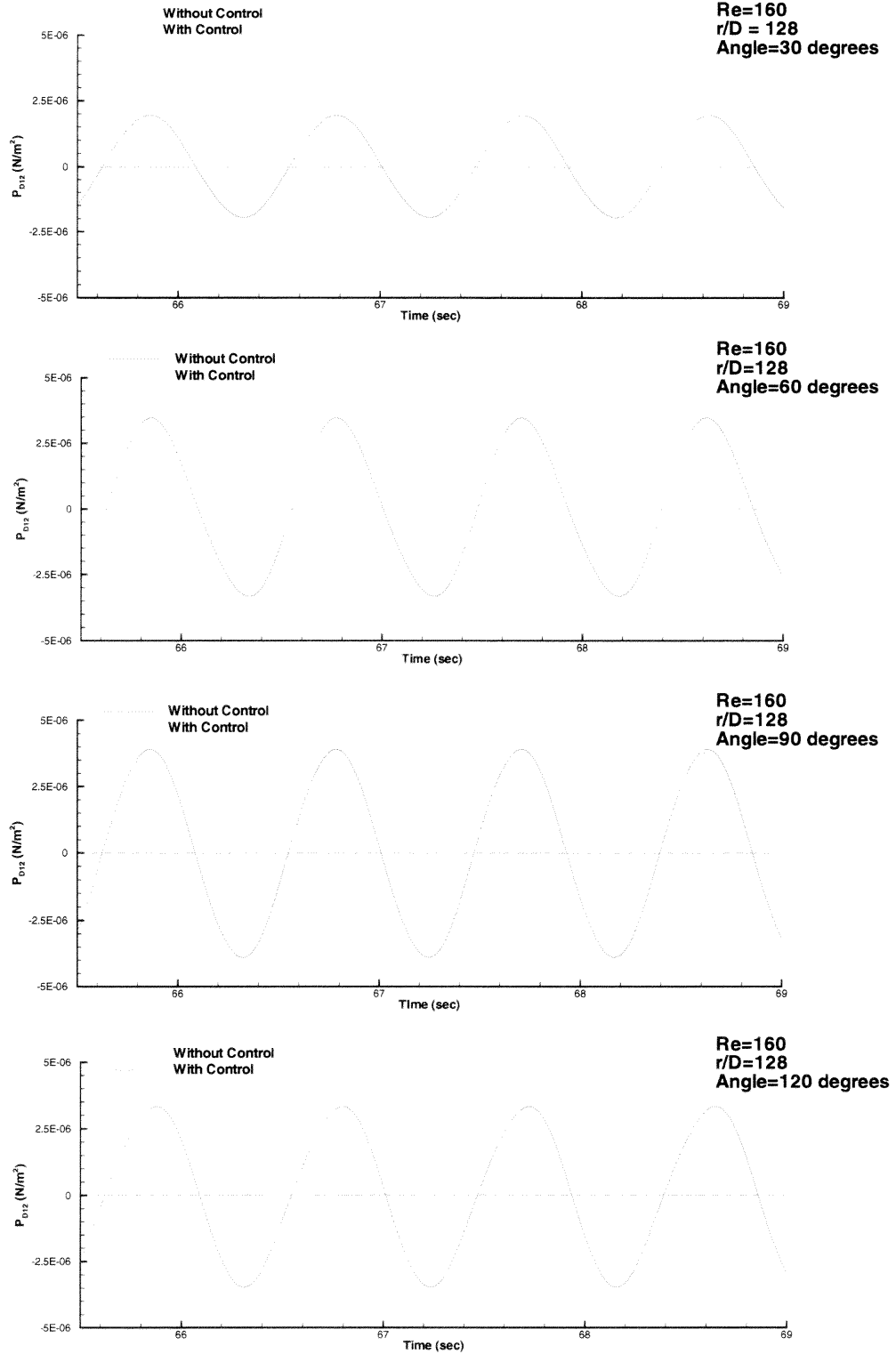


**Figure C.16** Acoustic Pressures generated by the total dipole sources with and without control at the Reynolds number value  $Re = 160$ , Mach number  $M = 0.000342$ , and cylinder diameter  $D = 0.02$  m using the number of subintervals  $Mterms = 5000$  in the integral of Equation (3.50) for observer positions at  $128D$  away from the cylinder. Acoustic Pressure calculated from degree  $\theta = 0^\circ$  to  $\theta = 120^\circ$  with a degree step  $\delta\theta = 30^\circ$  where angle direction shown in Figure 2.1



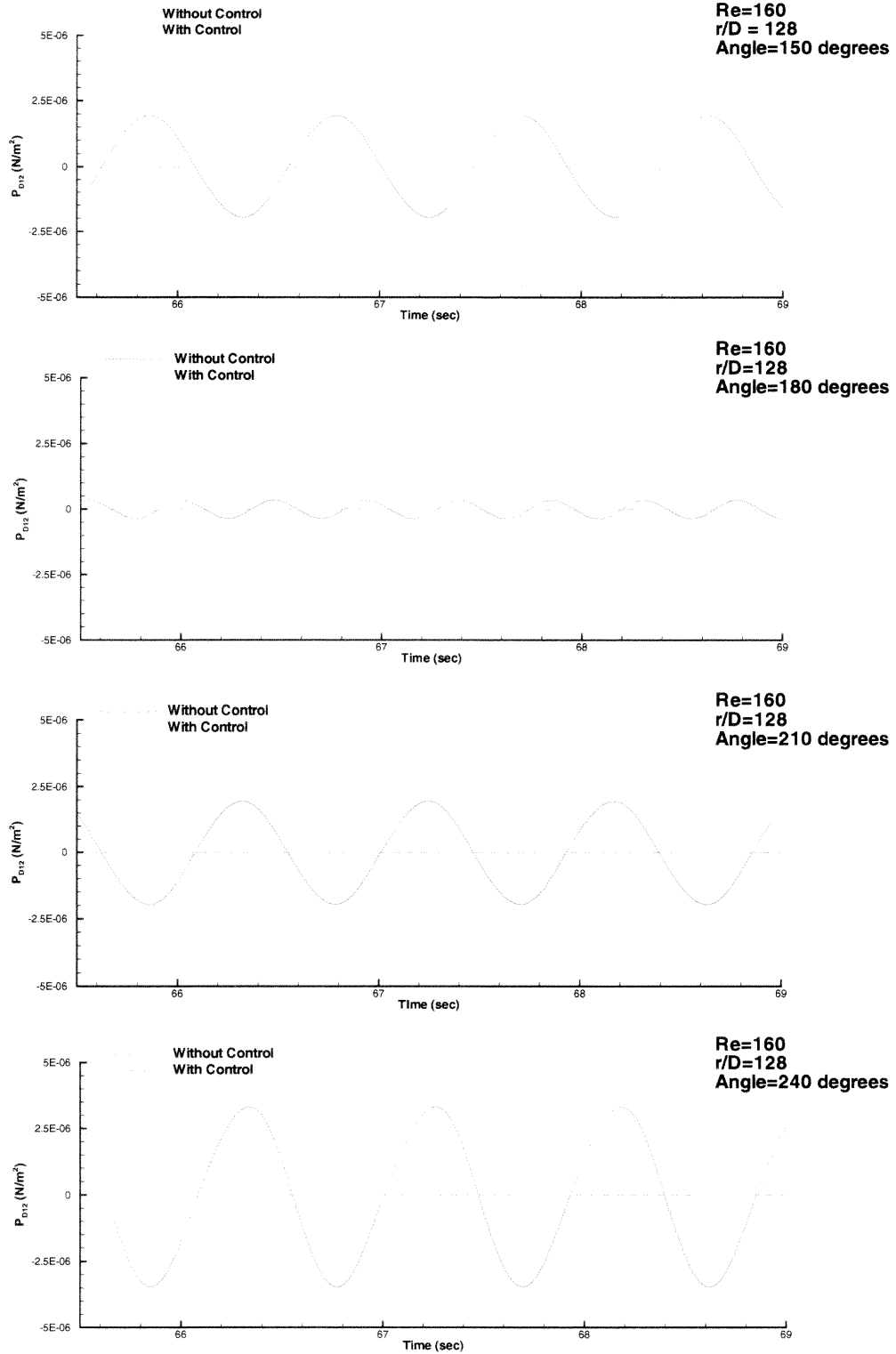


**Figure C.17** Acoustic Pressures generated by the total dipole sources with and without control at the Reynolds number value  $Re = 160$ , Mach number  $M = 0.000342$ , and cylinder diameter  $D = 0.02$  m using the number of subintervals  $Mterms = 5000$  in the integral of Equation (3.50) for observer positions at  $128D$  away from the cylinder. Acoustic Pressure calculated from degree  $\theta = 150^\circ$  to  $\theta = 240^\circ$  with a degree step  $\delta\theta = 30^\circ$  where angle direction shown in Figure 2.1

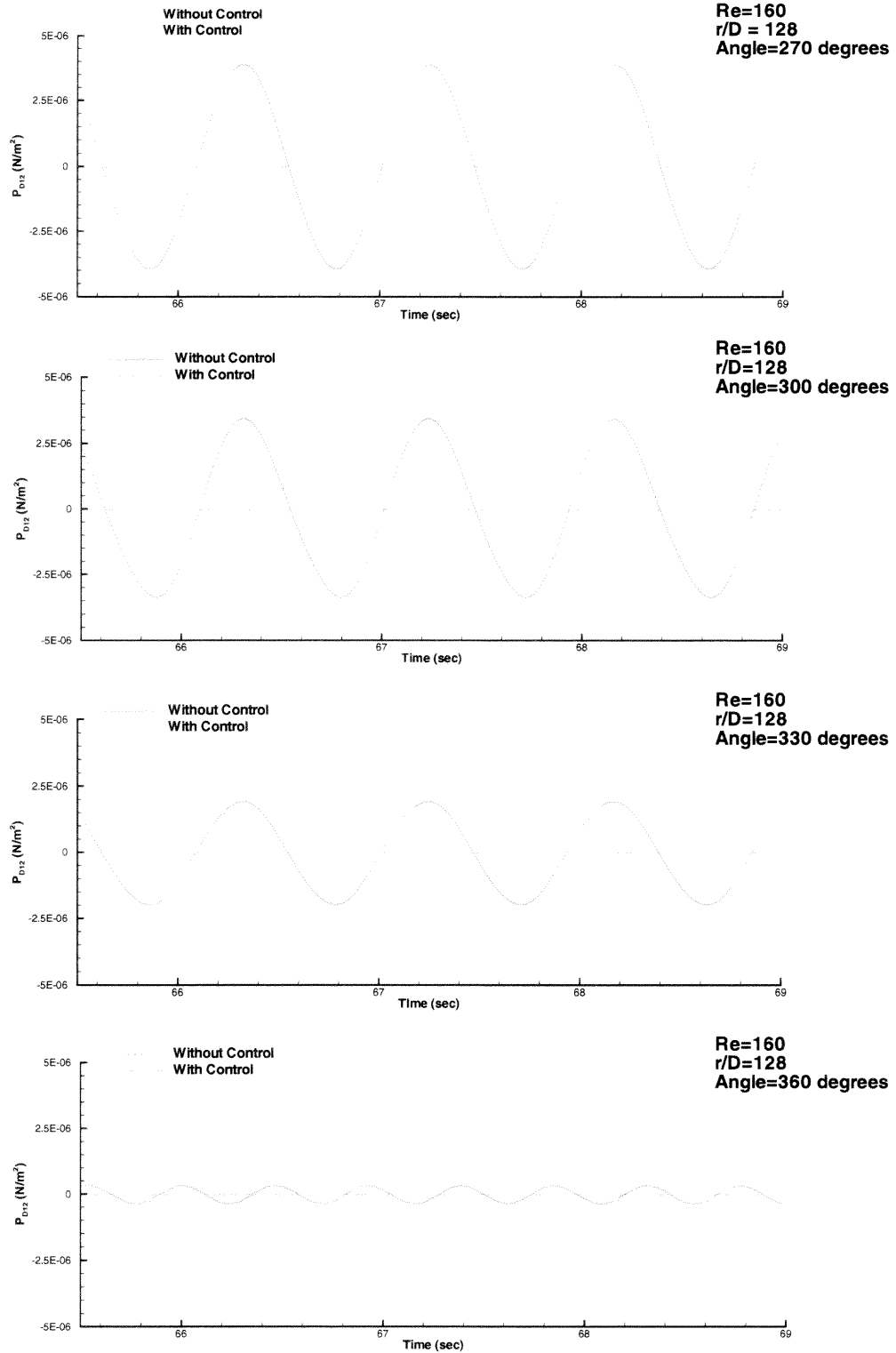


**Figure C.18** Acoustic Pressures generated by the total dipole sources with and without control at the Reynolds number value  $Re = 160$ , Mach number  $M = 0.000342$ , and cylinder diameter  $D = 0.02$  m using the number of subintervals  $M_{terms} = 5000$  in the integral of Equation (3.50) for observer positions at  $128D$  away from the cylinder. Acoustic Pressure calculated from degree  $\theta = 270^\circ$  to  $\theta = 360^\circ$  with a degree step  $\delta\theta = 30^\circ$  where angle direction shown in Figure 2.1

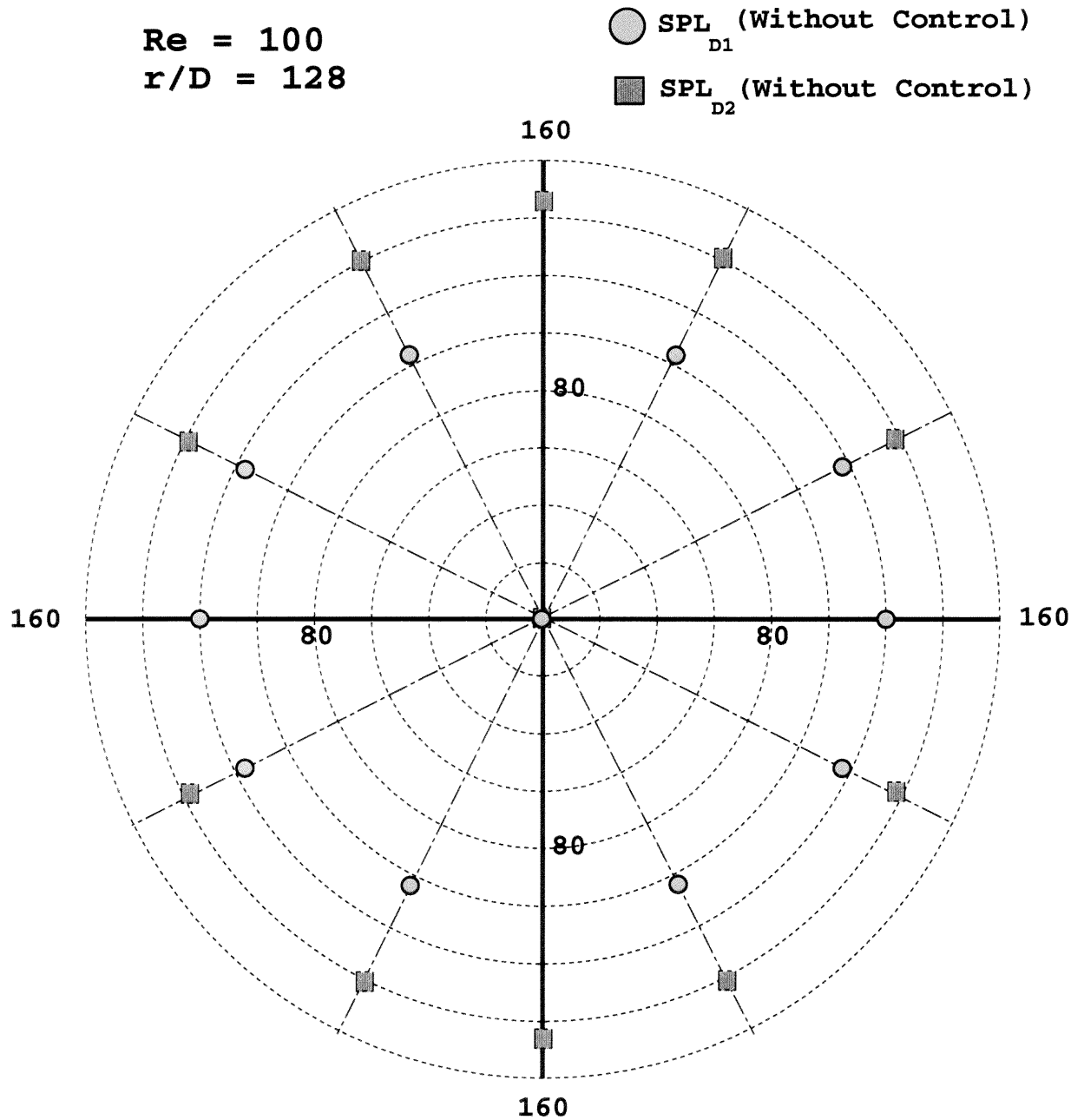


**Figure C.19** Directivity patterns for overall sound pressure level without control generated by the drag dipole ( $SPL_{D1}$ ) and lift dipole ( $SPL_{D2}$ ) at the Reynolds number  $Re = 100$ , Mach number  $M = 0.000215$ , and cylinder diameter  $D = 0.02$  m. The observers locations are at  $128D$  away from the cylinder. Axes units are decibels (dB, re:  $20 \times 10^{-15}$  )

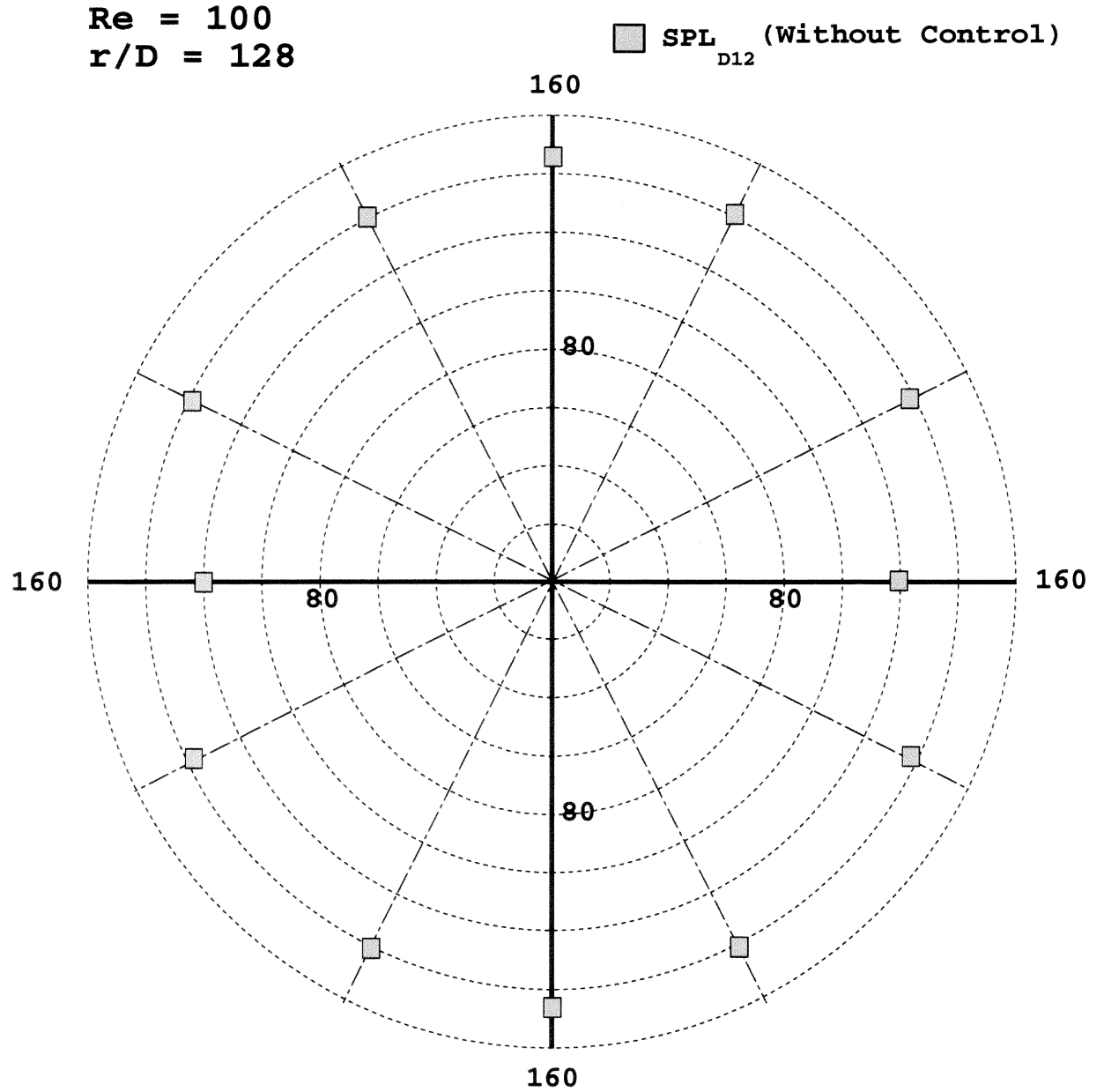


**Figure C.20** Directivity patterns for overall sound pressure level without control generated by the total dipole ( $SPL_{D12}$ ) at the Reynolds number  $Re = 100$ , Mach number  $M = 0.000215$ , and cylinder diameter  $D = 0.02$  m. The observers locations are at  $128D$  away from the cylinder. Axes units are decibels (dB, re:  $20 \times 10^{-15}$ )

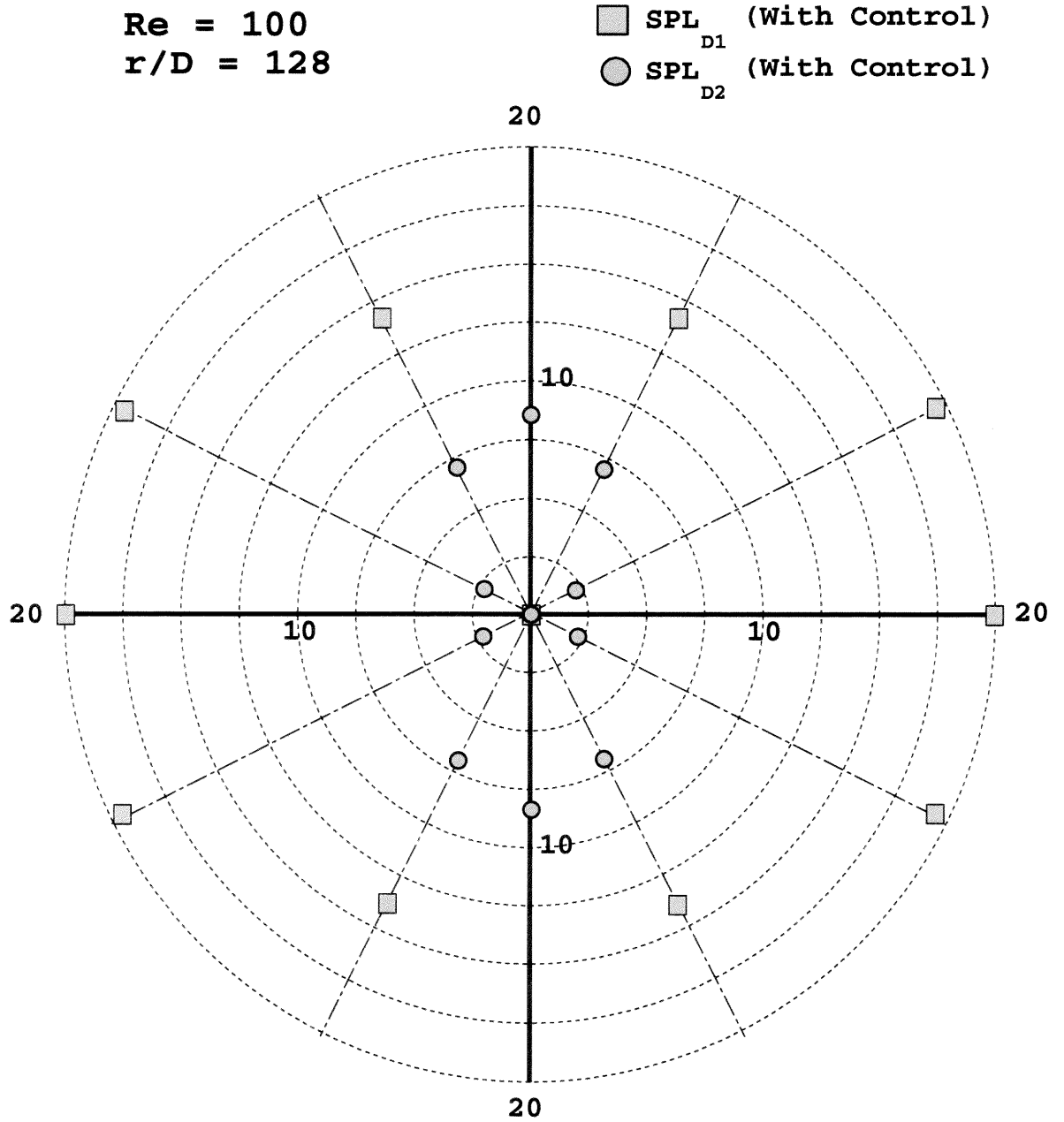


**Figure C.21** Directivity patterns for overall sound pressure level with control generated by the drag dipole ( $SPL_{D1}$ ) and lift dipole ( $SPL_{D2}$ ) at the Reynolds number  $Re = 100$ , Mach number  $M = 0.000215$ , and cylinder diameter  $D = 0.02$  m. The observers locations are at  $128D$  away from the cylinder. Axes units are decibels (dB, re:  $20 \times 10^{-15}$ )

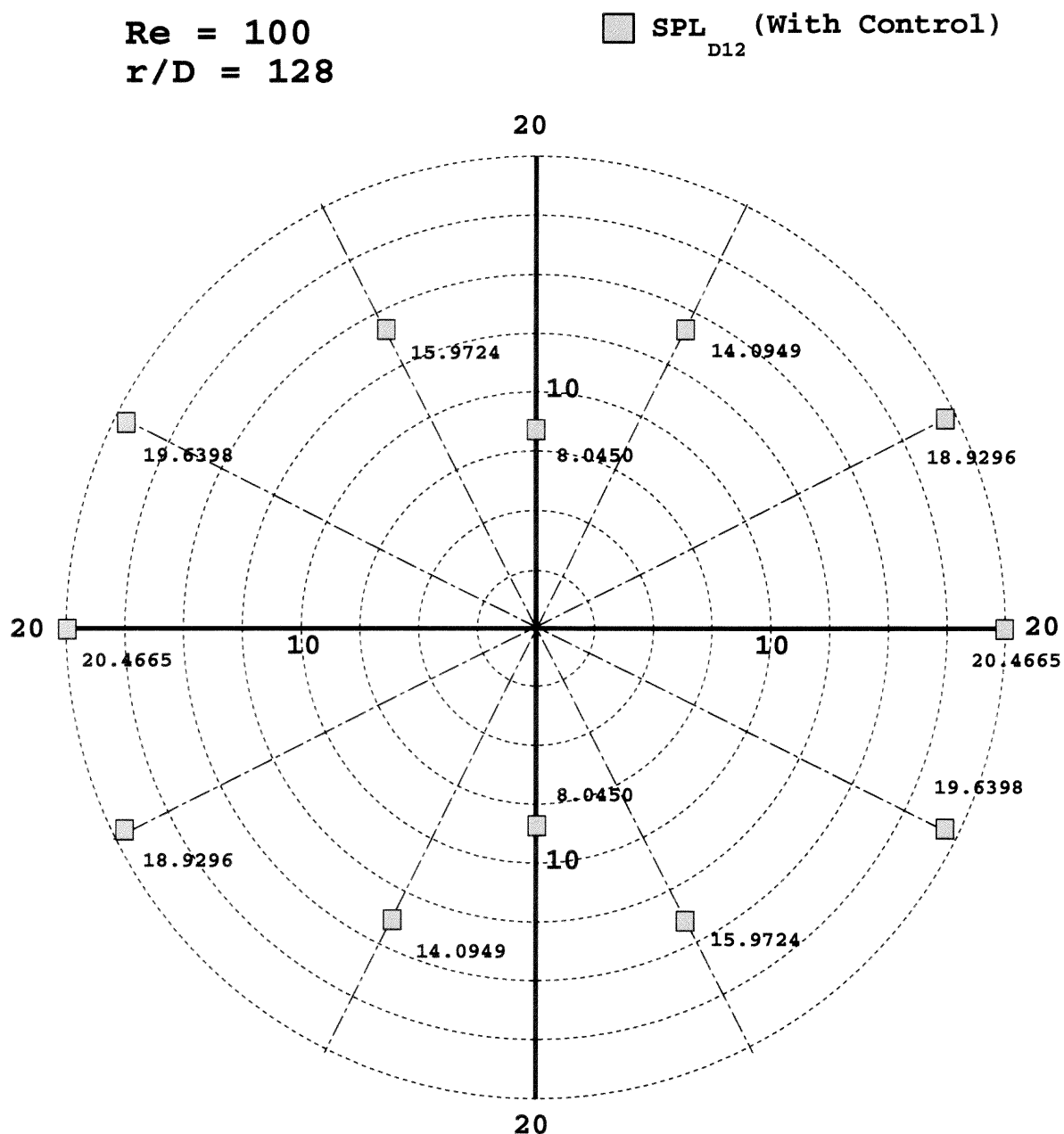


**Figure C.22** Directivity patterns for overall sound pressure level with control generated by the total dipole ( $SPL_{D12}$ ) at the Reynolds number  $Re = 100$ , Mach number  $M = 0.000215$ , and cylinder diameter  $D = 0.02$  m. The observers locations are at  $128D$  away from the cylinder. Axes units are decibels (dB, re:  $20 \times 10^{-15}$  )

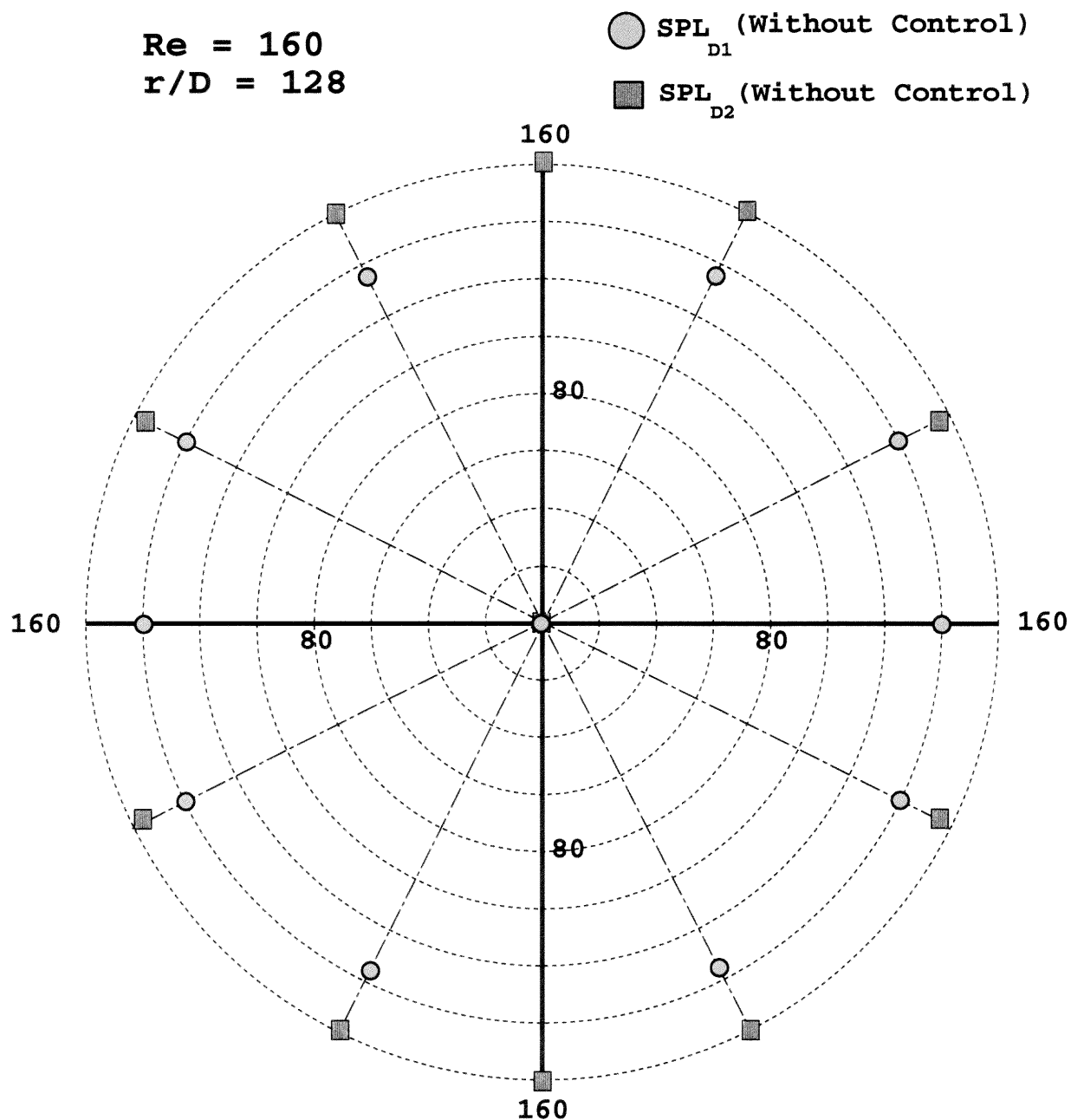


**Figure C.23** Directivity patterns for overall sound pressure level without control generated by the drag dipole ( $SPL_{D1}$ ) and lift dipole ( $SPL_{D2}$ ) at the Reynolds number  $Re = 160$ , Mach number  $M = 0.000342$ , and cylinder diameter  $D = 0.02$  m. The observers locations are at  $128D$  away from the cylinder. Axes units are decibels (dB, re:  $20 \times 10^{-15}$ )

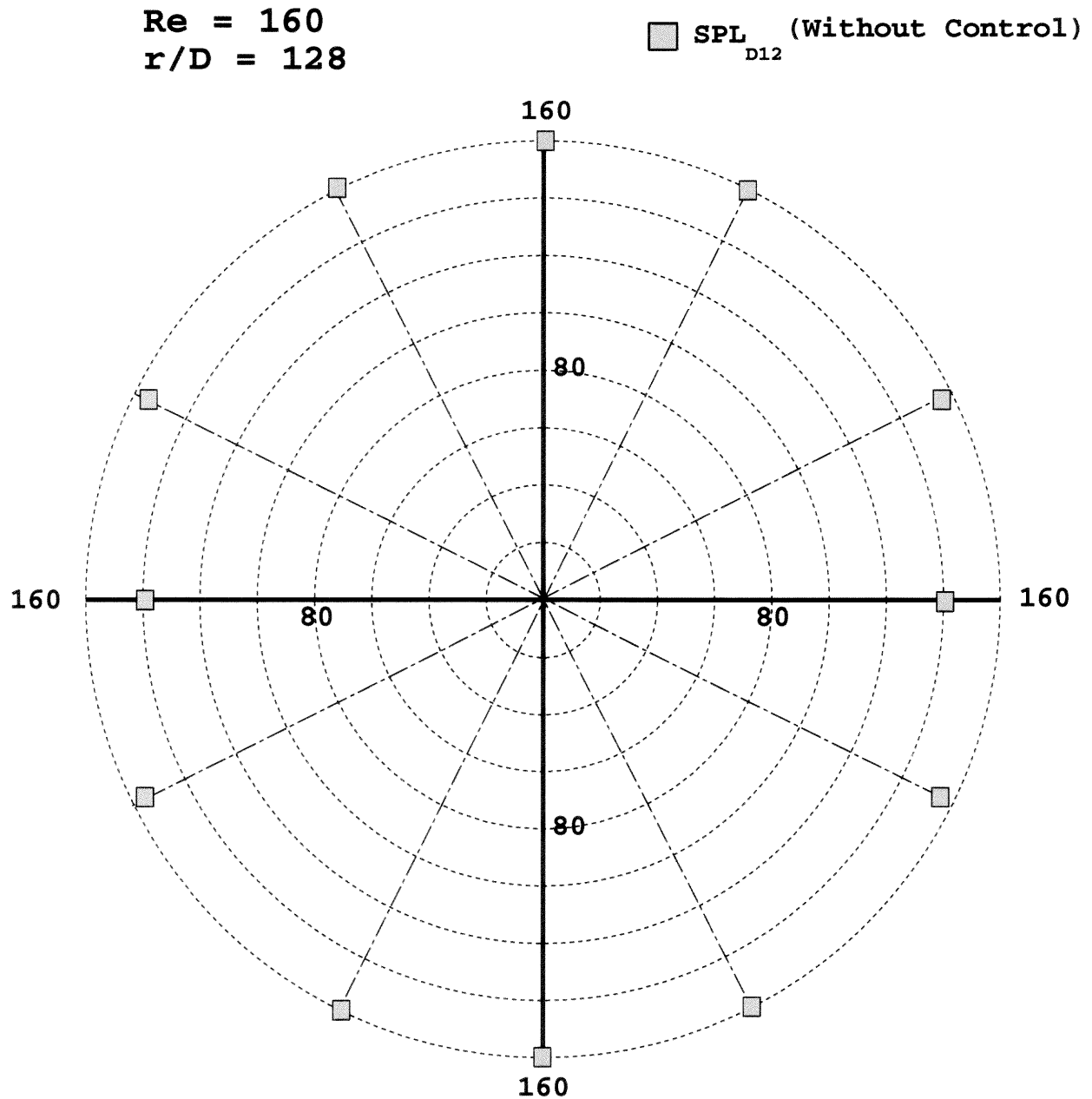


**Figure C.24** Directivity patterns for overall sound pressure level without control generated by the total dipole ( $SPL_{D12}$ ) at the Reynolds number  $Re = 160$ , Mach number  $M = 0.000342$ , and cylinder diameter  $D = 0.02$  m. The observers locations are at  $128D$  away from the cylinder. Axes units are decibels (dB, re:  $20 \times 10^{-15}$ )



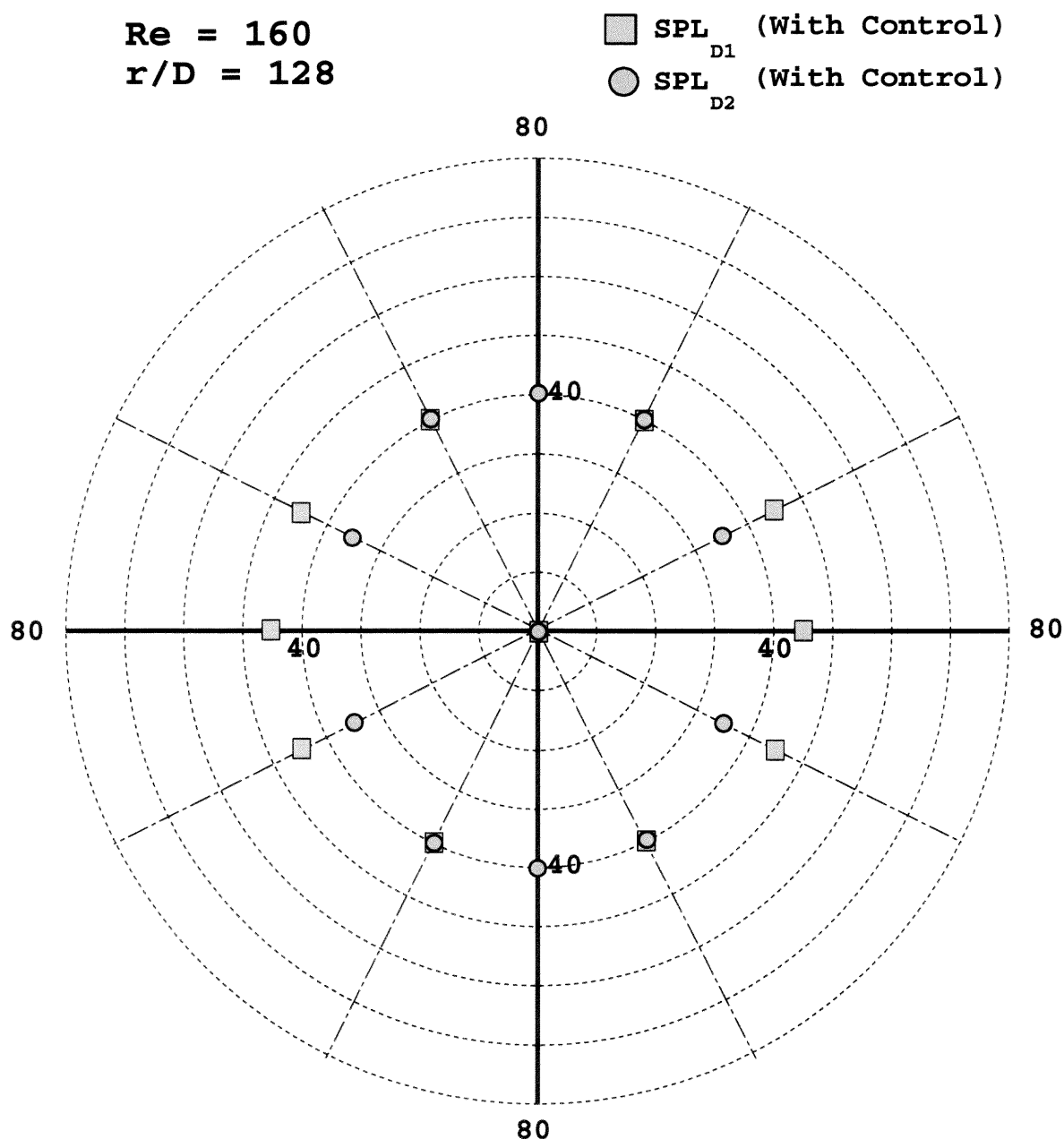


**Figure C.25** Directivity patterns for overall sound pressure level with control generated by the drag dipole ( $SPL_{D1}$ ) and lift dipole ( $SPL_{D2}$ ) at the Reynolds number  $Re = 160$ , Mach number  $M = 0.000342$ , and cylinder diameter  $D = 0.02$  m. The observers locations are at  $128D$  away from the cylinder. Axes units are decibels (dB, re:  $20 \times 10^{-15}$  )

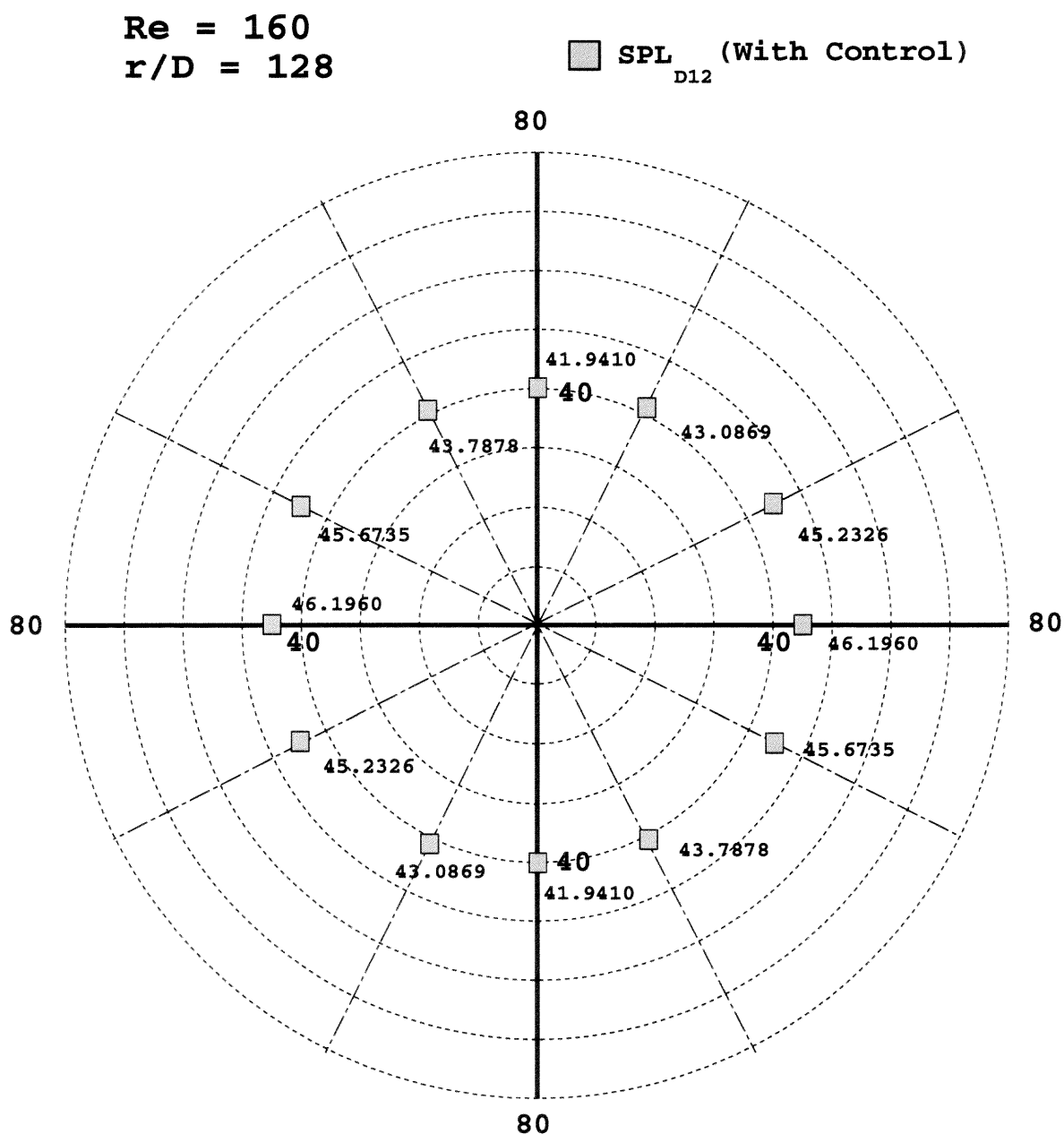


**Figure C.26** Directivity patterns for overall sound pressure level with control generated by the total dipole ( $SPL_{D12}$ ) at the Reynolds number  $Re = 160$ , Mach number  $M = 0.000342$ , and cylinder diameter  $D = 0.02$  m. The observers locations are at  $128D$  away from the cylinder. Axes units are decibels (dB, re:  $20 \times 10^{-15}$ )

## REFERENCES

1. Apelt, C. J. and West, G. S. 1975 The effects of wake splitter plates on bluff body in the range  $10^4 < R < 5 \times 10^4$ , Part 2: *J. Fluid Mech*, vol. 71, pp. 145-160.
2. Apelt, C. J., West, G. S., and Szewczyk, A. A. 1973 The effects of wake splitter plates on the flow past a circular cylinder in the range  $10^4 < R < 5 \times 10^4$ , *J. Fluid Mech*, vol. 61, pp. 187-198.
3. Bearman, P. W. 1967 The effect of base bleed on the flow behind a two-dimension model with a blunt trailing edge *Aero. Q.*, vol. 18, pp. 207-225.
4. Bechara, W., Lafon, P., Bailly, C., and Candel, S. M. 1995 Application of a  $\kappa - \epsilon$  turbulence model to the prediction of noise for simple and coaxial free jets. *J. Acoust. Soc. Am.*, vol.97(6), pp. 3518-3531.
5. Blevins, R. D. 1985 The effect of sound on vortex shedding from cylinders, *J. Fluid Mech*, vol. 161, pp. 217-237.
6. Chen, Z. and Aubry, N. 2000 Electro-magnetic feedback control of wake flows. *ICTAM Symposium*, Chicago, Illinois, USA.
7. Cimbala, J. M. and Grag, S. 1991 Flow in the wake of freely rotatable cylinder with splitter plate *AIAA*, vol. 29, pp. 1001-1003.
8. Colonnus, T., Lele, S. K., and Moin, P. 1994 The scattering of sound waves by a vortex: numerical simulation and analytical solutions. *J. Fluid Mech.*, vol. 206, pp. 271-298.
9. Crawford, C. and Karniadakis, G. E. 1997 Reynolds stress analysis of EMHD controlled wall turbulence. Part I Streamwise forcing. *Phys. Fluids*, vol. 9, 3, pp. 788-806.
10. Crighton, D. G. 1993 Computational aeroacoustics for low Mach number flows. In J. C. Hardin and M. Y. Hussaini, editors, *Computational Aeroacoustics*, Springer-Verlag Berlin. pp. 50-68.
11. Curle, N. 1955 The influence of solid boundaries upon aerodynamic sound. *Proc. Roy. Soc. A*, vol. 231, pp. 505-514
12. Farassat, F. and Succi, G.P. 1983 The prediction of helicopter discrete frequency noise, *Vertica*, pp. 309-320.
13. Ffowcs Williams, J. E., and Hawkins, D. L. 1969 Sound Generated by Turbulence and Surfaces in Arbitrary Motion, *Philosophical Transactions of the Royal Society*, vol. A264, No. 1151, pp. 321-342.

14. Lu, K. F., Wilson, R. D., Liu, H., and Stuessy, S. W. 1999 Experiments on Weakly-Ionized Air and Nitrogen Plasmas for Hypersonic Propulsion Facility Development, *AIAA*, paper 99-2448.
15. Lu, K. F., 2001 Personal Conversation.
16. Goldstein, M. E. 1974 *Aeroacoustics*, McGraw-Hill, New York.
17. Goldstein, M. E. and Rosenbaum, B. 1973 Effect of anisotropic turbulence on aerodynamic noise. *J. Acoust. Soc. Am.*, vol. 54, pp. 630-645.
18. Gunzburger, M. D. and Lee, H. C. 1996 Feedback control of Karman vortex shedding *J. Appl. Mech.*, vol. 63, pp. 828-835.
19. Henderson, R. D. and Barkley, D. 1996 Secondary instability in the wake of a circular cylinder, *Phys. Fluids*, vol. 8, pp. 1683-1685.
20. Henderson, R. D. and Karniadakis, G.E. 1995 Unstructured spectral element methods for simulation of turbulent flows, *J. Comput. Phys*, vol. 122, pp. 191-217
21. Henoch, C. and Stace, J. 1995 Experimental investigation of a salt water turbulent boundary layer modified by an applied streamwise magnetohydrodynamic body force. *Phys. Fluids*, vol. 7, 6, pp. 1371-1383.
22. Howe, M. S. 1975 Contributions to the theory of aerodynamic sound with applications to excess jet noise and the theory of the flute. *J. Fluid Mech*, vol. 71, pp. 625-673.
23. Howe, M. S. 1998 *Acoustic of fluid-structure interactions* , Cambridge University Press.
24. Kang, S.,Choi, H., and Lee, S. 1999 Laminar flow past a rotating circular cylinder, *Phys. Fluids*, vol. 11, pp. 3312-3321.
25. Kwon, K. and Choi, H. 1996 Control of laminar vortex shedding behind a circular cylinder using splitter plates, *Phys. Fluids*, vol. 8, pp. 479-486.
26. Lahjomri, J., Caperan, P., and Alemany, A. 1993 The cylinder wake in a magnetic field aligned with the velocity. *J. Fluid Mech*, vol. 253, pp. 421-448.
27. Lighthill, M. J. 1952 On sound generated aerodynamically, I: General theory, *Proceedings of the Royal Society*, vol. A221, pp. 564-587.
28. Lighthill, M. J. 1954 On sound generated aerodynamically, II: Turbulence as a source of sound, *Proceedings of the Royal Society*, vol. A222, pp. 1-32.
29. Lighthill, M. J. 1962 Sound generated aerodynamiclly: the Bakerian lecture. *Proc. Roy. Soc. Lond. A*, vol. 267, pp. 147-182.

30. Lighthill, M. J. 1963 Jet Noise. *AIAA*, vol. 1, pp. 1507-1517.
31. Lighthill, M. J. 1992 Report on the final discussion on computational aeroacoustics. *ICASE Report* 92-53.
32. Lilley, G. M. 1974 On the noise from jets. *AGARD CP-131*, pp. 13.1-13.12.
33. Lilley, G. M. 1993 Aerodynamic noise theory, *ICASE Report*.
34. Lilley, G. M. 1994 The radiated noise from isotropic turbulence. *Theor. Comput. Fluid Dyn.*, vol. 6, pp. 281-301.
35. Lilley, G. M. 1996 The radiated noise from isotropic turbulent with applications to theory of jet noise. *J. Sound Vibr.*, vol. 190(3), pp. 463-476.
36. Lush, P. A. 1971 Measurements of subsonic jet noise and comparison with theory. *J. Fluid Mech.*, vol. 46(3), pp. 477-500.
37. Mankbadi, R. R., Hayder, M. E., and Povinelli, L. A. 1994 Structure of supersonic jet flow and its radiated sound. *AIAA*, vol. 32(5), pp. 897-906.
38. Min, C. and Choi, H. 1999 Suboptimal feedback control of vortex shedding at low Reynolds numbers, *J. Fluid Mech*, vol. 401, pp. 123-156.
39. Mitchell, B. E., Lele, S. K., and Moin, P. 1992 Direct computation of sound from a compressible co-rotating vortex pair. *AIAA*, paper 92-0374.
40. Mitchell, B. E., Lele, S. K., and Moin, P. 1995 Direct computation of sound generated by subsonic and supersonic axisymmetric jets. Report TF-66, Department of Mech. Engineering, Stanford University.
41. Möhring, W. 1978 On vortex sound at low Mach number. *J. Fluid Mech*, vol. 85, pp. 685-691.
42. Mutschke, G., Gerbeth, G., and Shatrov, V. 1997 Two- and three-dimensional instabilities of the cylinder wake in an aligned magnetic field, *Phys. Fluids* vol. 9, pp. 3114-3116.
43. Park, D. S., Ladd, D. M., and Hendricks, E. W. 1993 Feedback control of a global mode in spatially developing flows, *phys. Lett.*, vol. 182, pp. 224-236.
44. Park, D. S., Ladd, D. M., and Hendricks, E. W. 1994 Feedback control of Von Karman vortex shedding behind a circular cylinder at low Reynolds numbers, *Phys. Fluids*, vol. 6, pp. 2390-2405.
45. Phillips, O. M., 1956 The intensity of Aeolian tones. *J. Fluid Mech.*, vol. 1, pp. 607-624.

46. Philips, O. M. 1960 On the generation of sound by supersonic shear layers. *J Fluid Mech.*, vol. 9, pp. 1-28.
47. Powell, A. 1964 Theory of vortex sound. *J. Acoust. Soc. America*, vol. 36, pp. 177-195.
48. Proudman, I. 1952 The generation of noise by isotropic turbulence, *Proc. Roy. Soc. A*, vol. 214, pp. 119-132.
49. Rayleigh, L. 1896 Theory of sound (2 vols.). *Macmillan*, London, 2nd edition.
50. Revell, J.D., Prydz, R. A., and Hays, A. P. 1977 Experimental study of airframe noise vs. drag relationship for circular cylinders, Lockheed Report 28074, Final Report for NASA contract NAS1-14403
51. Ribner, H. S. 1969 Quadrupole correlations governing the pattern of jet noise, *J. Fluid Mech.*, vol. 38(1), pp. 1-24.
52. Sarkar, S. and Hussaini, M. Y. 1993 Computation of sound generated by isotropic turbulent. *ICASE Report*, pp. 93-74.
53. Sarkar, S. and Hussaini, M. Y. 1993 Computation of the acoustic radiation from bounded homogeneous flows, *Computational Aeroacoustics*, Springer-Verlag, Eds. Hardin, J. C., Hussaini, M. Y..
54. Schumn, M., Berger, E., Monkewitz, P. A. 1994 Self-excited oscillations in the wake of two-dimensional bluff bodies and their control *J. Fluid Mech*, vol. 271, pp. 17-53.
55. Stokes, G. G. 1868 On the communication of vibrations from a vibrating body to a surrounding gas. *Phil. Trans.*, vol.158, pp. 447-463.
56. Strykowski, P. J. and Hannemann, H. 1991 Temporal simulation of the wake behind a circular cylinder in the neighborhood of the critical Reynolds number, *Acta. Mechanica*, vol. 90, pp. 1-20.
57. Tang, S. and Aubry, N. 1997 On the symmetry breaking instability leading to vortex shedding, *Phys. Fluids*, vol. 9, pp. 2250-2560
58. Tang, S. and Aubry, N. 1998 Controlling vortex shedding by insertion of vortices *Proceedings of the ASME Fluids Engineering Division Summer Meeting*, June 21-25, Washington, D. C..
59. Unal, M. F. and Rockwell, D. 1988 On the vortex formation from a cylinder, Part 2: Control by splitter-plate interference, *J. Fluid Mech* vol. 190, pp. 513-529.
60. Wang, M., Lele, S. K., and Moin, P. 1996 Sound radiation during local laminar breakdown in a low-Mach-number boundary layer. *J. Fluid Mech.*, vol. 319, pp. 197-218.

61. Wehrmann, O. H. 1965 Reduction of velocity fluctuations in a Karman vortex street by a vibrating cylinder, *Phys. Fluids*, vol. 8, pp. 760-761.
62. Weier, T., Fey, U., Gerbeth, G., Mutschke, G., Avilov, V. 2000 Boundary layer control by means of eletromagnetic forces. *ERCOFTAC* Bulletin 44, pp. 36-40.
63. Weier, T., Gerbeth, G., Mutschke, G., Platacis, E., and Lielausis, O. 1998 Experiments on cylinder wake stabilization in an electrolyte solution by means of electromagnetic forces localized on the cylinder surface. *Experimental Thermal and Fluid Science*, vol. 16, pp. 84-91.
64. White, A. F. 1975 *Our Acoustic Environment*, John Wiley & Sons, pp. 39-40.
65. Whitmore, J. and Sarkar, S. 1995 The computation of flow-generated sound using an acoustic analogy, *AIAA* paper 95-038.
66. Williamson, C. H. K. 1996 Mode A secondary instability in the wake of a circular cylinder, *Phys. Fluid*, vol. 8, pp. 1683-1685.
67. Williamson, C. H. K. and Roshko, A. 1988 Vortex formation in the wake of an oscillating cylinder, *J. Fluid Struct*, vol. 2, pp. 35-381.
68. Wood, C. J. 1946 The effect of base bleed on a periodic wake *J. R. Aeronaut*, vol. 68, pp. 477-482.
69. You, D., Choi, H., Choi, M., and Kang, S. 1998 Control of flow-induced noise behind a circular cylinder using splitter Plates, *AIAA*, vol. 36, No. 11.
70. Zorumski, W. E. 1993 Classical theoretical approaches to computational aeroacoustics, *Computational Aeroacoustics*, Springer-Verlag, Eds. Hardin, J. C., Hussaini, M. Y., pp. 41-49.